UNIVERSITY OF ICELAND

Ph.D. Dissertation

in Physics

Electrochemical Ammonia Synthesis on Transition Metal Carbides and Carbonitrides

Atef Iqbal

2024

FACULTY OF PHYSICAL SCIENCE
SCHOOL OF ENGINEERING AND NATURAL SCIENCES
UNIVERSITY OF ICELAND

Electrochemical Ammonia Synthesis on Transition Metal Carbides and Carbonitrides

Atef Iqbal

Dissertation submitted in partial fulfillment of a
Philosophiae Doctor degree in Physics

Supervisor
Prof. Egill Skúlason
Associate Prof. Younes Abghoui

Administrative Supervisor
Prof. Einar Örn Sveinbjörnsson

Ph.D. Committee
Prof. Egill Skúlason
Associate Prof. Younes Abghoui
Prof. Einar Örn Sveinbjörnsson
Dr. Helga Dögg Flosadóttir

Opponents
Prof. Max Garcia Melchor
Prof. Karoliina Honkala

Faculty of Physical Science
School of Engineering and Natural Sciences
University of Iceland
Reykjavik, November 2024

Electrochemical Ammonia Synthesis on Transition Metal Carbides and Carbonitrides
Dissertation submitted in partial fulfillment of a Philosophiae Doctor degree in Physics

Faculty of Physics
School of Engineering and Natural Sciences
University of Iceland
Dunhagi 5
107, Reykjavik
Iceland

Telephone: 525 4000

Bibliographic information:
Atef Iqbal, 2024, *Electrochemical Ammonia Synthesis on Transition Metal Carbides and Carbonitrides*, PhD dissertation, Faculty of Physics, University of Iceland,

Author ORCID: orcid.org/0009-0000-3364-1275
ISBN: 978-9935-9768-8-8

Printing:

Háskólaprent ehf., Fálkagötu 2, 107 Reykjavík

Reykjavík, Iceland, November 2024

Dedication

This thesis is dedicated to my beloved family, who have been my unwavering pillars of support and inspiration throughout this journey.

To my mother, your endless love, patience, and encouragement have been my guiding light. Your strength and determination have always inspired me to strive for excellence. Your sacrifices and unwavering belief in me have been the foundation of my success. I am eternally grateful for your unconditional support and the countless ways you have nurtured my dreams.

To the cherished memory of my late father, who taught me the value of hard work, integrity, and perseverance. Although you are no longer with us, your spirit and wisdom continue to guide me every day. This achievement is a testament to the values you instilled in me and the legacy of your love and dedication. I hope I have made you proud.

To my family, thank you for your endless love and encouragement. This accomplishment is as much yours as it is mine

Abstract

The world population is rising dramatically over the next 80 years, potentially reached to 11 billion people before stabilizing at the end of the century. This population growth will need higher food production, which can be accomplished more efficiently by using synthetic fertilizers instead of conventional manure. The large-scale catalytic Haber-Bosch process is currently used in the commercial production of synthetic fertilizers, notably ammonia. This method uses hydrogen gas (produced from natural gas or coal) and nitrogen as reagents to create ammonia over an iron-based catalyst, yielding carbon dioxide as a byproduct. Unfortunately, this strategy generates about 1% of world CO_2 emissions, increasing climate change. Furthermore, due to the enormous energy requirements required to break the stable dinitrogen molecule, the process occurs at high pressures and temperatures, necessitating massive, centralized ammonia production plants.

This thesis explores the electrochemical nitrogen reduction process, which has the potential to directly create ammonia from nitrogen and water using electricity as an energy source. This method could potentially result in a carbon-neutral process if the electricity is generated by renewable sources such as wind or solar power. Furthermore, the process may operate at (near) ambient conditions, allowing for localized production without the need for shipping or storage.

We present the computational design of potential new, cost-efficient electrocatalysts composed of transition metal carbides and carbonitrides in this thesis. These materials are predicted to facilitate the electrochemical reduction of molecular nitrogen to ammonia in aqueous media under ambient conditions with only a small applied bias. Electronic structure calculations at the density functional theory level are utilized to evaluate the performance of this new class of materials for electrochemical ammonia formation. The predominant reaction mechanism enabling this process is identified as the Mars-van Krevelen mechanism, rather than the conventional associative or dissociative mechanisms.

Among a range of transition metal carbides and carbonitrides explored in this thesis, WC, TaC, VCN, and NbCN emerge as the most promising electrocatalysts, based on a comprehensive density functional theory analysis. These four materials exhibit greater activity toward nitrogen reduction compared to the competing hydrogen evolution reaction, unlike pure metal catalysts, which predominantly evolve hydrogen. We also investigate its stability against possible decomposition under operating conditions and poisoning. It is shown that extremely effective ammonia creation depends on particular single-crystal surfaces since polycrystalline surfaces can cause catalyst decomposition.

This work represents a significant step toward the development of a reasonably affordable process for synthesizing ammonia, therefore allowing the synthesis of high-value nitrogenous compounds directly from air, water, and renewable electricity under ambient conditions.

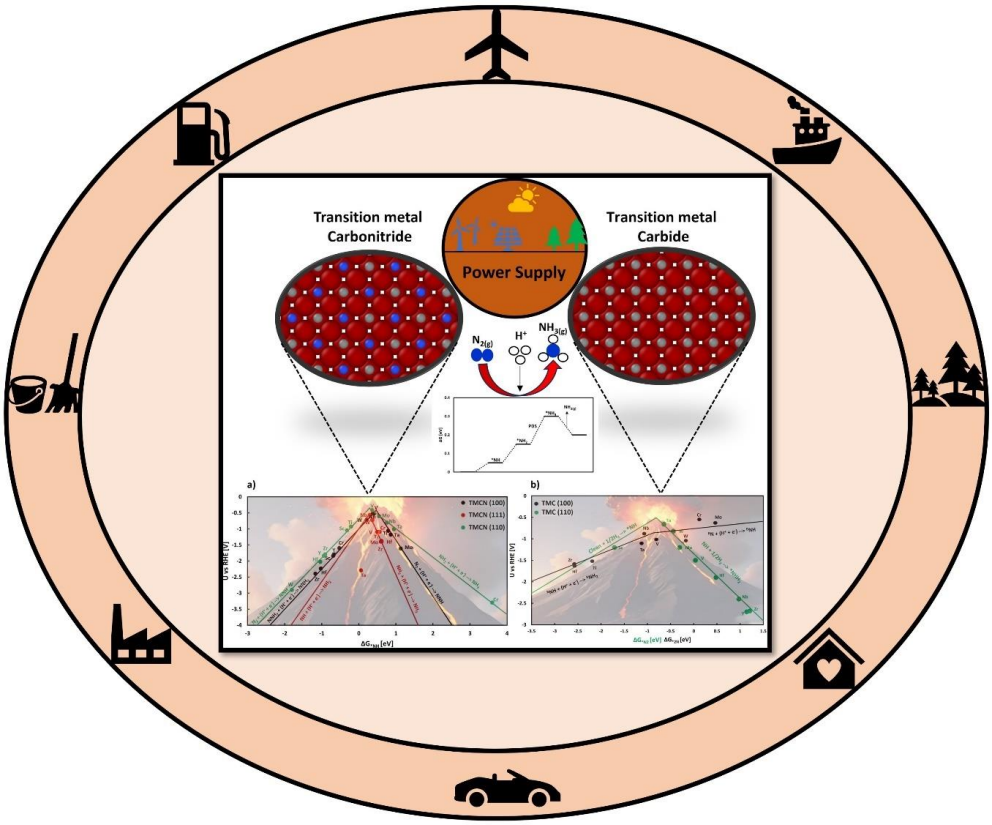

Figure 1 This picture provides an in-depth exploration of the research carried out in this thesis. It includes the Volcano plots for transition metal carbides and transition metal carbonitrides in the model structure (100) facets of the rocksalt structure, an example of a free energy diagram, and examples of ammonia applications.

Útdráttur

Á næstu 80 árum er spáð dramatísk fólksfjölgun í heiminum sem gæti leitt til þess að íbúafjöldi jarðarinnar muni ná 11 miljörðum áður en hann staðnar fyrir lok aldarinnar. Þessi fólksfjöldi mun krefjast aukinnar matvælaframleiðslu, sem hægt er að ná á skilvirkari hátt með tilbúnum áburði. Fjöldaframleiðsla á tilbúnum áburði, sér í lagi á ammóníaki, er framkvæmd með aðferð Haber-Bosch. Þessi aðferð notar vetni (búið til frá jarðgasi eða kolum) og köfnunarefni sem hvarfefni til að mynda ammóníak með járn-hvata, sem myndar koltvíoxíð sem aukaafurð. Þessi aðferð er því miður ástæðan fyrir um 1% af CO_2 losun mannkyns, sem eykur áhrif gróðurhúsaáhrifa á jörðinni. Þar að auki, vegna stögugleika niturs sameindarinnar þarf mikla orku til að brjóta efnatengi hennar, þess vegna þarf aðferðin háan þrýsting og hátt hitastig. Til þess að geta búið til þær aðstæður fyrir ferlið þarf risastórar miðlægar ammóníakframleiðslustöðvar.

Þessi ritgerð kannar rafefnaafoxun köfnunarefnis, sem hefur möguleika á að framleiða ammóníak úr köfnunarefni, vatni og rafmagni. Þessi aðferð gæti hugsanlega leitt til kolefnislauss ferlis ef rafmagnið er framleitt með endurnýjanlegum orkugjöfum eins og vind- eða sólarorku. Enn fremur getur ferlið gengið við (nánast) umhverfisaðstæður, sem gerir staðbundna framleiðslu mögulega án þess að þurfa flutning eða geymslu.

Í ritgerðinni kynnum við reikniefnafræðilega hönnun á mögulegum nýjum, hagkvæmum rafefnahvötum sem samanstanda af málmkarbíðum og málmkarbónítríðum. Við spáum fyrir að tilteknir efnahvatar geti rafafoxað köfnunarefnissameindinni í ammóníak, í vatnslausn við umhverfishita og -þrýsting með aðeins lítilli spennu. Þéttnifellafræðilegir reikningar á rafeindabyggingu eru notaðir til að meta frammistöðu þessara nýju rafhvataflokka fyrir ammóníakmyndun. Megin rafefnahvarfið sem gerir þetta ferli mögulegt eru svokallað Mars-van Krevelen hvarfið, frekar en hefðbundin samtengingarhvörf eða sundrunarhvarf.

Á meðal fjölmargra málmkarbíða og málmkarbónítríða efnahvata sem rannsakaðir eru í þessari ritgerð eru WC, TaC, VCN og NbCN spáð fyrir um að vera efnilegir rafefnahvatar, út frá yfirgripsmikilli greiningu með tölvureikningunum. Þessi fjögur efni sýna meiri virkni fyrir ammóníaksmyndun en fyrir vetnismyndun sem er samkeppnishvarfið í þessu ferli. Það er ólíkt hreinum málmhvötum sem framleiða aðalega vetni. Við rannsökum einnig stöðugleika þeirra gegn mögulegu niðurbroti þeirra við notkunaraðstæður sem og að þeir mengist. Sýnt er að mjög áhrifarík ammóníakmyndun byggist á sérstökum einkristallayfirborðum þar sem fjölkristallayfirborð geta valdið niðurbroti hvatanna.

Þessi vinna er stórt skref í átt að þróun á sjálfbæru ferli fyrir ammóníakframleiðslu, sem myndar verðmæt köfnunarefnissambönd beint úr lofti, vatni og endurnýjanlegu rafmagni við umhverfisaðstæður.

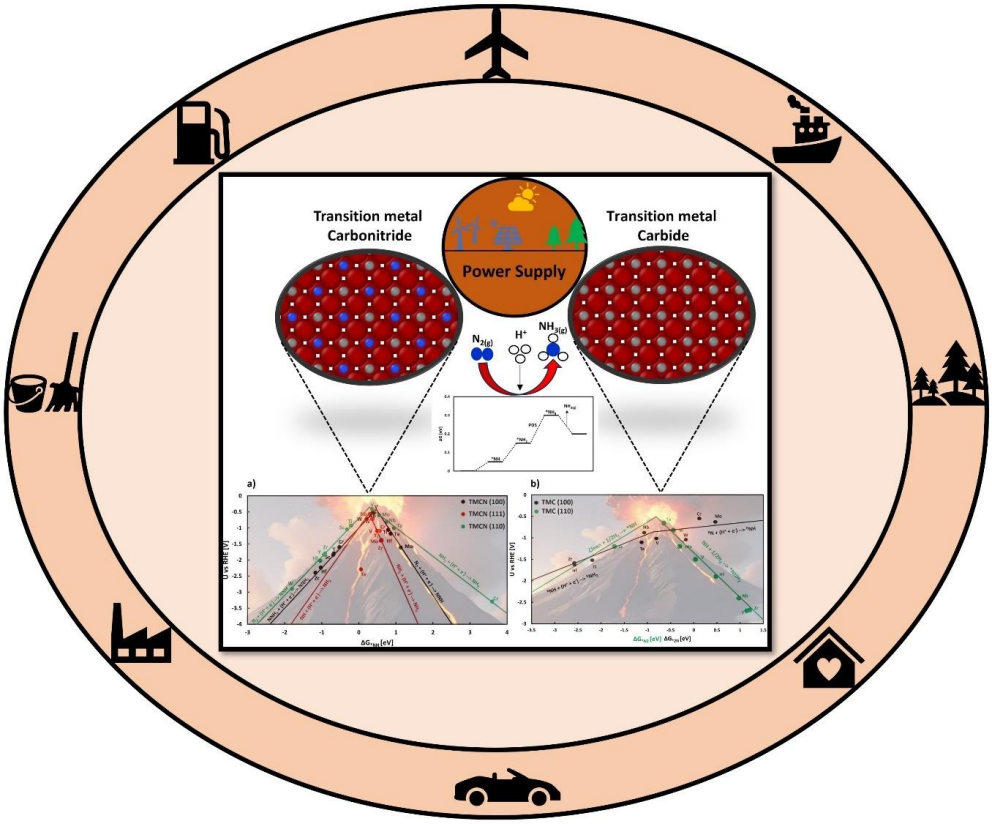

Figure 2 Þessi mynd tekur saman helstu rannsókninar sem unnar er í þessari ritgerð. Hún inniheldur: eldgosagraf fyrir karbít og karbónítríð úr hliðarmálmum í (100) fleti steinsalts krystalbyggingar, dæmi um fríorku graf og dæmi um notkun ammóníaks.

Preface

This thesis is submitted in candidacy for a Ph.D. degree from the University of Iceland. The work was conducted between November 2021 and November 2024 at the Faculty of Physical Science, School of Engineering and Natural Sciences supervised by Prof. Egill Skúlason and Associate Prof. Younes Abghoui.

A project grant from the Icelandic Research Fund (RANNÍS, grant no. 207056), financially supported the work.

Atef Iqbal

November 2024.

Contents

List of Figures

Publications Included in This Thesis

1. Ellingsson, V., **Iqbal, A.,** Skúlason, E., & Abghoui, Y. (2023). Nitrogen Reduction Reaction to Ammonia on Transition Metal Carbide Catalysts. *ChemSusChem*, DOI: 10.1002/cssc.202300947.
2. **Iqbal, A.,** Skúlason, E., & Abghoui, Y. (2024). Are (100) facets of transition metal carbonitrides suitable as electrocatalysts for nitrogen reduction to ammonia at ambient conditions?. *International journal of hydrogen energy*, DOI: 10.1016/j.ijhydene.2024.03.282.
3. **Iqbal, A.,** Skulason, E., & Abghoui, Y. (2024). Electrochemical Nitrogen Reduction to Ammonia at Ambient Condition on the (111) Facets of Transition Metal Carbonitrides. *ChemPhysChem*, DOI: 10.1002/cphc. 202300991
4. **Iqbal, A.,** Skúlason, E., & Abghoui, Y. (2024). Catalytic Nitrogen Reduction on the Transition Metal Carbonitride (110) Facet: DFT Predictions and Mechanistic Insights. *The Journal of Physical Chemistry C*. DOI: 10.1021/acs.jpcc.4c02148
5. **Iqbal, A.,** Skúlason, E., & Abghoui, Y. (2024). Understanding the Mechanistic Pathways of N_2 Reduction to Ammonia on (110) Facets of Transition Metal Carbides. *Crystals*, DOI: 10.3390/cryst14090770.

Publications Not Included in This Thesis

6. Abghoui, Y., **Iqbal, A.,** & Skúlason, E. (2023). The role of overlayered nitride electro-materials for N_2 reduction to ammonia. *Frontiers in Catalysis*, DOI: 10.3389/fctls.2022.1096824.

7. Ashraf, N., **Iqbal, A.,** & Abghoui, Y. (2024). Exploring reaction mechanisms for CO_2 reduction on Carbides. *Journal of Materials Chemistry A*. DOI: 10.1039/D4TA05592F

8. Ashraf, N., Diego Bitzenhofer Betolaza., Hálfdán Ingi Gunnarsson., Mohammad Iman Khatibi., **Iqbal, A.,** Abghoui, Y. How can phosphides catalyze CO_2 reduction reaction? Journal of *Electrochimica Acta*. (Submitted)

Patent

1) **Title: Process for electrolytic production of ammonia from nitrogen using metal carbide catalysts**
   Inventors: Egill Skúlason, Younes Abghoui, **Atef Iqbal,** Viktor Ellingsson, Helga Dögg Flosadóttir
   Application. number: PCT/IS2024/050004
   Application. date: 02.07.2024

2) **Title: Process for electrolytic production of ammonia from nitrogen using metal carbonitride catalysts**
   Inventors: Egill Skúlason, Younes Abghoui, **Atef Iqbal,** Helga Dögg Flosadóttir
   Application. number: PCT/IS2024/050005
   Application. date: 02.07.2024

My Contribution to the Publications

Article 1: I performed the dos and band structure calculation. I helped with writing and reading the manuscript.

Article 2: I performed all the DFT calculations and subsequent data analysis. I wrote the first draft of the manuscript and was the primary person responsible for its editing. I respond to the comments and suggestions raised during the peer-review process.

Article 3: I performed all the DFT calculations and subsequent data analysis. I wrote the first draft of the manuscript and was the primary person responsible for its editing. I respond to the comments and suggestions raised during the peer-review process.

Article 4: I performed all the DFT calculations and subsequent data analysis. I wrote the first draft of the manuscript and was the primary person responsible for its editing. I respond to the comments and suggestions raised during the peer-review process.

Article 5: I performed all the DFT calculations and subsequent data analysis. I wrote the first draft of the manuscript and was the primary person responsible for its editing. I respond to the comments and suggestions raised during the peer-review process.

Article 6: I performed the dos and band structure calculation. I helped with writing and reading the manuscript.

Article 7: I helped with writing and reading the manuscript.

Article 8: I helped with writing and reading the manuscript.

Contribution to Patent 1: I performed all the DFT calculations and subsequent data analysis.

Contribution to Patent 2: I performed all the DFT calculations and subsequent data analysis.

Abbreviations

NH_3 Ammonia

N_2 Nitrogen gas

2N Atomic Nitrogen

H_2O Water

CH_4 Methane

CO_2 Carbon dioxide

FAO Food and Agriculture Organization

DFT Density Functional Theory

TMC Transition Metal Carbide

TMCN Transition Metal Carbonitride

NRR Nitrogen Reduction Reaction

HK Hohenberg-Kohn

KS Kohn-Sham

V_{eff} Effective Potential

LDA Local Density Approximation

GGA Generalized Gradient Approximation

PAW Projector-Augmented-Wave method

PBE Perdew-Burke-Eernzerhof

RPBE Revised Perdew-Burke-Eernzerhof

VASP Vienna ab initio simulation package

E_{cut} Energy Cutoff

eV Electron Volt

RS Rocksalt

Å Angstrom

IS Initial State

TS Transition State

FS Final State

NEB Nudged Elastic Band

NMA Normal Mode Analysis

PES Potential Energy Surface

ΔG Gibbs Free Energy

ZPE Zero Point Energy

LA Longitudinal Acoustic

TA Transverse Acoustic

LO Longitudinal Optic

TO Transverse Optic

DM Dissociative Mechanism

AM Associative Mechanism

MvK Mars van Krevelen mechanism

PDS Potential Determining Step

RDS Rate Determining Step

SHE Standard Hydrogen Electrode

RHE Reversible Hydrogen Electrode

CI-NEB Climbing Image Nudged Elastic Band

ORR Oxygen Reduction Reaction

HER Hydrogen Evolution Reaction

Ψ Wave Function

H Hamiltonian Operator

$\mathbf{E_{xc}}$ Exchange Correlation Energy Chemical Potential

$\mathbf{E_a}$ Activation Energy

$\mathbf{E_d}$ Dissociation Energy

i Current Density

Acknowledgments

Completing this thesis has been a journey of intellectual and personal growth, and it would not have been possible without the support, guidance, and encouragement of many wonderful individuals.

First and foremost, I would like to extend my heartfelt gratitude to my esteemed supervisors, Egill Skúlason and Younes Abghoui. Your unwavering support, invaluable insights, and exceptional mentorship have been the cornerstone of my research. Egill, your profound knowledge, and critical feedback have consistently pushed me to refine my work, while Younes, your innovative ideas, and steadfast encouragement have inspired me to explore new horizons. Together, your guidance has been instrumental in shaping this thesis, and for that, I am eternally grateful.

I would like to extend my heartfelt gratitude to Dr. Helga Dögg Flosadóttir for the insightful discussions we had at Atmonia. Your expertise and thoughtful feedback were incredibly valuable and have significantly contributed to the refinement of my research. Thank you for your time, support, and the enriching exchange of ideas. I would like to express my sincere thanks to Prof. Einar Örn Sveinbjörnsson. Although we haven't had the opportunity to collaborate scientifically, your constant warm smiles and positive demeanor have always been uplifting. Additionally, I am truly grateful for your support in approving my credit, which has been immensely helpful in my academic journey.

I would like to express my deepest gratitude to my opponents, Dr. Max Garcia Melchor, Ikerbasque Research Professor at CIC Energigune, Vitoria, Spain, and Dr. Karoliina Honkala, Professor at the Department of Chemistry, University of Jyväskylä, Finland. Your expertise and insightful perspectives have not only enriched the quality of my work but also pushed me to think critically and refine my research. I am immensely grateful for the time and effort you have dedicated to reviewing my thesis.

I would also like to offer my sincere thanks to my family, specifically my brothers (Dr Muslim Khan, Qasim Khan, Yousaf Khan) and sisters, whose love and support have been my bedrock throughout this journey. Your constant encouragement and belief in my abilities have been a source of immense strength. A special acknowledgment goes to my beloved wife Unaiza Yashfeen. Your love, patience, and understanding have been a constant source of comfort and motivation. Your sacrifices and unwavering belief in me have enabled me to dedicate myself wholeheartedly to this research. Your support has been invaluable, and I am profoundly thankful for your presence in my life.

I would also like to thank my friends (Javed Hussain, Muhammad Umar, Muhammad Sulaman Nawaz) and colleagues (Naveed Ashraf, Muhammad Awais, and Diego Bitzenhofer Betolaza) who have provided a supportive and stimulating environment, fostering both my personal and professional growth. Your camaraderie and encouragement have made this journey all the more rewarding.

Finally, I wish to express my gratitude to all those who have contributed to this thesis in various ways, whether through academic collaboration, administrative support, or personal encouragement. Your contributions have not gone unnoticed, and I am deeply appreciative of your efforts.

In conclusion, this thesis would not have been possible without the collective support, guidance, and encouragement from all of you. Thank you for being a part of this incredible journey.

Atef Iqbal

1 Introduction

This chapter aims to clarify for you a basic justification for our project's motivation. Consider it as "Ammonia for beginners". I will start with a brief background of ammonia, discuss why it's essential nowadays, and then touch on a major problem we're facing: the worldwide climate crisis. We'll relate this to issues including overpopulation, groundwater pollution, and the necessity of fertilizer in less developed nations. All is related to things like clean water and food, two major UN objectives [1]. Let's start with Fritz Haber:

1.1 The Legacy of Fritz Haber: Hero or Villain?

Fritz Haber, a character torn by tragedy and controversy, serves as the foundation of our story. Although he was born in Prussia in incest, he was a fervent supporter of Germany after converting to Christianity from his Jewish background. This chapter could explain a lot more about the conflicting parts of his life. For example, he pioneered chemical warfare in World War I by developing toxic gasses that killed millions, yet his agricultural breakthroughs are critical to the survival of half of the world's population today. His personal life was as turbulent, as evidenced by his wife, Dr. Clara Immerwahr, who committed suicide, probably as a result of sorrow for his conduct during the war. Furthermore, the awful irony is that those substances he created were eventually used to kill members of his own extended Jewish family in detention camps by the nation he so fiercely defended. Rather than delving further here [2], I recommend reading his biography, which contains a thorough and intriguing account of his life.

One particularly crucial aspect of my research is how he fed half of the world's population [3]. Farmers have been aware for thousands of years that applying manure to fields promotes greater crop production [4]. It was discovered in the 1800s that nitrogen-containing manure was excellent for promoting greater crop growth after experimenting with various kinds of both natural and man-made manure [5]. The challenging aspect is that, although the air we breathe contains a lot of nitrogen, plants require a certain sort of nitrogen known as N_2, which cannot be used immediately [6]. It is "inert," meaning that its two nitrogen atoms are genuinely fond of one another and will only mingle with other atoms when absolutely necessary. Rest assured, though, that will be covered in more detail later.

Where can we therefore find nitrogen that plants can genuinely use? It happens that there are some far-off places, such as South America. One naturally occurring rock in Chile called caliche contains nitrogen that plants can use. There are also other islands, especially those near Peru, where guano, which is essentially bat and bird droppings, is found. Unbelievably, guano is high in nitrogen as well. Long-term, though, it's not exactly the best idea to gather all this stuff and ship it halfway around the world to be used as fertilizer. The caliche deposits will eventually run out, and it's not good either to disturb the homes of birds and bats [7]. Sir William Crookes brought to attention a serious issued in 1898. The biggest problem of the 20^{th} century, he underlined, would be figuring out how to boost food production without harming the environment. He thought that the discovery of answers would mostly depend on chemists [8]. Moreover, you know what? He could forecast the future really well even more so than Nostradamus!

In 1909, there was a big breakthrough to stop people from going hungry. Our chemist, Fritz Haber, figured out how to make ammonia (NH_3) in his lab. He made the lazy N_2 molecule mix with hydrogen, using a special trick called catalysis [9]. This was good news for the birds and bats leaving guano behind. It wasn't good for Chile's economy. [10].

1.2 BASF's Ammonia Revolution

The German company BASF quickly acquired the method for producing ammonia from air. They needed to expand the process, so they entrusted Carl Bosch with the task. Bosch efficiently scaled up the process within just one year, moving from Haber's small-scale model to a full-scale production facility. By 1913, Germany was able to produce 20 tons of ammonia per day [7]. This was crucial for Germany because the allied powers had cut off trade with Chile, where Germany had previously obtained fertilizer. Unfortunately, ammonia can also be used to make explosives, which significantly aided the German war effort and prolonged World War I [9].

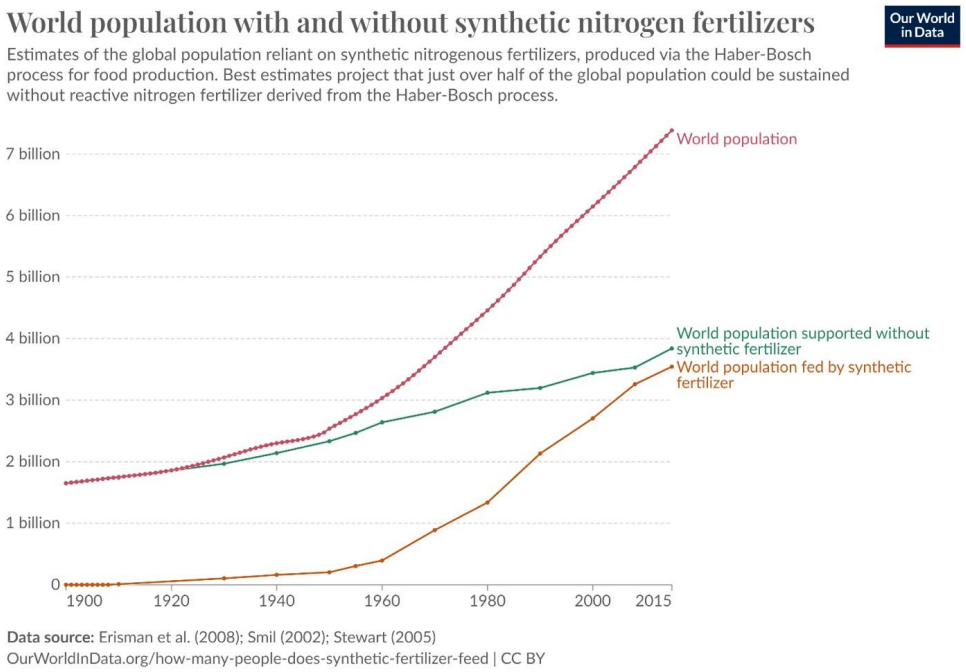

Figure 1.1 Data from 1900 to 2015, showing global population estimates with and without synthetic fertilizer "World population with and without synthetic nitrogen fertilizers". Accessed online at OurWorldInData.org. Available at:'https://ourworldindata.org/grapher/world-population-with-and-without-fertilizer?time=1900..2015' [3, 11, 12].

A novel method of producing ammonia, the Haber-Bosch process, was made widely available after the war. Large-scale manufacturing enabled ammonia to be widely available for crop fertilizing to feed the expanding population [13]. Over the last century, this discovery made by Fritz Haber has contributed to notable population growth (Figure 1.1) [14]. Approximately half of the nitrogen in our bodies now originates from the Haber-Bosch process [15]. However, producing ammonia from the extremely stubborn N_2 molecule requires tremendous heat and pressure, which are costly. Accordingly, these huge ammonia production plants can only be built by wealthy nations. The ammonia is sold at a higher price and sent to places that can't afford to make it themselves. Also, hydrogen, while it's everywhere, isn't easy to get in its pure form. There is plenty of it in methane (CH_4), which can be combined with water (H_2O) through a process called catalysis to produce pure hydrogen, which is useful for making ammonia. Sadly, the carbon from methane doesn't vanish; it combines with the oxygen from water to make carbon dioxide (CO_2) [16]. Unless you've been hiding under a rock, you've probably heard that CO_2 is a greenhouse gas, which isn't good for the environment [17]. These gases hang around in our atmosphere, like a big blanket for the earth, trapping heat and gradually warming up the planet. Since we're making a lot of ammonia nowadays, about 1% of the CO_2 we're adding to the air comes from the Haber-Bosch process [18].

1.3 The Two Faces of Ammonia: Sustenance vs. Strain

There's an ironic situation in this field. I have mentioned that ammonia is critical because it supports half the population's survival. However, as we feed more people and our population grows, it places greater stress on Earth's resources and worsens climate change [19]. Despite debates on overpopulation, ammonia production is not helping to reduce these pressures. Although our planet is under strain, as seen in Figure 1.2 the population growth rate has actually been decreasing since the 1960s due to reduced global poverty [20], lower child mortality, and improvements in education [21] and healthcare [22]. Since of all these reasons, women are having fewer children and establishing families later in life, mostly because they are better educated, and more children are living to adulthood. Lower birth rates in more developed nations aid to slow down population increase [23]. The world population is nevertheless increasing. Before the population stabilizes, researchers predict that it could reach 11 billion without significant interruptions like a worldwide pandemic or war [24].

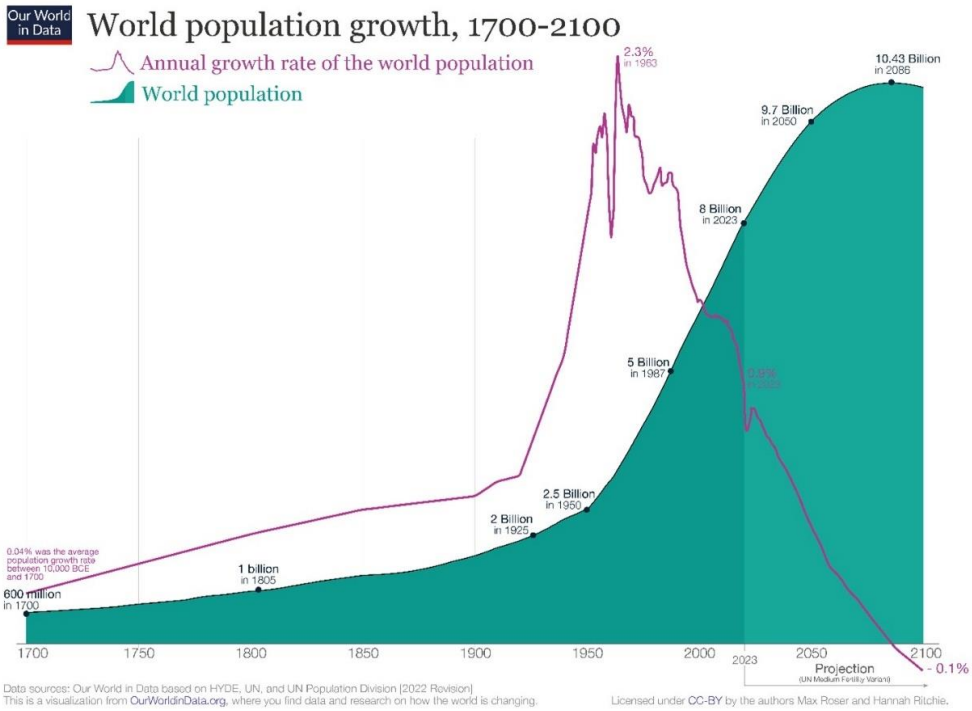

Figure 1.2 Global population trends and growth rates up to 2023, along with future projections until 2100. This information was provided by Max Roser in 2015 in "World Population Growth, 1750-2100," available on OurWorldInData.org. Access the full data at: https://ourworldindata.org/world-population-growth.

Making fertilizer available to developing nations is essential because lowering hunger can enhance living conditions and regulate growth in population, which proves beneficial for the environment. However, there are some issues. One concern is that the Haber-Bosch method for manufacturing fertilizer emits a lot of CO_2. Another issue is inefficient fertilizer application [3]. Farmers frequently purchase enormous amounts of fertilizer and use more than is necessary, believing that it will produce more harvests. However, a plant's ability to absorb fertilizer at one time is limited [25]. Certainly, the farmer wants to push the limits in order to maximize profits. They will use as much fertilizer as they can if they can get it cheaply. While this approach appears to increase crop yield, any extra fertilizer that the plants cannot take is washed away. You may have heard about groundwater pollution and nitrate run-offs [26], which are frequently caused by farmers applying too much fertilizer. Convincing farmers to minimize their fertilizer usage is difficult because they emphasize maximizing crop yield per square meter. As a result, they tend to use a lot of fertilizer, which harms the ecosystem [27].

These two major concerns, CO_2 emissions, and groundwater pollution will worsen as places without the infrastructure or early resources to create Haber-Bosch facilities get access to fertilizers during their development. Take Sub-Saharan Africa, which today has 1.1 billion people. According to estimates, by the end of this century, the population will range from 2.6 [28] to 4.2 billion [29]. Currently, they generate and use little synthetic fertilizer, as seen in Figure 1.3. However, with predicted developments, there will be an increasing demand for fertilizer to improve crop production efficiency, which is currently primarily based on the Haber-Bosch method [30].

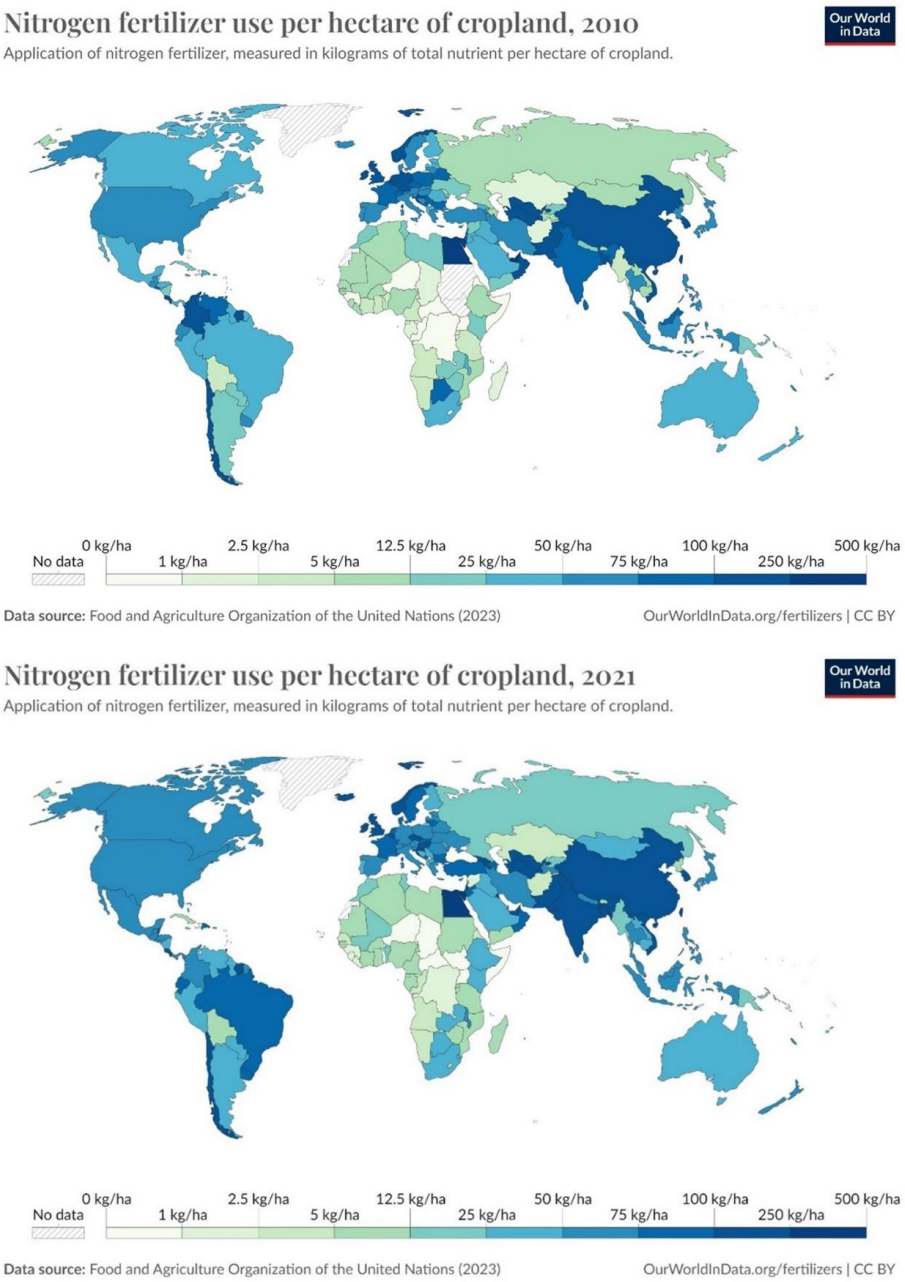

Figure 1.3 The top image displays global ammonia production in 2010, while the bottom image depicts global ammonia application in 2021. These data were sourced from the Food and Agriculture Organization of the United Nations (FAO) in 2020 and can be accessed online at OurWorldInData.org/fertilizers.

The scenario appears grim. Although demand for ammonia is large and likely to rise in the future, its manufacturing contributes to climate change and groundwater pollution. Furthermore, establishing the massive Haber-Bosch facility necessary for production requires a significant capital expenditure [31]. So, how do we handle these challenges? Enter my project, surrounded by the melodious sounds of a heavenly band and trumpets. By implementing the power of catalysis, it is possible to persuade the inert N_2 molecule to split using electricity rather than the high pressure and temperature conditions of the Haber-Bosch process [32-35]. By eliminating the requirement for high pressure, we can eliminate the demand for large facilities. Remember that high pressure requires pricey components, which favors large-scale facilities in terms of economic sustainability. Furthermore, the electricity required for this process can be obtained from renewable sources such as solar or wind power. Furthermore, a vital component, hydrogen, can be derived from water rather than methane, making the entire process carbon neutral. This entire operation can be housed in a small device, and conveniently put on a farm where ammonia is required. Operation requires only air, water, and electricity. The fertilizer can be given directly and continuously into the irrigation system in precise amounts, guaranteeing that the plants absorb all of it without any surplus seeping into groundwater. Although Haber-Bosch fertilizer can be used for precision application, it would require additional on-farm storage throughout the growing season. It is crucial to emphasize that concentrated ammonia carries hazards if mishandled [36]. This risk is lessened when the ammonia is created on-site by electrochemistry, eliminating the need for farmers to dilute it themselves.

Although the concept of this innovative device is captivating, its realization remains a distant prospect [37, 38]. Optimistically, I can say that my work over the past three years has nudged us a bit closer to this objective, as you will discover as you continue reading. Technical details might lose some readers, prompting them to skip to the conclusion for a brief summary. However, through this introduction, I aim to impart knowledge to you whether you are a friend, family member, colleague, opponent, or stranger about the pressing challenges humanity faces today and in the future. Climate change, access to clean water, and world hunger are inextricably linked, necessitating a comprehensive approach. It all starts with respecting expert evidence and data, especially in today's misinformation-filled environment. We can address the looming issues ahead of us by engaging in informed discussions based on facts.

1.4 Ammonia Significance in the Landscape

Over the last 200 years, industrialization has resulted in a wide range of human activities that have greatly harmed the natural environment. Increased amounts of CO_2 in the atmosphere, mostly as a result of fossil fuel use, have played a significant role in the greenhouse effect and global warming [39]. In recent decades, substantial research has concentrated on identifying alternative energy sources, such as hydrogen, to reduce CO_2 emissions [40]. Hydrogen production has been investigated using a variety of sustainable and renewable technologies, including solar water splitting. However, the storage and delivery of hydrogen provide additional obstacles and costs for the implementation of this technique. Using NH_3 instead of liquid hydrogen could make the hydrogen economy better in the future. Ammonia has more hydrogen in it (1.4 wt% more than methanol) and packs more energy into the same space compared to liquid hydrogen [41]. NH_3 is also really

important in food and energy industries, with 178 million tons used each year. Apart from making fertilizers, NH_3 is used to make explosives, plastics, resins, synthetic fibers, and refrigerants (Figure 1.4) [42]. It can also be used as a fuel in certain types of fuel cells, vehicles, and heating systems. Since it is liquid and has a lot of energy packed in, NH_3 is great for storing energy and can be used in lots of different ways without problems with capacity, transportation, or getting it to far-away places [43].

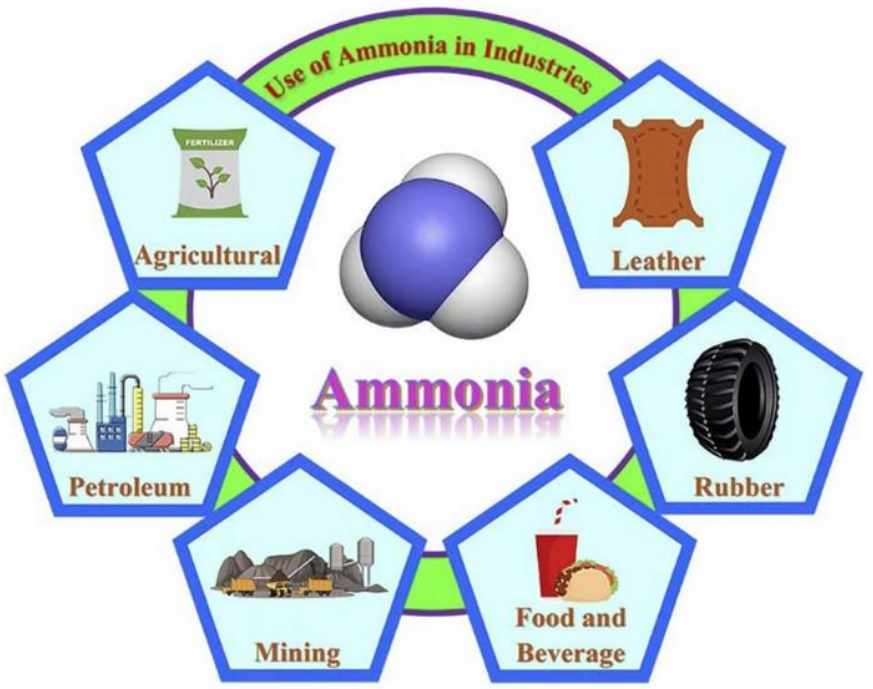

Figure 1.4 Shows the uses of ammonia [44].

1.4.1 Environmentally Friendly NH_3 Production

Recently, many approaches to green and sustainable energy production have been proposed, including molecular catalysis, photo-electrochemical processes, and electrochemical reduction of N_2 to yield NH_3. A variety of transition metal-based molecular catalysts for NH_3 synthesis, inspired by electrochemical N_2 reduction, have been developed and tested [45-47]. However, there are still issues in properly comprehending the processes and stability of these catalysts in this technique [48]. In addition, research has been conducted into photo-electrochemical N_2 reduction and N_2 oxidation into NH_3 and nitrates. Several photosensitive materials have been studied, including TiO_2, transition metal-based semiconductors, noble metals, chalcogenide-supported biomaterials, and polymeric polymers [49]. Nonetheless, certain catalytic materials continue to have drawbacks, such as poor stability and activity, which prevents their implementation in large-scale operations.

1.4.2 Strategic Catalyst Development

Experimental synthesis and testing, as well as insilico material development tailored to specific qualities, are currently common research methodologies. Advancements in density functional theory (DFT) have considerably improved the speed, accuracy, and treatable system size of catalysis design. This advancement provides comprehensive descriptions of catalytic reactions at surfaces, allowing computational results to be closely aligned with experimental data. DFT simulations can reliably estimate the interaction energies of molecules and atoms with metal surfaces, allowing for the identification of reactivity patterns across various catalyst families. Furthermore, DFT simulations make it easier to evaluate catalytic reaction kinetics by examining reaction barriers, energies, and associated entropy. The correlation between DFT-based modeling and experimental [50, 51] findings emphasize the precision and relevance of computationally predicted catalytic characteristics. (Figure 1.5).

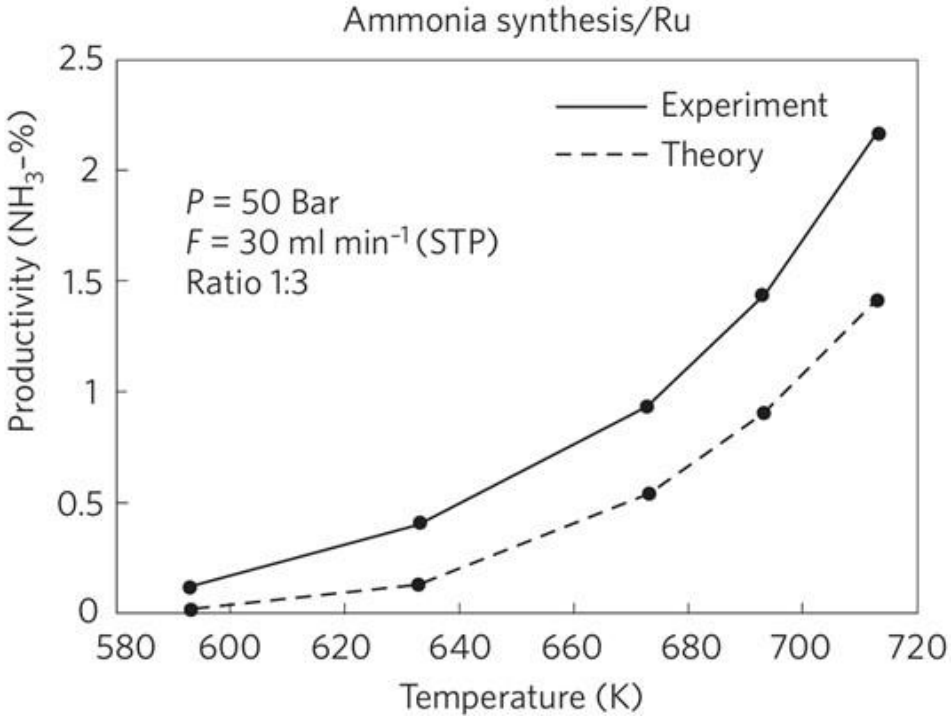

Figure 1.5 Analyzing the productivity of ammonia synthesis over ruthenium catalyst by comparing simulation and experimental results [52].

1.5 Research Outline

This PhD research project focuses on using DFT-based simulations to investigate catalysts, specifically two types: transition metal carbide (TMC) and transition metal carbonitride

(TMCN). The objective is to examine their efficacy in catalyzing the reduction of nitrogen to ammonia in natural environments. The thesis outline is shown below.

- Chapter 1 Overview/Introduction

The significance of ammonia, its relevance in today's world, and the necessity for innovative approaches to ambient ammonia processes are examined in the context of achieving the United Nations Sustainable Development Goals.

- Chapter 2 Methodology

Basic computational catalysis ideas are discussed, as well as density functional theory-based total energy simulations, which are widely used in this study.

- Chapter 3: Computational detail

In this chapter, I discussed the various parameters used throughout the project.

- Chapter 4: Results and discussion

In this chapter, I discussed all the results in detail only for the most promising materials

- Chapter 5: Summary of Papers

In this chapter, I offered a quick summary of my five papers, which are included in the appendix.

- Chapter 6: Conclusion

This chapter includes a brief history of all the research carried out. In the text, it is necessary to acknowledge collaborators and supporters, that is done in the Acknowledgements chapter or the Preface.

1.6 Research Objective/Questions

The thesis results are outlined in the five papers included in the appendix, to address the following research questions.

- Is there any other class of materials that can favor nitrogen reduction reaction (NRR)?

- Is the incorporation of compounds like carbon in the structure of nitride can offer more stability?

- Which facets of this material are more suitable for ammonia formation?

2 Methodology

2.1 Density Functional Theory

A major approach in many areas of chemistry and materials science, DFT is a remarkable accomplishment that provides the best possible balance between accuracy and computing efficiency. Credited as its founder, Walter Kohn was awarded the 1998 Chemistry Nobel Prize for his vital contributions to its advancement [53, 54]. DFT has a wide range of applications as of the writing of this thesis, including nuclei, quantum fluids, classical fluids, atoms, molecules, and solids among other systems. Among the many molecular attributes that it can predict with the molecular structures, total free energies, vibrational frequencies, reaction pathways, ionization energies, atomization energies, and electric and magnetic properties. DFT is versatile in handling, among other phenomena, spin-polarized systems, superconductors with electronic pairing mechanisms, multi-component systems like nuclei and electron-hole droplets, free energy at finite temperatures, relativistic effects, time-dependent phenomena, excited states, and molecular dynamics. Researchers can benefit much from DFT's quantum mechanical framework without having to deal with the complexities of the many-body Schrödinger equation. Though time-dependent DFT can handle excited states, its rigorous validity is limited to identifying the characteristics of a system's ground state rather than its whole eigenenergy spectrum. The Kohn-Sham (KS) equations [54] and basic theorems proposed by Kohn and Hohenberg (HK) [55] provide the conceptual foundations of DFT.

2.1.1 The Schrodinger Equation

The time-independent Schrödinger equations for an isolated system comprising N electrons are expressed as:

$$H\Psi = E\Psi \tag{2.1}$$

In this equation, E represents the system's electronic energy, and $\Psi = \Psi(r_1, r_2, ..., r_N)$ represents the many-body wave function based on the spatial coordinates of the electrons ri. The Hamiltonian is...

$$\widehat{H} = \sum_{i=1}^{N}(-\frac{1}{2}\nabla_i^2) + \sum_{i=1}^{N} v(r_i) + \sum_{i<j}^{N} \frac{1}{|r_i - r_j|} \tag{2.2}$$

The first term is the kinetic energy operator, denoted as Tˆ here. In the absence of external fields, the potential $v(r_i) = -\Sigma_a \frac{z_a}{|v_i - v_j|}$ represents the attractive force between nuclei and electrons. The symbols rα and Zα represent nuclear coordinates and charges, respectively. In the subsequent discourse, $\hat{V}_{ext}$ emphasizing its capacity to encompass elements beyond

the Coulomb potential originating from the nucleus. The term "$\hat{V}_{ext}$" is employed to denote interactions between electrons. Therefore, the Hamiltonian can be represented as

$$\hat{H} = T + \hat{V}_{ext} + \hat{V}_{ee} \tag{2.3}$$

2.1.2 The Hohenberg-Kohn Theorem

The Hohenberg-Kohn theorem, developed by Hohenberg and Kohn [55] in 1964, serves as the cornerstone for DFT. This theorem demonstrates a direct relationship between a system's potential and electron density in its ground state. Hence, the entire energy of the electron gas in its ground state is completely governed by its density, ρ(r), making it a distinctive functional.

$$\mathbf{E}[\boldsymbol{\rho}] = \{\boldsymbol{\Psi}[\boldsymbol{\rho}]|\mathbf{H}|\boldsymbol{\Psi}[\boldsymbol{\rho}] \tag{2.4}$$

In contrast to the wave function, the electron density can be observed. Therefore, the Raleigh-Ritz variational principle is used

$$\mathrm{E}_{gs} = \min_{\rho(r)} (\mathrm{E}[\rho(\mathrm{r})]) \tag{2.5}$$

and minimizes energy to determine the exact ground state energy and density.

2.1.3 The Kohn-Sham Equation

Kohn and Sham developed an indirect approach for calculating the energy functional E[ρ] in 1965 [54]. The many-electron system's intricate interplay can be approximated by a non-interacting system of individual electron states, {φi}, each experiencing the effective potential veff(r) generated from all other particles. The Kohn-Sham equations can be used to calculate single-electron wavefunctions.

$$\left\{-\frac{1}{2}\nabla^2 + v_{e_{ff}}(r)\right\}\phi_i(r) = \varepsilon_i\phi(r) \tag{2.6}$$

The electron density is obtained when the system is solved self consistently, but the effective potential v_{eff} and the wavefunctions φ_i remain unknown.

$$\rho(v) = \sum_{i=1}^{N}|\phi(\gamma)|^2 \tag{2.7}$$

The expression representing effective potential is

$$v_{eff}(r) = v(r) + vH(r) + v_{XC}(r)T \tag{2.8}$$

where v(r) represents the Hartree potential, and v(r) is the sum of the kinetic and ionic potentials.

$$v_H(r) = \int d^3v' \frac{\rho(r')}{|r-r'|} \tag{2.9}$$

and

$$v_{xL}(r) = \frac{\delta E_{xc}[\rho]}{\delta \rho(r)} \tag{2.10}$$

where

$$E_{xc}[\rho] = \int d^3r' \varepsilon_{nc}[\rho, r]\rho(v) \tag{2.11}$$

is a local function known as the exchange-correlation function, which characterizes the dynamic interaction between electrons.

2.1.4The exchange-correlation functional

Although the Kohn-Sham equations are theoretically precise, it is necessary to estimate the exchange-correlation energy Exc[ρ] due to the unknown functional shape. The fundamental challenge in resolving the Kohn-Sham equations is determining a sufficiently exact approximation for the exchange-correlation function. One way for approximating the exchange-correlation functional is to assume that the exchange-correlation energy at position r is the same as that of a uniform electron gas with a density of ρ = ρ(r),

$$E_{XC}^{LDA}[\rho] = \int d^3r \varepsilon_{XC}^{LDA}[\rho(r)]\rho(r) \tag{2.12}$$

Kohn and Sham [54] established this technique, called the local density approximation (LDA). In bulk materials and other systems with gradually changing densities, LDA works well; but it tends to overstate binding energies when used on molecules or atoms. The non-uniformity in electron density is addressed with a different approximation known as the generalized gradient approach (GGA). With this approach, the exchange-correlation function includes the density gradient. Knowing that the gradient by itself was inadequate, Langreth and Perdew [56] recommended using a lower-density gradient.

$$s(r) = \frac{|\nabla \rho(r)|}{2 \cdot 3\sqrt{3\pi^2 \rho(r)\rho(r)}} \tag{2.13}$$

The form of the GGA exchange-correlation function is then

$$E_{XC}^{LDA}[\rho] = \int d^3r \varepsilon_{XC}^{LDA}[\rho(r), s(r)]\rho(r) \tag{2.14}$$

GGA functionals typically produce more accurate findings than LDA, with atomic distances within ±0.02 Å and energy differences within ±0.1 eV of the experiment. All of our calculations use GGA based on the RPBE function [57].

2.1.5 Plane wave basis set

A predefined collection of known mathematical functions called the basis set, must be used to represent the unknown KS orbitals in DFT calculations. Bloch's theorem is especially applicable to periodic systems, hence in the calculations carried out for this thesis, the orbitals are extended using periodic plane-wave basis sets using the DFT software Vienna ab initio simulation package (VASP) [58-62].
According to this result, a crystal momentum, k, and a principal quantum number, n, define each eigenfunction of the KS equations for a periodic system. As a discrete collection of plane waves with wave vectors K + G, where G denotes the reciprocal lattice vectors

defined by G.l = 2πm for all lattice vectors, l, of the crystal and m is an integer, these eigenfunctions can be represented. Thus, the representation is as follows:

$$\psi_{nk}^{m}(r) = \sum_{G} c_{(k+G)}^{m} e^{[i(k+G)\cdot r]} \tag{2.15}$$

Through the application of Bloch's theorem, the challenge posed by the infinite electron problem is now reframed as the task of representing the wave function using an infinite set of reciprocal space vectors within the first Brillouin zone of the periodic cell, denoted as k. This issue is addressed by discretely sampling the Brillouin zone at specific sets of k-points. Subsequently, the electronic wave functions at each k-point can be expressed using a discrete plane wave basis set.

Although the kinetic energy in the Hamiltonian is diagonal, the plane waves are orthogonal. Thus, despite the theoretical necessity of an infinite number of plane waves for each k-point sampled in the Brillouin zone (which corresponds to a particular choice of the unit cell of the reciprocal lattice), the convergence of plane waves is rapid, allowing the expansion to be truncated at G_{cut}, where

$$\left(\frac{\hbar^2}{2m}\right)|k + G_{cut}|^2 \leq E_{cut} \tag{2.16}$$

One can use a pseudopotential to reduce the number of necessary plane waves and, in turn, the energy cutoff, E_{cut}. With contributions from the nucleus and core electrons, this pseudopotential shows the averaged potential that the valence electrons experience. Especially, extremely soft pseudopotentials can produce very precise findings [62]. The idea behind pseudopotential approximation is that, in an atomic system, core electrons are almost indestructible even in the face of changes in the chemical surroundings. The actions of the nucleus and core electrons can thus be combined to form an effective potential for an ion. The energy cutoff and the number of one-electron KS equations are thus greatly reduced by excluding the "frozen" core electrons from density calculations. The fact that the number of plane waves below E_{cut} is proportional to $E_{cut}^{\frac{3}{2}}$ makes this reduction very important. This reduction results from the requirement of high-frequency components in the basis set to characterize valence electrons and core electrons in the core region. Highly localized core orbitals are maintained by valence orbitals oscillating to keep them orthogonal. The orthogonality requirement is reduced and the need to explain core orbitals is eliminated by using the pseudopotential approximation.
Two different kinds of pseudopotentials are supported by VASP: projected augmented wave (PAW) potentials and ultra-soft pseudopotentials. We use the PAW potential for the computations in this thesis. Every one of these methods uses frozen core methods, which means that the core electrons are pre-calculated in an atomic environment and stay fixed during further calculations.

3 Calculation Details

3.1 Calculation detail

We used the RPBE [63] exchange-correlation functional in our computational simulations under DFT. For every surface calculation, Monkhorst-Pack K-point grid of 4 x 4 x 1 is used with the VASP [64]. The projector augmented wave (PAW) [62] a technique used by the VASP code enables the use of computationally efficient pseudopotentials, which considerably reduces computing time [61, 65]. A Fermi-Dirac distribution smoothed the Kohn-Sham orbital occupancy with a smearing value of kBT = 0.1 eV to address electron distribution. Every surface, while retaining a distinct surface orientation, is examined on the rocksalt (RS) crystallographic structure. The model systems are represented by a 5-layer 2x2 unit cell with 20 metal atoms and 20 carbon atoms for TMC and 20 metal atoms, 10 carbon atoms, and 10 nitrogen atoms for TMCN. The top three layers and any adsorbates are let to relax while the bottom two layers are maintained in their equilibrium bulk structure. In the x and y dimensions, periodic boundary restrictions are imposed, and each surface slab is kept at least 15 Å apart in the z-direction. When the total forces acting on every movable atom fall below 0.01 eV/Å, structural optimization is considered sufficient.

3.2 Computational Tools

3.2.1 Nudged Elastic Band Method

The slowest step in a reaction occurs less frequently than faster steps or molecular vibrations. The primary issue in catalysis is finding the activation energy barrier and transition state (TS) of a specific process. The TS, situated at the energetically highest point along the minimal energy path, connects the starting and final states (FS). The TS acts as a saddle point along this path, allowing for the highest reaction rate. The nudged elastic band (NEB) approach is used to determine the minimal energy path. This method connects the system's starting and final positions with a linear chain of pictures or replicas. A spring potential is introduced between adjacent images to ensure even dispersion throughout the path. The system is then relaxed and reduced in terms of total energy by combining the tangential component of the spring force and the perpendicular component of the real force. To position one of the images at the saddle point, release the image with the most energy from the spring system and relax it by reversing the force component along the travel direction. This technique is known as the climbing image NEB [66, 67].

3.2.2 Density Difference Analysis

Adsorption is the process by which an atom or molecule, known as an adsorbate, attaches to a surface. Chemisorption is an attachment that occurs through chemical bonding,

whereas physisorption occurs through van der Waals forces. The shift in electron density that happens during adsorption can be described as

$$\Delta\rho = \rho_{tot} - \rho_{pristine} - \rho_{gas} \tag{3.1}$$

where ρ_{tot} represents the electron density of the combined adsorbate-surface system, whereas ρ_{gas} and $\rho_{prestine}$ are the densities of the adsorbate and the pristine surface. It's important to note that these electron densities are calculated with the atoms in identical positions as in the adsorbate-surface system, utilizing the same computational cell. This ensures the assessment of changes in electron density attributed to charge transfer between atoms rather than disparities in relaxation geometries between the surface with and without the adsorbate. In numerous cases, visualizing the charge transfer between various segments of the system can be achieved by analyzing the charge transfer along the surface normal. This can be accomplished by defining the integrated density difference.

$$\Delta\rho_i = \int dxdy\Delta\rho(x, y. z) \tag{3.2}$$

where the z-axis is perpendicular to the surface.

3.2.3 Bader Analysis

Quantum mechanical theory does not precisely describe atomic charges within molecules or solids since they cannot be directly examined. DFT simulations and other quantum mechanical computations provide a constant electronic charge density, which causes ambiguity in assigning electrons to system fragments such as atoms or molecules.

R.F.W. Bader developed an intuitive approach for separating molecules into atoms [68]**.** His approach is exclusively based on the electrical charge density. Bader analysis uses zero flux surfaces to divide space into discrete zones.

$$\Delta\rho(r_s).n(r_s) = 0, \tag{3.3}$$

$n(r_s)$ represents a unit vector perpendicular to the surface at r_s. As a result, a zero-flux surface (equation 3.3) is a two-dimensional surface with a charge density that is minimal perpendicular to the surface. Within molecular systems, there is often a minimum in charge density between atoms, which acts as a natural border for separating atoms. The volume element associated with an atom is used to calculate a variety of 'atomic' properties. For example, the charge trapped within the Bader volume is a good approximation of the atom's total electronic charge. It is also feasible to calculate the multipole moments of interacting atoms or molecules. Bader's technique has also helped to define atomic hardness, providing insight into how much energy is necessary to deplete an atom's charge.

3.2.4 Normal Mode Analysis

Particularly for adsorbed species on a surface, normal mode analysis (NMA) provides a consistent approach for vibrational frequency computation. The fundamental presumption is that, when these species are located at a local minimum on the potential energy surface (PES), their vibrations can be described as harmonic oscillators. There are, nevertheless,

some cases when this approach reaches saddle points found by the NEB approach or TS. Two conditions define this extension: either the PES shows adequate curvature at the TS, or the harmonic approximation is true. A TS's vibrational frequency is therefore one less than the ground state since it has one less degree of freedom. The TS shows a maximum along one direction, hence one of the vibrational eigenvalues is negative, indicating a single imaginary frequency. Whereas for non-linear molecules the number of normal modes is 3N - 6 where N is the atom count of the molecule, for linear molecules it is 3N - 5. For both linear and non-linear molecules, the deduction of five or six accounts for the three translational modes and two or three rotational modes accordingly. As illustrated in Figure 3.1, a 4-atom non-linear molecule such as NH_3 shows six normal modes: one N-H symmetric stretching (3330 cm^{-1}), two N-H asymmetric stretching (3428 cm^{-1}), two H-N-H scissoring (1601 cm^{-1}), and one N-H wagging (1004 cm^{-1}) [69].

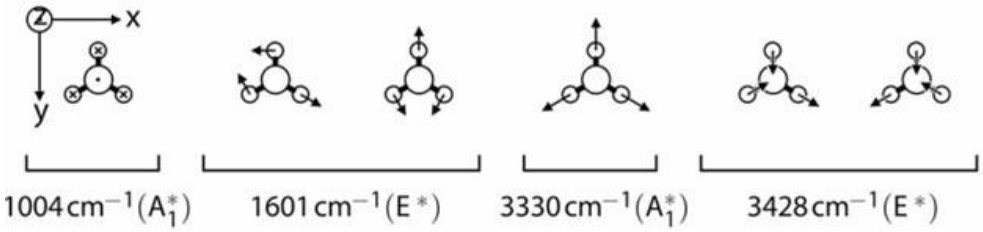

Figure 3.1 The graphic presentation shows the normal modes of ammonia together with their symmetry classification. Large circles in the diagram symbolize nitrogen (N) atoms; smaller circles symbolize hydrogen (H) atoms. Dots and crosses show the out-of- plane umbrella mode; they indicate atom displacements forward and backward correspondingly. Arrows sized properly for each mode represent atomic displacements within the paper plane. Asterisks indicate infrared-active modes. This figure is taken from [69].

When an atom is adsorbed onto a surface, it has three normal modes. This assumption is based on the idea that it remains motionless on the surface (thus, zero translational modes) and lacks rotational freedom as a single atom linked to an immobile surface. Consequently, the atom vibrates in three directions: x, y, and z. The following equation can be used to determine the vibrational frequencies, written as v, of an adsorbed atom on a surface.

$$v = \frac{1}{2\pi}\sqrt{\frac{k}{m}} \tag{3.4}$$

The adsorbed atom's mass is represented by m, whereas the force constant in the x direction is denoted by k. The force constant can be calculated using the second derivative of the potential energy function $V(x) = \frac{1}{2}kx^2$.

A similar approach is taken for the y and z directions. In practice, once the atom has been relaxed to its minimum on the PES, it suffers little displacements in each direction around this minimum, and the potential energy and gradient are determined. Each direction has three separate potential energy values, each of which corresponds to a different coordinate. By fitting a parabolic function between these points, the curvature, or second derivative, determines the force constant and, as a result, the normal mode. The wave number (measured in cm^{-1}) is calculated by dividing the frequencies by the speed of light.

3.2.5 Calculating Gibbs Free Energy

The Gibbs free energy (ΔG) is a critical parameter in computational assessments of the electrocatalytic potential of a material. The natural variables of this potential, which are temperature, pressure, and particle number, are all thermodynamic in nature. However, in the context of electrocatalytic reaction simulations, these variables are typically constrained. In the absence of applied voltage and under constant pressure and temperature, the Gibbs free energy of a system reaches its minimum at chemical equilibrium. The Gibbs free energy difference between the reactant and product states provides a metric for evaluating the feasibility of a reaction. A chemical reaction can solely transpire spontaneously in a closed system under constant temperature and pressure, as stipulated by the second law of thermodynamics, provided that the corresponding change in free energy is negative.

$$\Delta G = G_{initial} - G_{final} < 0 \tag{3.5}$$

Additionally, ΔG quantifies the maximum potential for non-pV work accomplished by the chemical reaction, such as the electrical work achievable if the reaction transpires reversibly. If a reaction exhibits an uphill trend in Gibbs free energy ΔG, it might still occur spontaneously by injecting energy into the system, typically in the form of electrical work. Consequently, applying an electric potential can expedite the reaction, a crucial consideration in electrocatalysis.

$$\Delta G = \Delta H - T\Delta S \tag{3.6}$$

For a given reaction, ΔG relates to the change in enthalpy ΔH and entropy ΔS by:
The output of DFT calculations usually yields the ground state energy of a system at 0 K. To obtain the system's enthalpy, one must add quantum-mechanical zero-point energy (ZPE) correction to account for the inherent energy present, yielding:

$$\Delta H = \Delta E + \Delta E_{ZPE} \tag{3.7}$$

Where ΔE denotes the DFT-calculated binding energy. Extrapolating to non-zero temperatures, an estimate for ΔG can be derived by subtracting TΔS from the enthalpy expression, resulting in:

$$\Delta G = \Delta E + \Delta E_{ZPE} - T\Delta S \tag{3.8}$$

While this expression provides a useful approximation, it overlooks the temperature dependence of the enthalpy for metallic systems, wherein thermal excitations from the ground state are significant. Although a comprehensive quantum mechanical treatment incorporating Boltzmann statistics for such corrections would be computationally prohibitive for complex systems, a simplified yet practical correction for the enthalpy at finite temperatures can be obtained by integrating the system's heat capacity at constant pressure C_p from 0 K to the desired temperature. This correction is often negligible for free energy differences between similar states at room temperature, primarily due to error cancellation, and thus omitted in the presented works.

3.2.6 Phonon dispersion and phonon Plots

Thin films contain crystals made up of different elements, each organized into three-dimensional lattices filled with atoms [70]. These atoms are connected to their nearest neighbors via potentials that may be modeled using harmonic oscillators, allowing the entire lattice to be represented similarly. Thermal energy or other external forces can cause vibrations in these atoms, resulting in the propagation of mechanical waves throughout the material. The lattice's periodic boundary conditions ensure that the system's energy levels are distinct and quantized [71]. As a result, these mechanical vibrations can be described as quasiparticles known as phonons. The material's crystal structure influences phonon behavior, which can be investigated using phonon dispersion relations. Using the wave vector $\vec{k}$ and the reciprocal lattice, these relations connect the angular frequency ω_{Ph} or phonon frequency f_{Ph} to the crystal structure of the material. The phonon dispersion relation allows one to determine parameters such as the phonon's velocity through the material. Figure 3.2 illustrates a phonon dispersion relation for a three-dimensional material.

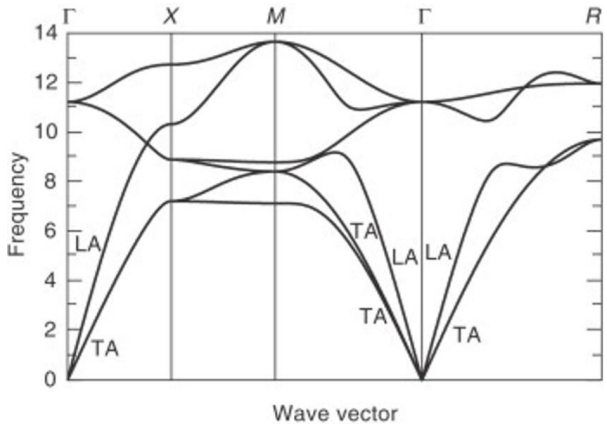

Figure 3.2 An illustration of the phonon dispersion relationship of a material in three dimensions. (Extracted from [72])

In a phonon dispersion relation, the wave vector $\vec{k}$ describes the reciprocal lattice. As previously mentioned, the material lattice experiences periodic boundary conditions, which also affect the reciprocal lattice. As a result, only the particular region within the reciprocal lattice, known as the first Brillouin zone [71], must be investigated to identify the material's overall properties. The first Brillouin zone comes with several high-symmetry points and axes. These points and the pathways linking them carry a wealth of information about the material, making them important elements in phonon dispersion theories. Figure 3.2 depicts phonon dispersion relations through various plots and vertical lines. The vertical lines and letters above them represent the selected high-symmetry points. The plot lines, or branches, represent various kinds of phonon oscillation. The number of branches in a phonon dispersion relation is equivalent to the number of degrees of freedom in the material's first Brillouin zone [72]. The Γ-point marks the center of the first Brillouin zone. Every phonon dispersion relation contains three vibrational modes with zero frequency at the Γ-point.

Acoustic modes refer to the vibrational modes that cross at $\omega_{ph}(\vec{k}) = 0$. During these acoustic modes, nearby atoms vibrate in phase. Optics refer to non-zero vibrational modes at the Γ-point when surrounding atoms vibrate in antiphase. The vibrational modes of particular crystals with great symmetry along specified directions demonstrate polarization. They can be polarized parallel or perpendicular to the propagation direction of the wave vector k (longitudinal waves or transverse waves). This polarization affects both acoustic and optical modes, yielding four possible modes: longitudinal acoustic (LA), transverse acoustic (TA), longitudinal optic (LO), and transverse optic (TO). Figure 3.2 particularly labels the LA and TA modes.

4 Results and Discussions

We provide a summary of the results obtained for this PhD dissertation in this chapter. For a more comprehensive study of the results, interested readers can explore the articles obtained from this thesis which can be found in the appendix.

Structure Stability

We studied the (100) and (110) facets of TMC, (100), (111), and (110) TMCN as shown in Figure 4.1, and each slab is relaxed, and the total energies are compared to find the most stable facet. The majority of the TMC and TMCN of the early transition metals (d1-4) are found to be more stable in the RS crystal structure, with the (100) and (110) facets being more stable than the (111) facets. These are ScX, TiX, VX, CrX, YX, ZrX, NbX, MoX, HfX, TaX, and WX (with X=C for TMC and X=C, N for TMCN the carbon and nitrogen are in 1:1 ratio).

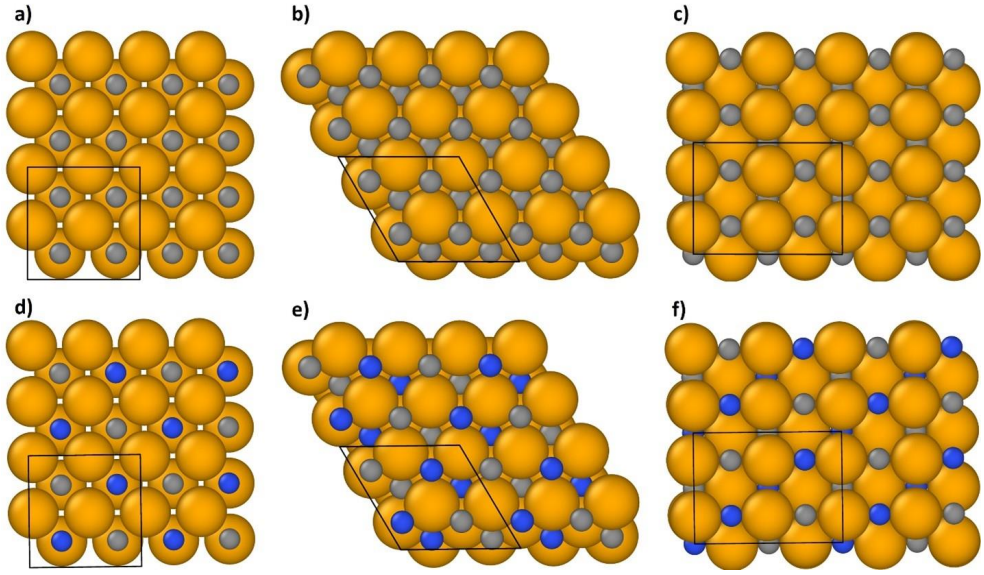

Figure 4.1 Shows the top view of the model diagram of TMC (a) (100) facet (b) (111) facet (c) (110) facet and TMCN (d) (100) facet (e) (111) facet (f) (110) facet. Metal, carbon, and nitrogen atoms are depicted by dark yellow, gray, and blue spheres, respectively.

Phonon analysis is a fundamental way to assess the stability of materials using vibrational properties. All phonon frequencies in the Brillouin zone are true and positive in a dynamically stable crystal structure, indicating that the material can endure minor disturbances without structural changes. In contrast, the presence of imaginary phonon

frequencies suggests dynamical instability, meaning that the structure is likely to have spontaneous distortions and may relax into a more stable state. This is especially useful for detecting unstable structures and determining phase transitions. Soft phonon modes with frequencies approaching zero often suggest that the material is nearing a phase transition, indicating the possibility of structural changes caused by changing variables such as temperature or pressure. Furthermore, phonon calculations help to accurately determine thermodynamic properties like as specific heat, entropy, and free energy, all of which are necessary for understanding material stability and phase behavior. Phonon investigations, which include harmonic effects, provide information on thermal expansion, thermal conductivity, and material stability under thermal stress. Overall, phonon analysis not only explains materials' dynamical stability and potential phase transitions, but it also helps predict their behavior and influences the design of materials with specific properties. As shown in Figure 4.2, we compared the phonon dispersion of various TMNs (VN, NbN, TaN, ZrN, and WN) with TMC and TMCN and discovered that only ZrN was stable at normal temperature. When we incorporated carbon instead of nitrogen to generate carbides, all were found to be stable except WC remained unstable. Then we used a 1:1 ratio of carbon and nitrogen to create carbonitride, and only VCN, NbCN, and ZrCN remained stable. This analysis reveals that TMC and TMCN are more stable then TMN.

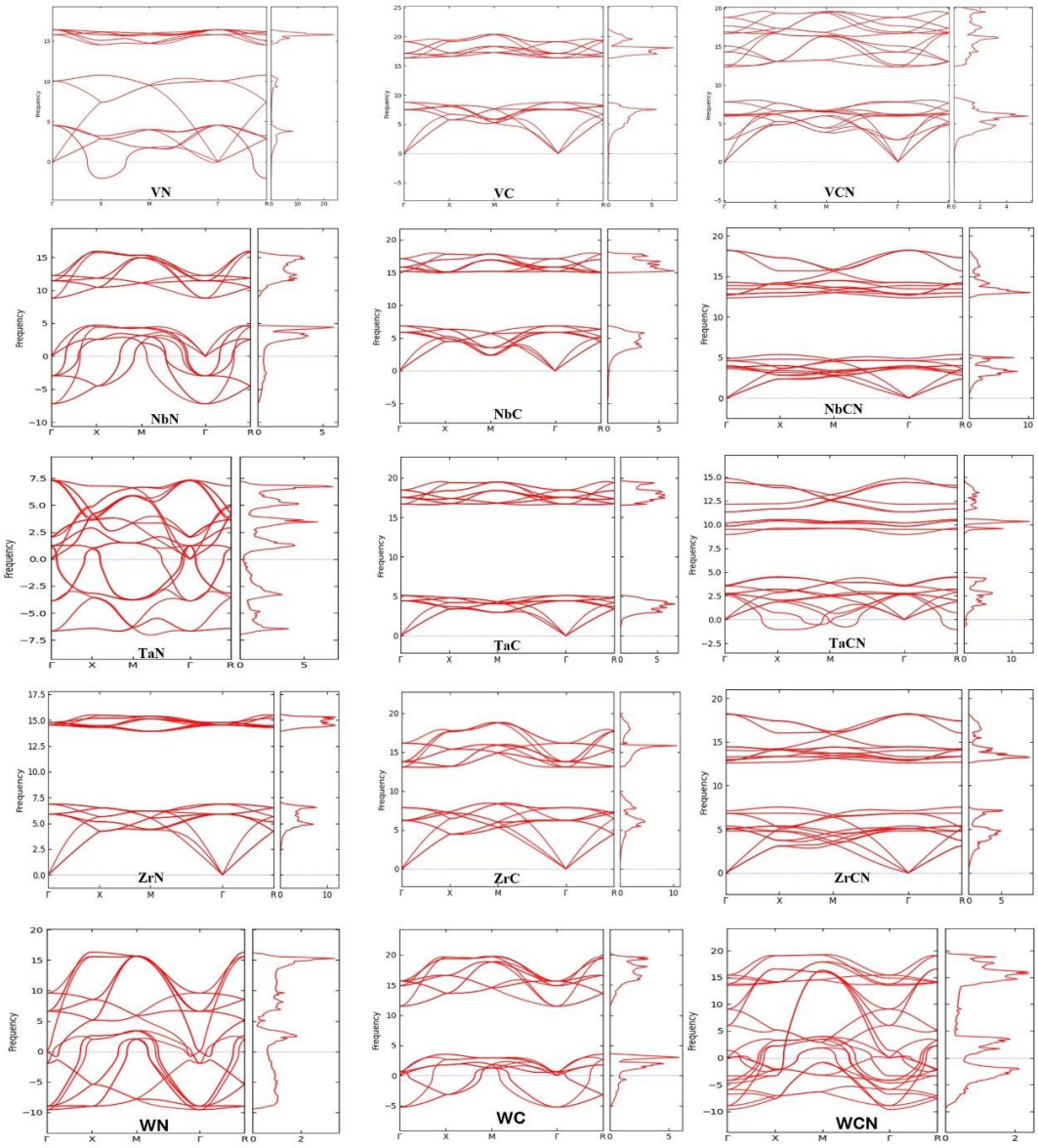

Figure 4.2 Shows the phonon band structure and density of states of various nitrides, carbides, and carbonitrides.

Nitrogen Reduction Reaction

We investigated three mechanisms for NRR: 1) dissociative mechanism (DM), 2) associative mechanism (AM), and 3) Mars-van Krevelen mechanism (MvK), as shown in Figure 4.3. The strong triple bond that exists between the nitrogen atoms is broken apart in the DM and is utilized to break down N_2 when the gas comes into contact with the surface of a catalyst, such as a carbon/metal atom. Each nitrogen atom will adhere to the catalyst in its own unique manner as a result of this splitting. In the beginning, we concentrated on calculating the changes in energy (thermodynamics) that could occur as a result of this splitting. We did not give any consideration to the energy that would be required to initiate or accelerate the reaction (kinetic barriers). Despite this, we discovered later on in our research that this strategy results in extremely high energy requirements along the chemical pathway. As a result, it is not only inefficient but also difficult to implement in practice. In light of this, we came to the conclusion that it would be best not to compute the kinetic barriers for this process.

In the AM, N_2 adsorbs on the catalyst surface and then suffers bond cleavage at a certain step of the hydrogenation reaction. This progressive dissociation differs from the direct cleavage seen in the dissociative mechanism. Furthermore, using the AM framework, we looked at the potential role of *NNH (adsorbed NNH) as an intermediary in the reaction pathway. The addition was important to get a complete comprehension of the mechanism, thus we incorporated *NNH adsorption into our free energy diagrams. This allowed us to more precisely describe the energy landscape and find thermodynamically favorable steps, providing better insights into the overall reaction kinetics and AM efficiency in promoting ammonia creation.

The MvK method converts the lattice nitrogen and carbon atoms on the surface of TMCs and TMCNs into ammonia or methane, depending on whether proton adsorption occurs on the nitrogen or carbon sites, respectively. This process creates surface vacancies, which are required to keep the catalyst active. These vacancies can be chemically filled by nitrogen molecules via either an associative (associative MvK) or dissociative (dissociative MvK) mechanism, successfully regenerating the catalyst.

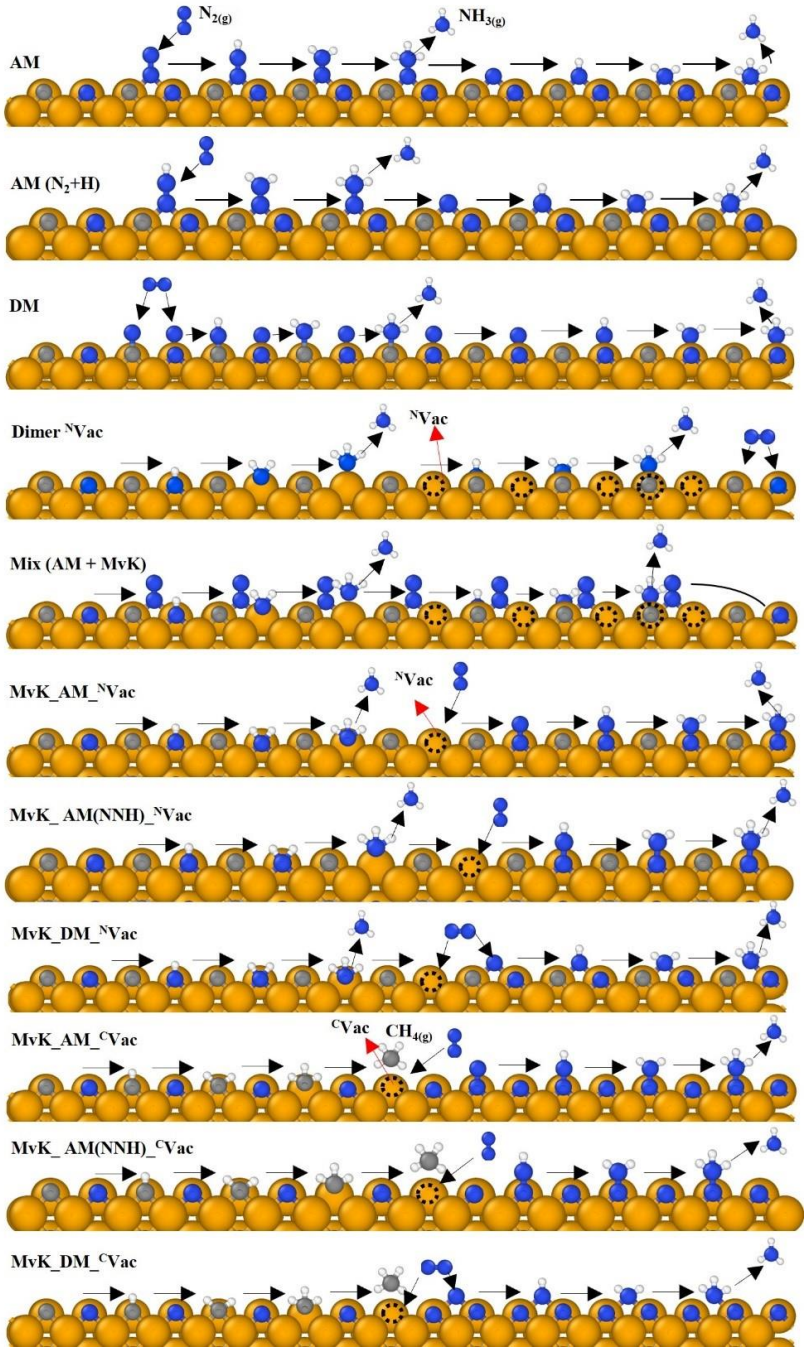

Figure 4.3 Shows the schematic diagram for the nitrogen reduction reaction.

Catalytic Activity

An extensive examination was undertaken in our research to determine the mechanisms underlying the formation of ammonia on the RS, (100), and (110) facets of TMCs, as well as the (100), (111), and (110) facets of TMCNs. Twenty-two TMCs and TMCNs were the primary focus of our investigation, with the most probable candidates and their corresponding free energy diagrams being emphasized. The comprehensive analysis that follows synthesizes the most important findings and mechanisms pertaining to various materials and aspects.
TaC was not promising for ammonia formation in (100) facets and was found to be a promising candidate in (110) facets. The most efficient route involves the simultaneous adsorption of nitrogen and protons as shown in Figure 4.4a, which results in the formation of NNH. After further protonations, the protons first cover all the surface carbon to make half monolayers then the next proton just binds with NNH to make NNH_2. Furthermore, after nine protonation steps, two ammonia molecules are released, each of which has an ΔG_{RDS} value of 0.66 eV. This method provides an illustration of the potential of TaC (110) aspects for effective ammonia generation, notably through the judicious management of nitrogen and proton.

On WC (100), the MvK mechanism was found to be the most appropriate pathway for the formation of ammonia after extensive investigation. In the beginning, carbon vacancies are introduced by CH_4 as shown in Figure 4.4b (blue pathway), and subsequently, N_2 gas is used to replenish the vacancy. To facilitate the process, exergonic N_2 adsorption is utilized. For this particular process, the rate is determined by the sixth protonation step, which occurs after the first ammonia molecule formation. The ΔG_{RDS} value for this mechanism is 0.35 eV. The whole eight-protonation process results in the release of two molecules of ammonia. This trajectory emphasizes the necessity of regulating carbon vacancies to maximize nitrogen adsorption and, consequently, protonation processes to produce ammonia efficiently. When it comes to the (110) facets of WC, it was discovered that a mixed mechanism that included both the AM and the MvK was realistic. The process of protonation began when N_2 adsorbs on the surface of the catalyst as shown in Figure 4.4b (black pathway). It is the carbon site that the initial proton attaches to, rather than the N_2 that has been adsorbed. Once all of the carbon sites have been coated with protons as monolayers, the seventh proton is connected with nitrogen to form NNH, which will then release the first ammonia molecule. This will occur after the ninth protonation step. With an ΔG_{RDS} value of 0.82 eV, the reaction ultimately results in the production of two molecules of ammonia. This mixed mechanism highlights the complex interaction that occurs between nitrogen and carbon sites, as well as the necessity of understanding surface dynamics to achieve optimal ammonia formation performance.

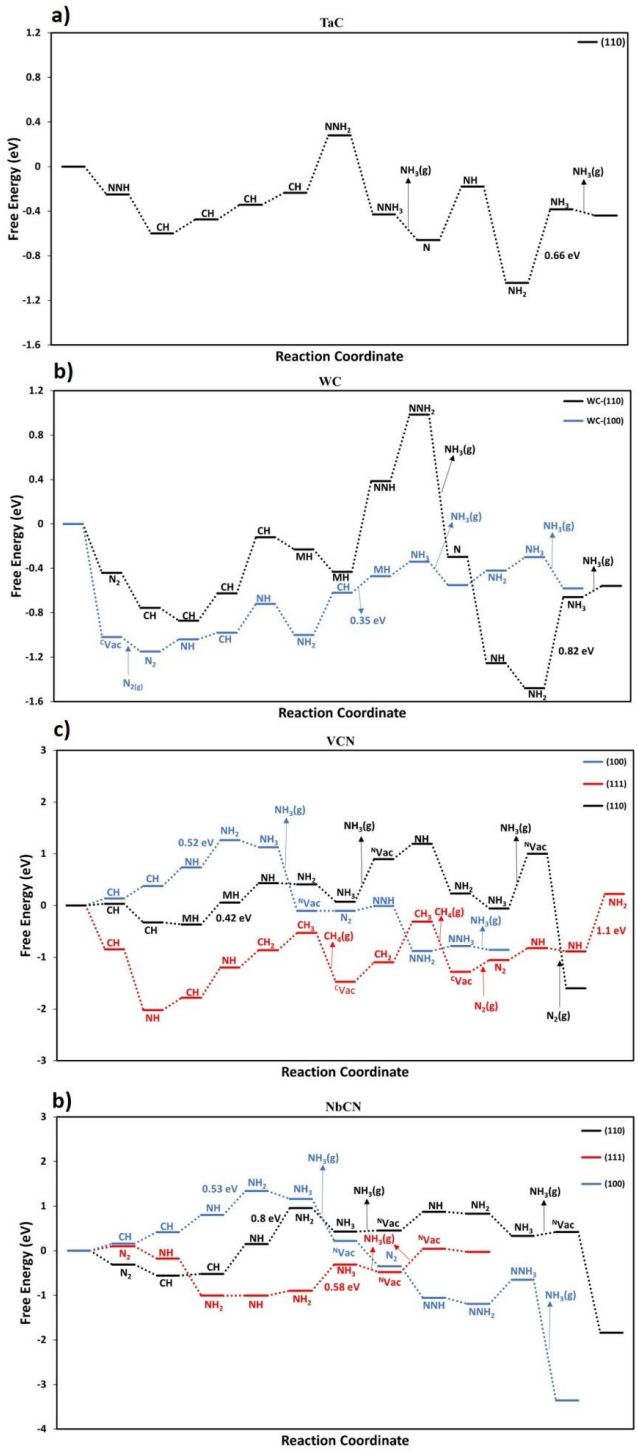

Figure 4.4 Shows the free energy diagram for (a) TaC 110 facets (b) WC 100, 110 facets (c) VCN 100, 111, and 110 facets (d) NbCN 100, 111, and 110 facets respectively at zero potential.

The MvK mechanism works especially well with VCN (100) facets, showing how well they work to speed up this catalytic process. In this process, the fourth protonation step, which makes the $*NH_2$ intermediate, sets the rate-determining step (RDS) as shown in Figure 4.4c (blue pathway). A change in ΔG_{RDS} of 0.52 eV makes this step unique. The formation of the first molecule of ammonia is a major turning point in this process. After this, the nitrogen-vacancy made by this process can be filled in two different ways: the associative MvK mechanism, in which N_2 is directly involved, or the dissociative MvK mechanism, in which two nitrogen atoms (2N) are involved. The efficient route ends with the release of two ammonia molecules, following eight steps of protonation. This clearly shows that VCN (100) facets are very good at catalyzing the MvK process, which makes them perfect for making ammonia. VCN (111) facets, on the other hand, are not active for ammonia formation as shown in Figure 4.4c (red pathway). The most successful method for VCN (110) facets to produce ammonia is a combination of AM and MvK processes. This hybrid system takes advantage of the best aspects of both methods to improve ammonia efficiency. Figure 4.4c (black pathway) shows that after the seventh protonation step, the first ammonia molecule is released with an ΔG_{RDS} of 0.42 eV. The protonation process continues beyond the tenth step, producing two ammonia molecules. This route's effectiveness is further demonstrated by the fact that N_2 can effectively fill dimer vacancies with a kinetic barrier of 0.42 eV. This low barrier indicates that the route is very likely to operate under normal conditions. This suggests that VCN (110) is extremely effective at assisting in the generation of ammonia via a combination of AM and MvK methods.

NbCN offers enormous potential in ammonia production, with multiple facets demonstrating diverse efficiency and procedures. The NbCN (100) facets are particularly effective at following the MvK mechanism, in which the fourth protonation step results in the formation of the $*NH_2$ intermediate with the PDS of 0.53 eV, as illustrated in Figure 4.4d (blue pathway). This phase is important for the creation of the first ammonia molecules. After eight protonation steps, the material can replenish nitrogen vacancies with nitrogen gas (N_2) or atomic nitrogen (2N), allowing the formation of two ammonia molecules. This efficient cycle exhibits the ability of the NbCN (100) facets to continuously generate ammonia via the MvK mechanism. The NbCN (111) and (110) facets, on the other hand, exhibit a hybrid of associative and MvK pathways, but with different efficiency and challenges. In (111) facets, the first proton binds to surface nitrogen atoms rather than adsorbing N_2. After six additions, two ammonia molecules are produced, with a comparatively small ΔG_{RDS} of 0.58 eV as illustrated in Figure 4.4d (red pathway). Furthermore, this facet has a low kinetic barrier of only 0.29 eV for replacing nitrogen vacancies with N_2 (which is already on the surface), indicating a high level of efficiency in nitrogen incorporation and continuous ammonia formation. In contrast, the NbCN (110) facets require eight protonation steps to create two ammonia molecules, resulting in a greater energy requirement of ΔG_{RDS} of 0.8 eV and a significant problem in nitrogen replenishment with a relatively a little high kinetic barrier of 0.78 eV as shown in Figure 4.4d (black pathway). These characteristics emphasize the operational differences and optimization potentials of various NbCN facets, shedding light on their roles and effectiveness in industrial ammonia manufacturing processes.

Stability Against Poisoning

As we discussed the MvK mechanism throughout this thesis, a critical aspect is that once surface nitrogen/carbon atoms have reacted and vacancies are formed, these vacancies

must be replenished with N_2 from the electrolyte for the catalytic cycle to proceed. But H^+, O_2, or OH species from the aqueous electrolyte may occupy these vacancies that could block these active sites, therefore preventing nitrogen from filling the vacancy and hence poisoning the catalyst. Analyzing the free energy of substituting these species for nitrogen, represented as $\Delta G_{(2N-X)}$, allows one to understand the struggle between nitrogen and H^+, O_2, or OH to fill the gap. Under operating conditions, these ions come from hydronium ions in the electrolyte or water molecules. We determine the difference in adsorption energy of these species in comparison to nitrogen at the onset potential for ammonia formation. In the gas phase, these free energies are compared to N_2, H_2O, and H_2. A negative value of $\Delta G_{(2N-X)}$ suggests that it is thermodynamically more advantageous to occupy the vacancy with nitrogen than with the other three species. In addition to the onset potential (V vs. RHE), Figure 4.5 illustrates these values for the most potential TMC and TMCN that were investigated in this thesis. For the majority of the catalysts under consideration, N atoms typically exhibit a stronger binding to the surface vacancy than H, OH, and O atoms, as demonstrated. Consequently, it is probable that none of these species will contaminate the surface vacancy. The predicted weaker binding of O to the N vacancy in comparison to H is due to the fact that the O species bonds to the surface less strongly in the gas phase than H_2O under more negative bias.

$$H_2O + * \rightarrow *O + 2H^+ + 2e^- \quad (4.1)$$

Lowering the bias results in a higher negative H adsorption-free energy.

$$H^+ + e^- \rightarrow *H \quad (4.2)$$

However, for the (111) facets of WCN, the surface vacancy is poisoned by H, O, and OH. Data for WCN on the (110) facets was not calculated because this facet is not active for NRR. In the case of TaC, while it is not active for NRR on the (100) facets, it is active on the (110) facets, but no vacancy formation was observed.

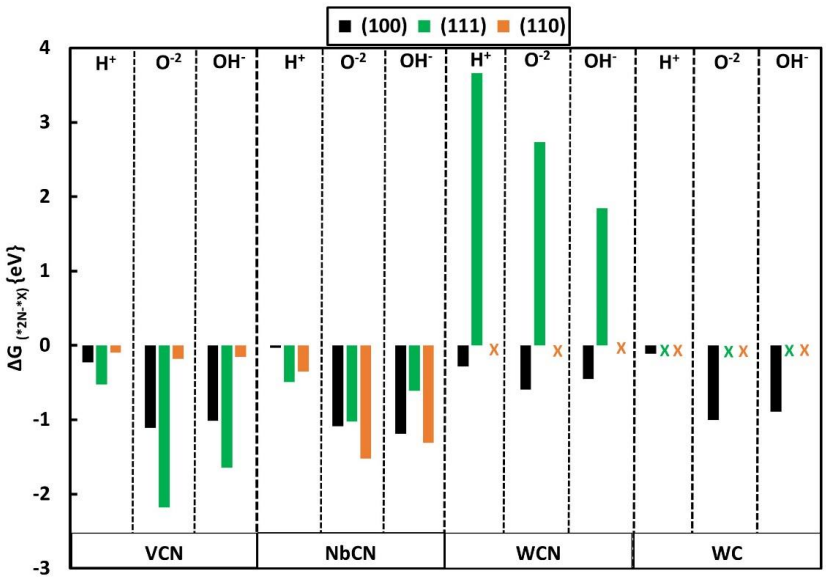

Figure 4.5 Shows the vacancy poisonous against H^+, O^-, and OH^+. The "X" represents that there is no vacancy or data has not been calculated in that case.

Stability Against Decomposition

As previously discussed, the MvK mechanism reduces a surface nitrogen/carbon atom to generate NH_3/CH_4, resulting in a vacancy that must be filled by an N_2 molecule from the electrolyte. For this replenishment to be effective, the vacancy at the surface must be stable. If the vacancy is unstable, it may migrate into the bulk of the catalyst, filling the surface nitrogen/carbon vacancy with nitrogen/carbon from within the catalyst rather than the electrolyte. In principle, this process might continue until all of the nitrogen and carbon atoms in the TMC and TMCN are reacted and reduced to NH_3 and CH_4, leaving only the pure metal. To estimate the stability of the vacancy at the surface and, thus, the stability of the TMC and TMCN against decomposition, we compare the energy difference between their slab with a single nitrogen/carbon vacancy in the surface layer ($_{Evac,i}$) and one with a single nitrogen/carbon vacancy in the first subsurface layer ($E_{vac,f}$). The minimum energy configuration for each slab is found, and the energy difference ($\Delta E_{vac} = E_{vac,f} - E_{vac,i}$) is utilized to assess the thermodynamic stability of the surface vacancy. Activation energies for vacancy migration ($E_{a,vac}$) are also estimated using CI-NEB calculations. It can be seen from Figure 4.6 that most of the TMC and TMCN are thermodynamically favorable but because of the high kinetic barrier, it will slow down the rate of reaction. Only WCN was found to be unstable because kinetically as well as thermodynamically the vacancy will migrate from the sublayer to the surface layer.

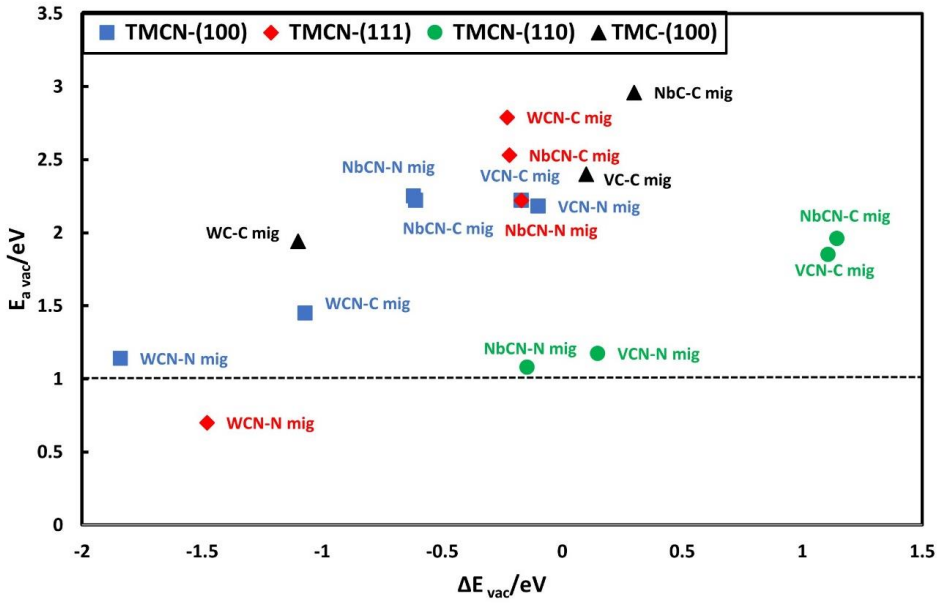

Figure 4.6 Shows the vacancy migration of TMC and TMCN.

Volcano

The volcano plot is a fundamental analytical tool in electrocatalysis, offering a visual representation of the relationship between the catalytic activity of materials and the binding energy of key reaction intermediates. This plot, named for its distinctive 'volcano' shape, captures the essence of Sabatier's principle, which posits that the optimal catalyst binds intermediates neither too strongly nor too weakly. At the peak of the volcano plot lies the ideal binding energy, where catalytic activity is maximized because the intermediate binds just strongly enough to facilitate the reaction but not so strongly that it cannot be released. If the binding is too weak, the catalyst cannot effectively activate the reactants, leading to low catalytic activity. Conversely, if the binding is too strong, the catalyst is poisoned by the intermediate, resulting in decreased activity. This balancing establishes an easier and more informative framework for comprehending and forecasting the performance of distinct catalytic materials.

DFT calculations are useful in generating and analyzing volcanic plots. DFT enables the exact estimation of the binding energies of reaction intermediates on various catalytic surfaces. By carefully calculating these energies for a wide range of possible catalysts, researchers can map out catalytic activity and discover materials with the best performance. In the hydrogen evolution reaction (HER), the Gibbs free energy of hydrogen adsorption (ΔG_H) is an essential indicator. Platinum (Pt) is frequently found near the volcano's summit, indicating that it has superior catalytic activity. Similarly, in the oxygen reduction reaction (ORR), the binding energies of oxygen or hydroxyl intermediates serve as descriptors, with materials such as platinum alloys usually identified as optimum. These plots not only help estimate catalytic performance, but also provide insights into the

fundamental concepts of catalytic reactions, leading to the development of new and improved catalysts.

TMC and TMCN have emerged as promising electrocatalysts, notably for NRR reactions. DFT-based volcano plots were used to investigate the catalytic potential of various TMCs and TMCN. Materials such as VCN, NbCN (Figure 4.7a), and TaC, WC (Figure 4.7b) have showed promising positions on the volcano plots for NRR, indicating that they have favorable binding energies with the key intermediates. The versatility of TMC and TMCN allows for the fine-tuning of their electronic properties through composition and structural modifications, which can be systematically studied using DFT calculations. This makes them highly attractive for practical applications, as they can potentially match or even surpass the performance of traditional noble metal catalysts while being more abundant and cost-effective. Thus, the integration of DFT calculations with volcano plot analysis provides a powerful framework for advancing the development of these TMC and TMCN in electrocatalysis.

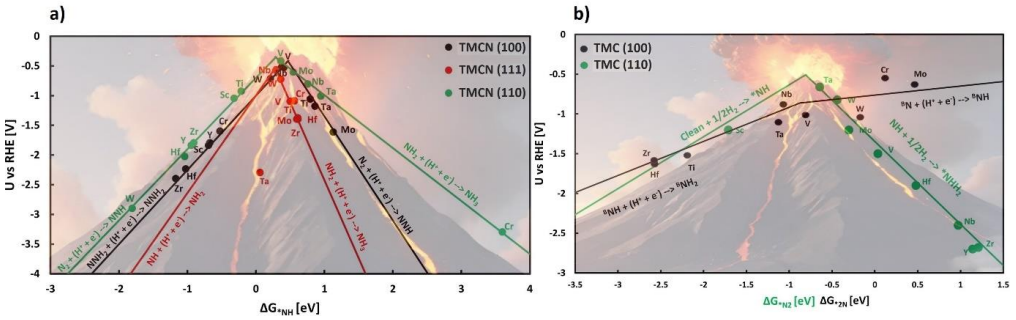

Figure 4.7 Shows the NRR predicted volcano plot for (a) TMCN and (b) TMC

5 Summary of Articles

Article I: Nitrogen Reduction Reaction to Ammonia in Transition Metal Carbide Catalyst

Our extensive investigation of the feasibility of TMCs as catalysts for the NRR demonstrates that, without surface defects, various TMCs (VC, CrC, YC, HfC, NbC, ScC, ZrC, TiC, TaC, WC, and MoC) exhibit limited reactivity due of the endergonic adsorption of nitrogen. Among them, ZrC is the only TMC able to semi-favorably adsorb nitrogen and so generate ammonia. However, ZrC tends to protonate carbon sites over nitrogen, rendering it unsuitable as a selective NRR catalyst in aqueous solutions. Common on real surfaces, the negative nitrogen adsorption reported for these TMCs can be minimized in the presence of a carbon vacancy, which is prone to develop under working circumstances. Most TMC surfaces absorbed nitrogen favorably when a vacancy was introduced; WC, NbC, and VC then generated ammonia. TMCs with highly exergonic nitrogen adsorption, however, did not produce ammonia most likely because the stability nitrogen gained in the vacancy exceeded the inclination for protonation.
Further calculations on potential poisoning and kinetic barriers revealed that although high activation energy for dissociative nitrogen adsorption makes NbC not promising under ambient conditions, under certain temperature and pressure conditions it may exhibit good activity. Proton adsorption at the vacancy site reduces catalytic activity for VC, so protonation of carbon sites replaces nitrogen adsorption. This complicates VC's possible reaction routes, which might generate ammonia by less desirable nitrogen adsorption or by the formation of a second vacancy either encouraging or hindering ammonia generation. Despite these challenges, VC demonstrates interesting behavior deserving of further study. With good activity, stability, resistance to poisoning, low starting potential (0.35 V), and selectivity, WC turned up as the most interesting prospect. For additional research and possible scale-up and commercialization for NRR uses, we highly suggest WC to experimentalists. ZrC displayed catalytic activity in the presence of a vacancy but promise on a clean surface. The practicality of utilizing surfaces such as CrC or ZrC with vacancies that show generally favorable energetics but suffer from somewhat endergonic adsorption energies or strongly bound nitrogen in vacancy sites is yet unknown. If more complicated chemical pathways such as those involving higher concentrations of vacancies are taken into account, these surfaces may generate ammonia.

Article II: Are (100) Facets of Transition Metal Carbonitrides Suitable as Electrocatalysts for Nitrogen Reduction to Ammonia at Ambient Conditions?

Using DFT calculations, we investigated various potential reaction mechanisms for ammonia formation the MvK, AM, and DM mechanisms on the (100) facets of eleven carbonitrides: ScCN, TiCN, VCN, CrCN, YCN, ZrCN, NbCN, MoCN, HfCN, TaCN, and WCN. We computed the free energies of all stable intermediates along different reaction pathways. By creating free energy diagrams for each carbonitride, we determined the free

energy change for each step influencing the onset potential. Additionally, we estimated the activation energy for N_2 adsorption and dissociation and evaluated the free energy of adatoms on the surface.

Our findings indicate that reducing nitrogen to ammonia under ambient conditions using either DM or AM may not be advantageous for most of these materials, except for ZrCN, HfCN, and WCN. For most materials at ambient conditions, the DM is inactive for ammonia formation due to high kinetic barriers for N_2 dissociation. Except for WCN, YCN, and ScCN, the adsorption of N_2 by AM on the pristine surface of these carbonitrides is often endothermic. However, it should be noted that the transfer barriers for electrochemical proton-electron processes were not accounted for in this work, so the rates for these methods have not yet been assessed. A thermochemical model was utilized to predict the onset potentials for these processes.

Except for ScCN, YCN, and TaCN, which were found to be more selective for the hydrogen evolution reaction (HER) in an electrochemical environment, all other carbonitrides were able to suppress HER. CrCN and MoCN were found to be vulnerable to poisoning in electrochemical media. VCN and NbCN required low onset potentials (0.52 V and 0.53 V vs. RHE) via MvK for ambient NRR. ZrCN and HfCN (via DM) and WCN (via AM) showed promise for non-ambient NRR with very small PDS of 0.25 eV, and 0.34 eV, respectively, making them interesting materials for further experimental tests in non-ambient NRR as temperature and pressure tuning would facilitate nitrogen adsorption and dissociation on these surfaces. Therefore, we highly encourage experimentalists to explore these novel DFT-based catalysts for the potential of enhanced ammonia synthesis under ambient conditions.

Article III: Electrochemical Nitrogen Reduction to Ammonia at Ambient Condition on the (111) Facets of Transition Metal Carbonitrides

We investigated various potential reaction mechanisms for ammonia formation, focusing on the MvK, AM, and DM pathways on the (111) facets of nine carbonitride materials (TiCN, VCN, CrCN, ZrCN, NbCN, MoCN, HfCN, TaCN, and WCN) in a rocksalt structure. We computed the free energies associated with stable intermediates along these reaction pathways. By constructing free energy diagrams for each carbonitride, we assessed the free energy changes at each step determining the onset potential (OP). Additionally, we determined the activation energy for N_2 dissociation and evaluated the free energy of adatoms on the pristine surfaces of all the studied TMCNs and within nitrogen vacancies only for the NRR-promising TMCNs, NbCN and WCN.

Our findings suggest that, for these carbonitrides, achieving the reduction of nitrogen to ammonia under ambient conditions through either DM or AM mechanisms may not be favorable. Under ambient conditions, the DM mechanism is generally ineffective for ammonia formation in most of these materials due to high PDS. We employed a thermochemical model and the computational hydrogen electrode model to predict the OP for these various processes. All the carbonitrides on (111) facets were found capable of inhibiting the HER because they do not tend to bind protons on the metal sites. However, the majority of them do not favor NRR at ambient conditions.

WCN was found to be susceptible to poisoning in electrochemical environments, while only NbCN favored NRR via a mixed associative-MvK mechanism. NbCN required a low OP (0.58 V vs. RHE) for ammonia synthesis under ambient conditions. However, the N_2 adsorption step is slightly uphill in free energy (0.09 eV) using the xc-functional of choice here, which could slow down the reaction. Experimentalists are encouraged to further explore these findings, particularly the potential of NbCN as a catalyst for ammonia synthesis under ambient conditions.

Article IV: Catalytic Nitrogen Reduction on Transition Metal Carbonitride (110) Facet: DFT Predictions and Mechanistic Insights

Focusing on the (110) facets of rock salt structures of ScCN, TiCN, VCN, CrCN, YCN, ZrCN, NbCN, MoCN, HfCN, TaCN, and WCN, we performed a theoretical study to investigate the possible of nitrogen electroreduction to ammonia under ambient settings. Our results showed that TaCN and ScCN are unstable; WCN, TiCN, YCN, HfCN, CrCN, and ZrCN are inactive for ammonia synthesis.

We investigated whether the nitrogen/carbon vacancy produced during the catalytic cycle would be replenished with N_2 molecules or become unstable and migrate into the bulk of the carbonitride considering the kinetics. The calculations of activation free energy for both processes revealed that only VCN and NbCN are interesting candidates able of regeneration and maintaining the catalytic cycle of nitrogen activation and ammonia generation under ambient circumstances. With corresponding potential efficiency, VCN and NbCN have shown onset potentials of -0.42 V and -0.78 V respectively against RHE. Strong candidates for additional experimental study, this implies that VCN and NbCN can help nitrogen adsorption, dissociation, and consequent ammonia synthesis. The outcomes of this work emphasize the need to know the stability and regeneration capacity of nitrogen vacancies in the catalytic cycle, which is essential for building effective catalysts for ammonia synthesis under ambient circumstances.

For their potential in nitrogen electroreduction to ammonia, we advise experimentalists to investigate VCN and NbCN further since these materials exhibit good activity and stability in theoretical models. This work creates fresh directions for catalyst design and optimization for environmentally friendly ammonia generation.

Article V: Understanding the Mechanistic Pathways of N_2 Reduction to Ammonia on (110) Facets of Transition Metal Carbides

An important step toward environmentally friendly and sustainable ammonia production could be achieved by softly converting N_2) into NH_3. One potential strategy that could help accomplish this goal while using less energy and renewable power is the electrochemical reduction of N_2. Finding effective electrocatalysts for this process, especially at ambient temperature and pressure, is still mostly unexplored, despite the technique's potential. To address this knowledge gap, this paper investigates possible catalysts for ambient-temperature nitrogen electro-reduction to ammonia in tremendous depth. We study the (110) facets of rocksalt structures for 11 distinct transition metal carbides using density functional theory calculations. The Mars-van Krevelen, associative, and dissociative reaction mechanisms' free energy diagrams are used to evaluate the materials' catalytic activity. In addition, we assess the materials' resistance to electrochemical poisoning and

breakdown into their constituent metals while they are in use. Under ambient environments, tantalum carbide (TaC) and tungsten carbide (WC) display exceptionally low onset potentials (-0.66 V and -0.82 V vs RHE), respectively, highlighting the fact that only a small number of candidates demonstrate any potential for nitrogen reduction processes. This study adds to our knowledge of nitrogen electro-reduction and points the way for more effective and environmentally friendly methods of producing ammonia.

6 Conclusion

In this thesis, we investigated a novel class of materials and promising electrocatalysts for nitrogen electroreduction to ammonia. Our goal was to explore a new class of materials that allows the electrochemical reduction of molecular nitrogen to ammonia in aqueous environments under normal conditions and with a low applied bias. One particularly exciting feature of this thesis is the possibility of ammonia formation on the surfaces of TMC and TMCN via the MvK mechanism. Under normal conditions, this pathway provides a thermodynamically simpler approach to producing ammonia. However, it is important to note that this method can make the catalytic active site susceptible to poisoning or decomposition while in use. As a result, it is critical to thoroughly assess these criteria for TMC and TMCN that show activity in the reaction.

This thesis provides a comprehensive analysis of TMC and TMCN electrocatalysts to assist experimentalists in their research for NRR. We discovered promising electrocatalysts for the electrochemical synthesis of ammonia in aqueous media by taking into account five important factors: (1) the stability of carbides and carbonitrides in comparison to nitrides, (2) identification of the reaction mechanism and calculation of the nitrogen dissociation barrier, (3) assessment of catalytic activity and quantification of the potential-determining and rate-determining steps, (4) determination of kinetic or thermodynamic barriers for nitrogen/carbon vacancy diffusion into the bulk, which can lead to the loss of nitrogen/carbon content from TMC/TMCN catalysts, and (5) evaluation of the stability of TMC and TMCN against poisoning in an electrochemical environment.

By evaluating the most predominant crystal facets in a greater comprehensive manner, we determined which facets of carbides and carbonitrides are most active for ammonia generation to attain high reaction rates and efficiency. Figure 6.1 highlights the thesis by showing the electrocatalytic activity of the most promising and stable catalysts found in naturally occurring d-block elements of the periodic table. The most promising TMCs were discovered to be the (110) facets of the rocksalt structure of TaC as well as the (100) and (110) facets of the rocksalt structure of WC. In carbonitrides, VCN showed promise in the (100) and (110) facets, while NbCN showed promise in the (100), (111), and (110) facets. These promising TMC and TMCN catalysts are stable except WC and oppose poisoning and decomposition in the electrochemical environment and may be regenerated to maintain the catalytic cycle of ammonia production. Furthermore, our mechanistic model predicts that none of these features will produce hydrogen, which alleviates concerns about the HER.

We strongly advise experimentalists to investigate these intriguing alternatives within the recommended structure and bias range to obtain higher-yield ammonia synthesis under ambient conditions.

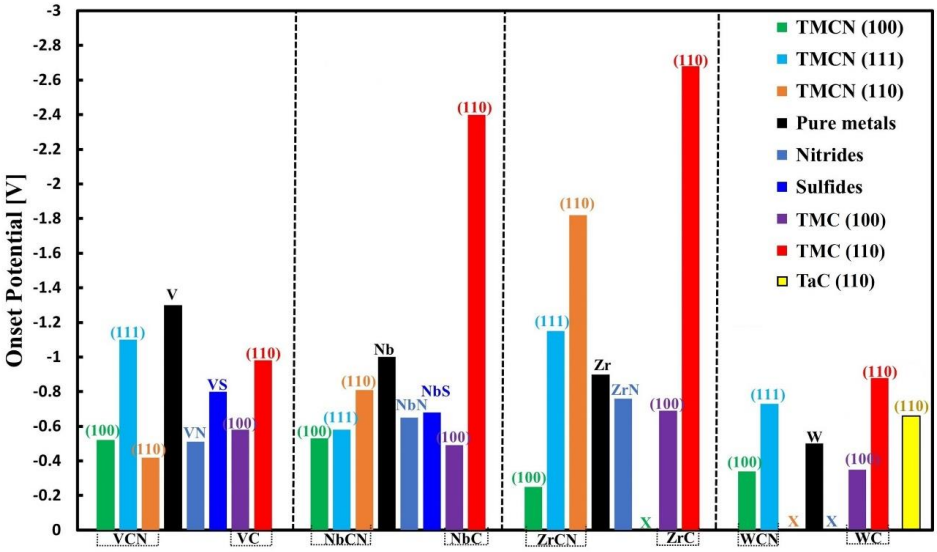

Figure 6.1 Shows the onset potential for the most promising TMC [73] and TMCN [74-76] in different facets and compares it with pure metal [38], sulfides [47], and nitrides [45,77-82] catalysts respectively. "X" shows it's inactive for NRR or hasn't been studied.

References

1. Bexell, M. and K. Jönsson. Responsibility and the United Nations' sustainable development goals. in Forum for development studies. 2017. Taylor & Francis.
2. Charles, D., Master mind: The rise and fall of Fritz Haber, the Nobel laureate who launched the age of chemical warfare. 2005.
3. Smil, V., *N*itrogen and food production: proteins for human diets. AMBIO: *A Journal of the Human Environment*, 2002. **31**(2): p. 126-131.
4. Bogaard, A., et al., Crop manuring and intensive land management by Europe's first farmers. *Proceedings of the National Academy of Sciences*, 2013. **110**(31): p. 12589-12594.
5. Silvertown, J., et al., The Park Grass Experiment 1856–2006: its contribution to ecology. *Journal of Ecology*, 2006. **94**(4): p. 801-814.
6. Jia, H.-P. and E.A. Quadrelli, Mechanistic aspects of dinitrogen cleavage and hydrogenation to produce ammonia in catalysis and organometallic chemistry: relevance of metal hydride bonds and dihydrogen. *Chemical Society Reviews*, 2014. **43**(2): p. 547-564.
7. Hager, T., The Alchemy of Air: A Jewish Genius, a Doomed Tycoon, and the Discovery that Changed the Course of History. 2008: Harmony Books.
8. "Science and Food Supplies". *In: Nature* 126.3171 (1930), pp. 193–194.
9. Smil, V., Enriching the earth: Fritz Haber, Carl Bosch, and the transformation of world food production. 2004: *MIT press*.
10. Bown, S.R., A Most Damnable Invention: Dynamite, Nitrates, and the Making of the Modern World. 2005: *Macmillan*.
11. Erisman, J.W., et al., How a century of ammonia synthesis changed the world. *Nature geoscience*, 2008. **1**(10): p. 636-639.
12. Stewart, W., et al., The contribution of commercial fertilizer nutrients to food production. *Agronomy journal*, 2005. **97**(1): p. 1-6.
13. Smil, V., Detonator of the population explosion. *Nature*, 1999. **400**(6743): p. 415-415.
14. Ertl, G., Reactions at surfaces: From atoms to complexity (Nobel lecture). *Angewandte Chemie International Edition*, 2008. **47**(19): p. 3524-3535.
15. Montgomery, D.R. and A. Biklé, The hidden half of nature: The microbial roots of life and health. 2015: *WW Norton & Company*.
16. Chorkendorff, I. and J.W. Niemantsverdriet, Concepts of modern catalysis and kinetics. 2017: *John Wiley & Sons*.
17. Karl, T.R. and K.E. Trenberth, Modern global climate change. *science*, 2003. **302**(5651): p. 1719-1723.
18. Fertilizers, I., Climate Change and Enhancing Agricultural Productivity Sustainably. *International Fertilizer Industry Association*, France, 2009.
19. Murtaugh, P.A. and M.G. Schlax, Reproduction and the carbon legacies of individuals. *Global Environmental Change*, 2009. **19**(1): p. 14-20.
20. Peltzman, S., Mortality inequality. *Journal of Economic Perspectives*, 2009. **23**(4): p. 175-190.

21. Gakidou, E., et al., Increased educational attainment and its effect on child mortality in 175 countries between 1970 and 2009: a systematic analysis. *The lancet*, 2010. **376**(9745): p. 959-974.
22. Galor, O., The demographic transition: causes and consequences. *Cliometrica*, 2012. **6**(1): p. 1-28.
23. Lutz, W., W. Sanderson, and S. Scherbov, The coming acceleration of global population ageing. *Nature*, 2008. **451**(7179): p. 716-719.
24. Department of Economic and Social Affairs. "Population Division". In: United Nations ST/ESA/SER (2015), pp. 1–148.
25. Mueller, N.D., et al., Closing yield gaps through nutrient and water management. *Nature*, 2012. **490**(7419): p. 254-257.
26. Erisman, J., et al., *R*educed nitrogen in ecology and the environment. *Environmental pollution*, 2007. **150**(1): p. 140-149.
27. Good, A.G. and P.H. Beatty, Fertilizing nature: a tragedy of excess in the commons. *PLoS biology*, 2011. **9**(8): p. e1001124.
28. S. J. Karam. How many people will live in Africa in 2050 and 2100? 2015.
29. United Nations Department of Economic and Social Affairs Population Division. World Population Prospects 2019. 2019.
30. L. K. Boerner. "Taking the CO2 out of NH3". In: Chemical and Engineerings News 97.24 (2019), pp. 18–21.
31. Yara. Yara and BASF open world-scale ammonia plant in Freeport, Texas. 2018.
32. Shipman, M.A. and M.D. Symes, Recent progress towards the electrosynthesis of ammonia from sustainable resources. *Catalysis Today*, 2017. **286**: p. 57-68.
33. Jewess, M. and R.H. Crabtree, Electrocatalytic nitrogen fixation for distributed fertilizer production? 2016, *ACS Publications*.
34. Nørskov, J., et al., Sustainable Ammonia Synthesis–Exploring the scientific challenges associated with discovering alternative, sustainable processes for ammonia production. 2016, *US DOE Office of Science*.
35. Ye, L., et al., Reaction:"Green" ammonia production. *Chem*, 2017. **3**(5): p. 712-714.
36. New York State Department of Health. "The fact about ammonia". In: Technical Information July (2004).
37. Singh, A.R., et al., Electrochemical Ammonia Synthesis□ The Selectivity Challenge. 2017, *ACS Publications.* p. 706-709.
38. Skulason, E., et al., A theoretical evaluation of possible transition metal electro-catalysts for N_2 reduction. *Physical Chemistry Chemical Physics*, 2012. **14**(3): p. 1235-1245.
39. Wu, T., et al., Electrochemical synthesis of ammonia: Progress and challenges. *Materials Today Physics*, 2021. **16**: p. 100310.
40. aJ. Lim, C. A. Fernández, S. W. Lee, M. C. Hatzell, ACS Energy Letters 2021, 6, 3676-3685; bJ. R. Gomez, F. Garzon, *International Journal of Energy Research* 2021, 45, 13461-13470.
41. Ghavam, S., et al., Sustainable ammonia production processes. *Frontiers in Energy Research*, 2021. **9**: p. 34.
42. MacFarlane, D.R., et al., *A roadmap to the ammonia economy.* Joule, 2020. **4**(6): p. 1186-1205.
43. Soloveichik, G., Electrochemical synthesis of ammonia as a potential alternative to the Haber–Bosch process. *Nature Catalysis*, 2019. **2**(5): p. 377-380.

44. Hosseini, H., Dielectric barrier discharge plasma catalysis as an alternative approach for the synthesis of ammonia: a review. *RSC advances*, 2023. **13**(40): p. 28211-28223.
45. Abghoui, Y., et al., Electroreduction of N_2 to ammonia at ambient conditions on mononitrides of Zr, Nb, Cr, and V: A DFT guide for experiments. *Acs Catalysis*, 2016. **6**(2): p. 635-646.
46. Höskuldsson, Á.B., et al., High-throughput computational screening of doped transition metal oxides as catalysts for nitrogen reduction. *Cell Reports Physical Science*, 2023. **4**(10).
47. Abghoui, Y., S.B. Sigtryggsson, and E. Skúlason, Biomimetic nitrogen fixation catalyzed by transition metal sulfide surfaces in an electrolytic cell. *ChemSusChem*, 2019. **12**(18): p. 4265-4273.
48. Hanifpour, F., et al., Operando quantification of ammonia produced from computationally-derived transition metal nitride electro-catalysts. *Journal of Catalysis*, 2022. **413**: p. 956-967.
49. aA. J. Medford, M. C. Hatzell, ACS Catalysis 2017, 7, 2624-2643; bA. Li, Y. Chen, W. Duan, C. Wang, K. Zhuo, RSC Advances 2017, 7, 19694-19700; cK. A. Brown, D. F. Harris, M. B. Wilker, A. Rasmussen, N. Khadka, H. Hamby, S. Keable, G. Dukovic, J. W. Peters, L. C. Seefeldt, P. W. King, Science 2016, 352, 448-450; dY. Bai, L. Ye, T. Chen, L. Wang, X. Shi, X. Zhang, D. Chen, ACS *Applied Materials & Interfaces* 2016, 8, 27661-27668.
50. Honkala, K., et al., Ammonia synthesis from first-principles calculations. *science*, 2005. **307**(5709): p. 555-558.
51. Reuter, K., D. Frenkel, and M. Scheffler, The steady state of heterogeneous catalysis, studied by first-principles statistical mechanics. *Physical review letters*, 2004. **93**(11): p. 116105.
52. Nørskov, J.K., et al., Towards the computational design of solid catalysts. *Nature chemistry*, 2009. **1**(1): p. 37-46.
53. Hohenberg, P. and W. Kohn, Inhomogeneous electron gas. *Physical review*, 1964. **136**(3B): p. B864.
54. Kohn, W. and L.J. Sham, Self-consistent equations including exchange and correlation effects. *Physical review*, 1965. **140**(4A): p. A1133.
55. Hohenberg, P. and W. Kohn, Density functional theory (DFT). *Phys. Rev*, 1964. **136**(1964): p. B864.
56. Langreth, D.C. and J.P. Perdew, Exchange-correlation energy of a metallic surface: Wave-vector analysis. *Physical Review B*, 1977. **15**(6): p. 2884.
57. Hammer, B., B.; Hansen, LB; Nørskov, JK Improved Adsorption Energetics within Density-Functional Theory using Revised Perdew-Burke-Ernzerhof Functionals. *Phys. Rev. B*, 1999. **59**: p. 7413.
58. Kresse, G. and J. Hafner, Ab initio molecular dynamics for liquid metals. *Physical review B*, 1993. **47**(1): p. 558.
59. Kresse, G. and J. Hafner, Ab initio molecular-dynamics simulation of the liquid-metal–amorphous-semiconductor transition in germanium. *Physical Review B*, 1994. **49**(20): p. 14251.
60. Kresse, G. and J. Furthmüller, Efficiency of ab-initio total energy calculations for metals and semiconductors using a plane-wave basis set. *Computational materials science*, 1996. **6**(1): p. 15-50.

61. Kresse, G. and J. Furthmüller, Efficient iterative schemes for ab initio total-energy calculations using a plane-wave basis set. *Physical review B*, 1996. **54**(16): p. 11169.
62. Kresse, G. and D. Joubert, From ultrasoft pseudopotentials to the projector augmented-wave method. *Physical review b*, 1999. **59**(3): p. 1758.
63. Hammer, B., L.B. Hansen, and J.K. Nørskov, Improved adsorption energetics within density-functional theory using revised Perdew-Burke-Ernzerhof functionals. *Physical review B*, 1999. **59**(11): p. 7413.
64. Kresse, G., G. Kresse and J. Furthmüller. *Phys. Rev. B*, 1996. **54**: p. 11169.
65. Blöchl, P.E., Projector augmented-wave method. *Physical review B*, 1994. **50**(24): p. 17953.
66. Henkelman, G., B.P. Uberuaga, and H. Jónsson, A climbing image nudged elastic band method for finding saddle points and minimum energy paths. T*he Journal of chemical physics*, 2000. **113**(22): p. 9901-9904.
67. Henkelman, G. and H. Jónsson, Improved tangent estimate in the nudged elastic band method for finding minimum energy paths and saddle points. *The Journal of chemical physics*, 2000. **113**(22): p. 9978-9985.
68. Matta, C.F. and R.J. Boyd, An introduction to the quantum theory of atoms in molecules. *The quantum theory of atoms in molecules: from solid state to DNA and drug design*, 2007.
69. Preuss, M., & Bechstedt, F. (2006). Vibrational spectra of ammonia, benzene, and benzene adsorbed on Si (001) by first principles calculations with periodic boundary conditions. *Physical Review B*, 73(15), 155413.
70. S Perkowitz. Phonon. Jan. 2018. url: https://www.britannica.com/science/phonon.
71. Hook, J.R. and H.E. Hall, *Solid state physics*. 2013: John Wiley & Sons.
72. K. Parlinski. Lattice Dynamics: Vibrational Modes. In: Encyclopedia of Condensed Matter Physics. Ed. by Franco Bassani, Gerald L. Liedl, and Peter Wyder. Oxford: Elsevier, 2005, pp. 98102. isbn: 978-0-12-369401-0. doi: 10.1016/B0-12-369401-9/00509-X.
73. Ellingsson, V., Iqbal, A., E. Skulason, and Y. Abghoui, Nitrogen Reduction Reaction to Ammonia on Transition Metal Carbide Catalysts. *ChemSusChem*, 2023. **16**(22): p. e202300947.
74. Iqbal, A., E. Skúlason, and Y. Abghoui, Are (100) facets of transition metal carbonitrides suitable as electrocatalysts for nitrogen reduction to ammonia at ambient conditions? *International journal of hydrogen energy*, 2024. **64**: p. 744-753.
75. Iqbal, A., E. Skulason, and Y. Abghoui, Electrochemical Nitrogen Reduction to Ammonia at Ambient Condition on the (111) Facets of Transition Metal Carbonitrides. *ChemPhysChem*, 2024: p. e202300991.
76. Iqbal, A., E. Skúlason, and Y. Abghoui, Catalytic Nitrogen Reduction on the Transition Metal Carbonitride (110) Facet: DFT Predictions and Mechanistic Insights. *The Journal of Physical Chemistry C*, 2024.
77. Abghoui, Y., Garden, A. L., Hlynsson, V. F., Björgvinsdóttir, S., Ólafsdóttir, H., & Skúlason, E. (2015). Enabling electrochemical reduction of nitrogen to ammonia at ambient conditions through rational catalyst design. *Physical Chemistry Chemical Physics*, 17(7), 4909-4918.
78. Abghoui, Y., & Skúlason, E. (2017). Onset potentials for different reaction mechanisms of nitrogen activation to ammonia on transition metal nitride electro-catalysts. *Catalysis Today*, *286*, 69-77.

79. Abghoui, Y., & Skúlason, E. (2017). Electrochemical synthesis of ammonia via Mars-van Krevelen mechanism on the (111) facets of group III–VII transition metal mononitrides. *Catalysis Today*, *286*, 78-84.
80. Abghoui, Y., & Skúlason, E. (2017). Computational predictions of catalytic activity of zincblende (110) surfaces of metal nitrides for electrochemical ammonia synthesis. *The Journal of Physical Chemistry C*, *121*(11), 6141-6151.
81. Abghoui, Y. (2017). Novel electrocatalysts for sustainable ammonia production at ambient conditions.
82. Anna L. Garden, Younes Abghoui, and Egill Skúlason (2014). Applications of Nitrides as Electrocatalysts *Royal Society of Chemistry Book Series entitled Novel Catalytic Materials, edited by Justin Hargreaves, Andrew McFarlane and Said Laassiri , February (2017).*

Paper I

Nitrogen Reduction Reaction to Ammonia on Transition Metal Carbide Catalysts

Ellingsson, V., Iqbal, A., E. Skulason, and Y. Abghoui,

ChemSusChem, DOI: 10.1002/cssc.202300947

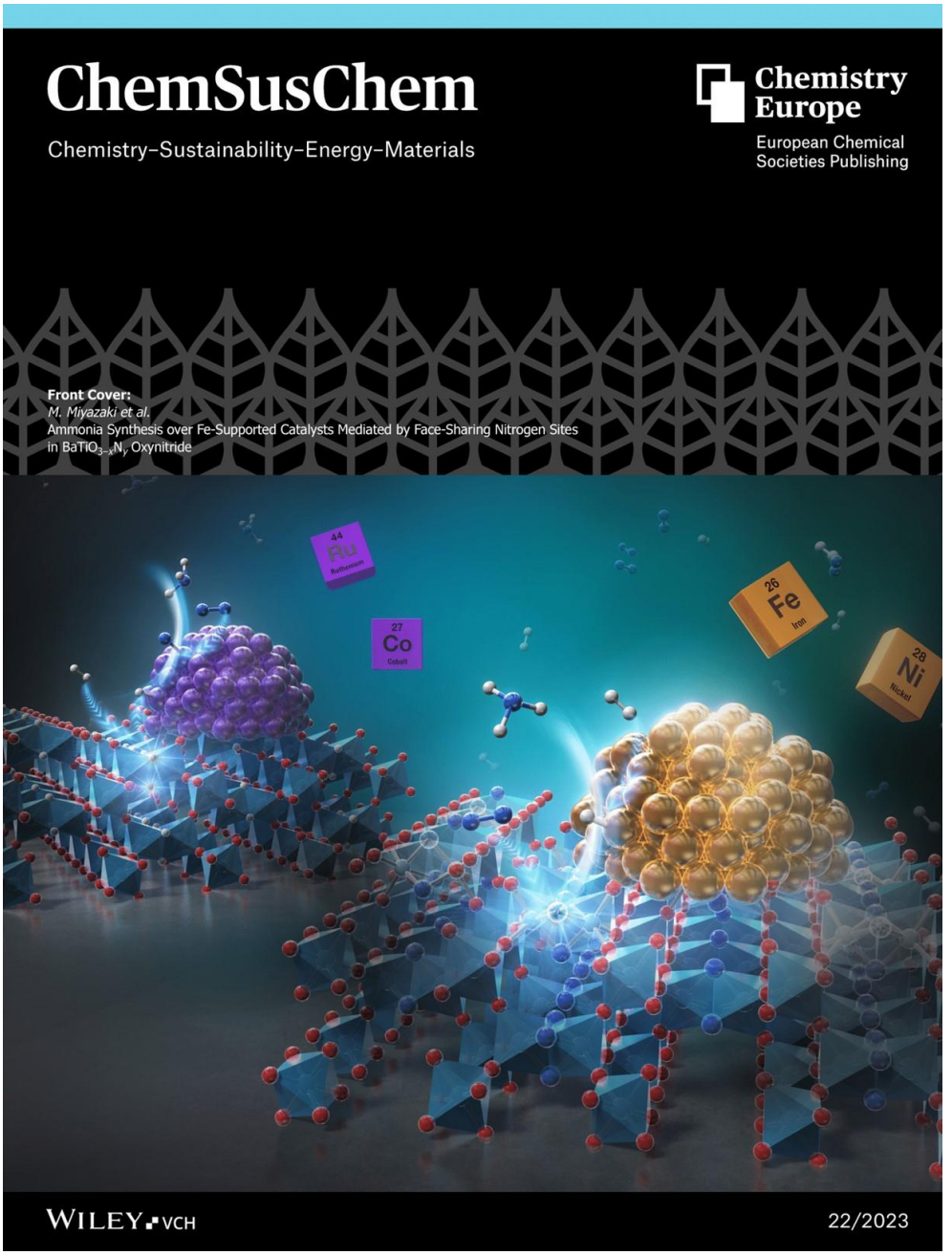
ChemSusChem
Chemistry–Sustainability–Energy–Materials
Chemistry Europe
European Chemical Societies Publishing
Front Cover:
M. Miyazaki et al.
Ammonia Synthesis over Fe-Supported Catalysts Mediated by Face-Sharing Nitrogen Sites in BaTiO3-xNy Oxynitride
44 Ru Ruthenium
27 Co Cobalt
26 Fe Iron
28 Ni Nickel
WILEY VCH
22/2023

ChemSusChem

Research Article
doi.org/10.1002/cssc.202300947

Chemistry Europe
European Chemical Societies Publishing

www.chemsuschem.org

Special Collection

Nitrogen Reduction Reaction to Ammonia on Transition Metal Carbide Catalysts

Viktor Ellingsson,[a] Atef Iqbal,[a] Egill Skúlason,[a, b] and Younes Abghoui*[a]

The development of a low-cost, energy-efficient, and environmentally friendly alternative to the currently utilized Haber-Bosch process to produce ammonia is of great importance. Ammonia is an essential chemical used in fertilizers and a promising high-density fuel source. The nitrogen reduction reaction (NRR) has been explored intensively as a potential avenue for ammonia production using water as proton source, but to this day a catalyst capable of producing this chemical at high Faradaic efficiency (FE) and commercial yield and rates has not been reported. Here, we investigate the activity of transition metal carbide (TMC) surfaces in the (100) facets of the rocksalt (RS) structure as potential catalysts for the NRR. In this study, we use density functional theory (DFT) to model reaction pathways, estimate stability, assess kinetic barriers, and compare adsorbate energies to determine the overall performance of each TMC surface. For pristine TMC surfaces (with no defects) we find that none of the studied TMCs possess both exergonic adsorption of nitrogen and the capability to selectively protonate nitrogen to form ammonia in the desired aqueous solution. ZrC, however, is shown to be a potential catalyst if used in a non-aqueous electrolyte. To circumvent the endergonic adsorption of nitrogen onto the surface, a carbon vacancy was introduced. This provides a well-defined high coordination active site on the surface. In the presence of a vacancy VC, NbC, and WC showed efficient nitrogen adsorption, selectivity towards ammonia, and a low overpotential (*OP*). NbC did, however, display an unfeasible kinetic barrier to nitrogen dissociation for ambient-condition purposes, and thus it is suggested for high tempearture/pressure ammonia synthesis. Both WC and VC in their RS (100) structure are promising materials for experimental investigations in aqueous electrolytes, and ZrC could potentially be interesting for non-aqueous electrolytic systems.

Introduction

In modern industry and agriculture, NH_3 is used to make fertilizers and other chemicals but is also considered a suitable hydrogen energy vector with high hydrogen density and low liquefying pressure.[1] Industrial NH_3 production relies on the Haber–Bosch process, consumes approximately 2% of the world's total energy production and accounts for the release of more than 400 Mt. of CO_2 annually.[2] Energy crises and environmental issues motivate researchers to seek eco-friendly NH_3 synthesis technologies that conserve energy and minimize CO_2 emissions.

Electrocatalytic N_2 reduction is an interesting technique for artificial N_2-to-NH_3 reduction under ambient conditions; nevertheless, effective electrocatalysts for the N_2 reduction reaction (NRR) are required to overcome the high activation barrier for breaking the N_2 triple bonds.[3] Much work has been done on the development of a commercially viable NRR catalyst, but one must be careful when reading publications on the efficiency of NRR catalysts as much of the reported research is not sufficiently rigorous, and does not follow the best practices defined by Greenlee et al.[4] Here most of the reported references have been deemed probably reliable by a comprehensive review of the reliability of reported NRR publications.[5] Noble metals have been a popular choice for catalyst material for a variety of reactions, such as the hydrogen evolution reaction (HER). Noble metals have, however, been shown to not possess favorable properties for the NRR *via* computational studies.[6] Additionally, the scarcity and high cost of utilizing these materials make them an unattractive option. Despite this, the activity of noble metal catalysts for the NRR has been widely explored.[7,11] Another popular approach, a much more promising avenue for NRR noble metal catalysts, is the development of composites that utilize noble metals as the active site, which has been extensively tested.[12–24] These catalysts are, however, still expensive to manufacture and do not display the necessary activity, therefore, much effort has been given to the investigation of NRR electrocatalysts comprised of earth-abundant substitutes.[25,38] Transition metals (TMs) are a good example of a cheap replacement for the noble metal catalyst. For example, Molybdenum is an essential component of nitrogenases for biological N_2 fixation, and its complexes have been manufactured for artificial N_2 reduction. A group of TM-based materials that have been studied extensively as a potential HER and NRR catalyst is the transition metal

[a] *V. Ellingsson, A. Iqbal, Prof. E. Skúlason, Dr. Y. Abghoui*
Science Institute of the University of Iceland
101 Reykjavik (Iceland)
E-mail: younes@hi.is

[b] *Prof. E. Skúlason*
Faculty of Industrial Engineering, Mechanical Engineering and Computer Science
University of Iceland
101 Reykjavik (Iceland)

Supporting information for this article is available on the WWW under https://doi.org/10.1002/cssc.202300947

Special Collection *This publication is part of a collection of invited contributions focusing on "Sustainable Ammonia Synthesis". Please visit chemsuschem.org/collections to view all contributions.*

nitrides (TMNs).[39–51] Due to their unique electronic structure, high electrical conductivity, excellent chemical stability, captivating electrocatalytic activity, and good mechanical durability, TMNs are of great interest for the NRR. Other materials of interest also include transition metal oxides (TMOs) and transition metal sulfides (TMS) for similar reasons as the TMNs.[52–54] However, to the authors' best knowledge, a material capable of producing ammonia at commercially viable yields and rates has not yet been reported. A recent publication reporting a close to 100% Faradaic efficiency (FE) was reported by Du et al. where the role of $LiNTf_2$ as the Li-NRR electrolyte at a nickel wire electrode was investigated.[55] The interface is generated by a high-concentration imide-based lithium-salt electrolyte, providing stabilized ammonia yield rates of around $1.5*10^{-7}$ mol s^{-1} cm^{-2}. This is just an example of a promising work on the NRR that almost achieves the commercial requirements of 50% FE and rate of (4.3–8.7)$*10^{-1}$ mol s^{-1} cm^{-2} but more work is still required, so here we intend to explore the activity of transition metal carbides (TMCs).[56] TMCs are closely related to the promising TMN materials and have been reported to have many desirable characteristics. Not only can TMCs with vacant d orbitals easily adsorb reactant molecules, but they can also enhance the molecular orbital back-donation process.[57,58] Correspondingly, the activation barrier for splitting N_2 is significantly lower in the electrocatalytic NRR of TMCs, endowing TMCs with a high potential for NRR electrocatalysis.[59–61]

Depending on their location in the periodic table and preferred coordination transition metals can produce carbides with different structures and stoichiometries.[62,63] Early transition metal monocarbides and non-stoichiometric carbides have stable rock-salt bulk structures, while mid-transition metals have more complicated stoichiometries and structures.[64–72] It has been found that early (groups 4–6) TMCs exhibit similar electrical and catalytic behaviors as Pt-group metals and may be employed as supports to minimize the total loading of the precious metals.[73–75] The parent metals of TMCs are orders of magnitude more common and less costly than Pt-group metals in the earth's crust. Economically, any replacement of novel metals with TMCs can significantly reduce the cost of the catalyst.[76,77] These characteristics of TMCs make them good supports for metals of the Pt group. Tungsten carbide (WC) has been intensively studied both as a stand-alone electrocatalyst and as a support for Pt-group metals for the hydrogen evolution reaction (HER), hydrogen oxidation reaction (HOR), methanol oxidation reaction, and oxygen reduction reaction (ORR).[76,78–84] However, the promising qualities of other TMCs may also be helpful; for instance, the low synthesis temperature of titanium carbide (TiC) allows for the commercialization of powders with a large surface area.[85] It has been demonstrated that Pt-group metals supported by vanadium (VC) and tantalum (TaC) carbides have synergistic effects on the ORR, while zirconium carbide (ZrC) is a suitable support for the HOR.[86–88] An important factor to keep in mind when exploring experimental publications on the activity of TMC catalysts is the possibility of the formation of oxycarbides. We encourage experimentalists to prioritize rigorous characterization techniques in their work such as X-ray diffraction (XRD), X-ray photoelectron spectroscopy (XPS), and electron microscopy, to verify the composition and structure of the carbide materials synthesized before use in ammonia formation experiments. We predict that most of the tested carbides do not bind oxygen favorably in the presence of nitrogen, which would be the first step in the formation of an oxycarbide system, and so not explored further at the present but warrants future exploration.

In the current work, TMC catalysts for the electrochemical production of ammonia under ambient circumstances are studied with a focus on pure carbide systems with a 1:1 metal-to-carbon ratio. Before exploring more complicated systems, such as different stoichiometries, carbides with more than one metal species, or carbides with dopant atoms we must first characterize the pure carbides to be able to better understand the chemistry and provide a point of comparison for other carbide systems. We report the activity of the (100) facets of the rocksalt (RS) structure of TMCs surfaces using density functional theory (DFT) to collect thermodynamic data and other activity descriptors. The onset potentials necessary for ammonia production, free energy diagrams, poisoning tendencies, kinetic barriers, and surface stability are among the collected data used to determine the activity of TMC surfaces. The computational standard hydrogen electrode is used to account for the influence of an external potential, which is considered in the context of activity and stability of the surface at the operating potential.[89]

Computational Methods

Modeling parameters

All calculations were performed using Density functional theory (DFT) with the RPBE exchange-correlation functional.[90] The Vienna ab-initio simulation package (VASP) was used with a 4×4×1 Monkhorst-Pack K-point mesh and a 400 eV energy cutoff for all the surfaces.[91] The Projector augmented wave (PAW) method was used as implemented in the VASP code; this gives access to the full wavefunction by utilizing computationally efficient pseudopotentials, significantly reducing computation time.[92] The occupation of the Kohn-Sham orbitals was smeared according to a Fermi-Dirac distribution with a smearing parameter of $k_BT = 0.1$ eV.

All the surfaces were considered in the RS crystallographic structure and the (100) surface orientation. This structure and surface orientation was chosen to allow comparison to similar studies performed on the TMN surfaces published by our group.[41,47–51] The TMC surfaces were modeled with a 5-layer 2×2 unit cell, containing 20 metal atoms and 20 carbon atoms, see Figure 1. The two bottom layers were fixed in place while the three top layers, along with any adsorbates, were allowed to relax. Boundary conditions were periodic in the x and y directions, and each surface slab was separated with at least 12 Å of vacuum in the z direction, to minimize the influence of neighboring slabs. The structural optimization was considered converged when the forces in any direction on all moveable atoms were below 0.01 eV $Å^{-1}$. Activation energies were calculated as the highest point along the minimum energy path

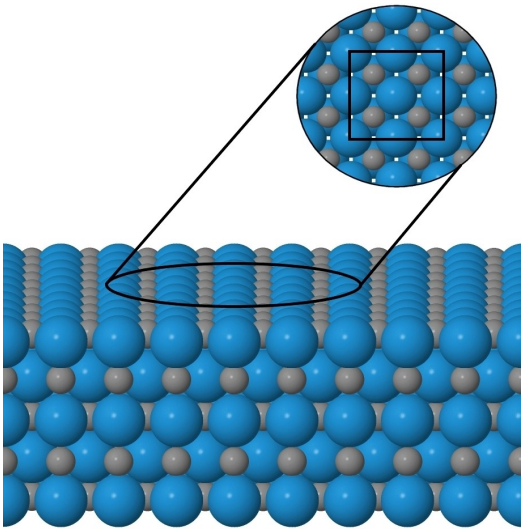

Figure 1. *A schematic representation of a 5-layer WC in the (100) facets of the RS surface as used in the computational calculations. A top view of the unit cell used can be found in the upper right-hand corner, denoted with a black square.*

(MEP) using the climbing image nudged elastic band method (CI-NEB).[93]

Reaction pathways and electrochemical modeling

The total reaction pathway for the formation of ammonia can be modeled *via* the following equations:

$$N_2 + 6(H^+ + e^-) \rightleftharpoons 2NH_3 \quad (1)$$

$$H_2 \rightleftharpoons 2(H^+ + e^-) \quad (2)$$

In the electrochemical cell, the reactants required for the formation of ammonia at the cathode (Eq. 1) are supplied by nitrogen in the atmosphere, protons formed at the anode (Eq. 2), and electrons from the applied potential. Since the protons required for the reaction are formed exclusively at the anode, we can make a direct comparison of the applied potential to the standard hydrogen electrode (SHE) or the reversible hydrogen electrode (RHE). The reaction pathway was modeled *via* an unconstrained mechanism where for each protonation step the most thermodynamically favorable adsorption site was found and used for the next protonation until a product was formed. An unconstrained mechanism gives the best insight into the catalytic activity of the catalyst and which product(s) it tends to form. For each reaction step the free energy change, at $U=0$ V vs. RHE and pH = 0, can be calculated *via* the following equation:

$$\Delta G(0) = \Delta E + \Delta E_{ZPE} - T\Delta S \quad (3)$$

where $\Delta G(0)$ is the free energy change at $U=0$, ΔE is the difference in electronic energies calculated *via* DFT, ΔE_{ZPE} and $T\Delta S$ are the calculated zero point energy and entropy corrections, see Table S1. To calculate the free energy change at a given potential and pH value (ΔG(U, pH)) we use the implicit computational hydrogen electrode approach as:

$$\Delta G(U, \text{pH}) = \Delta G(0) - neU - k_B T \ln(10) \times \text{pH} \quad (4)$$

where n is the number of electrons involved in the reaction step, e is the charge of an electron, and U is the applied potential.[89] All reported data is calculated at pH = 0. For each reaction pathway, we define the potential determining step (PDS) to be the electrochemical reaction step with the highest positive free energy change. From the PDS we can define the overpotential (*OP*) as the potential required to make the free energy change of the PDS zero, from Eq. 4,

$$OP = -\Delta G/e \quad (5)$$

The *OP* (in volts) is simply equal to the negative magnitude of the free energy change associated with the PDS in electron volts.

Results and Discussion

The reactivity of TMC surfaces in the RS structure with the (100) crystallographic orientation for the NRR was tested by modeling adsorption energies and reaction pathways for each candidate; VC, CrC, YC, HfC, NbC, ScC, ZrC, TiC, TaC, WC, and MoC. These candidates were chosen based on reported stability on the Materials Project website, with the addition of MoC and WC which are reported to be meta-stable, possibly decomposing to other structures or stoichiometries.[94] Firstly, for any reactivity to occur adsorption of a nitrogen species onto the surface should be investigated. For the adsorption of nitrogen three possible mechanisms were considered, the associative binding of nitrogen gas (*N_2), the dissociative binding of nitrogen gas (*2 N), and the associative binding of NNH (*NNH). For each of these options, all possible adsorption sites were tested, and the most favorable adsorption was used for comparison, the results for the adsorption of nitrogen and possible active site poisoning by other species can be seen in Figure 2.

Along with the adsorption energies of nitrogen species, Figure 2 shows the energy associated with the protonation of a metal site which is a good indicator of the likelihood of the hydrogen evolution reaction (HER), which is usually the main competing reaction to the NRR. As can be seen in Figure 2, only YC and ScC can favorably bind nitrogen, however, all the carbides shown here are expected to bind nitrogen stronger than protons onto the metal site. Although for ZrC the dissociative binding of nitrogen gas is only very slightly endergonic and so ZrC will also be further considered. For YC and ScC, after the binding of nitrogen, the favored reaction pathway was found by sequential protonation of the surface *via* an unconstrained mechanism. This means that for each protonation step

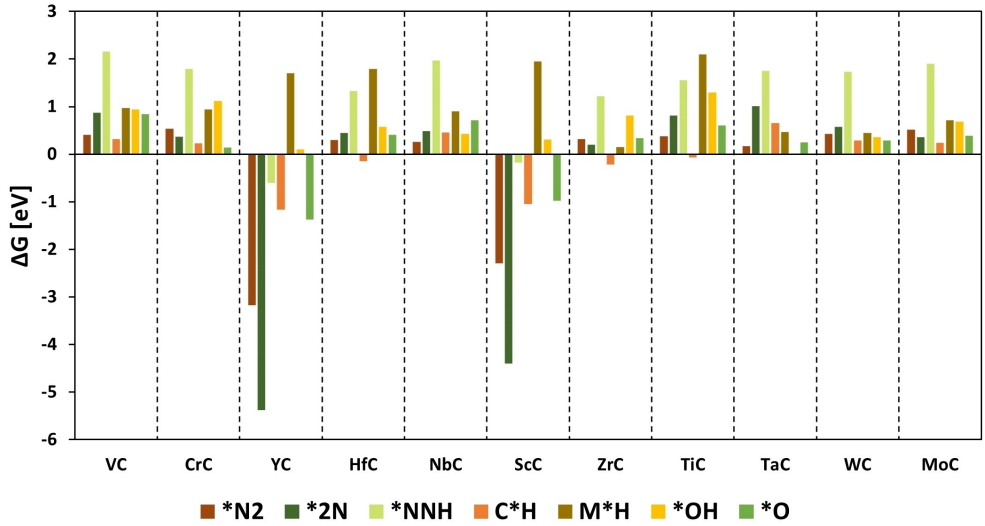

Figure 2. *Comparison of adsorption energies of different nitrogen and oxygen species onto clean TMC surfaces as well as protonation of a metal and carbon site at zero potential. *N2 signifies the associative binding of N_2(g), *2 N is the dissociative binding of N_2(g), and *NNH is the associative binding of NNH.*

all possible adsorption sites were considered and the most favorable chosen to continue the reaction. For both these surfaces in all three cases (the three different nitrogen species) the formation of ammonia (NH_3) was not observed. The favorable protonation of carbon sites over nitrogen led to the formation of either methane (CH_4) or hydrogen (H_2) at which point calculations were terminated. The formation of methane or hydrogen indicates a tendency for either the decomposition of the surface or the prevalent presence of the HER, both of which are not desired for an NRR catalyst. This behavior is reflected in the exergonic protonation of carbon sites on some of these TMCs, YC, and ScC included. In addition to not forming the desired product, YC and ScC are the only two TMC surfaces that favorably bind the oxygen species O^{2-} at zero potential. Such oxidation of the TMC surface can render the catalyst inactive and in the case of exergonic adsorption, partial or total oxidation is difficult to prevent when moving the catalyst from the growth chamber to the electrolytic cell. For ZrC, however, oxidation is endergonic, but it still suffers from exergonic protonation of a carbon site. This means the activity of ZrC will be hindered in an aqueous electrolyte but might be promising in a system using an ionic liquid/molten salts. For the full FED of ZrC see Figure S1.

As can be seen in Figure S1 (a), although the initial adsorption of nitrogen is slightly endergonic on ZrC the surface proceeds to ammonia formation with a PDS of 0.69 eV. The PDS is the electrochemical reaction step with the largest free energy change, this will determine the potential required to make the entire path exergonic and the formation of ammonia spontaneous. The reaction pathway for ZrC at the required overpotential (*OP*) is shown in Figure S1 (b). Also, Figure S1 (a) shows a comparison between the dissociative binding of nitrogen, associative binding of nitrogen, binding of NNH, the adsorption of hydrogen onto a metal site, and the adsorption of hydrogen onto a carbon site on the clean surface. ZrC is, therefore, a potential catalyst for the NRR, the required *OP* is modest (−0.69 V), and the reaction pathway only requires 9 protonation steps, meaning there is minimal proton coverage on the surface. Increased surface coverage means a higher possibility of the HER occurring or in the case of TMC surfaces, the formation of methane. If experimentalists have a way of circumventing the endergonic dissociative adsorption of nitrogen onto the ZrC surface (either by pressure or temperature tuning), we recommend exploring this possible catalyst. In general, however, for the clean TMC surfaces, it is apparent that there is not much potential for catalytic activity, the main problem being the initial binding of the required nitrogen species.

To better facilitate nitrogen adsorption the idea of creating a carbon vacancy on the surface may be promising. It should also be noted that in real experiments, TMC should have a large number of defects such as carbon vacancies, because usually a full stoichiometry is hard to reach. To test this hypothesis next, we will look at the TMC surfaces in the presence of a carbon vacancy, the vacancy is created by removing one carbon from the surface as CH_4 and letting the resulting structure relax. Here we make the assumption that either the surface has pre-existing vacancies formed in the manufacturing of the material or that the surface will create CH_4 at standard operating conditions. For all the surfaces tested the free energy associated with the formation of CH_4 was exergonic at the respective *OP* for each material. The presence of a vacancy on the surface provides an active site where nitrogen can more easily bind due to the lower coordination associated with the vacancy and potentially facilitates higher selectivity towards nitrogen adsorption and then protonation. First, we will look at the binding of nitrogen species in the vacancy of these TMC surfaces, see Figure 3.

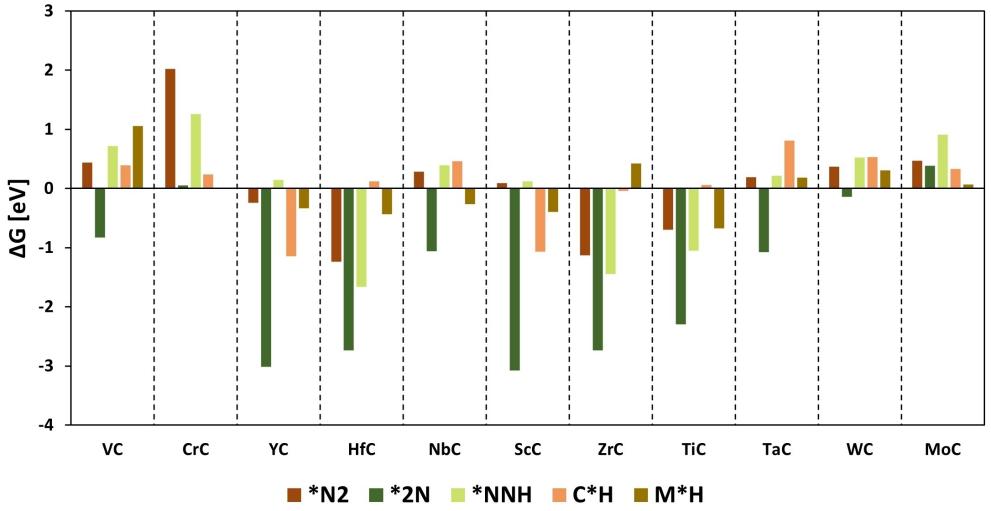

Figure 3. *Comparison of binding energies of different nitrogen species onto TMC surfaces with a carbon vacancy at zero potential. *N2 signifies the associative binding of N_2(g) horizontally in the vacancy, *2 N is the dissociative binding of N_2(g) where one N sits in the vacancy and the other on a neighboring carbon atom, *NNH is the binding of NNH horizontally in the vacancy, C*H is the protonation of a surface carbon, and M*H is the protonation of a surface metal atom.*

As can be seen in Figure 3 the adsorption energies of the required nitrogen species are vastly improved in the presence of a vacancy when compared with Figure 2. Especially promising is the dissociative binding of nitrogen, which is exergonic for most of the TMCs, this does however eliminate MoC which does not bind any nitrogen species favorably. CrC is an outlier, having only slightly endergonic dissociative adsorption of nitrogen, and so as in the case for clean ZrC we will include CrC in our promising candidates for now. The reaction pathways were calculated for each of the exergonic nitrogen adsorptions until the formation of either two molecules of ammonia or the first by-product (H_2 or CH_4) was achieved. The only surfaces that proceeded to ammonia formation were WC, VC, NbC, and CrC when binding nitrogen dissociatively, see Figure 6 and S3-5. Since the dissociative binding of nitrogen is always favored over the other nitrogen adsorbates, we will now focus on the dissociative binding of nitrogen on the aforementioned TMC surfaces in the presence of a carbon vacancy. Although the presence of a vacancy gets around the problem of the endergonic dissociative N_2 adsorption energy, some TMCs that produced ammonia with a clean surface (without the presence of C-vacancy) did not do so in the presence of a vacancy, see Figure S2. These surfaces are HfC, ZrC, TiC, and TaC. As an example, comparing the reaction pathways of ZrC with a vacancy to that of ZrC without a vacancy we can see the negative effect the presence of a vacancy has on the selectivity of this catalyst, and conversely, the positive effect on the adsorption energy of nitrogen, see Figure S2. For ZrC, there is a significant lowering of the adsorption energy of nitrogen, and also a lowering of the required *OP* which would enhance activity, but we lose a measure of selectivity due to the tightly bound nitrogen molecule in the vacancy. The protonation of the surface nitrogen, ^{A}N, proceeds without a hitch, and one molecule of ammonia is developed, but protonation of the nitrogen in the vacancy site seems to be hindered. We believe that due to the very favorable adsorption of nitrogen, the stability gained by keeping the nitrogen atom in the vacancy is favored over protonation. This would mean that to achieve the desired activity the adsorption of nitrogen would have to be exergonic but below some threshold energy. Looking at Figure 3 we can see that this threshold energy would be approximately up to −1.0 eV since that would correctly predict that only WC, NbC, and VC would be active catalysts. There is one outlier, that is TaC, which does not produce ammonia despite having very similar adsorption energy to NbC, only a difference of 0.01 eV. For TaC, and the rest of the TMC that bind the vacancy nitrogen too strongly, it would be interesting to test these surfaces further by exploring the possibility of alternative reaction pathways. For example, investigating the activity in the case of additional nitrogen adsorption after the formation of one molecule of ammonia or the presence of a higher quantity of vacancies. The *OP* associated with each TMC surface in the presence of a vacancy can be found in Figure 4.

As can be seen in Figure 4, all of the TMC vacancy surfaces require an *OP* of less than 1 eV, which is generally considered the threshold value for good activity. Not all of the TMC vacancy surfaces produce ammonia along the reaction pathway calculated, as previously mentioned, only VC, CrC, NbC, and WC produce 2 equivalents of ammonia, marked as green or with a* in Figure 4. The other surfaces produce either H_2(g) or CH_4(g) along the most favorable reaction pathway.

The introduction of a vacancy not only provides a catalytic site for nitrogen adsorption but can also cause surface poisoning by other ions present in the electrolytic solution. To explore the possibility of poisoning the vacancy site and check the stability of the catalyst against poisoning, the adsorption energies of H^+,

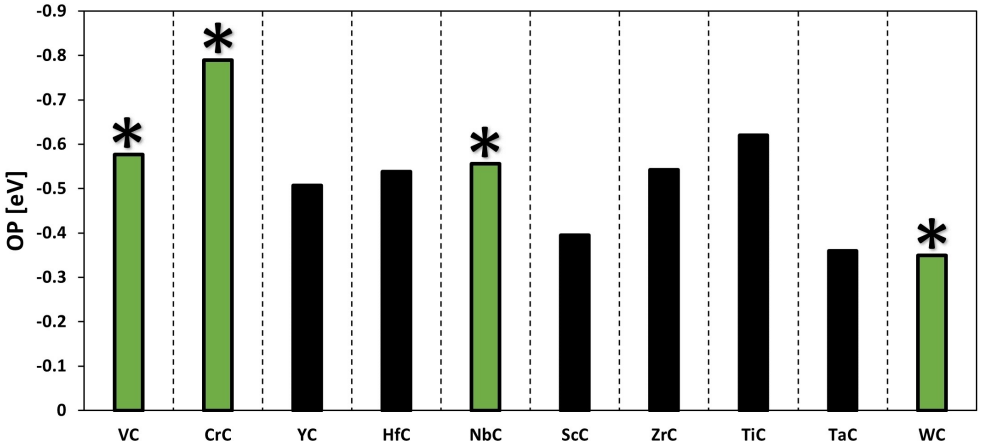

Figure 4. *The OP of each TMC surface in the presence of a carbon vacancy. Bars colored in green, or marked with a* (for non colorized version), proceed to ammonia formation along the reaction pathway used to obtain the OP value. The black bars indicate surfaces that do not proceed to form two equivalents of ammonia, but rather produce either H_2 (g) or CH_4 (g).*

O^{2-} and OH^- in the vacancy were calculated and compared to the dissociative binding of nitrogen at the operating potential of each TMC, see Figure 5.

The poisoning of the catalytic site seems to only be a concern in the case of VC and CrC, which prefer to bind protons in the vacancy over the dissociative binding of nitrogen. To explore whether this would hinder the catalytic activity of VC, CI-NEB calculations were performed to see if nitrogen could displace a proton in the vacancy of VC, see Figure S6.

As can be seen in Figure S6, the adsorption of nitrogen into the vacancy is not kinetically hindered by the presence of hydrogen and the total reaction, adsorption of nitrogen and rotation of NH, is exothermic. After the protonation of the vacancy on the VC surface, the next thermodynamically favorable step, at the required *OP*, is the protonation of the neighboring carbon atom. The dissociative adsorption of nitrogen is, however, only slightly less favorable (circa 0.03 eV), see Figure S3, and so VC will still be considered promising in this study. This branching path starting with the protonation of the vacancy followed by the protonation of the adjacent carbon atom may lead to the formation of a second vacancy that could offer a different catalytic pathway for the formation of ammonia with both nitrogen atoms adsorbing into vacancies, this may be explored in a later publication.

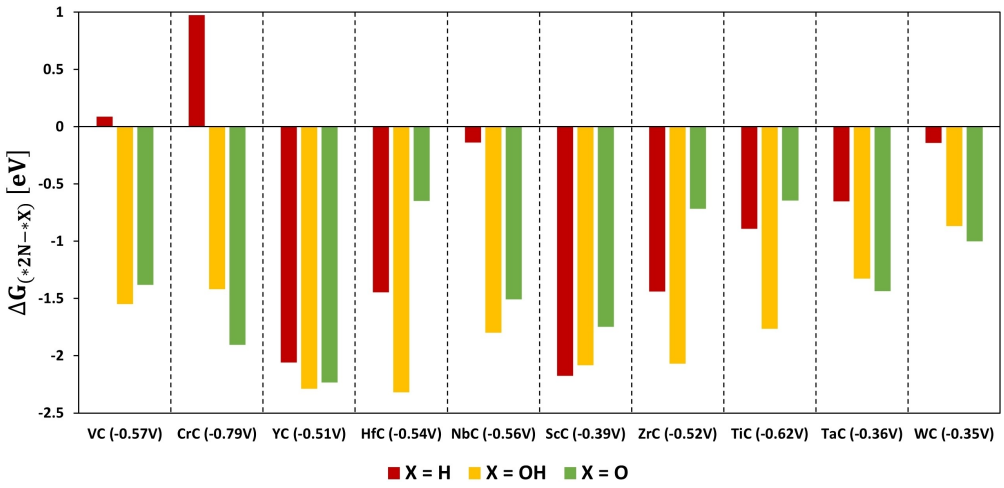

Figure 5. *Comparison of binding energies of protons, hydroxyl, and oxygen species in the vacancy of the TMCs, only the TMCs that favorably bind nitrogen dissociatively are shown. The energies are plotted as the difference between the adsorption energy of the relevant species, at the required OP for operation, and the dissociative adsorption of N_2. The required OP for each material can be found next to their respective name under each column.*

Now considering CrC, it was observed that the same rotation as is depicted in Figure S6 for VC was exothermic for CrC, and so is assumed to also have an insubstantial barrier. CrC, however, suffers from the same subsequent protonation of a neighboring carbon atom which is much more favorable than the dissociative adsorption of nitrogen. What makes CrC interesting, however, is that if these branching protonation paths can be circumvented the formation of the first equivalent of ammonia only requires an *OP* of 0.19 V, see Figure S4. Although when the full path is considered, the required *OP* is −0.79 V, a mechanism utilizing the lower *OP* by forming one equivalent of ammonia and then regeneration of the surface or with both nitrogen molecules adsorbed in vacancies would be interesting to investigate. Consequently, we recommend investigating CrC further either in non-aqueous electrolyte or in the presence of a higher concentration of surface vacancies, but the surface will not be considered further in the present publication.

Another kinetic barrier that must be considered is the activation energy of N_2 adsorption. NEB calculations for the four promising candidates: ZrC (without a vacancy), WC, NbC, and VC were performed, and the results are shown in Figure S7 and Table S2. The kinetic barrier for dissociative nitrogen adsorption onto the NbC surface in the presence of a vacancy is too high (1.54 eV) to consider NbC a promising catalyst under ambient conditions. The catalyst must be able to adsorb nitrogen on a reasonable timescale for the production to be commercially viable, and a kinetic barrier over 1.0 eV is certainly going to impede that process at ambient conditions. For the other candidates, the kinetic barrier is acceptable and surmountable at ambient conditions, but it is important to compare these values to the kinetic barriers associated with the migration of a sub-layer carbon to fill the surface vacancy. This comparison gives a measure of how likely the surface is to decompose under operating conditions and thus could be considered a good indicator of stability. If the barrier for migration (causing decomposition) is lower than the barrier for nitrogen adsorption (causing regeneration), surface vacancies are more likely to be filled by sub-layer carbon. Another carbon surface vacancy might subsequently form, and the process continues to erode the catalyst and decomposes it to its parental metal. The path of migration for a second-layer carbon to fill a surface vacancy along with the associated energy values is shown in Figure S8. In all cases, the barrier for carbon sub-layer migration is more than 1 eV higher than the barrier for dissociative N_2 adsorption. This means the migration of sub-layer carbon to a surface vacancy should not be of concern, and these TMCs are expected to show stability against decomposition. It is important to note that for NbC, although the barrier for dissociative nitrogen adsorption is very high (approx. 1.54 eV) since the barrier for sub-layer carbon migration is much higher (2.96 eV) the catalyst might still show good stability under the correct temperature and pressure conditions. For instance, tuning the temperature, increasing it above ambient conditions, could make the adsorption barrier of 1.54 eV surmountable while keeping carbon migration kinetically hindered, for the full reaction pathway of NbC see Figure S5.

The activity of TM-based catalysts for the NRR has been shown to be limited by scaling relations.[95] The linear scaling of certain reactions on the catalyst surface causes the thermodynamics of the optimal catalyst to be limited. These scaling relations can be a valuable way to predict the activity of a potential catalytic surface and to determine if any of the tested materials display the optimal energetics. To determine whether TMCs are limited by scaling relations, in the case of dissociative nitrogen adsorption in the presence of a vacancy, the energies of all reaction steps involved in the reaction pathways calculated were plotted as a function of dissociative nitrogen adsorption. This reaction pathway, TMC vacancy surfaces with dissociative nitrogen adsorption, was chosen due to displaying the most promising catalytic properties. These calculations, however, did not yield a volcano plot, as the reaction pathways for each TMC surface were too varied, and no discernable trend was obtained. There was no shared limiting reaction step for all of the TMC surfaces. The presence of scaling relations was also investigated in the case of a simplified reaction mechanism that only considers reaction steps leading to ammonia formation. This limits the reaction configurational space, making it more likely a trend can be obtained. All possible reaction pathways leading to ammonia formation were calculated *via* a restricted MvK mechanism, and the pathway leading to the average lowest *OP* was plotted, see Figure S9. From the total reaction pathway, a volcano plot was extracted, see Figure S10. This volcano plot, however, provides limited information due to the simplified reaction mechanism but can be used to assess the relative tendency of a surface to produce ammonia in the absence of undesirable side reactions.

Considering the most promising candidate, the reaction pathway for WC is shown in Figure 6.

Figure 6 shows that WC is a very promising catalyst that produces ammonia after 9 protonation steps at a low *OP* (−0.35 V), and is very selective towards NH_3. For further analysis, the electronic properties of the promising candidates; CrC, VC, NbC, and WC for the clean surface, the vacancy surface, and the vacancy surface with nitrogen dissociatively adsorbed were performed. For the band structures results see Figure S11 and for the density of states (DOS) see Figure S12.

A recent study on the VC (100) surface by Zhang et al. supports our conclusion here, with both experimental and theoretical results, that the activity of the surface VC for the NRR is greatly enhanced in the presence of a carbon vacancy.[96] In their publication, a VC surface with periodic carbon vacancies, the surface stoichiometry was V_8C_7 (this is 12.5% vacancy coverage as compared to the 25% coverage tested in this paper) with a (100) orientation, was synthesized and tested for NRR activity. The results show a stable FE of 18,3% and a yield of 23.2 $\mu g\,h^{-1}\,mg_{cat}^{-1}$ over a time period of 20 hours. What is curious about these results is that they are reported at −0.1 V vs RHE, a potential that neither our study, we predict a required *OP* of −0.58 V, nor theirs predicts to be sufficiently high to drive the reaction on the (100) VC surface in the presence of a vacancy. Zhang et al. report a predicted required *OP*, acquired by DFT calculations, of −0.36 V which corresponds with the desorption of NH_3. That is, however, not an electrochemical step, so in actuality, the true predicted *OP* should be the protonation of the nitrogen sitting in the vacancy (after creating one equivalent of

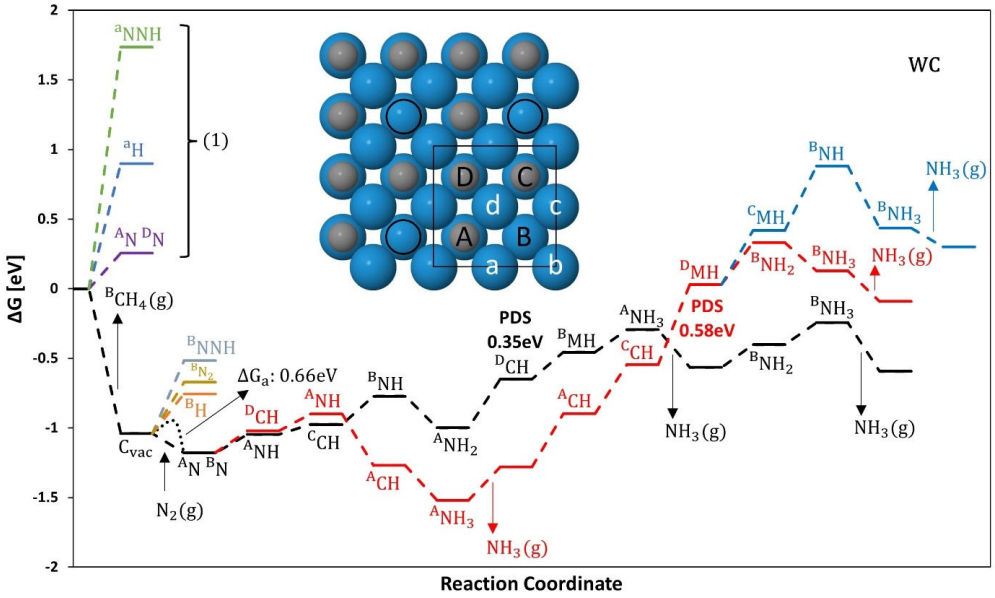

Figure 6. *Non-restricted FED for WC at zero potential. The black path describes the unconstrained mechanism, each reaction step proceeds via the most favorable intermediate, starting with the formation of a carbon vacancy on the surface. The steps labeled (1) are adsorption energies onto the clean surface, also included is the adsorption of NNH (light gray) and H (orange) into the vacancy. The two branching paths Blue and Red describe pathways resulting from the formation of an alternative intermediate with slightly higher energy as compared to the black path. The activation free energy for the dissociation of adsorbed N_2 is labeled ΔG_a ($\Delta G_a = \Delta E_a + 0$) for the appropriate reaction step, see Table S2. The labeling ^{A}X refers to the positioning of the adsorbed species in the unit cell, in this case, site A as defined in the inset figure in the top middle. The inset figure found in the top middle defines all relevant adsorption sites as well as the unit cell (black square).*

ammonia, value: −0.35 V) which corresponds to one of the predicted limiting reactions when investigating the restricted mechanism (see scaling relations Figure S10). In addition, Zhang et al., do not adequately describe the mechanism in question. The most favorable adsorption of nitrogen onto the vacancy surface is reported to be associatively into the carbon vacancy, however, as can be seen in Figure S3, we predict this adsorption pathway to be not only less favorable than the dissociative pathway but significantly endergonic. Although Zhang et al. also report this adsorption step to be endergonic, it's significantly less so (only 0.19 eV) whereas we predict this adsorption energy to be 0.37 eV. Even if we consider the value Zhang et al. report, it is interesting that they use these energetics to support the claim that V_8C_7 shows good NRR activity, since the endergonic adsorption is quite damaging to the activity of the catalyst. These discrepancies, in reported thermodynamics, could be blamed on unorthodox methodology, their paper uses DFT calculations on a 2-layer 8x4 unit cell with 10 angstroms of vacuum using the PBE (Perdew-Burke-Ernzerhof) functional. This choice of system neglects all contributions from the bulk atoms and gives rise to extended relaxation, in addition, the PBE functional has been shown to predict worse average adsorption energies than the RPBE functional used in this publication and thus the RPBR is better than PBE for adsorption energies on surfaces.[97] Additionally, unlike this publication, the mechanism seems to be modeled, although never stated in the paper, *via* the simplified constrained mechanism where protons are forced on the nitrogen sites without investigating the metal or carbon site protonation. This, along with a lack of kinetic barriers, stability considerations, and potential poisoning gives an incomplete picture of the activity of this catalyst in a paper by Zhang et al. Although their publication lacks computational rigor, the experimental results, which are validated with ^{15}N labeled tests, are quite promising and eloquently display our main result, which is the increased activity of these TMC surfaces in the presence of a carbon vacancy.

Another recent study done on V_8C_7 nanoparticles by Feng et al. showed very promising activity.[98] Their publication is purely experimental and reports the activity of these nanoparticles with Ar gas and N^{15} control measurements. Feng et al. report a maximum FE of 12.2% and a yield of 34.62 $mg\,h^{-1}\,mg_{cat}^{-1}$ at a potential of −0.40 V vs RHE. This is a lower FE than reported by Zhang et al., likely due to the higher *OP*, but yet Feng et al. achieve a much higher yield, about a 150% increase. The higher yield is to be expected of nanoparticle catalysts, it is interesting, however, that the *OP* reported by Feng et al. is much closer to the value we predicted in this paper, the difference could be attributed to the different structures of the catalyst. Feng et al. support our conclusions regarding the activity of VC with surface irregularities, the nature of the nanoparticle simulating the presence of a vacancy, but does not propose any potential reaction pathways or mechanisms. Although this FE and yield are promising, it is not enough to be commercially viable and so determining the material properties

that lead to good reactivity, such as mechanisms, poisoning, scaling relations, etc. are vital, such as is done here in this paper.[56]

Conclusions

The outcome of our comprehensive analysis of the suitability of TMCs as catalysts for the NRR reveals that without the presence of a surface defect these TMCs (VC, CrC, YC, HfC, NbC, ScC, ZrC, TiC, TaC, WC, and MoC) are limited in their reactivity due to endergonic adsorption of nitrogen. ZrC was the only TMC that could semi-favorably adsorb nitrogen and subsequently produce ammonia. ZrC is, however, prone to protonate carbon sites over nitrogen and so not recommended as a selective NRR catalyst in aqueous solution. Since these surfaces are prone to form surface carbon vacancies at their respective operating conditions, the unfavorable nitrogen adsorption observed for these TMCs could be circumvented in the presence of a carbon vacancy, which should also be common on a real surface. When the vacancy was introduced, most of the TMC surfaces adsorbed nitrogen favorably and WC, NbC, VC subsequently produced ammonia. A lack of ammonia formation was observed for the TMCs that featured highly exergonic nitrogen adsorption; the lack of reactivity is likely due to the stability gained by having nitrogen in the vacancy outweighing the tendency for protonation. For the catalysts with promising activity, subsequent calculations on potential poisoning and kinetic barriers only ruled out NbC due to high activation energy for the dissociative adsorption of N_2. NbC is therefore not a promising candidate under ambient conditions but might display good activity under the correct temperature and pressure conditions. For VC, poisoning of the vacancy site by adsorption of a proton, hinders the activity of the catalyst, causing subsequent protonation of carbon sites over the adsorption of N_2. This complicates the potential reaction pathways of VC, which might either proceed to ammonia formation *via* the slightly less favorable adsorption of N_2 or the formation of a second vacancy which might promote or impede the formation of ammonia. VC shows promising activity which is worth testing or exploring further. WC was the most promising candidate, displaying good activity, stability, resistance to poisoning, low *OP* (−0.35 V), and selectivity. We highly recommend WC to experimentalists to explore the possibility of utilization for the NRR in real-life applications and if promising then possibility of scale-up and commercialization. Although ZrC was promising when exploring the clean TMC surface, it did not display catalytic activity in the presence of a vacancy. More work is required to understand the viability of using surfaces such as CrC or ZrC in the presence of a vacancy, which display mostly favorable energetics but suffer either from slightly endergonic adsorption energies or binding nitrogen too tightly in vacancy sites. These surfaces might produce ammonia if more complex reaction pathways are considered, such as a reaction pathway involving a higher concentration of vacancies.

Acknowledgment

This work was supported by the Icelandic Research Fund (No. 207056-053), and the Research Fund of the University of Iceland.

Conflict of Interests

The authors declare no conflict of interest.

Data Availability Statement

The data that support the findings of this study are available from the corresponding author upon reasonable request.

Keywords: density functional theory · nitrogen reduction reaction · ammonia · transition metal carbides · defects

[1] R. Z. Sørensen, J. S. Hummelshøj, A. Klerke, J. B. Reves, T. Vegge, J. K. Nørskov, C. H. Christensen, *J. Am. Chem. Soc.* **2008**, *130*, 8660.
[2] C. Shiming, S. Perathoner, C. Ampelli, G. Centi, in *Horizons in Sustainable Industrial Chemistry and Catalysis*, Elsevier.**2019**, 31.
[3] C. Guo, J. Ran, A. Vasileff, S.-Z. Qiao, *Energy Environ. Sci.* **2018**, *11*, 45.
[4] L. F. Greenlee, J. N. Renner, S. L. Foster, *ACS Catal.* **2018**, *8*, 7820.
[5] F. Rezai, S. Læsaa, N. Şahin, J. Catalano, E. Dražević, *Low-Temperature Electrochemical Ammonia Synthesis: Measurement Reliability and Comparison to Haber-Bosch in Terms of Energy Efficiency*, **2023**, ChemRxiv. Cambridge: Cambridge Open Engage; 2023; This content is a preprint and has not been peer-reviewed.
[6] E. Skúlason, T. Bligaard, S. Gudmundsdóttir, F. Studt, J. Rossmeisl, F. Abild-Pedersen, T. Vegge, H. Jónsson, J. K. Nørskov, *Phys. Chem. Chem. Phys.* **2012**, *14*, 1235.
[7] M. R. Nazemi, P. Ou, A. Alabbady, L. Soule, A. Liu, J. Song, T. Sulchek, M. Liu, M. El-Sayed, *ACS Catalysis* **2020**, *28*, 2781.
[8] M. R. Nazemi, L. Soule, M. Liu, M. El-Sayed, *J. Electrochem. Soc.* **2020**, *167*, 054511.
[9] W. Cai, Y. Han, Y. Pan, X. Zhang, J. Xu, Y. Zhang, Y. Sun, S. Li, J. Lai, L. Wang, *J. Mater. Chem. A* **2021**, *9*, 13483.
[10] X. Wei, M. Pu, Y. Jin, M. Wessling, *ACS Appl. Mater. Interfaces* **2021**, *13*, 21411.
[11] C. Du, C. Qiu, Z. Fang, P. Li, Y. Gao, J. Wang, W. Chen, *Nano Energy* **2022**, *92*, 106784.
[12] C. Yang, B. Huang, S. Bai, Y. Feng, Q. Shao, X. Huang, *Adv. Mater.* **2020**, *32*, 2001267.
[13] S. Zhao, H.-X. Liu, Y. Qiu, S.-Q. Liu, J.-X. Diao, C.-R. Chang, R. Si, X.-H. Guo, *J. Mater. Chem. A* **2020**, *8*, 6586.
[14] X. Wei, D. Vogel, L. Keller, S. Kriescher, M. Wessling, *ChemElectroChem* **2020**, *7*, 4679.
[15] X. Zhao, Z. Yang, A. V. Kuklin, G. V. Baryshnikov, H. Ågren, X. Zhou, H. Zhang, *ACS Appl. Mater. Interfaces* **2020**, *12*, 42821.
[16] C. Yao, N. Guo, S. Xi, C.-Q. Xu, W. Liu, X. Zhao, J. Li, H. Fang, J. Su, Z. Chen, H. Yan, Z. Qiu, P. Lyu, C. Chen, H. Xu, X. Peng, X. Li, B. Liu, C. Su, S. J. Pennycook, C.-J. Sun, J. Li, C. Zhang, Y. Du, J. Lu, *Nat. Commun.* **2020**, *11*, 4389.
[17] J. Zhang, B. Zhao, W. Liang, G. Zhou, Z. Liang, Y. Wang, J. Qu, Y. Sun, L. Jiang, *Adv. Sci.* **2020**, *7*, 2002630.
[18] W. Cai, Y. Han, H. Li, W. Qi, J. Xu, X. Wu, H. Zhao, X. Zhang, J. Lai, L. Wang, *J. Mater. Chem. A* **2020**, *8*, 20331.
[19] Z. Wang, W. Tian, H. Yu, T. Zhou, P. Wang, Y. Xu, X. Li, L. Wang, H. Wang, *Nanoscale* **2021**, *13*, 13809.
[20] Z. Wang, W. Tian, Z. Dai, T. Zhou, Q. Mao, Y. Xu, X. Li, L. Wang, H. Wang, *Inorg. Chem. Front.* **2021**, *8*, 4276.
[21] Y. Guo, J. Liu, Q. Yang, P. Khemthong, Z. Huang, Y. Zhao, Z. Chen, B. Dong, X.-Z. Fu, J.-L. Luo, C. Zhi, *Nano Energy* **2021**, *86*, 106099.
[22] D. Gupta, A. Kafle, S. Kaur, P. P. Mohanty, T. Das, S. Chakraborty, R. Ahuja, T. C. Nagaiah, *J. Mater. Chem. A* **2022**, *10*, 20616.

[23] S. Fan, F. Zhao, X. Wang, Q. Wang, Q. Zhao, J. Li, G. Liu, *Dalton Trans.* **2022**, *51*, 11163.
[24] M. Han, M. Guo, Y. Yun, Y. Xu, H. Sheng, Y. Chen, Y. Du, K. Ni, Y. Zhu, M. Zhu, *Adv. Funct. Mater.* **2022**, *32*, 2202820.
[25] K. Chu, Y. Liu, Y. Cheng, Q. Li, *J. Mater. Chem. A* **2020**, *8*, 5200.
[26] W. Fang, J. Zhao, T. Wu, Y. Huang, L. Yang, C. Liu, Q. Zhang, K. Huang, Q. Yan, *J. Mater. Chem. A* **2020**, *8*, 5913.
[27] Y.-X. Luo, W.-B. Qiu, R.-P. Liang, X.-H. Xia, J.-D. Qiu, *ACS Appl. Mater. Interfaces* **2020**, *12*, 17452.
[28] K. Chu, Q. Li, Y. Cheng, Y. Liu, *ACS Appl. Mater. Interfaces* **2020**, *12*, 11789.
[29] H.-B. Wang, J.-Q. Wang, R. Zhang, C.-Q. Cheng, K.-W. Qiu, Y. Yang, J. Mao, H. Liu, M. Du, C.-K. Dong, X.-W. Du, *ACS Catal.* **2020**, *10*, 4914.
[30] K. Chu, Y. Liu, Y. Li, Y. Guo, Y. Tian, H. Zhang, *Appl. Catal. B* **2020**, *264*, 118525.
[31] S. Zhang, M. Jin, T. Shi, M. Han, Q. Sun, Y. Lin, Z. Ding, L. R. Zheng, G. Wang, Y. Zhang, H. Zhang, H. Zhao, *Angew. Chem. Int. Ed.* **2020**, *59*, 13423.
[32] M. Yuan, H. Zhang, D. Gao, H. He, Y. Sun, P. Lu, S. Dipazir, Q. Li, L. Zhou, S. Li, Z. Liu, J. Yang, Y. Xie, H. Zhao, G. Zhang, *J. Mater. Chem. A* **2020**, *8*, 2691.
[33] M. Wang, S. Liu, H. Ji, T. Yang, T. Qian, C. Yan, *Nat. Commun.* **2021**, *12*, 3198.
[34] X.-W. Lv, X.-L. Liu, Y.-J. Suo, Y.-P. Liu, Z.-Y. Yuan, *ACS Nano* **2021**, *15*, 12109.
[35] P. Shen, X. Li, Y. Luo, Y. Guo, X. Zhao, K. Chu, *ACS Nano* **2022**, *16*, 7915.
[36] Y. Tian, B. Chang, G. Wang, L. Li, L. Gong, B. Wang, R. Yuan, W. Zhou, *J. Mater. Chem. A* **2022**, *10*, 2800.
[37] Y. Fang, Y. Xue, L. Hui, H. Yu, C. Zhang, B. Huang, Y. Li, *Adv. Sci.* **2022**, *9*, 2102721.
[38] S. Zhang, M. Han, T. Shi, H. Zhang, Y. Lin, X. Zheng, L. R. Zheng, H. Zhou, C. Chen, Y. Zhang, G. Wang, H. Yin, H. Zhao, *Nature Sustainability* **2023**, *6*, 169.
[39] Y. Abghoui, E. Eskulason, *J. Phys. Chem. C* **2017**, *121*, 24036.
[40] Y. Abghoui, *Topics in Catalysis* **2022**, *65*, 262.
[41] Y. Abghoui, A. L. Garden, J. G. Howalt, T. Vegge, E. Skúlason, *ACS Catal.* **2016**, *6*, 635.
[42] H. Wang, J. Li, K. Li, Y. Lin, J. Chen, L. Gao, V. Nicolosi, X. Xiao, J.-M. Lee, *Chem. Soc. Rev.* **2021**, *50*, 1354.
[43] X. Yang, J. Nash, J. Anibal, M. Dunwell, S. Kattel, E. Stavitski, K. Attenkofer, J. G. Chen, Y. Yan, B. Xu, *J. Am. Chem. Soc.* **2018**, *140*, 13387.
[44] R. Manjunatha, A. Karajić, H. Teller, K. Nicoara, A. Schechter, *ChemCatChem* **2020**, *12*, 438.
[45] M. Gudmundsson, V. Ellingsson, E. Skúlason, Y. Abghoui, *Top. Catal.* **2022**, *65*, 252.
[46] F. Hanifpour, C. P. Canales, E. G. Fridriksson, A. Sveinbjörnsson, T. K. Tryggvason, J. Yang, C. Arthur, S. Jónsdóttir, A. L. Garden, S. Ólafsson, K. Leósson, L. Árnadóttir, E. Lewin, Y. Abghoui, Á. S. Ingason, F. Magnus, H. D. Flosadóttir, E. Skúlason, *J. Catal.* **2022**, *413*, 956.
[47] Y. Abghoui, A. L. Garden, V. F. Hlynsson, S. Björgvinsdóttir, H. Ólafsdóttir, E. Skúlason, *Phys. Chem. Chem. Phys.* **2015**, *17*, 4909.
[48] Y. Abghoui, E. Skúlason, *Catal. Today* **2017**, *286*, 69.
[49] Y. Abghoui, E. Skúlason, *Catal. Today* **2017**, *286*, 78.
[50] Y. Abghoui, E. Skúlason, *J. Phys. Chem. C* **2017**, *121*, 6141.
[51] Y. Abghoui, A. Iqbal, E. Skúlason, *Frontiers in Catalysis* **2023**, *2*.
[52] Á. B. Höskuldsson, Y. Abghoui, A. B. Gunnarsdóttir, E. Skúlason, *ACS Sustainable Chem. Eng.* **2017**, *5*, 10327.
[53] Y. Abghoui, S. B. Sigtryggsson, E. Skúlason, *ChemSusChem* **2019**, *12*, 4265.
[54] F. Hanifpour, C. P. Canales, E. G. Fridriksson, A. Sveinbjörnsson, T. K. Tryggvason, E. Lewin, F. Magnus, Á. S. Ingason, E. Skúlason, H. D. Flosadóttir, *Electrochim. Acta* **2022**, *403*, 139551.
[55] H.-L. Du, M. Chatti, R. Y. Hodgetts, P. V. Cherepanov, C. K. Nguyen, K. Matuszek, D. R. MacFarlane, A. N. Simonov, *Nature* **2022**, *609*, 722.
[56] S. Giddey, S. P. S. Badwal, A. Kulkarni, *Int. J. Hydrogen Energy* **2013**, *38*, 14576.
[57] R. Michalsky, Y.-J. Zhang, A. J. Medford, A. A. Peterson, *J. Phys. Chem. C* **2014**, *118*, 13026.
[58] R. Zhao, H. Xie, L. Chang, X. Zhang, X. Zhu, X. Tong, T. Wang, Y. Luo, P. Wei, Z. Wang, X. Sun, *EnergyChem* **2019**, *1*, 100011.
[59] G. Yu, H. Guo, W. Kong, T. Wang, Y. Luo, X. Shi, A. M. Asiri, T. Li, X. Sun, *J. Mater. Chem. A* **2019**, *7*, 19657.
[60] A. Szymańska, M. Lewandowski, C. Sayag, G. Djéga-Mariadassou, *J. Catal.* **2003**, *218*, 24.
[61] X. Ren, J. Zhao, Q. Wei, Y. Ma, H. Guo, Q. Liu, Y. Wang, G. Cui, A. M. Asiri, B. Li, B. Tang, X. Sun, *ACS Cent. Sci.* **2019**, *5*, 116.
[62] J. Häglund, A. Fernández Guillermet, G. Grimvall, M. Körling, *Phys. Rev. B* **1993**, *48*, 11685.
[63] T. L. E., *Transition Metal Carbides and Nitrides*, Academic Press, New York **1971**.
[64] A Neckel, P Rastl, R Eibler, P Weinberger, K Schwarz, *J. Phys. C* **1975**, *9*, 579.
[65] A. Kelly, D. J. Rowcliffe, *Physica Status Solidi* **1966**, *14*, K29.
[66] X. Fan, B. Chen, M. Zhang, D. Li, Z. Liu, C. Xiao, *Mater. Des.* **2016**, *112*, 282.
[67] D. W. Lee, S. V. Alexandrovskii, B. K. Kim, *Mater. Lett.* **2004**, *58*, 1471.
[68] S. C. Tjong, Z. Y. Ma, *Mater. Sci. Eng. R* **2000**, *29*, 49.
[69] F. Silveri, M. G. Quesne, A. Roldan, N. H. de Leeuw, C. R. A. Catlow, *Phys. Chem. Chem. Phys.* **2019**, *21*, 5335.
[70] A. L. Stottlemyer, T. G. Kelly, Q. Meng, J. G. Chen, *Surf. Sci. Rep.* **2012**, *67*, 201.
[71] W. Yang, S. Rehman, X. Chu, Y. Hou, S. Gao, *ChemNanoMat* **2015**, *1*, 376.
[72] S. R. Shatynski, *Oxid. Met.* **1979**, *13*, 105.
[73] D. J. Ham, J. S. Lee, *Energies* **2009**, *2*, 873.
[74] H. H. Hwu, J. G. Chen, *Chem. Rev.* **2005**, *105*, 185.
[75] T. G. Kelly, J. G. Chen, *Chem. Soc. Rev.* **2012**, *41*, 8021.
[76] D. V. Esposito, J. G. Chen, *Energy Environ. Sci.* **2011**, *4*, 3900.
[77] D. V. Esposito, S. T. Hunt, A. L. Stottlemyer, K. D. Dobson, B. E. McCandless, R. W. Birkmire, J. G. Chen, *Angew. Chem. Int. Ed.* **2010**, *49*, 9859.
[78] W.-F. Chen, J. T. Muckerman, E. Fujita, *Chem. Commun.* **2013**, *49*, 8896.
[79] S. Wirth, F. Harnisch, M. Weinmann, U. Schröder, *Appl. Catal. B* **2012**, *126*, 225.
[80] D. D. Vasić, I. A. Pašti, S. V. Mentus, *Int. J. Hydrogen Energy* **2013**, *38*, 5009.
[81] Y. Hara, N. Minami, H. Matsumoto, H. Itagaki, *Appl. Catal. A* **2007**, *332*, 289.
[82] E. C. Weigert, A. L. Stottlemyer, M. B. Zellner, J. G. Chen, *J. Phys. Chem. C* **2007**, *111*, 14617.
[83] I. J. Hsu, D. A. Hansgen, B. E. McCandless, B. G. Willis, J. G. Chen, *J. Phys. Chem. C* **2011**, *115*, 3709.
[84] I. J. Hsu, Y. C. Kimmel, Y. Dai, S. Chen, J. G. Chen, *J. Power Sources* **2012**, *199*, 46.
[85] Y. C. Kimmel, L. Yang, T. G. Kelly, S. A. Rykov, J. G. Chen, *J. Catal.* **2014**, *312*, 216.
[86] Z. Hu, C. Chen, H. Meng, R. Wang, P. K. Shen, H. Fu, *Electrochem. Commun.* **2011**, *13*, 763.
[87] J. Polonský, I. M. Petrushina, E. Christensen, K. Bouzek, C. B. Prag, J. E. T. Andersen, N. J. Bjerrum, *Int. J. Hydrogen Energy* **2012**, *37*, 2173.
[88] M. Horigome, K. Kobayashi, T. M. Suzuki, *Int. J. Hydrogen Energy* **2007**, *32*, 365.
[89] J. K. Nørskov, J. Rossmeisl, A. Logadottir, L. Lindqvist, J. R. Kitchin, T. Bligaard, H. Jónsson, *J. Phys. Chem. B* **2004**, *108*, 17886.
[90] B. Hammer, L. B. Hansen, J. K. Nørskov, *Phys. Rev. B* **1999**, *59*, 7413.
[91] G. Kresse, J. Furthmüller, *Phys. Rev. B* **1996**, *54*, 11169.
[92] P. E. Blöchl, *Phys. Rev. B* **1994**, *50*, 17953.
[93] G. Henkelman, B. P. Uberuaga, H. Jónsson, *J. Chem. Phys.* **2000**, *113*, 9901.
[94] A. Jain, S. P. Ong, G. Hautier, W. Chen, W. D. Richards, S. Dacek, S. Cholia, D. Gunter, D. Skinner, G. Ceder, K. A. Persson, *APL Mater.* **2013**, *1*, 011002.
[95] J. H. Montoya, C. Tsai, A. Vojvodic, J. K. Nørskov, *ChemSusChem* **2015**, *8*, 2180.
[96] C. Zhang, D. Wang, Y. Wan, R. Lv, S. Li, B. Li, X. Zou, S. Yang, *Mater. Today* **2020**, *40*, 18.
[97] K. Yang, J. Zheng, Y. Zhao, D. G. Truhlar, *J. Chem. Phys.* **2010**, *132*, 164117.
[98] J. Feng, X. Zhu, Q. Chen, W. Xiong, X. Chen, Y. Luo, A. A. Alshehri, K. A. Alzahrani, Z. Jiang, W. Li, *J. Mater. Chem. A* **2019**, *7*, 26227.

Manuscript received: June 30, 2023
Revised manuscript received: September 12, 2023
Accepted manuscript online: September 13, 2023
Version of record online: October 9, 2023

ChemSusChem

Supporting Information

Nitrogen Reduction Reaction to Ammonia on Transition Metal Carbide Catalysts

Viktor Ellingsson, Atef Iqbal, Egill Skúlason, and Younes Abghoui*

The Nitrogen Reduction Reaction, A study of Transition Metal Carbides

-Electronic supplementary information

Authors: Viktor Ellingsson, Atef Iqbal, Egill Skúlason, Younes Abghoui

Zero-point energy and entropy corrections

Zero-point energy (ZPE) and entropy (TΔS) corrections were found for all the adsorbed species *via* vibrational normal modes calculated from DFT. The values for the correction terms were assumed to be structure dependent rather than dependent on the atomic species, the calculated correction values were determined for the rock salt (RS) (100) VC surface and applied to each surface investigated. For the gas phase species, the values were taken from ref [1].

Table S1: The ZPE and TΔS values for all of the used adsorbed and gas phase species. The values for the adsorbed species were calculated on the (100) VC surface, and gas phase values were taken from ref [1]. For the adsorbed species, denoted by *, adsorption onto the surface is differentiated from adsorption into a vacancy by the ^{vac} notation.

(100) TMC surfaces [eV]	ZPE	TΔS
NH_3 (g)	0.89	0.74
H_2 (g)	0.27	0.41
CH_4 (g)	0.825	0.58
*N	0.1	0.035
*NH	0.4	0.042
*NH_2	0.73	0.064
*NH_3	1.02	0.146
*N_2	0.2	0.173
*NNH	0.46	0.168
*H	0.24	0.014
*N^{vac}	0.08	0.036
*NH^{vac}	0.36	0.056
*N_2^{vac}	0.18	0.089
*NNH^{vac}	0.49	0.088
*H^{vac}	0.13	0.011
*CH_2	0.46	0.121
*CH_3	0.83	0.074
*OH^-	0.33	0.112
*O^{2-}	0.08	0.048
*$OH^{- vac}$	0.34	0.0981
*$O^{2- vac}$	0.06	0.0566

Free energy diagrams

Free energy diagrams (FEDs) for ZrC both at zero applied potential and the required OP (-0.69 V) without the presence of a vacancy (S1) and also a comparison between the activity with and without a vacancy (S2). FEDs for VC, CrC, and NbC in the presence of a vacancy can be found in fig S3, fig S4, and fig S5 respectively.

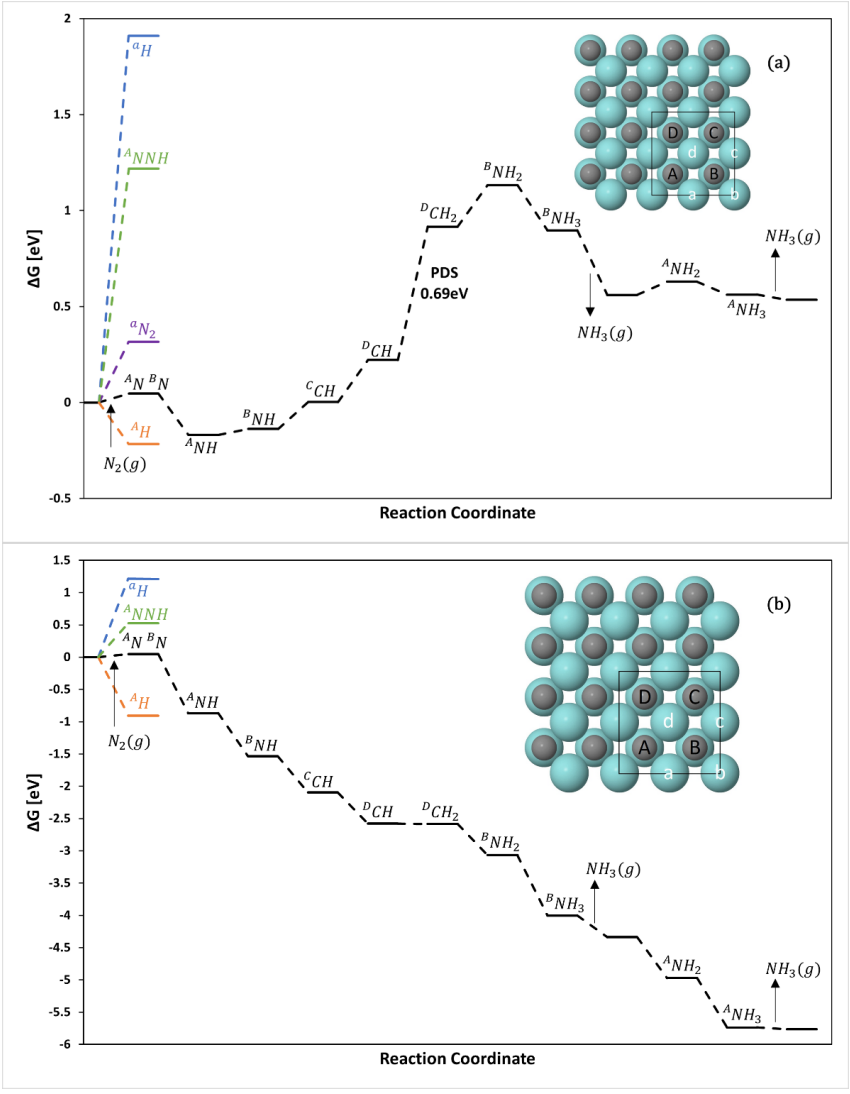

Fig S1: Non-restrictive FED for ZrC resulting in ammonia formation via a dissociative mechanism at zero potential (a) and at the OP: -0.69 V (b). The labeling ^{A}X refers to the positioning of the adsorbed species

in the unit cell, in this case, site A as defined in the inset figure in the top right. The inset figure found in the top right defines all relevant adsorption sites as well as the unit cell (black square). The PDS, for the plot at zero potential, and the free energy change associated with it can be found under the relevant adsorbed species. In addition to the reaction pathway, additional adsorbates are shown for the initial step (green, blue, purple, orange).

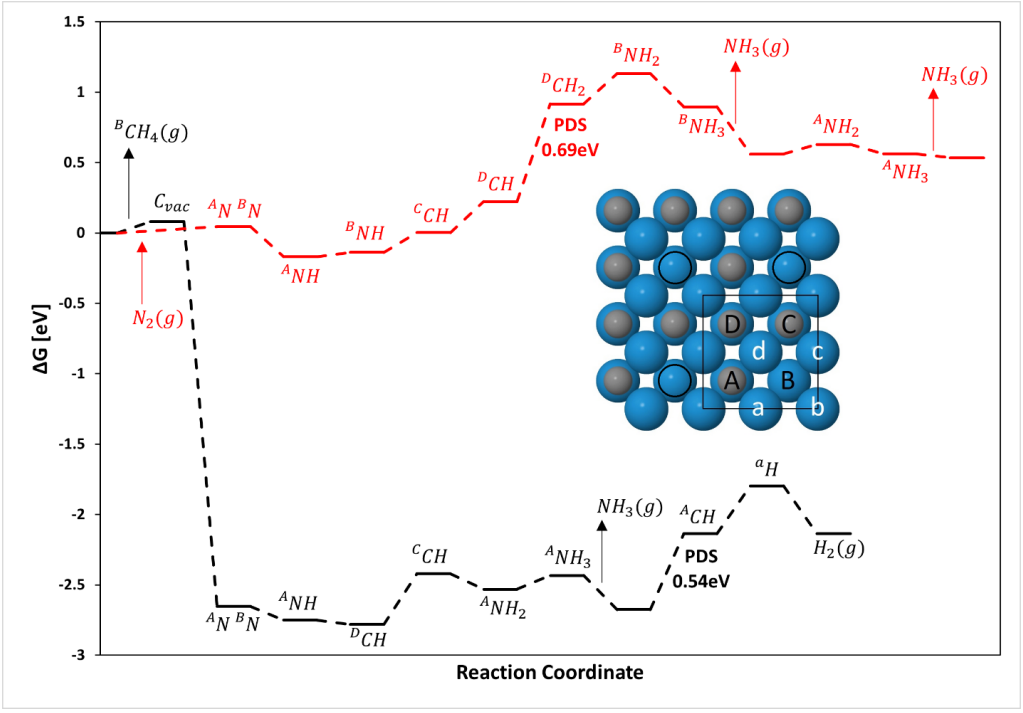

Fig S2: Comparison of the FEDs for ZrC with a vacancy (black) and without a vacancy (red) at zero potential. The labeling ^{A}X refers to the positioning of the adsorbed species in the unit cell, in this case, site A as defined in the inset figure in the middle. The inset figure found in the middle defines all relevant adsorption sites as well as the unit cell (black square), black circles indicate the periodic vacancy formation. The PDS and the free energy change associated with it can be found under the relevant adsorbed species.

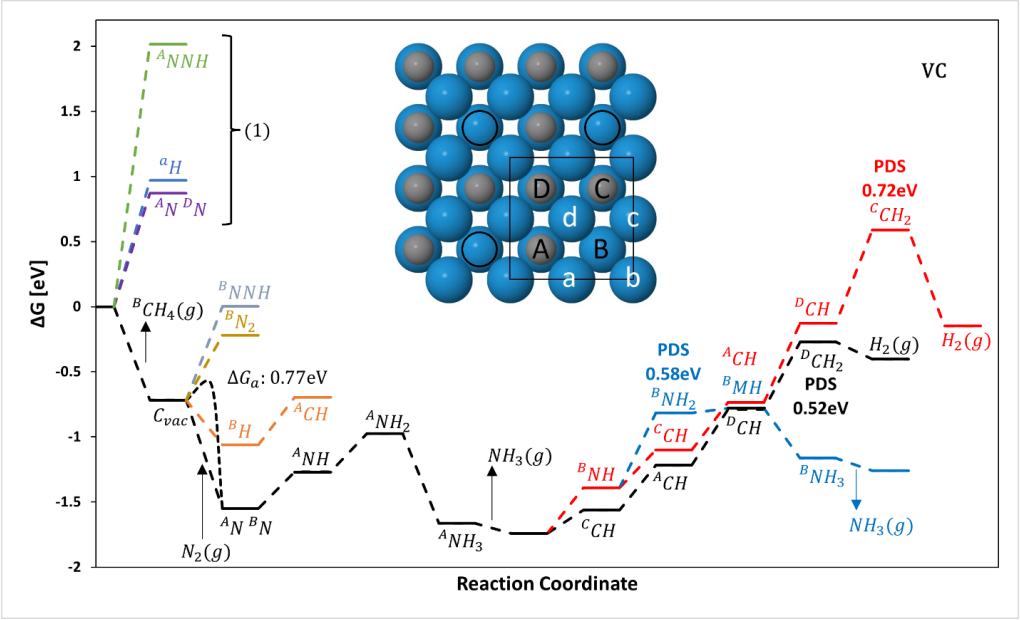

Fig S3. Non-restricted FED for VC at zero potential. The black path describes the unconstrained mechanism, each reaction step proceeds via the most favorable intermediate, starting with the formation of a carbon vacancy on the surface. The steps labeled (1) are adsorption energies onto the clean surface, also included is the adsorption of NNH (light gray) and H (orange) into the vacancy. The orange path also describes the most favorable reaction step following the protonation of the vacancy (poisoning). The value of the required OP (defined by the PDS) is denoted next to the corresponding reaction step on each pathway. The two branching paths Blue and Red describe pathways resulting from the formation of an alternative intermediate with slightly higher energy as compared to the black path. The activation free energy for the dissociation of adsorbed N_2 is labeled ΔG_a (ΔG_a = 0.1) for the appropriate reaction step, see Table S2. The labeling ^{A}X refers to the positioning of the adsorbed species in the unit cell, in this case, site A as defined in the inset figure in the top middle. The inset figure found in the top middle defines all relevant adsorption sites as well as the unit cell (black square).

As can be seen in Fig S3, the VC surface only produces two equivalents of ammonia along one of the three possible pathways at the OP of -0.58 V, while the other two paths produce hydrogen. At this required OP (-0.58 V) the red path would remain endergonic and the blue path, which makes ammonia, would be energetically favored over the black path, which makes hydrogen. In addition to the black and red paths that lead to hydrogen formation, the poising of the vacancy site leads to further carbon protonation and the possible formation of another vacancy *via the* formation of methane. Thus, if the formation of hydrogen and protonation of the vacancy site could somehow be discouraged, with the use of a non-aqueous electrolyte for example, the VC surface might prove to be a good catalyst capable of producing ammonia at a low overpotential with good kinetic properties (see Fig 4, S7, S8, S10, and Table S2).

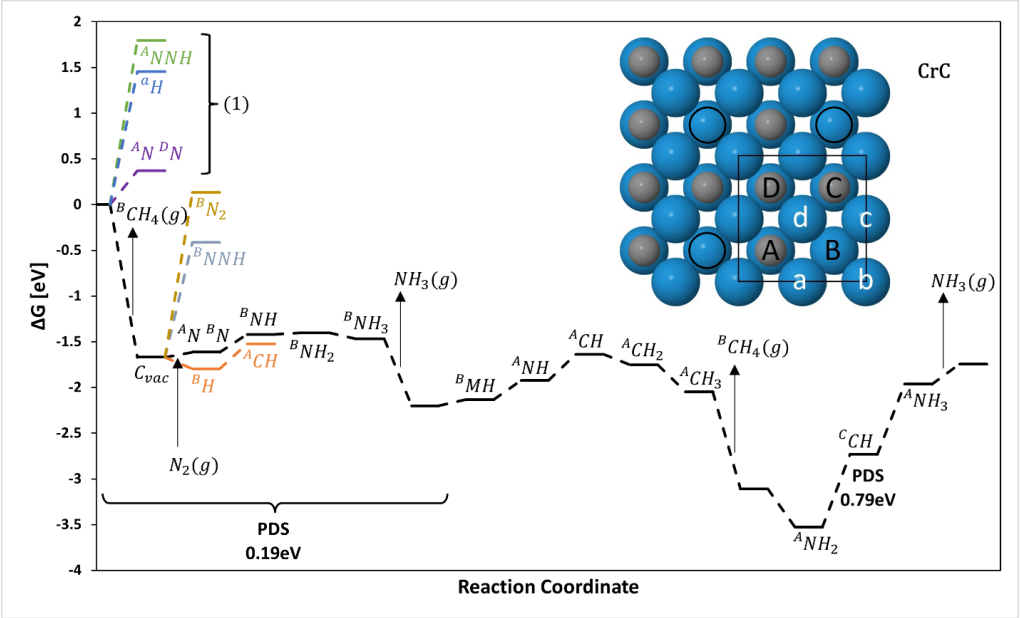

Fig S4. Non-restricted FED for CrC at zero potential. The black path describes the unconstrained mechanism, each reaction step proceeds via the most favorable intermediate, starting with the formation of a carbon vacancy on the surface. The steps labeled (1) are adsorption energies onto the clean surface, also included is the adsorption of NNH (light gray) and H (orange) into the vacancy. The orange path also describes the most favorable reaction step following the protonation of the vacancy (poisoning). The value of the required OP (defined by the PDS) is denoted next to the corresponding reaction step on the path, as well as the PDS for the formation of the first equivalent of ammonia along the reaction path denoted by brackets. The labeling ^{A}X refers to the positioning of the adsorbed species in the unit cell, in this case, site A as defined in the inset figure in the top middle. The inset figure found in the top right defines all relevant adsorption sites as well as the unit cell (black square).

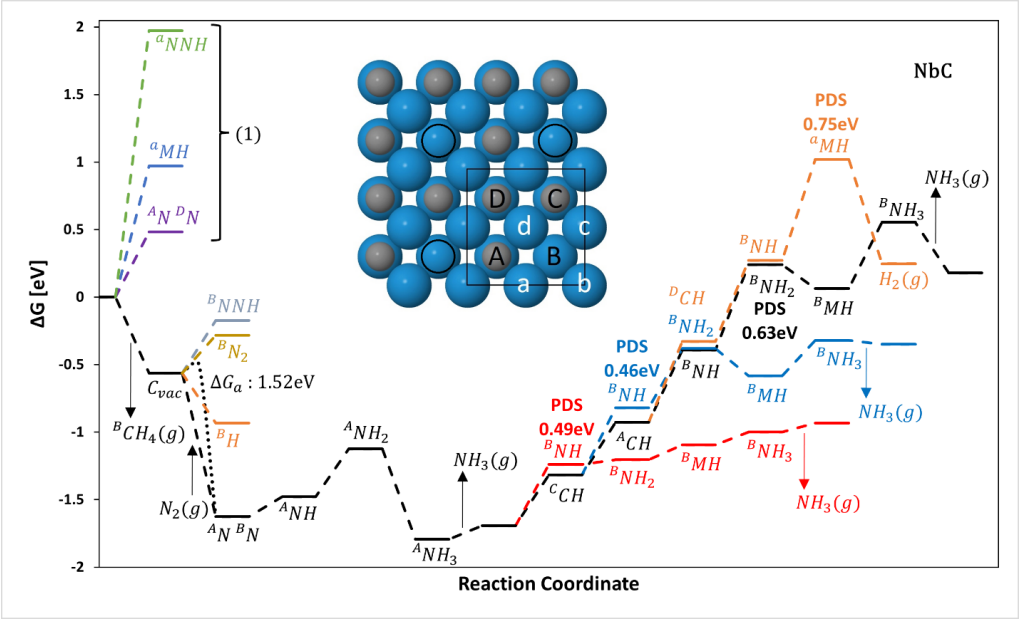

Fig S5. Non-restricted FED for NbC at zero potential. The black path describes the unconstrained mechanism, each reaction step proceeds via the most favorable intermediate, starting with the formation of a carbon vacancy on the surface. The steps labeled (1) are adsorption energies onto the clean surface, also included is the adsorption of NNH (light gray) and H (orange) into the vacancy. The value of the required OP (defined by the PDS) is denoted next to the corresponding reaction step for each pathway. The three branching paths Blue, Red, and Orange describe pathways resulting from the formation of an alternative intermediate with slightly higher energy as compared to the black path. The three branching paths Blue and Red describe pathways resulting from the formation of an alternative intermediate with slightly higher energy as compared to the black path. The activation free energy for the dissociation of adsorbed N_2 is labeled ΔG_a ($\Delta G_a = \Delta E_a + 0.2$) for the appropriate reaction step, see Table S2. The labeling ^{A}X refers to the positioning of the adsorbed species in the unit cell, in this case, site A as defined in the inset figure in the top middle. The inset figure found in the top middle defines all relevant adsorption sites as well as the unit cell (black square).

As can be seen in Fig S5, NbC is a very promising candidate for the NRR if the initial activation barrier for the adsorption of nitrogen can be circumvented. The surface can produce ammonia at a low OP (0.49 V) and does not make any side products at said OP.

Nudge Elastic Band

Nudge elastic band (NEB) results for the rotation of a NH molecule in the vacany of VC, see Fig S6. The activation energy (E_a) for dissociative binding of N_2 onto NbC, VC, and WC in the presence of a carbon vacancy and ZrC without a vacancy, see Fig S7. The Ea values for NbC, VC, and WC in Fig S7, along with the ZPE and $T\Delta S$ corrections associated with the bottom and top of each potential barrier, were used to find the associated activation free energies (ΔG_a), see Table S2. The Ea for the migration of a sub-layer carbon into the vacancy of NbC, VC, WC and CrC was also investigated, see Fig S8.

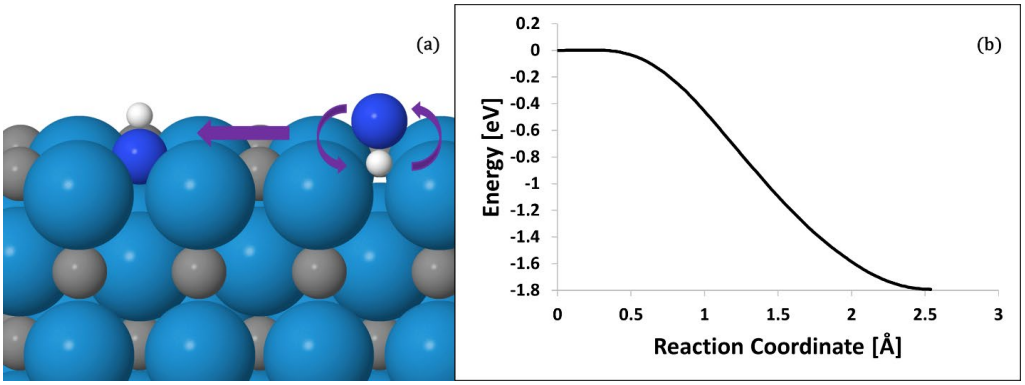

Fig S6: (a) Visualization of nitrogen displacing a proton in the vacancy of VC. (b) NEB energy profile associated with NH rotation in vacancy

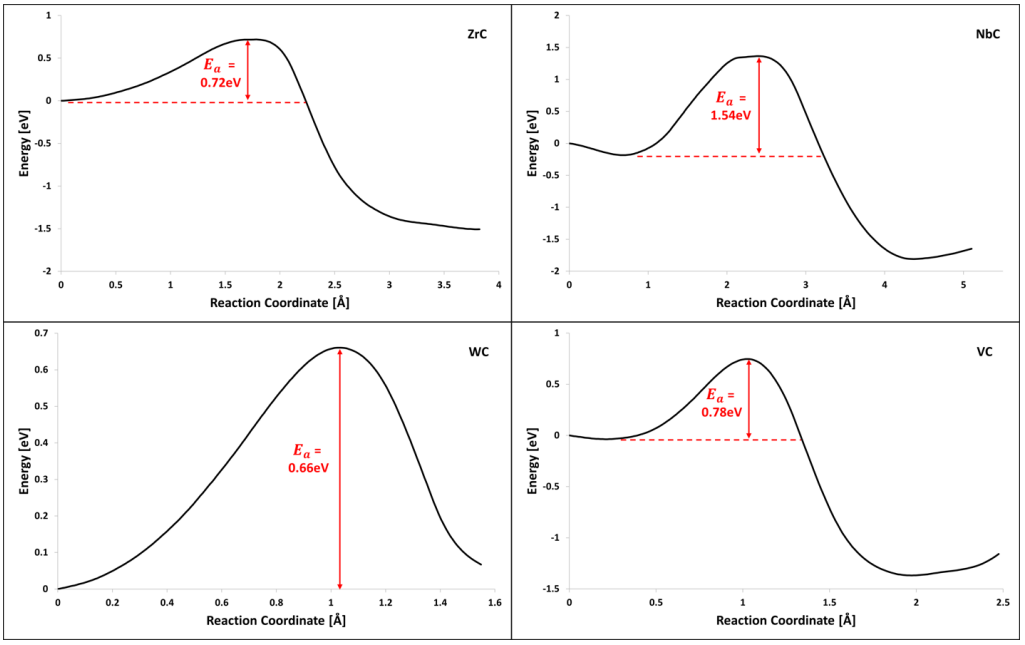

Fig S7: The NEB path for dissociative N_2 adsorption onto ZrC (without a vacancy), WC, NbC, and VC in the presence of a vacancy. The transition state resulting in the highest activation barrier is marked with red arrows and its numerical value (from the dotted line) is given in red.

Table S2: The ΔG_a values for the dissociative N_2 adsorption onto WC, NbC, and VC in the presence of a vacancy calculated based on the E_a values and the difference between the ZPE and $T\Delta S$ calculated at the bottom and top of each respective barrier (Δcorrection*).*

Surface	E_a [eV]	Δcorrection [eV]	ΔG_a [eV]
WC	0.66	0.0	0.66
NbC	1.54	0.2	1.52
VC	0.78	0.1	0.77

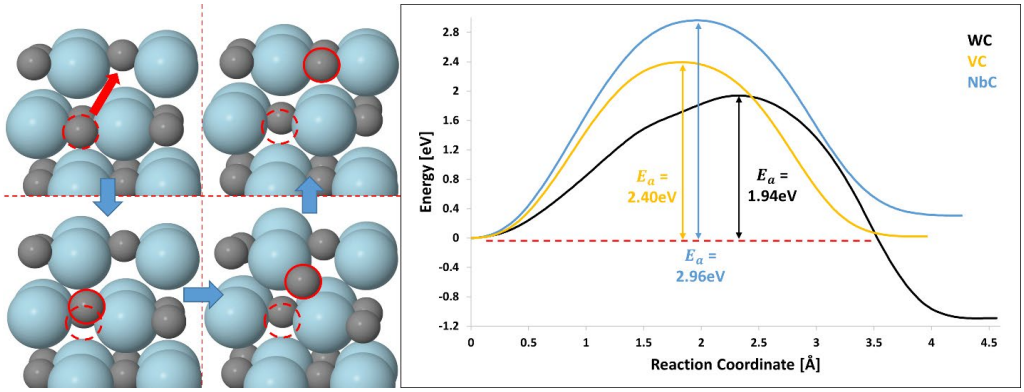

Fig S8: Visualization of a sub-layer carbon atom migrating to a vacancy in the surface along with the NEB paths calculated for WC, VC and NbC. The numerical value of the kinetical barrier is given for each material in its respective color.

Scaling relations

The scaling relations for each of the nesseccary reaction steps for the NRR were calculated on the TMC surfaces in the presence of a vacancy and plotted as a function of the dissociative adsorption energy of N_2, see Fig S9.

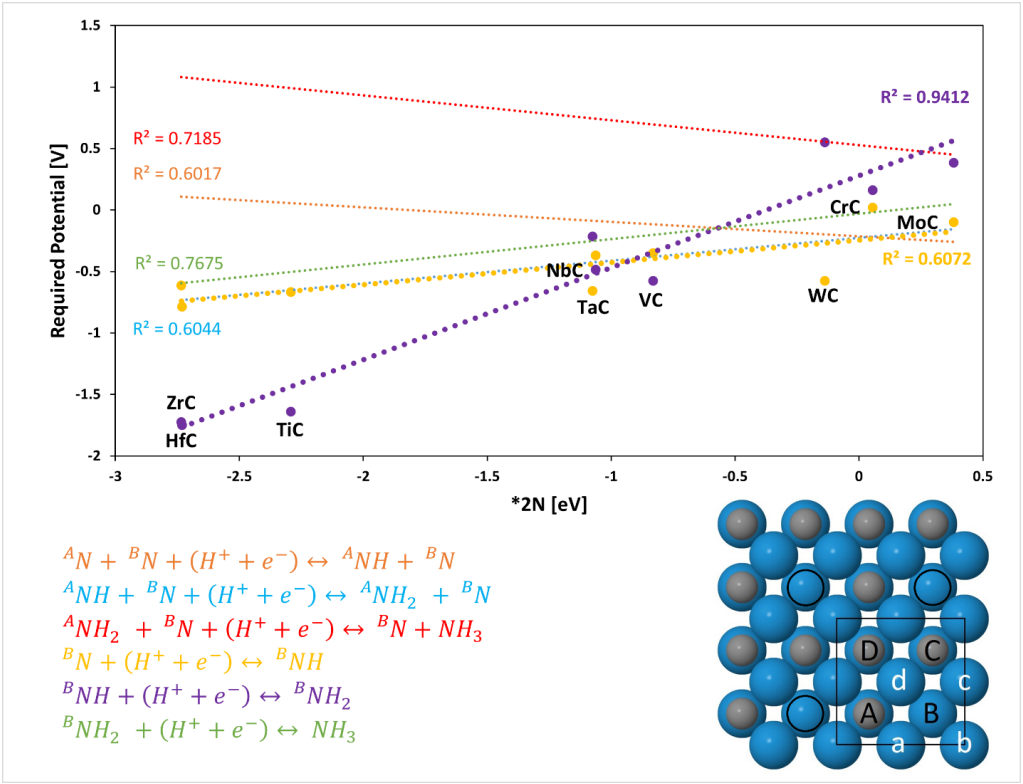

Fig S9: The required potential to drive the reactions corresponding to the most favorable reaction pathway for the restricted formation of ammonia on the TMC surfaces in the presence of a vacancy as a function of the dissociative adsorption energy of nitrogen. All the reactions plotted are labeled by color in the lower left corner of the plot. For each reaction, the linear best fit has been drawn as a dotted line with the corresponding R-value displayed. For each TMC the limiting reaction has been labeled with the appropriate molecular symbol.

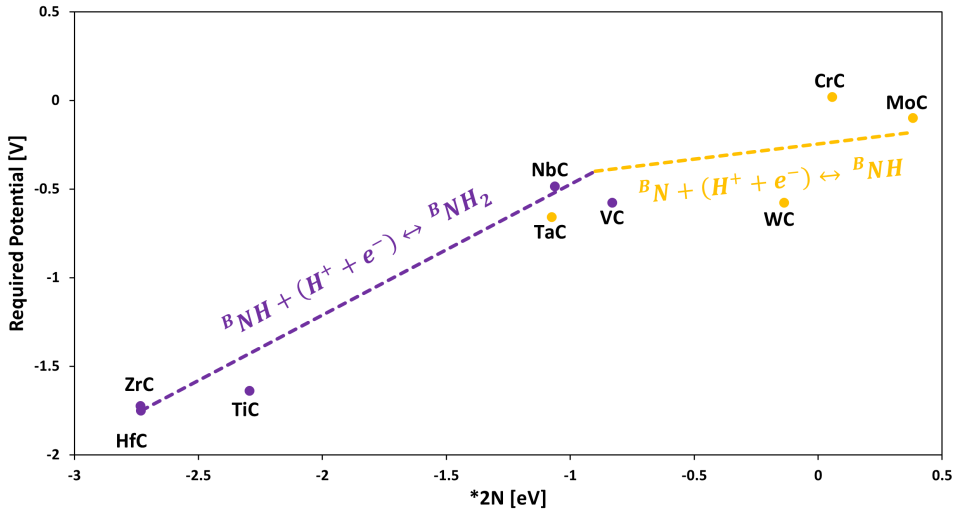

Fig S10. The required potential to drive the reactions as a function of the dissociative binding energy of nitrogen on the TMC surfaces in the presence of a vacancy. This is derived from the scaling relation plots shown in Fig S9. For each reaction, the linear best fit has been drawn as a dotted line with the corresponding R-value displayed. The individual data points are only displayed for the two limiting reactions (purple and yellow), and the reaction with the highest required potential is labeled with the corresponding TMC.

As can be seen in Fig S10, we do not observe a volcano plot when considering scaling relations on these TMC surfaces. There is however a clear limitation on the performance of these surfaces, the first and second protonation of the nitrogen sitting in the vacancy limits the activity on the left side. The positive slope of the trend means that a lower overpotential is required as we move from left to right, and a lower overpotential can be a good indicator of better activity. However, as we move further right the dissociative adsorption energy of nitrogen becomes more endergonic, until the surface can no longer adsorb nitrogen, rendering the surface inactive. This defines WC, VC, NbC, and TaC to have the most promising energetics with regard to the scaling relations, even though CrC and MoC have a very low required OP, they do not favorably adsorb nitrogen. This does however validate our decision to still investigate CrC as a potential catalytic surface, according to the volcano plot if CrC could favorably adsorb nitrogen it would be a very promising candidate due to the absence of a required potential to drive NRR reactivity. Of the surfaces predicted to have good activity by the scaling relations, only TaC does not produce two equivalents of ammonia, testing this surface further could be of interest to determine the source of the anomaly.

Density of States and Band structures

The band structures for the promising TMC surfaces are demonstrated in Fig S11, where it can be observed that all the materials appear to cross the Fermi level and possess metallic properties. The electronic density of states aids in the comprehension of the bonding features of the investigated carbides. The partial density of states (PDOS) for the TMCs in the RS phase are computed at the GGA-RP

level using the PBE functional, and the results are shown in Fig S12. The Brillouin zone was sampled using a 8 × 8 × 1 and 12 × 12 × 1 k-grid meshes, respectively, for structural relaxations and electronic calculations.

The DOS curves for the TMCs shown in Fig S12 may be partitioned into two peaks: the valence band and the conduction band. The PDOS curves of TMC show that the carbon p orbital and the transition metal d orbital overlap across the energy range of -5 to 5 eV, and in some cases beyond -5 eV, which indicates covalent connections between them due to their high hybridization. Comparing the total and partial DOS of TMC, it can be concluded that the peak in the valence band is primarily dominated by the carbon p-state with contribution from the TM-d state, which is primarily determined by the hybridization of TM-d and C-2p states, with a small contribution of the TM-p state; whereas the peak in the conduction band is primarily derived from the contribution of the TM-d state, but also contains a small contribution from carbon p-state. With the vacancy and N_2 doping in the vacancy, the arrangement of the bands does not vary much due to the very low concentration, but the nitrogen p-state contributed between -3 and -5 eV in each case, as seen in the image. In the rock-salt phase, it is evident that charges collect significantly between the transition metal atoms Zr, Nb, V, W, Cr, and C, indicating that strong directional bonds exist between them. Despite the presence of an ionic component with considerable charge transfer between metal and carbon atoms, the materials are metallic. Consequently, the bonding consists of covalent, metallic, and ionic components. Due to the hybridization of carbon and metal atoms, these materials exhibit covalent-like bonding.

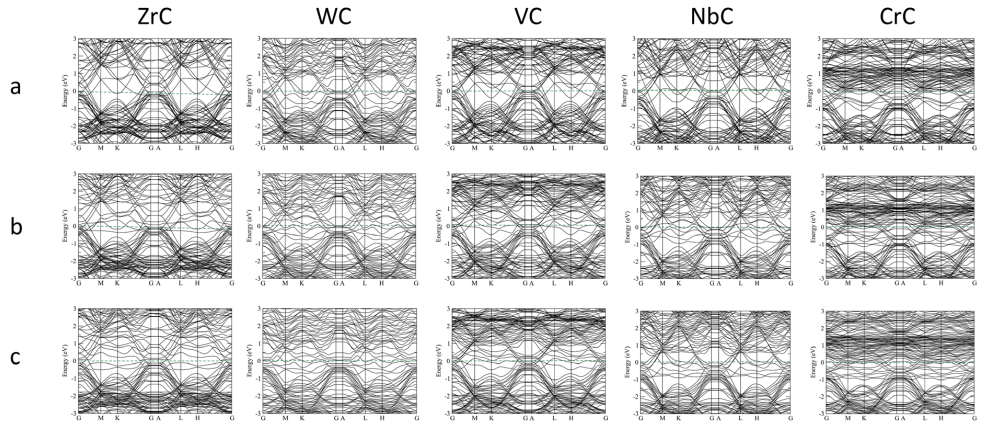

Fig S11: Band structure for the promising TMC surface candidates for a) the clean surface, b) in the presence of a vacancy, c) with 2N dissociatively adsorbed on the vacancy surface

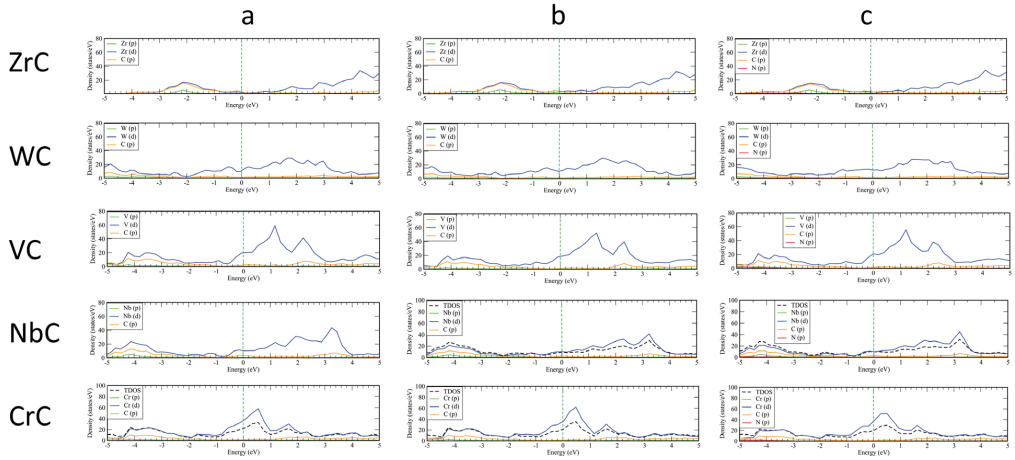

Fig S12: Partial density of states (PDOS) for the promising TMC candidates for a) the clean surface, b) in the presence of a vacancy, c) with 2N dissociatively adsorbed on the vacancy surface

Paper II

Are (100) facets of transition metal carbonitrides suitable as electrocatalysts for nitrogen reduction to ammonia at ambient conditions?

Iqbal, A., E. Skulason, and Y. Abghoui,

International journal of hydrogen energy, DOI: 10.1016/j.ijhydene.2024.03.282.

Graphical Abstract: Using DFT, we uncover the nitrogen reduction mechanism on transition metal carbonitrides, showcasing their remarkable efficiency as electrocatalysts for ammonia formation under ambient conditions.

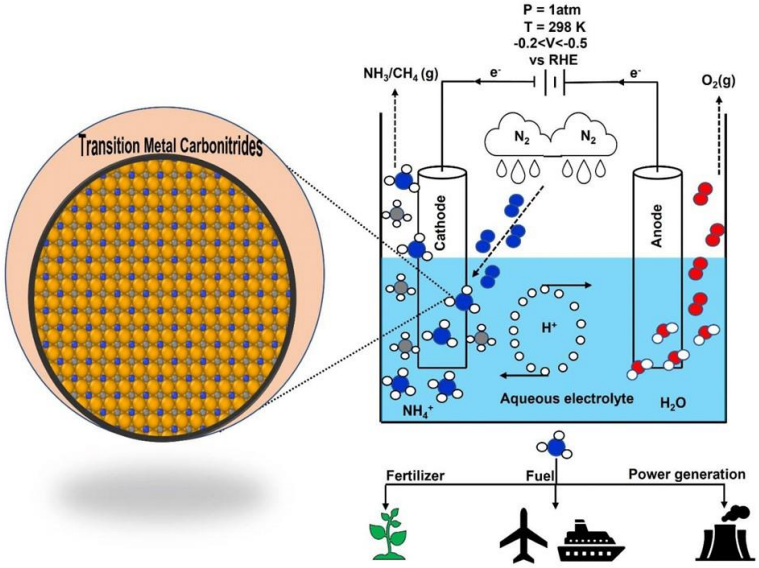

International Journal of Hydrogen Energy 64 (2024) 744–753

Contents lists available at ScienceDirect

International Journal of Hydrogen Energy

journal homepage: www.elsevier.com/locate/he

Are (100) facets of transition metal carbonitrides suitable as electrocatalysts for nitrogen reduction to ammonia at ambient conditions?

Atef Iqbal [a,*], Egill Skúlason [b], Younes Abghoui [a]

[a] Science Institute of the University of Iceland, Iceland
[b] Faculty of Industrial Engineering, Mechanical Engineering and Computer Science, University of Iceland, Iceland

ARTICLE INFO

Handling Editor: Prof. A.B. Basile

Keywords:
Density functional theory calculations
Electrochemical ammonia synthesis
Transition metal carbonitrides
Heterogenous catalysis
Mars-van krevelen mechanism

ABSTRACT

Sustainable and energy-efficient ammonia production requires facile nitrogen reduction for hydrogen preservation and inorganic fertilizers. A nitrogen reduction apparatus with optimal stability, selectivity, and activity for ambient temperatures and pressure is needed to catalyze ammonia synthesis. This paper describes the investigation of using transition metal carbonitrides as catalyst to reduce molecular nitrogen electrochemically to NH_3 at room temperature and atmospheric pressure. Density functional theory calculations determine the competition among associative, dissociative, and Mars-van Krevelen mechanisms where in most cases the Mars-van Krevelen is a more favorable reaction pathway. VCN and NbCN are the best candidates for ammonia production via the Mars-van Krevelen mechanism at low onset potentials of −0.52 V and −0.53 V vs reversible hydrogen electrode on the (100) facets. These carbonitrides are predicted to favor nitrogen reduction reaction rather than hydrogen evolution reaction.

1. Introduction

After over a hundred years of dedicated research and advancement, heterogeneous catalysis has accumulated extensive empirical and theoretical information. This information essentially establishes a connection between the electronic structure of a catalyst and the speed of fundamental steps within a catalytic process. As a result, this forms the foundation for a catalyst genome [1]. However, the existing database lacks a clear and organized explanation of the characteristics of electronic promoters. These promoters are pivotal in improving the effectiveness, selectivity, and durability of catalysts for various processes, including but not limited to ammonia and Fischer-Tropsch synthesis, water-gas shift, and hydrocarbon dehydrogenation [2].

Ammonia holds a central role in today's economy as it is vital for agricultural practices that support approximately half of the global population [3]. Nonetheless, the production of ammonia requires a substantial amount of the world's natural gas, ranging from 3% to 5%. In various regions, scientists are actively investigating the practicality of electrocatalytic methods for synthesizing ammonia through nitrogen reduction reactions (NRR) under standard conditions. This novel approach serves as a potential substitute for the well-established Haber-Bosch process that has been in use for over a century [4]. The hydrogen evolution reaction (HER) occurs in the same frequency frame as the NRR, making it a competitive process, and the solubility problem of N_2 in the electrolyte medium is another important challenge to this electrochemical process. Most metals have an intense preference toward proton adsorption rather than N_2 adsorption, thus the counter-oxidation mechanism at the anode is somewhat slow [5]. These are significant issues, as they have a direct impact on the yield, rate of production, and Faradaic efficiency (FE) of NH_3 synthesis. An unfavorable kinetics of NRR permits a straightforward HER procedure [6,7]. In addition, if there is any nitrogenous sources other than the consuming gas, which needs to be cleaned before used, a false positive NH_3 generation is frequently observed [8]. Consequently, the NRR procedure must incorporate a number of preventative steps. Initiated in the late 1960s, this strategy has just lately begun to evolve. In an effort to achieve NH_3 production on an industrial scale, catalyst design, and electrolyte development have opened up a number of new paths. While some scientists began working on barriers to capture protons and facilitate the diffusion of N_2 so that there is less H^+ ion interference and more restricted HER, Others looked at the mechanisms that occur during NRR to see how they work. Consequently, there is ample opportunity for future research and development in this subject, which has vastly expanded [9–11].

* Corresponding author.
E-mail address: ati4@hi.is (A. Iqbal).

https://doi.org/10.1016/j.ijhydene.2024.03.282
Received 16 September 2023; Received in revised form 13 March 2024; Accepted 22 March 2024
Available online 1 April 2024

Other than transition metal oxides (TMOs) [12–15], transition metal nitride (TMNs) [16–23], transition metal (TMs) [24–26] and transition metal carbides (TMC) [27] have been demonstrated to be good catalysts for the NRR, although few nitrides were predicted to favor the HER [28,29]. According to recent research [30], the adsorption capacity for N_2 is significantly controlled by the electronic features of the element because atoms possessing partially filled d-orbitals and appropriate symmetry possess the capability to effectively acquire electrons from N_2 and subsequently transfer them back to N_2, a notable technique involving p-back-donation comes into play. This technique serves the dual purpose of weakening N–N bonds while simultaneously reinforcing metal-N interactions [31].

To initiate activation of the N–N bond, the creation of electron-donating electrocatalysts with a substantial number of catalytically active sites is imperative. Following the principles of the well-established d-band model [32,33], TMCs [34] showcase an electronically advantageous structure and adsorption behavior [35]. This behavior resembles that of noble metals, a trait attributed to the dense d-orbitals inherent to transition metals. Consequently, this feature creates numerous opportunities for p-back donation to the adsorbates [36]. Chang et al. [37] have demonstrated that the introduction of nitrogen can enhance the elastic properties of TMC TMC (M = Zr and Hf). Using techniques such as X-ray Diffraction (XRD), Transmission Electron Microscopy (TEM), and Energy Dispersive Spectroscopy (EDS), Cao and co-workers [38] analyzed the structure, composition, and crystal arrangement of micro-alloyed carbonitride precipitates within hot-rolled Nb–Mo steels. Their investigation revealed that these steels form finely dispersed MC-type carbonitrides with a crystal structure akin to NaCl. Liu et al. [39] calculated the compositional coefficient of V (C_xN_{1-x}) within the austenite of 35Mn_2V steel. They found that for temperatures below 900 °C, the value of x in V(C_xN_{1-x}) is equal to or greater than 0.5. Wen et al. [40] successfully produced and assessed the thermal and mechanical attributes of a novel high-entropy nitride--carbide, namely ($Hf_{0.2}Zr_{0.2}Ta_{0.2}Nb_{0.2}Ti_{0.2}$) ($N_{0.5}C_{0.5}$), boasting an equal ratio of carbon to nitrogen.

Because of their high hardness, excellent wear resistance, and oxidation resistance properties, transition metal carbides, nitrides, and carbonitrides have attracted a lot of attention and found widespread application in hard coatings and cutting tools [41–56] and as diffusion barrier layers [57–60]. The rocksalt structure (RS) allows for the crystallization of a wide variety of TMNs and carbonitrides, including ScN [61], TiN [62], HfN [44], ZrN [63], VN [64], NbN [65], TaN [66], CrN [67], MoN [68], WN [69], FeN [70], $NbC_{1-x}N_x$ [48], $TaC_{1-x}N_x$ [71], $VC_{1-x}N_x$ [38], $HfC_{1-x}N_x$ [72], $ZrC_{1-x}N_x$ [73], and $TiC_{1-x}N_x$ [74]. The structure and phase stability of nitrides, carbides, and carbonitrides of the early transition metals are particularly well studied, and they possess excellent mechanical properties that are predicted to improve with an increase in the number of valence electrons [75,76], leading to increased ductility and toughness as we move to the right in the periodic table [77–81]. Recent research on transition-metal binary compounds has attained its highest point. Small particle size makes it challenging to directly examine transition-metal carbonitrides in experiments. So far, the electrocatalytic NRR has emerged as an alternative approach, functioning under room temperature and atmospheric pressure conditions. This method has garnered significant attention in academic circles due to its sensitivity to reaction conditions like pH and applied voltage. Additionally, it leverages pollution-free, sustainable energy sources such as solar and wind energy, resulting in a reduction of energy input by over 20% [82–87].

In this work, transition metal carbonitride (TMCN) catalysts are studied for the first time for the electrochemical generation of ammonia under ambient conditions. Using density functional theory (DFT) we collected thermodynamic data and other activity descriptors and reported the activity of TMCNs in a RS crystal structure using the energy lowest (100) facet as a model system. The onset potentials required for ammonia formation, free energy diagrams, poisoning tendencies from the aqueous solution, kinetic barriers for N_2 adsorption, electronic properties and surface stability are among the data obtained for determining the activity of TMCN surfaces. The computational standard hydrogen electrode [88] is implemented to account for the influence of an external potential, which is examined in the context of surface activity and stability at the onset potential.

2. Methodology

2.1. Modeling parameters

In all simulations, the density functional theory (DFT) was applied utilizing the RPBE [89] exchange-correlation functional. The Vienna ab initio simulation package (VASP) [90] was employed, incorporating a 4 x 4 x 1 Monkhorst-Pack K-point grid and a 500 eV energy cutoff for each surface. The implementation of the projector augmented wave (PAW) method [91] was integrated into the VASP code, enabling the exploitation of computationally efficient pseudopotentials to access the entire wavefunction, thereby significantly reducing computational time. To account for electron distribution, the Kohn-Sham orbital occupancy was smoothed using a Fermi-Dirac distribution characterized by a smearing value of $k_BT = 0.1$ eV. All surfaces underwent analysis in the RS crystallographic structure while maintaining a (100) surface orientation. Because of more stability of this structure and facets, they were chosen to also enable comparison with analogous studies done on the TMN surfaces published by the group [18,19,92–94]. The TMCN surfaces were modeled with a 5-layer 2 × 2 unit cell consisting of 20 metal atoms, 10 carbon atoms and 10 nitrogen atoms (see Fig. 1). The bottom two layers were locked in place, while the upper layers and any adsorbates were allowed to relax. Periodic boundary conditions were maintained along the x and y dimensions and lattice constant were shown in Table S2, and between each surface slab, a gap of at least 15 Å of vacuum was maintained in the z direction. The structural optimization was considered successful when the cumulative forces exerted on all movable atoms amounted to less than 0.01 eV. For the calculation of activation energies, the climbing image nudged elastic band technique (CI-NEB) was employed to identify the highest point along the minimum energy path (MEP) [95].

2.2. Electrochemical modeling and reaction pathways

In order to simulate the whole chemical pathway leading to ammonia production, the following equations is used:

$$N_2 + 6(H^+ + e^-) \rightleftharpoons 2NH_3 \quad (1)$$

$$H_2 \rightleftharpoons 2(H^+ + e^-) \quad (2)$$

Within the electrochemical cell, the essential components needed for ammonia synthesis at the cathode (Equation (1)) encompass atmospheric nitrogen, protons generated at the anode (Equation (2)), and electrons originating from the applied voltage. As the necessary protons are exclusively formed at the anode, it becomes possible to directly compare the applied voltage to the standard hydrogen electrode (SHE) or the reversible hydrogen electrode (RHE). The chemical progression was simulated via an unrestrictive mechanism, wherein the most thermodynamically favorable adsorption site was chosen for each protonation step, subsequently utilized for successive protonation stages leading to product formation. For a comprehensive understanding of a catalyst's catalytic activity and the resulting products, the optimal approach lies in employing an unrestrictive mechanism. The following equation is applied to compute the change in free energy for each reaction step:

$$\Delta G_i(U_{RHE}) = \Delta G_i\,(U_{RHE} = 0) + neU_{RHE} \quad (3)$$

$$eU_{RHE} = eU_{SHE} + 2.3k_BTpH \quad (4)$$

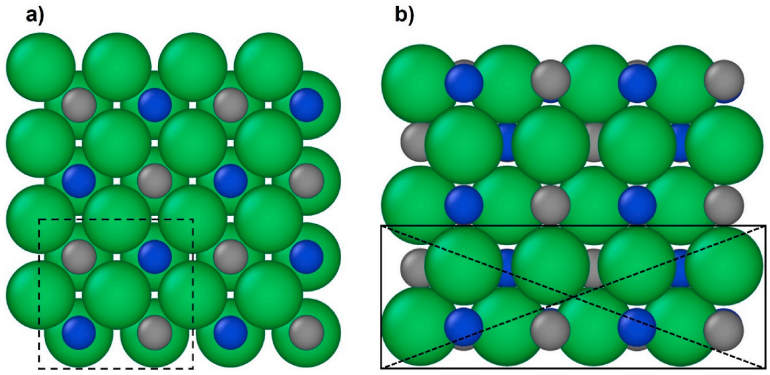

Fig. 1. Model system of a 5-layer VCN. (a) Top view (b) Side view of the (100) facet of the RS structure used in the computational simulations. The green, gray, and blue spheres represent V, C, and N atoms respectively. The bottom two layers presented by a big cross are fixed. (For interpretation of the references to colour in this figure legend, the reader is referred to the Web version of this article.)

Here, U_{SHE} represents the applied potential relative to the standard hydrogen electrode, n denotes the number of electrons, e is the elementary charge, k_B is the Boltzmann constant, and T signifies the temperature. By inserting Eq. (4) into Eq. (3), we obtain:

$$\Delta G_i(U_{RHE}, pH) = \Delta G_i\,(U_{RHE} = 0) + n(eU_{SHE} + 2.3k_BTpH) \quad (5)$$

In this study, we adopt a pH value of 0. Importantly, overpotentials are typically unaffected by the electrolyte pH, and as such, our predicted overpotentials remain valid across different pH values. The calculation of $\Delta G_i(U = 0)$ for each elementary step is carried out as follows:

$$\Delta G_i(U = 0) = \Delta E_{DFT} + \Delta E_{ZPE} + \Delta H_{0K\to T} - T\Delta S \quad (6)$$

where ΔE_{DFT} is calculated with DFT and ΔE_{ZPE} and ΔS are zero-point energy corrections and entropy differences which are calculated within harmonic approximation of the adsorbed intermediates but taken from table values for gas phase molecules [96]. $\Delta H_{0K\to T}$ is the change in internal energy because of temperature and calculated as:

$$\Delta H_{0K\to T} = \int_0^T C_P\,(T')\,dT' \quad (7)$$

In equation (7), $C_P(T')$ represents the specific heat capacity at constant pressure. The integral term in the equation makes a negligible contribution to the internal energy at room temperature and this contribution can be even smaller than 0.1 eV [97]. Within any reaction pathway, the potential-determining step (PDS) refers to the electrochemical reaction with the most substantial positive alteration in free energy. Starting from the PDS, the onset potential (OP) can be defined as the potential needed to nullify the change in the free energy of the PDS. Subsequently, as described by Eq. (4), all subsequent reaction steps experience a decrease in free energy, leading to a downhill trajectory.

$$OP = -\Delta G/e \quad (8)$$

The OP (in volts) is simply equal to the electron-volt magnitude of the negative shift in free energy associated with the PDS. According to the studies on the intrinsic DFT errors when modeling the energetics of gas-phase compounds, a +0.34 eV correction to N_2 gas adsorption was reported [98,99], so we considered this correction for all the data presented in this work.

3. Results and discussion

Initially, group III-XII possible transition metal carbonitride catalysts were subjected to computational screening of the RS in (100) facets; Only VCN, NbCN, ZrCN, TiCN, TaCN, CrCN, MoCN, HfCN, WCN, YCN, and ScCN were selected for further investigation due to stable structure (which was not distorted upon relaxation). Seven factors were studied in order to evaluate the viability of all candidate for electrochemically producing ammonia under ambient conditions: i) mechanism for nitrogen reduction reaction (ii) surface poisonous (iii) catalytic activity (iv) poisoning of the catalyst surface vacancy, (v), stability against the composition by calculating the surface N/C-vacancy migration into the bulk, (vi) calculated kinetic barrier for vacancy regeneration by N_2 dissociation and (vii) theoretical volcano plot for activity. We also considered studying the electronic properties and chemical bonding features of TMCN shown in the electronic supporting information (ESI).

3.1. Mechanism of nitrogen reduction reaction

We investigated three mechanisms for NRR: 1) dissociative mechanism (DM), 2) associative mechanism (AM), and 3) Mars-van Krevelen mechanism (MvK), as shown in Fig. 2. In the DM, the strong N_2 triple bond is broken during the adsorption phase, resulting in the adsorption of separate N atoms at a discrete distance apart on two adsorption sites. In subsequent phases, the hydrogenation of each N atom results in the creation of ammonia, which is then released. In the AM, the N_2 bond stays intact following N_2 adsorption and only breaks during a specific phase of the hydrogenation process. In the AM, we also investigated the possibility of *NNH formation/adsorption and plotted it in free energy diagrams. In the MvK, the lattice N/C atoms on the surface of TMCNs could be reduced to ammonia/methane and, as a result, vacancies are produced. These vacancies shall chemically be replenished by nitrogen molecules either associatively (via associative MvK) or dissociatively (via dissociative MvK) to regenerate the catalyst.

Adsorption free energies and reaction pathways for each candidate, VCN, CrCN, YCN, HfCN, NbCN, ScCN, ZrCN, TiCN, TaCN, WCN, and MoCN, was investigated to assess the reactivity of TMCN surfaces in the designated structure for the NRR. Before any reaction may occur, the adsorption of a nitrogen species onto the surface is going to be studied. This will provide an idea of stability of these surfaces against poisoning, where proton adsorption, OH and O adsorption on clean surface will be compared with adsorption of nitrogen species, as shown in Fig. 3. To find the most energetically favorable configuration of any adsorbates, all possible adsorption sites were examined, and the most favorable adsorption was selected for comparison; the findings for the adsorption of nitrogen and potential active site poisoning by other species are depicted in Fig. 3.

In addition to the adsorption energies of nitrogen species, Fig. 3 depicts the energy associated with the protonation of a metal site, which is a useful indicator of the probability of the HER. This is typically the

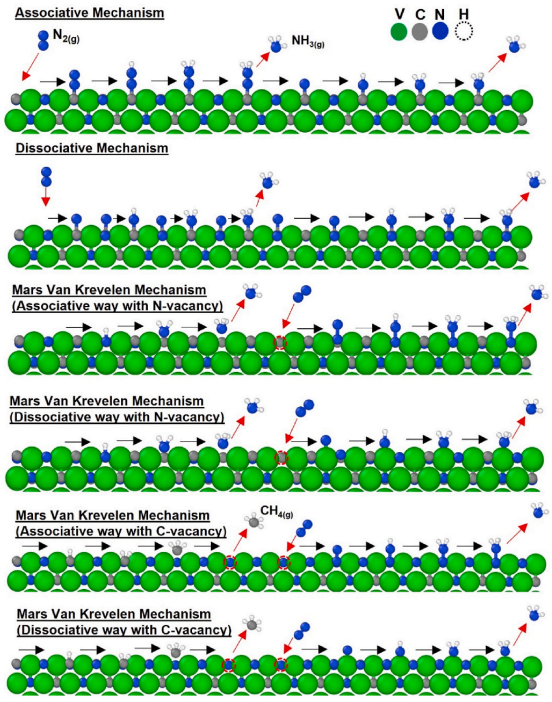

Fig. 2. Schematic diagram of the nitrogen reduction reaction mechanism in this paper.

very important competitive side reaction to the NRR. According to Fig. 3, it can be seen that N_2 dissociation for most of the surfaces is endergonic except YCN and ScCN. This eliminates all other candidates, however, ZrCN, CrCN, MoCN and HfCN will also be evaluated because the dissociative binding of nitrogen gas is only a little uphill in energy (endergonic). After the associative binding of nitrogen to YCN and ScCN, the preferred reaction route was identified as successive protonation of the surface via an unrestricted mechanism. YCN produces the first ammonia molecule but then proceeds to formation of carbon vacancy

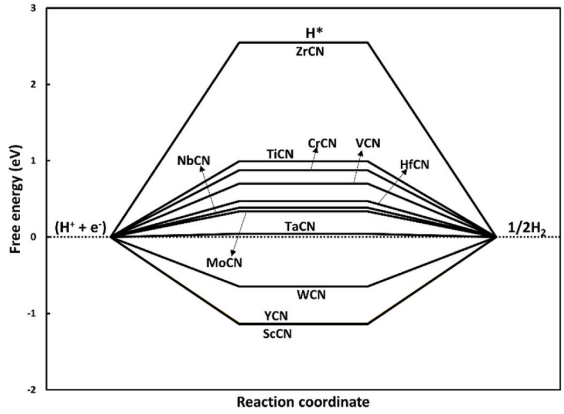

Fig. 4. Free-energy diagram of hydrogen evolution activity on transition metal carbonitrides.

(CH_4), but for ScCN surface the formation of ammonia (NH_3) was not detected for any configuration. The protonation of carbon sites over nitrogen results in the creation of methane (CH_4), and therefore, at that point simulations were terminated. Both methane and hydrogen production are undesirable byproducts of TMCNs as NRR catalyst because they indicate a tendency for surface breakdown or the dominance of HER. The exergonic protonation of carbon sites on several of these TMCNs, YCN and ScCN included, reflects this behavior. In addition to failing to generate the desired product, there are a number of TMCN surfaces that preferentially bind the oxygen species O^{2-} at zero potential, however they could be removed at negative operational potential experimentally. Therefore, this should not be a problem at negative potentials because these oxygen species should be released from the negatively charged surface.

As the initial stage in the formation of hydrogen, we evaluate and illustrate the free energy associated with proton adsorption onto the metal site, as illustrated in Fig. 4. Within the surfaces investigated, only ScCN (−1.13 eV), YCN (−1.13 eV), and WCN (−0.64 eV) exhibit robust proton binding on their metal sites. In contrast, the remaining TMCNs undergo this process in an endergonic manner, suggesting that HER is unlikely for the majority of them. A clear comparison has been made shown in Fig. S12 between pure metal and these carbonitrides for HER

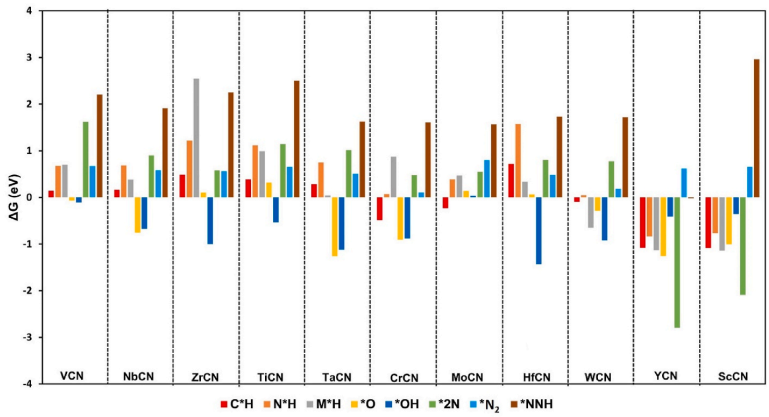

Fig. 3. Comparison of the adsorption energies of various nitrogen and oxygen species on clean TMCN surfaces, in addition to the protonation of metal, nitrogen, and carbon site at zero potential. *N_2 denotes the associative binding of $N_{2(g)}$, *2 N denotes the dissociative binding of N_2, and *NNH denotes the associative binding of NNH.

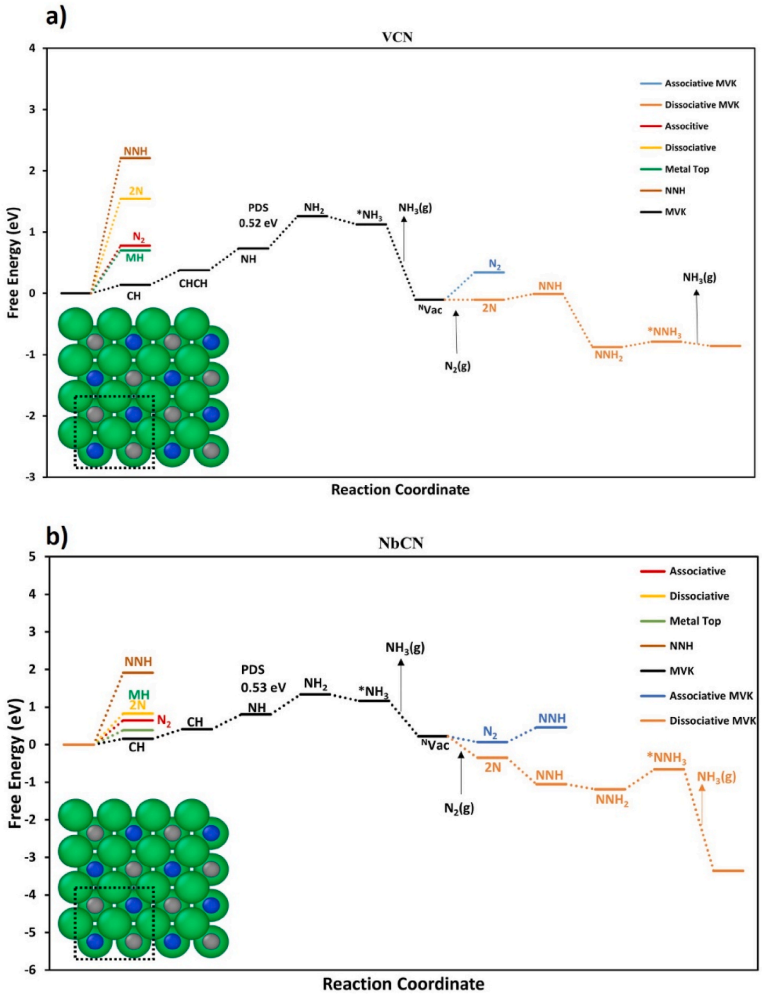

Fig. 5. (a) Free energy diagrams for NH_3 formation via the most favorable pathway of RS crystal structures in (100) facets (a) VCN and (b) NbCN at zero potential.

which shows that most of the TMCN is unlikely go for HER.

On the RS (100) facets of TMCNs, we have done a full analyses of the reaction via different mechanisms for eleven TMCNs, but only show the free energy diagrams for the most promising candidates and the rest are provided in the ESI. As illustrated in Fig. 5 (a and b), the most favorable pathway for ammonia production on VCN and NbCN is via the MvK mechanism where the PDS is the fourth protonation step (associated with formation of $*NH_2$) following the formation of the first ammonia, with $\Delta G_{PDS} = 0.52$ and 0.53 eV, respectively. After formation of the first ammonia molecule, the N-vacancy can be exergonically replenished by either N_2 (via associative MvK) or 2 N (via dissociative MvK), and two ammonia molecules are released eventually after $8(H^+ + e)$ transfer under ambient conditions. Other mechanisms are endergonic and less probable compared to the MvK, but they have been fully investigated and the full pathways are shown in the ESI.

For WCN, the ΔG_{PDS} is 0.72 eV via MvK and it is related with the fourth protonation step and the formation of $*NH_2$. As seen from the free energy diagram (illustrated in Fig. S3) filling the produced vacancy with nitrogen will not be thermodynamically facile by neither associative MvK nor dissociative MvK. Unlike the MvK, the AM appears to be less favorable with endergonic adsorption of N_2 molecule on the pristine surface. However, following hydrogenation of the surface with the presence of $*N_2$ (through the red pathway), as shown in Fig. S3, it was observed that protons tend to rather bind the surface N/C atoms instead of binding the $*N_2$ (associatively adsorbed on the clean surface). This mechanism contributes to formation of ammonia with a ΔG_{PDS} of 0.34 eV. Upon formation of the vacancy, it is replenished by diffusion of adsorb nitrogen from the surface to the vacancy and its subsequent dissociation which is thermodynamically feasible but having high kinetic barrier (with activation energy 1.0 eV as in Fig. S14a).

For ZrCN, the initial step for all the possible mechanisms is found to be endergonic and thus not interesting. However, nitrogen adsorption via the DM is only slightly uphill in free energy, and thus we explored it further together with the MvK mechanism. When we investigated the full pathway via the MvK, it was found out that the step associated with formation of the ammonia molecule is very endergonic (around 2.4 eV as illustrated in Fig. S4) and thus not desirable. Surprisingly, via DM, the PDS for ammonia formation was found to be only 0.25 eV. When we investigated the kinetics of N_2 dissociation on ZrCN, a relatively large activation energy of 2.99 eV was calculated (as shown in Fig. S14b)

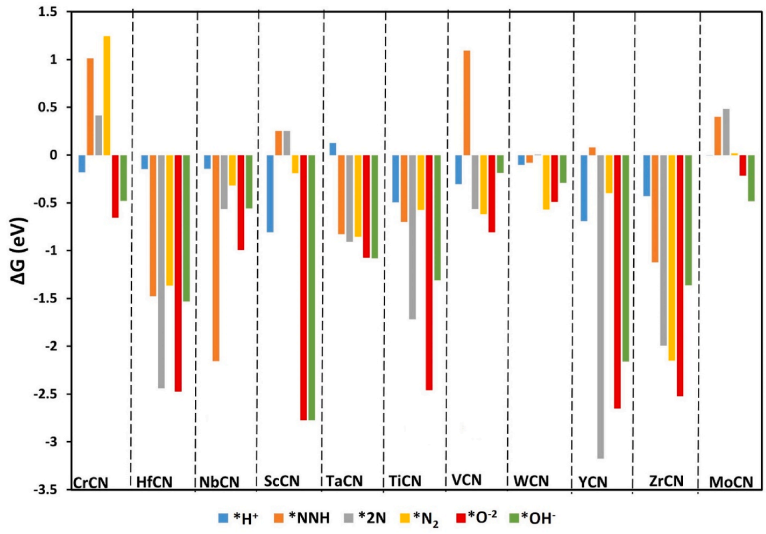

Fig. 6. Examining the free binding energies of several nitrogen species to nitrogen/carbon vacancies on TMCN surfaces at zero potential. H denotes protonation of a surface metal atom, $*N_2$ indicates associative binding of N_2 vertically in the vacancy, *2 N indicates dissociative binding of N_2 with one N sitting in the vacancy and the other on a adjacent metal/nitrogen/carbon atom, *NNH indicates binding of NNH vertically in the vacancy, and so on.

which could make this process slow at ambient conditions but motivates further analyses of using ZrCN in non-ambient ammonia synthesis systems as tuning temperature or pressure could facilitate kinetics of nitrogen adsorption on the clean surface.

For all other materials, there is no favorable pathway to ammonia formation after various protonation steps, as described in S5–S11, either due to high PDS or formation of undesired product. For example, ScCN and YCN are not interesting candidates due to the high PDS step found for the MvK or unfavorable path via other mechanisms. For CrCN and MoCN, the free energy diagrams are shown in Figs. S8 and S9, where a pathway to NH_3 creation via MvK and all other mechanisms is depicted, and it can be observed that none of the mechanisms are in favor of ammonia formation under ambient circumstances. Hence carbonitrides demonstrated superior performance or were more effective than pure metal catalysts in promoting the nitrogen to ammonia as shown in Fig. S13. The adsorption free energies are shown in Table S3 ESI, and optimized coordinates for the most promising candidate VCN are also included in ESI.

Figure S1–S11 compare the various pathways, i.e. dissociative binding of nitrogen, associative binding of nitrogen, binding of NNH, adsorption of hydrogen onto a metal site, adsorption of hydrogen onto a nitrogen site, and adsorption of hydrogen onto a carbon site on the clean surface of these TMCNs. An interesting observation here is that the presence of a vacancy on the surface offers an active site where nitrogen may attach more easily due to the stronger coordination associated with the presence of vacancy, and this promotes a greater selectivity for nitrogen activation. The preliminary investigation of the binding of nitrogen species in the vacancy of these TMCN surfaces is depicted in Fig. 6.

When comparing Fig. 3 (nitrogen adsorption on surfaces without vacancy) and Fig. 6 (nitrogen adsorption on surfaces with vacancy), it reveals that the adsorption energies of the nitrogen species are considerably enhanced in the presence of a vacancy. For a few surfaces O^{-2} binds stronger to the vacancy at zero potential but at the onset potential (see Fig. 7) this will be released from the electrode surface and therefore of no concern. The dissociative binding of nitrogen in the presence of vacancy becomes exothermic for the majority of TMCN, which is particularly promising. However, this eliminates CrCN, which does not

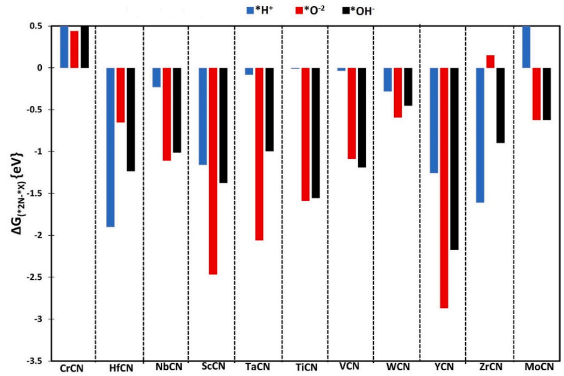

Fig. 7. Comparing the free energy of adsorption of O, OH, or H (relative to 2 N) to the surface vacancy of catalytically active carbonitrides ($G_{(*2N-*X)}$ in eV). Calculate the free energies with respect to $N_{2(g)}$, $1/2H_{2(g)}$, and $H_2O_{(g)}$. All free energies are evaluated at the predicted onset potential of each carbonitride (based on the most favorable reaction mechanism and displayed versus RHE). The adsorption energy of two N atoms is compared to that of one O, one OH, or one H, when the nitrogen originates from N_2 filling the vacancy and one of the N atoms adsorbs to the vacancy while the second N atom adsorbs on top of the neighboring metal atom.

bind any nitrogen species strongly, while MoCN and ScCN only bind it associatively. VCN, and NbCN are the only surfaces that proceeded to ammonia formation when binding nitrogen dissociatively in vacancy. For economically feasible production, the catalyst must be able to adsorb nitrogen in a very short amount of time, and a kinetic barrier greater than 1 eV will undoubtedly inhibit this process at room temperature. Thus, it is necessary to calculate the kinetic barrier that is represented by the activation energy of N_2 to adsorbs and dissociates on the surface. Here we showed the NEB calculations for the five candidates i.e ZrCN and HfCN (without a vacancy), and VCN, NbCN, WCN (with vacancy) in Fig. S14. We assume that due to the extremely preferential

adsorption of nitrogen, maintaining the nitrogen atom in the vacant site is preferable to protonation. This would imply that in order to attain the appropriate activity, nitrogen adsorption must be exergonic yet below a certain threshold energy. Looking at Fig. S14 (a), we can see that this threshold energy is below 1.0 eV, as this would accurately predict that only VCN, and NbCN would be active catalysts, whereas the kinetic barrier for dissociative nitrogen adsorption onto the ZrCN and HfCN surfaces is too high (2.99 eV and 1.81 eV as shown in Fig. S14 (b)), which shows that N_2 dissociation on clean surface of ZrCN and HfCN should be difficult/slow and thus these two material would be of better choice for high temperature/pressure NRR rather than for ambient-condition NRR.

3.2. Poisoning of the defects/vacancies

In order for the catalytic cycle to continue, N_2 must fill the surface vacancies that are created. There is a probability that the nitrogen-vacancy is not occupied with nitrogen because it is blocked by a proton, an oxygen atom, or a hydroxyl atom from the aqueous electrolyte. Therefore, the free energy of filling the vacancy with any of these species compared to nitrogen ($\Delta G_{(*2N\text{-}*X)}$), where X = O, H, or OH, is used to study the rivalry between N and O, H, and OH for filling the surface vacancy. Under operational circumstances, these ions are derived from the water in the electrolyte, which results in the creation of O^{-2}, OH^-, and H^+. A negative value of $\Delta G_{(*2N\text{-}*X)}$ implies that nitrogen adsorption is thermodynamically preferable to the other three species for filling the vacancy. The values are shown in Fig. 7 for the whole group of catalytically active carbonitrides at the predicted onset potential.

N atoms absorb more strongly than O atoms to surface vacancies in all carbonitrides except CrCN and ZrCN, although for ZrCN this phenomenon might not be critical as the favorable pathway towards ammonia is not via formation of the vacancy. It is predicated that the surface vacancies of most of these carbonitrides will not be poisoned by these species. For all carbonitrides besides CrCN, N atoms attach to surface vacancies with greater affinity than OH species. For MoCN, the vacancy will be filled by O and H instead. For the rest of the carbonitrides, the vacancy will likely be filled by nitrogen, so the catalytic cycle may keep making NH_3. Overall, VCN and NbCN stand out as the most viable choices, both in terms of activity (Fig. 5) and stability against poisoning (Fig. 7). These carbonitrides will have the ability to convert nitrogen to ammonia at potentials of −0.52 V and −0.53 V. We did not consider solvation here because Höskuldsson et al. [100] calculated for W catalyst with and without a water bilayer. The effect is small in most cases (less than 0.05 eV) except for NNH species (0.14 eV) and NH_3 species (0.13 eV). Here we are doing a screening study for a range of carbonitrides. Therefore, in this work, we did not consider this small correction here as this is within the typical uncertainty of DFT.

3.3. Stability against decomposition

Reduction of a surface nitrogen/carbon atom within the MvK generates NH_3/CH_4, following which a gaseous N_2 molecule fills the ensuing vacancy. Stability of the surface N/C-vacancy is required for this replenishment to occur. If not, the N/C-vacancy could move to the bulk of the catalyst, where it would be replenished with additional nitrogen/carbon from the bulk of catalyst, as opposed to gaseous N_2. Theoretically, the cycle remains until all of the carbon and nitrogen atoms in carbonitrides have reduce to form NH_3/CH_4. This could lead to TMCN decomposition to the parental metal. The energy difference between a carbonitride slab with a single N/C-vacancy in the surface layer ($E_{vac,1}$) and the first subsurface layer ($E_{vac,2}$) determines the stability of the N/C-vacancy at the catalytic surface. Energy difference ($\Delta E_{vac} = E_{vac,2} - E_{vac,1}$) is used to estimate the thermodynamic stability of the vacancy at the carbonitride's surface. Kinetic barriers for vacancy migration ($E_{a,vac}$) are also calculated, and Fig. 8 displays a comparison of both thermodynamics (ΔE_{vac}) and kinetics ($E_{a,vac}$) of this process. It is revealed that, for the majority of carbonitrides, it is thermodynamically favorable for the vacancy to migrate to the bulk. Due to the large kinetic barrier for the vacancy migration, however, these carbonitrides are going to have stable surface vacancies. The kinetic barrier of all carbonitrides for vacancy migration is greater than 1 eV and are thus preserved for further screening, as a barrier of this size at room temperature is improbable to be overcome.

3.4. Exploring the scaling relations and formation of volcano plots

Using the linear relations for various reaction steps as a function of the ΔG of *NH (as descriptor), we can generate volcano diagram to determine which value of ΔG of *NH would result in the lowest onset potential for electrochemical ammonia synthesis. In Ref. [101], this method was applied to the electrolysis of water on oxide surfaces. In this analysis, the potential related to the potential limiting step can be used as a direct indicator of electrocatalytic activity. The free energy of the reaction for every fundamental step can be expressed as a function of the

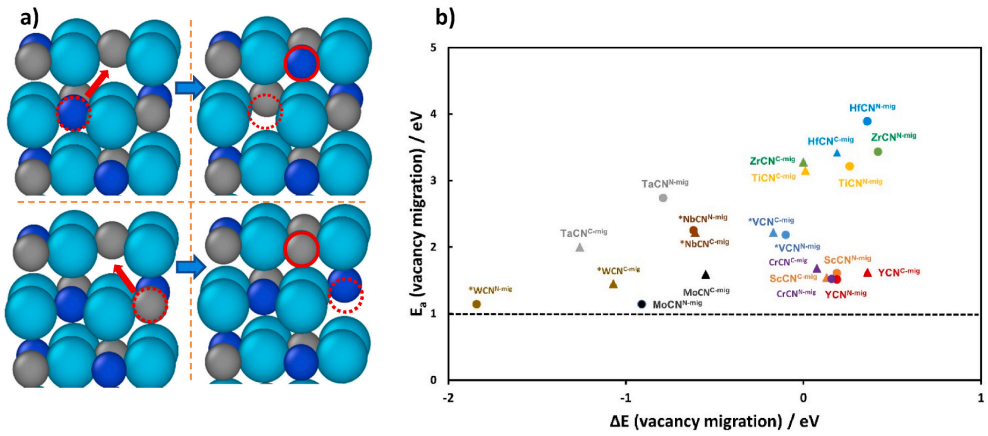

Fig. 8. (a) A depiction of a sub-layer nitrogen/carbon atom migrating to a surface vacancy of a carbonitrides, (b) as well as the vacancy migration activation energy ($E_{a,vac}$). The dotted line at $E_{a,vac} = 1$ eV represents the stability threshold beyond which metal carbonitrides are considered adequately stable for further investigation. C-mig represents carbon migration from sub-layer to the surface layer while N-mig means nitrogen migration from the sub-layer to the surface layer. The elements having * means they have nitrogen vacancy while all others represent carbon vacancy.

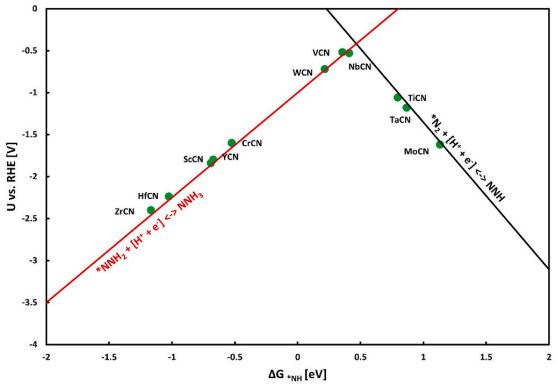

Fig. 9. Theoretical volcano plot for the formation of ammonia by using *NH as a descriptor.

applied bias U and the ΔG of the NH, denoted by *NH. Using the linear scaling relationships from Fig. S15, we can construct the volcano plot as shown in Fig. 9 considering the MvK. It can be seen that VCN and NbCN are at the summit of the MvK volcano representing the most promising materials for the formation of ammonia at ambient conditions.

4. Conclusions

Using DFT calculations, we investigated different possible reaction mechanisms for ammonia formation; the MvK, the AM, and DM for the rocksalt structure of eleven carbonitrides in (100) facets: ScCN, TiCN, VCN, CrCN, YCN, ZrCN, NbCN, MoCN, HfCN, TaCN, and WCN. We computed the free energies of all stable intermediates along different pathways of the reaction. By creating free energy diagrams for each carbonitride, we were able to determine the free energy change of every step that determines the onset potential. Additionally, we estimated the activation energy of N_2 dissociation and evaluated the free energy of adsorption of N_2 adatoms on the surface. The conclusion is that reducing nitrogen to ammonia under ambient circumstances using either DM or AM may not be advantageous for these materials except for ZrCN, HfCN and WCN. For most of these materials at ambient condition the DM is inactive for ammonia formation due to the high kinetic barriers of N_2 dissociation. Except for WCN, YCN, and ScCN, adsorption of the N_2 molecule by AM on the pristine surface of these carbonitrides is often endothermic. However, it should be emphasized that none of the transfer barrier for electrochemical proton-electron have been accounted for in this work, therefore the rates for these various methods have not yet been assessed. In this work, a thermochemical model was utilized to predict the onset potentials for these various processes. Except for ScCN, YCN, and TaCN, which were exposed to be more selective for the HER in an electrochemical environment, all other carbonitrides were found to be able to suppress HER. It was found that CrCN and MoCN are vulnerable to poisoning in electrochemical media. VCN and NbCN were discovered to need low onset potential (−0.52 V and −0.53 V vs. RHE) via MvK toward ambient NRR among all the carbonitride compounds tested, while ZrCN and HfCN (via DM) and WCN (via AM) were discovered promising for non-ambient NRR with very small PDS of 0.25 eV, 0.34 eV, and 0.34 eV, respectively, interesting materials for further experimental tests in non-ambient NRR as temperature/pressure tuning would facilitate nitrogen adsorption/dissociation on these surfaces. Therefore, experimentalists are highly urged to explore this novel kind of potential DFT-based catalysts for the prospect of enhanced ammonia synthesis under ambient circumstances.

Funding

This work was supported by Icelandic Research Fund [grant numbers 185051–051 and 207056–053].

Declaration of competing interest

The authors declare that they have no known competing financial interests or personal relationships that could have appeared to influence the work reported in this paper.

Appendix A. Supplementary data

Supplementary data to this article can be found online at https://doi.org/10.1016/j.ijhydene.2024.03.282.

References

[1] Jia Q, et al. Experimental observation 2 of redox-induced FeN switching 3 behavior as a determinant role 4 for oxygen reduction activity. ACS Nano 2015; 11:12.
[2] Ertl G, Knözinger H, Weitkamp J. Handbook of heterogeneous catalysis, vol. 2. VCH Weinheim; 1997.
[3] Smil V. Detonator of the population explosion. Nature 1999;400(6743). 415-415.
[4] Soloveichik G. Electrochemical synthesis of ammonia as a potential alternative to the Haber–Bosch process. Nat Catal 2019;2(5):377–80.
[5] Ceballos BM, et al. Roads less traveled: nitrogen reduction reaction catalyst design strategies for improved selectivity. Curr Opin Electrochem 2021;28: 100723.
[6] Ren Y, et al. Strategies to suppress hydrogen evolution for highly selective electrocatalytic nitrogen reduction: challenges and perspectives. Energy Environ Sci 2021;14(3):1176–93.
[7] Choi C, et al. Understanding potential-dependent competition between electrocatalytic dinitrogen and proton reduction reactions. Nat Commun 2021;12 (1):1–11.
[8] Li L, et al. Electrochemical nitrogen reduction: identification and elimination of contamination in electrolyte. ACS Energy Lett 2019;4(9):2111–6.
[9] Hou J, Yang M, Zhang J. Recent advances in catalysts, electrolytes and electrode engineering for the nitrogen reduction reaction under ambient conditions. Nanoscale 2020;12(13):6900–20.
[10] Qing G, et al. *Recent advances and challenges of electrocatalytic N_2 reduction to ammonia.* Chem Rev 2020;120(12):5437–516.
[11] Shen H, et al. Electrochemical ammonia synthesis: mechanistic understanding and catalyst design. Chem 2021;7(7):1708–54.
[12] Zhang L, et al. *Electrochemical ammonia synthesis via nitrogen reduction reaction on a MoS_2 catalyst: theoretical and experimental studies.* Adv Mater 2018;30(28): 1800191.
[13] Li X, et al. *Boosted electrocatalytic N2 reduction to NH_3 by defect-rich MoS_2 nanoflower.* Adv Energy Mater 2018;8(30):1801357.
[14] Hoskuldsson AB, Abghoui Y, Gunnarsdottir AB, Skulason E. Computational screening of rutile oxides for electrochemical ammonia formation. ACS Sustainable Chem Eng 2017;5(11):10327–33.
[15] Liu Z, et al. Efficient and durable N_2 reduction electrocatalysis under ambient conditions: β-FeOOH nanorods as a non-noble-metal catalyst. Chem Commun 2018;54(80).
[16] Abghoui Y, Iqbal A, Skúlason E. The role of overlayered nitride electro-materials for N2 reduction to ammonia. Frontiers in Catalysis 2023;2:1096824.
[17] Hanifpour F, Canales CP, Fridriksson EG, Sveinbjörnsson A, Tryggvason TK, Lewin E, Flosadóttir HD. Investigation into the mechanism of electrochemical nitrogen reduction reaction to ammonia using niobium oxynitride thin-film catalysts. Electrochim Acta 2022;403:139551.
[18] Dražević E, Skulason E. Are there any overlooked catalysts for electrochemical NH3 synthesis—new insights from analysis of thermochemical data. iScience 2020;23(12).
[19] Abghoui Y, Garden AL, Howalt JG, Vegge T, Skúlason E. Electroreduction of N2 to ammonia at ambient conditions on mononitrides of Zr, Nb, Cr, and V: a DFT guide for experiments. ACS Catal 2016;6(2):635–46.
[20] Du Hoang-Long, et al. Critical assessment of the electrocatalytic activity of vanadium and niobium nitrides toward dinitrogen reduction to ammonia. ACS Sustainable Chem Eng 2019;7(7):6839–50.
[21] Gudmundsson M, Ellingsson V, Skúlason E, Abghoui Y. Optimizing nitrogen reduction reaction on nitrides: a computational study on crystallographic orientation. Top Catal 2022;65(1–4):252–61.
[22] MacLaughlin C. Role for standardization in electrocatalytic ammonia synthesis: a conversation with leo liu, lauren greenlee, and douglas MacFarlane. ACS Energy Lett 2019;4(6):1432–6.
[23] Hanifpour F, Canales CP, Fridriksson EG, Sveinbjörnsson A, Tryggvason TK, Yang J, Arthur C, Jónsdóttir S, Garden AL, Ólafsson S, Leósson K, Árnadóttir f L, Lewin g E, Abghoui Y, Ingason ÁS, Magnus F, Flosadóttir HD, Skúlason E. Operando quantification of ammonia produced from computationally-derived transition metal nitride electro-catalysts. J Catal 2022;413:956–67.

[24] Tayyebi E, Abghoui Y, Skulason E. Elucidating the mechanism of electrochemical N2 reduction at the Ru (0001) electrode. ACS Catal 2019;9(12):11137–45.
[25] Höskuldsson ÁB, Dang T, Sakai Y, Ishikawa A, Skúlason E. High-throughput computational screening of doped transition metal oxides as catalysts for nitrogen reduction. Cell Reports Physical Science 2023;4:101595.
[26] Skulason E, Bligaard T, Gudmundsdóttir S, Studt F, Rossmeisl J, Abild-Pedersen F, Nørskov JK. A theoretical evaluation of possible transition metal electro-catalysts for N 2 reduction. Phys Chem Chem Phys 2012;14(3):1235–45.
[27] Ellingsson V, Iqbal A, Skúlason E, Abghoui Y. Nitrogen reduction reaction to ammonia on transition metal carbides catalysts. ChemSusChem 2023;16(Issue 22):e202300947.
[28] Abghoui Y, Skúlason E. Hydrogen evolution reaction catalyzed by transition-metal nitrides. J Phys Chem C 2017;121(43):24036–45.
[29] Abghoui Y. Superiority of the (100) over the (111) facets of the nitrides for hydrogen evolution reaction. Top Catal 2022;65(1–4):262–9.
[30] Hirakawa H, et al. Photocatalytic conversion of nitrogen to ammonia with water on surface oxygen vacancies of titanium dioxide. J Am Chem Soc 2017;139(31):10929–36.
[31] Power PP. Main-group elements as transition metals. Nature 2010;463(7278):171–7.
[32] Hammer B, Norskov JK. Why gold is the noblest of all the metals. Nature 1995;376(6537):238–40.
[33] Hammer B, Morikawa Y, Nørskov JK. CO chemisorption at metal surfaces and overlayers. Phys Rev Lett 1996;76(12):2141.
[34] Gao Q, et al. Structural design and electronic modulation of transition-metal-carbide electrocatalysts toward efficient hydrogen evolution. Adv Mater 2019;31(2):1802880.
[35] Xu H, et al. A new platinum-like efficient electrocatalyst for hydrogen evolution reaction at all pH: single-crystal metallic interweaved V8C7 networks. Adv Energy Mater 2018;8(23):1800575.
[36] Shi Z, et al. *Phosphorus-Mo_2C@ carbon nanowires toward efficient electrochemical hydrogen evolution: composition, structural and electronic regulation*. Energy Environ Sci 2017;10(5):1262–71.
[37] Brykała U, et al. Hot pressing of gadolinium zirconate pyrochlore. Ceram Int 2015;41(2).
[38] Wuyi Z, Huang B-y. Analysis on the reliability and validity of a questionnaire. In: Stat info forum; 2005.
[39] Sheng-xin LIU, Yong CHEN, Guo-quan LIU, Shao-kang GUAN, Qing-kui LI, Ji-tai NIU. Theoretical calculation of carbonitrides in medium-carbon V-Ti-N microalloyed steel. Mater Mech Eng 2007;31(1):78–81.
[40] Wen T, et al. Thermophysical and mechanical properties of novel high-entropy metal nitride-carbides. J Am Ceram Soc 2020;103(11):6475–89.
[41] Chong X, et al. *Tailoring the anisotropic mechanical properties of hexagonal M_7X_3 (M= Fe, Cr, W, Mo; X= C, B) by multialloying*. Acta Mater 2019;169:193–208.
[42] Maeda K, et al. In situ observation of grain boundary groove at the crystal/melt interface in Cu. Scripta Mater 2018;146:169–72.
[43] Martınez E, et al. Tribological performance of TiN supported molybdenum and tantalum carbide coatings in abrasion and sliding contact. Wear 2002;253(11–12):1182–7.
[44] Esteve J, et al. Microtribological characterization of group V and VI metal-carbide wear-resistant coatings effective in the metal casting industry. Surf Coating Technol 2000;133:314–8.
[45] Zhang S. Material development of titanium carbonitride-based cermets for machining application. Key engineering materials. Trans Tech Publ 1997;138:521–44.
[46] Santhanam A. Application of transition metal carbides and nitrides in industrial tools. In: The chemistry of transition metal carbides and nitrides. Springer; 1996. p. 28–52.
[47] Musil J. Flexible hard nanocomposite coating. RSC Advaces 2015;5(74):60482–95.
[48] Choe HJ, Kwon S-H, Lee J-J. Tribological properties and thermal stability of TiAlCN coatings deposited by ICP-assisted sputtering. Surf Coating Technol 2013;228:282–5.
[49] Seo H-S, et al. Growth and physical properties of epitaxial HfN layers on MgO (001). J Appl Phys 2004;96(1):878–84.
[50] Koseki S, et al. Comparison of TiN-coated tools using CVD and PVD processes during continuous cutting of Ni-based superalloys. Surf Coating Technol 2015;283:353–63.
[51] Yasuoka M, Wang P, Murakami R-i. *Comparison of the mechanical performance of cutting tools coated by either a TiC_xN_{1-x} single-layer or a TiC/TiC0. 5N0. 5/TiN multilayer using the hollow cathode discharge ion plating method*. Surf Coating Technol 2012;206(8–9):2168–72.
[52] Vera E, et al. A study of the wear performance of TiN, CrN and WC/C coatings on different steel substrates. Wear 2011;271(9–10):2116–24.
[53] Su Y-L, Liu T-H. *Tribological properties of Ti_2N–W_x% coatings deposited by magnetron sputtering*. Vacuum 2005;77(3):343–54.
[54] Pugh S. XCII. Relations between the elastic moduli and the plastic properties of polycrystalline pure metals. London, Edinburgh Dublin Phil Mag J Sci 1954;45(367):823–43.
[55] Kral C, et al. Critical review on the elastic properties of transition metal carbides, nitrides and carbonitrides. J Alloys Compd 1998;265(1–2):215–33.
[56] Hultman L. Thermal stability of nitride thin films. Vacuum 2000;57(1):1–30.
[57] Navinsek B, Seal S. Transition metal nitride functional coatings. Jom 2001;53(9):51–4.
[58] Jeon S, et al. *Interfacial stability and diffusion barrier ability of $Ti_{1-x}Zr_xN$ coatings by pulsed laser thermal shock*. Appl Surf Sci 2014;320:602–8.
[59] Becker JS, Gordon RG. Diffusion barrier properties of tungsten nitride films grown by atomic layer deposition from bis (tert-butylimido) bis (dimethylamido) tungsten and ammonia. Appl Phys Lett 2003;82(14):2239–41.
[60] Balasubramanian K, Khare SV, Gall D. Valence electron concentration as an indicator for mechanical properties in rocksalt structure nitrides, carbides and carbonitrides. Acta Mater 2018;152:175–85.
[61] Gall D, et al. *Growth of poly-and single-crystal ScN on MgO (001): Role of low-energy N_2^+ irradiation in determining texture, microstructure evolution, and mechanical properties*. J Appl Phys 1998;84(11):6034–41.
[62] Sundgren J-E. Structure and properties of TiN coatings. Thin Solid Films 1985;128(1–2):21–44.
[63] Mei A, et al. Physical properties of epitaxial ZrN/MgO (001) layers grown by reactive magnetron sputtering. J Vac Sci Technol A: Vacuum, Surfaces, and Films 2013;31(6):061516.
[64] Mei A, et al. Elastic constants, Poisson ratios, and the elastic anisotropy of VN (001),(011), and (111) epitaxial layers grown by reactive magnetron sputter deposition. J Appl Phys 2014;115(21):214908.
[65] Zhang K, et al. Growth and mechanical properties of epitaxial NbN (001) films on MgO (001). Surf Coating Technol 2016;288:105–14.
[66] Shin C-S, et al. Growth and physical properties of epitaxial metastable cubic TaN (001). Appl Phys Lett 1999;75(24):3808–10.
[67] Gall D, et al. Growth of single-crystal CrN on MgO (001): effects of low-energy ion-irradiation on surface morphological evolution and physical properties. J Appl Phys 2002;91(6):3589–97.
[68] Ozsdolay B, Balasubramanian K, Gall D. Cation and anion vacancies in cubic molybdenum nitride. J Alloys Compd 2017;705:631–7.
[69] Ozsdolay B, et al. Cubic β-WNx layers: growth and properties vs N-to-W ratio. Surf Coating Technol 2016;304:98–107.
[70] Rissanen L, et al. The new cubic iron-nitride phase FeN prepared by reactive magnetron sputtering. J Alloys Compd 1998;274(1–2):74–82.
[71] Pescosolido BA, Perry BL, Krendl AC. Empowering the next generation to end stigma by starting the conversation: bring change to mind and the college toolbox project. J Am Acad Child Adolesc Psychiatr 2020;59(4):519–30.
[72] Piedrahita W, et al. Evolution of physical properties in hafnium carbonitride thin films. J Alloys Compd 2017;690:485–96.
[73] Grigore E, et al. Zirconium carbonitride films deposited by combined magnetron sputtering and ion implantation (CMSII). Surf Coating Technol 2010;204(12–13):1889–92.
[74] Li Y, et al. Preparation of titanium carbonitride nanoparticles from a novel refluxing-derived precursor. Mater Lett 2009;63(22):1904–6.
[75] Abadias G, et al. *Structure, phase stability and elastic properties in the $Ti_{1-x}Zr_xN$ thin-film system: Experimental and computational studies*. Acta Mater 2012;60(15):5601–14.
[76] Ivashchenko V, Turchi P, Shevchenko V. First-principles study of elastic and stability properties of ZrC–ZrN and ZrC–TiC alloys. J Phys Condens Matter 2009;21(39):395503.
[77] Kindlund H, et al. Toughness enhancement in hard ceramic thin films by alloy design. Apl Mater 2013;1(4):042104.
[78] Povstugar I, et al. Elemental partitioning and mechanical properties of Ti-and Ta-containing Co–Al–W-base superalloys studied by atom probe tomography and nanoindentation. Acta Mater 2014;78:78–85.
[79] Kindlund H, et al. *Effect of WN content on toughness enhancement in $V_{1-x}W_xN$/MgO (001) thin films*. J Vac Sci Technol A: Vacuum, Surfaces, and Films 2014;32(3):030603.
[80] Sangiovanni D, Chirita V, Hultman L. Toughness enhancement in TiAlN-based quaternary alloys. Thin Solid Films 2012;520(11):4080–8.
[81] Edström D, et al. Elastic properties and plastic deformation of TiC-and VC-based pseudobinary alloys. Acta Mater 2018;144:376–85.
[82] Li K, Liu YQ, Cui B, Sima D, Wang D, Ye Y, Zheng Z. Nitrogen reduction to ammonia at ambient conditions using hydrochar prepared from cigarette filters as catalyst. Int J Hydrogen Energy 2020;45(41):20875–82.
[83] Zhang Y, Hu J, Zhang C, Cheung AT, Zhang Y, Liu L, Leung MK. Mo2C embedded on nitrogen-doped carbon toward electrocatalytic nitrogen reduction to ammonia under ambient conditions. Int J Hydrogen Energy 2021;46(24):13011–9.
[84] Cao N, Liu Y, Xu X, Xu Y, Wang X, Bi L. Ambient electrosynthesis of NH3 from N2 using Bi-doped CeO2 cube as electrocatalyst. Int J Hydrogen Energy 2021;46(62):31523–32.
[85] Singh S, Mohammed AK, AlHammadi AA, Shetty D, Polychronopoulou K. Hypes and hopes on the materials development strategies to produce ammonia at mild conditions. Int J Hydrogen Energy 2023.
[86] Du X, Wang K, Wang T, Guo H, Chen JS, Wang J, Li T. Constructing n-type TiO2 by Nb doping for electrocatalytic nitrate reduction to ammonia at ambient conditions. Int J Hydrogen Energy 2023;48(89):34700–39.
[87] Sveinbjörnsson A, Gunnarsdóttir AB, Creel EB, Canales CP, Zulevi B, Lyu X, Jafta CJ, Skúlason E, Serov A, Flosadóttir HD. Demonstration of no catalytical activity of Fe-N-C and Nb-N-C electrocatalysts toward nitrogen reduction using in-line quantification. SusMat 2022;2(4):476–86.
[88] Nørskov JK, et al. Origin of the overpotential for oxygen reduction at a fuel-cell cathode. J Phys Chem B 2004;108(46):17886–92.
[89] Hammer B, et al. Improved adsorption energetics within density-functional theory using revised Perdew-Burke-Ernzerhof functionals. Phys Rev B 1999;59(11):7413–21.
[90] Kresse G, Furthmüller J. Efficient iterative schemes for ab initio total-energy calculations using a plane-wave basis set. Phys Rev B 1996;54(16):11169.
[91] Blöchl PE. Projector augmented-wave method. Phys Rev B 1994;50(24):17953.

[92] Abghoui Y, et al. Enabling electrochemical reduction of nitrogen to ammonia at ambient conditions through rational catalyst design. Phys Chem Chem Phys 2015; 17(7):4909–18.
[93] Abghoui Y, Skúlason E. Electrochemical synthesis of ammonia via Mars-van Krevelen mechanism on the (111) facets of group III–VII transition metal mononitrides. Catal Today 2017;286:78–84.
[94] Abghoui Y, Skúlason E. Computational predictions of catalytic activity of zincblende (110) surfaces of metal nitrides for electrochemical ammonia synthesis. J Phys Chem C 2017;121(11):6141–51.
[95] Henkelman G, Uberuaga BP, Jónsson H. A climbing image nudged elastic band method for finding saddle points and minimum energy paths. J Chem Phys 2000; 113(22):9901–4.
[96] Bagger A, Arán-Ais RM, Halldin Stenlid J, Campos dos Santos E, Arnarson L, Degn Jensen K, Escudero-Escribano M, Roldan Cuenya B, Rossmeisl J. Ab initio cyclic voltammetry on Cu (111), Cu (100) and Cu (110) in acidic, neutral and alkaline solutions. ChemPhysChem 2019;20(22):3096–105.
[97] Nørskov JK, Studt F, Abild-Pedersen F, Bligaard T. Fundamental concepts in heterogeneous catalysis. John Wiley & Sons; 2014.
[98] Tursun M, Wu C. No electroreduction by transition metal dichalcogenides with chalcogen vacancies. Chemelectrochem 2021;8(16):3113–22.
[99] Urrego-Ortiz R, Builes S, Calle-Vallejo F. Fast correction of errors in the DFT-calculated energies of gaseous nitrogen-containing species. ChemCatChem 2021; 13(10):2508–16.
[100] Höskuldsson ÁB, Tayyebi E, Skúlason E. Computational examination of the kinetics of electrochemical nitrogen reduction and hydrogen evolution on a tungsten electrode. J Catal 2021;404:362–70.
[101] Rossmeisl J, et al. Electrolysis of water on oxide surfaces. J Electroanal Chem 2007;607(1–2):83–9.

Are (100) Facets of Transition Metal Carbonitrides Suitable as Electrocatalysts for Nitrogen Reduction to Ammonia at Ambient Conditions?

-Electronic supplementary information

Authors: Atef Iqbal, Egill Skulason, Younes Abghoui

Zero-point energy and entropy corrections

Zero-point energy (ZPE) and entropy corrections were discovered for all the adsorbed species by calculating vibrational normal modes with DFT. The values for the correction terms were considered to be reliant on the structure as opposed to the atomic species. The computed correction values were obtained for the [100] VCN surface and then applied to each analyzed surface.

Table S1: The ZPE and entropy correction values for all of the used adsorbed and gas phase species. The values for the adsorbed species were calculated on the [100] VCN surface, and gas phase values were taken from ref [1]. For the adsorbed species, denoted by *, adsorption onto the surface is differentiated from adsorption into a vacancy by the ^{vac} notation.

[100] TMCN surfaces	ZPE (eV)	TΔS (eV)
NH_3 (g)	0.89	0.74
H_2 (g)	0.27	0.41
CH_4 (g)	0.82	0.57
N_2 (g)	0.15	0.6
*N	0.10	0.025
*NH	0.29	0.007
*NH_2	0.70	0.063
*NH_3	0.98	0.169
*N_2^{vac}	0.13	0.077
*NNH vac	0.50	0.077
*NNH2 vac	0.74	0.103
*$2N^{vac}$	0.12	0.099
*$N.NH^{vac}$	0.44	0.105
*$N.NH_2^{vac}$	0.71	0.123
*H^{vac}	0.14	0.016
*CH	0.23	0.019
*CH_2	0.63	0.092
*CH_3	0.89	0.090
*OH^-	0.31	0.040
*O^{2-}	0.07	004
*$OH^{- vac}$	0.31	0.079
*$O^{2- vac}$	0.06	0.057
*N2	0.18	0.189
*NNH	0.52	0.057
*NNH2	0.70	0.078

Table S2 shows the lattice constants of all the TMCN.

TMCN	VCN	NbCN	WCN	ZrCN	HfCN	TaCN	TiCN	MoCN	CrCN	ScCN	YCN
a (Å)	5.82	6.28	5.99	6.58	6.48	6.25	6.05	6.14	5.82	6.46	7.01
b (Å)	5.82	6.28	5.99	6.58	6.48	6.25	6.05	6.14	5.82	6.46	7.01

Table S3 shows the adsorption free energies [eV] of VCN and NbCN through MVK.

system	CH*	CH*	NH*	NH_2*	NH_3*	N_2*	NNH*	NNH_2*	NNH_3*
VCN at U = 0	0.13	0.23	0.49	0.76	0.36	0.14	-0.49	-0.38	-0.40
VCN at U = -0.52 V	3.77	3.35	3.09	2.84	1.92	1.70	0.54	0.13	-0.40
NbCN at U = 0	0.16	0.25	0.55	0.78	0.37	-0.53	-0.86	-0.32	-0.32
NbCN at U = -0.53 V	3.87	3.59	3.45	3.45	2.75	0.90	-0.33	-0.66	-0.65

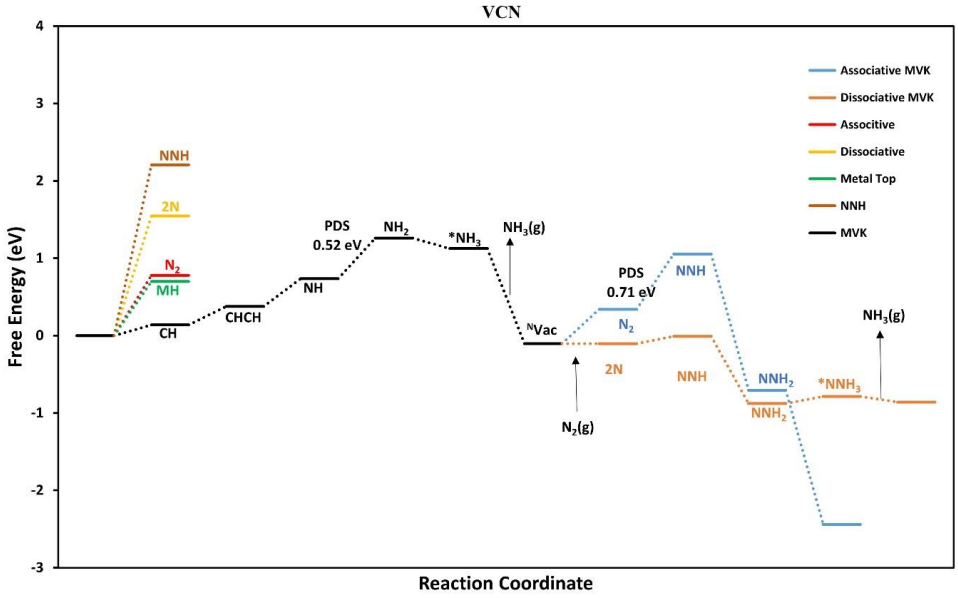

Figure S1 Shows all the possible pathways for VCN

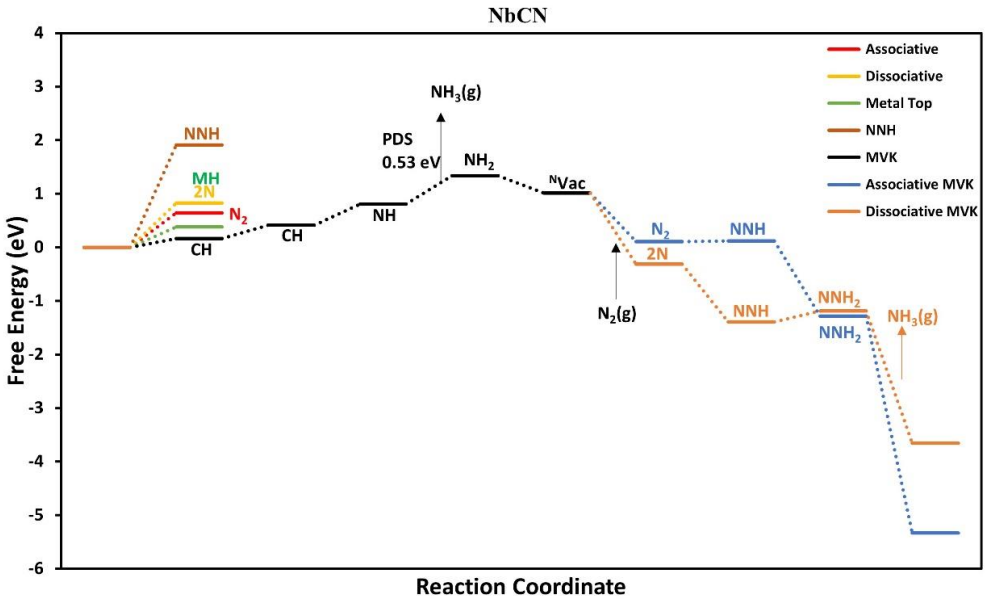

Figure S2 Shows all the possible pathways for NbCN

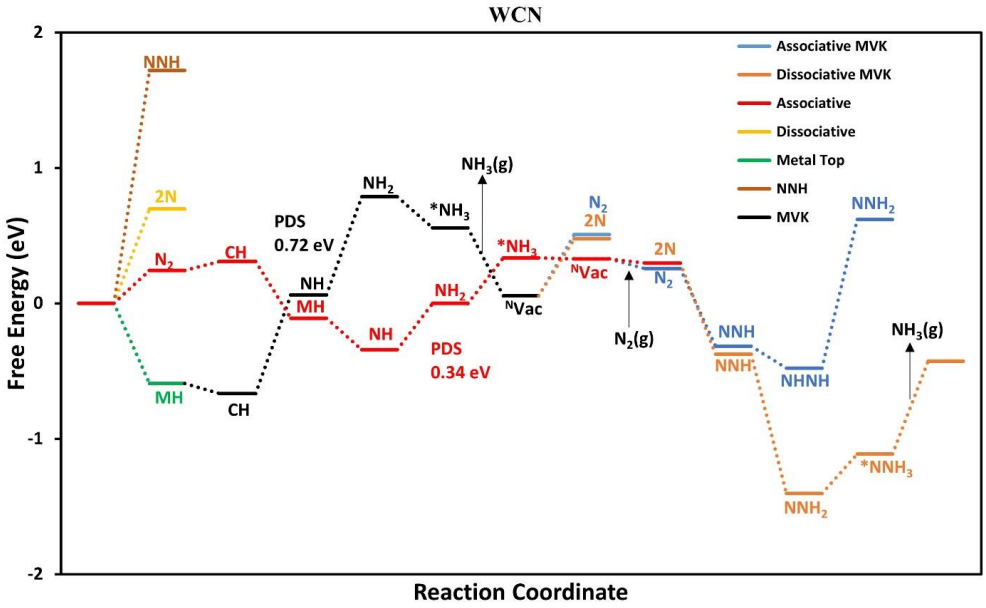

Figure S3 Shows all the possible pathways for WCN

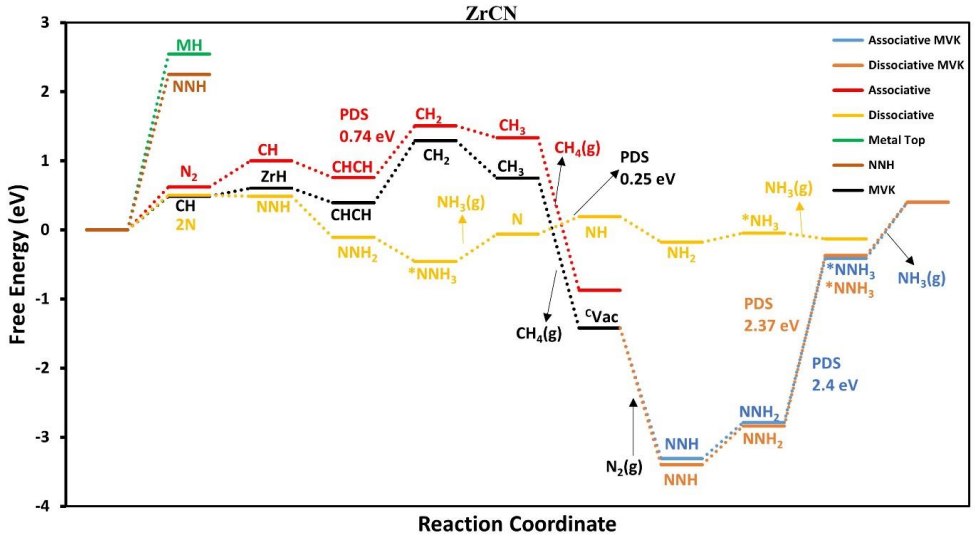

Figure S4 Shows all the possible pathways for ZrCN

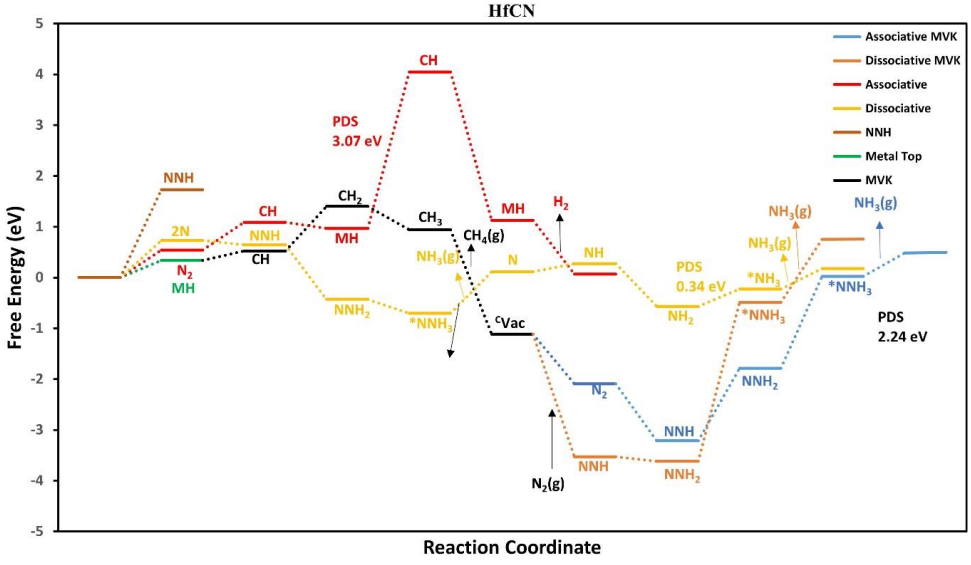

Figure S5 Shows all the possible pathways for HfCN

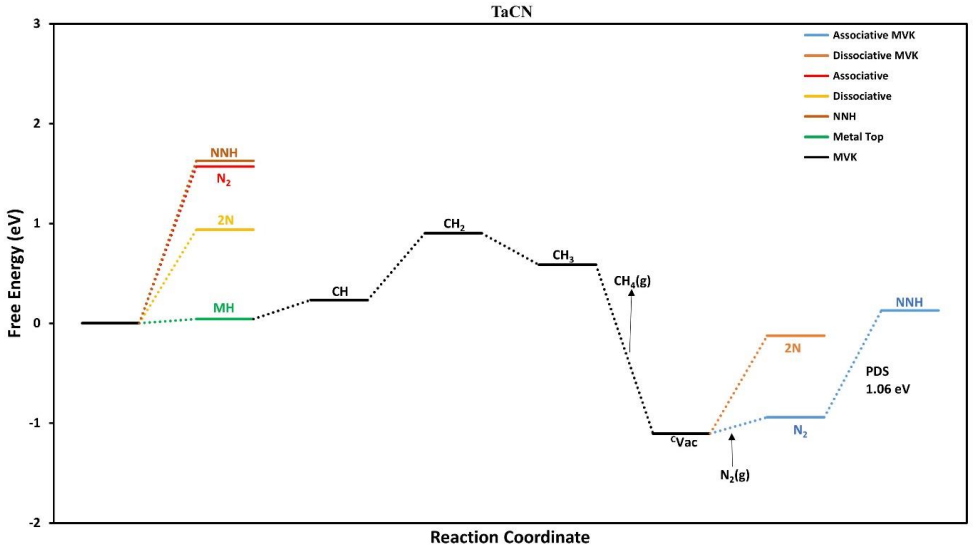

Figure S6 Shows all the possible pathways for TaCN

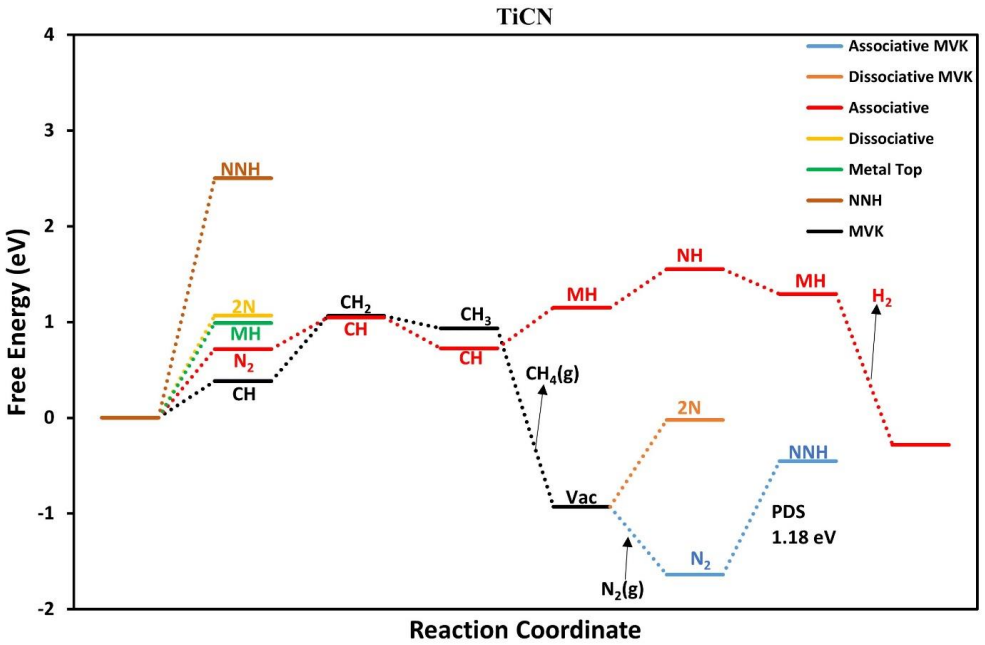

Figure S7 Shows all the possible pathways for TiCN

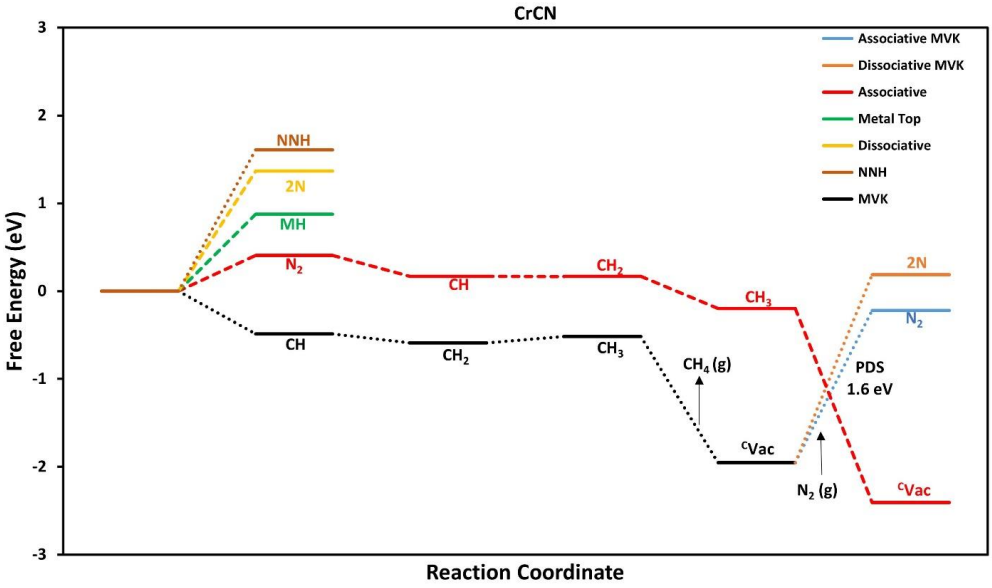

Figure S8 Shows all the possible pathways for CrCN

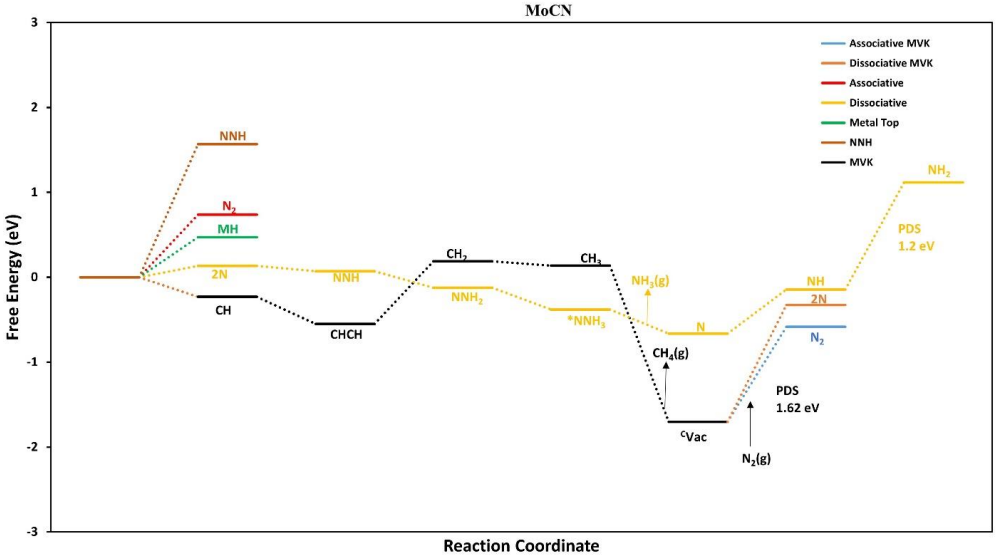

Figure S9 Shows all the possible pathways for MoCN

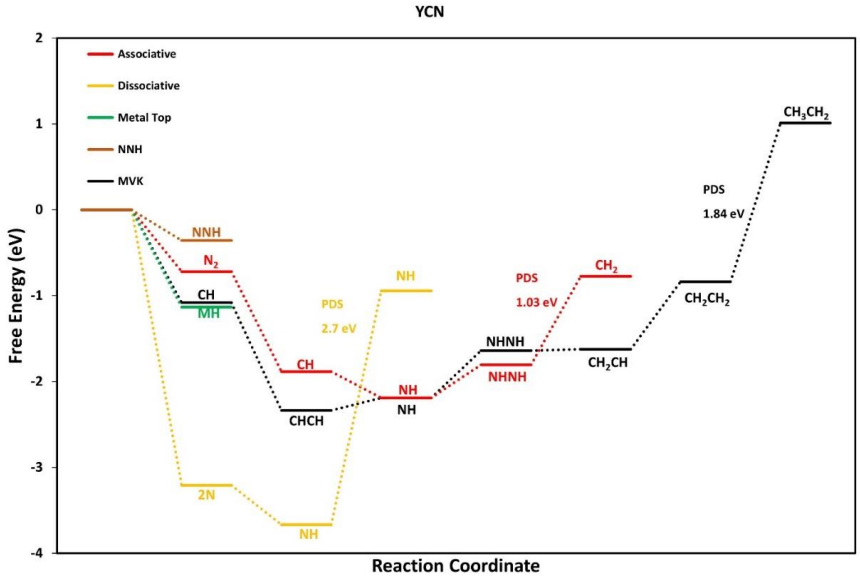

Figure S10 Shows all the possible pathways for YCN

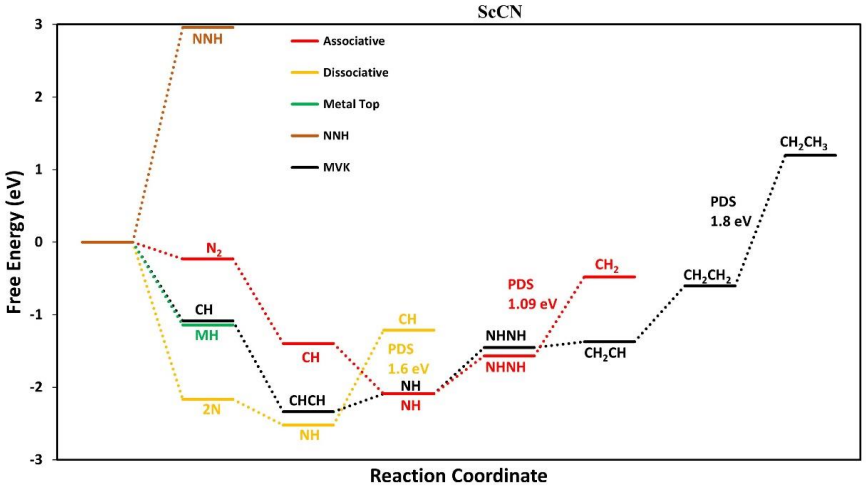

Figure S11 Shows all the possible pathways for ScCN

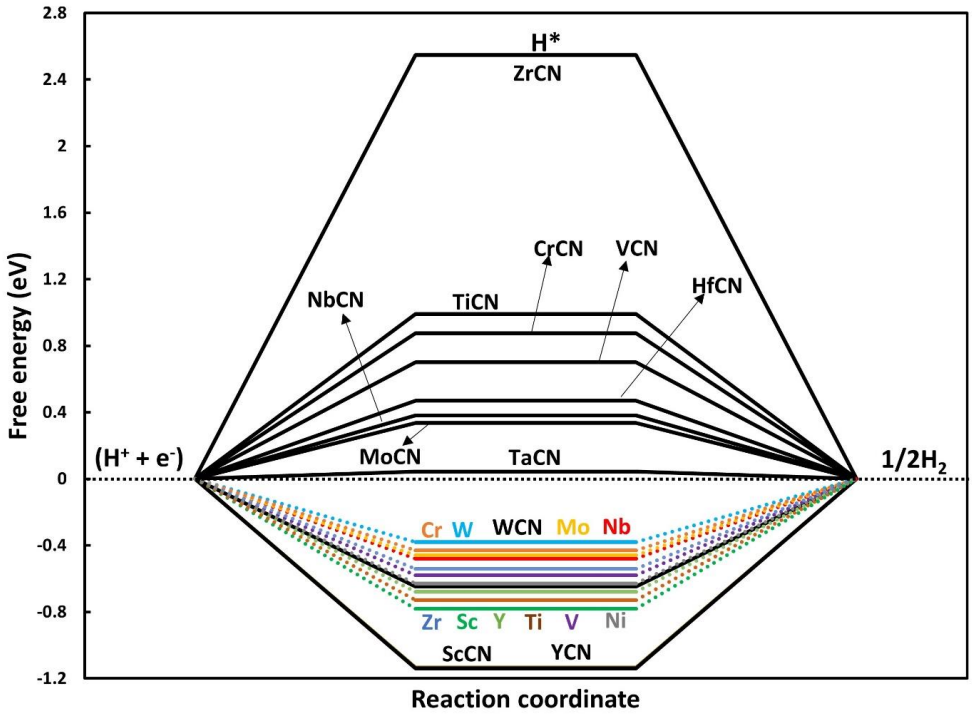

Figure S12: Free-energy diagram of hydrogen evolution activity on transition metal carbonitrides (black lines) and in comparison, with pure metals (colors).[2] Pure metals are represented by their respective color codes.

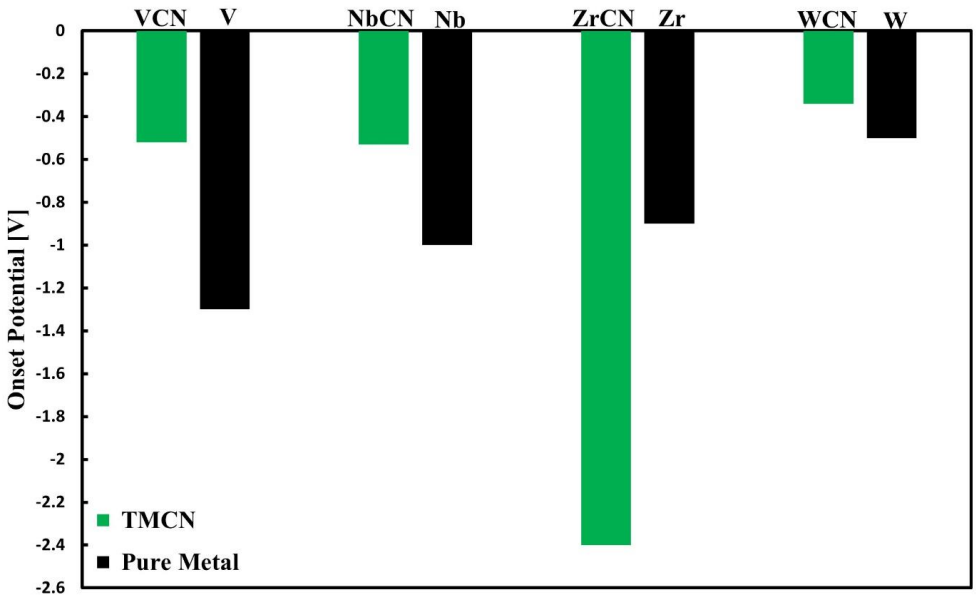

Figure S13. Comparison of the predicted onset potentials for NRR on the surface of transition metal carbonitrides and their pure metallic [2] counterparts. As shown, these TMCNs are expected to be more NRR-active than their metallic parents except ZrCN.

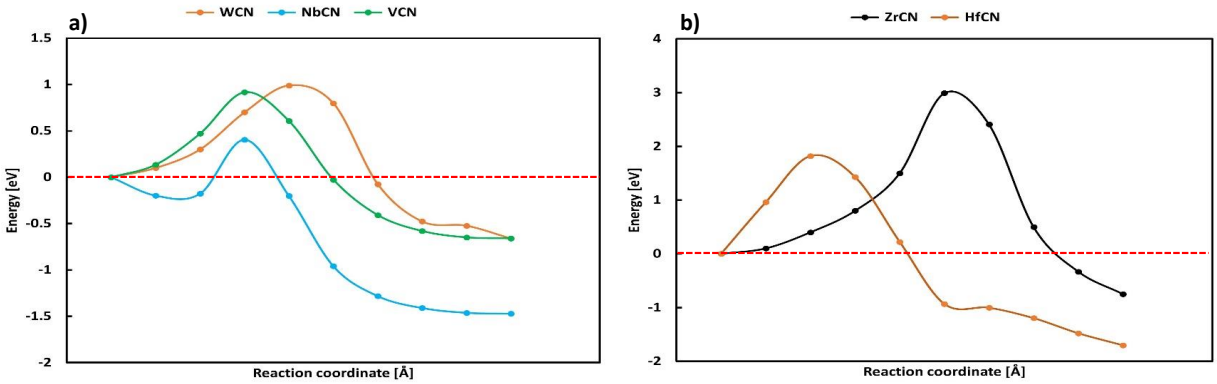

Figure S14: (a) The minimum energy path (MEP) for dissociative N_2 on WCN, NbCN, and VCN in the presence of a vacancy and (b) onto ZrCN, and HfCN (without a vacancy). The MEPs are represented for each material in its respective color.

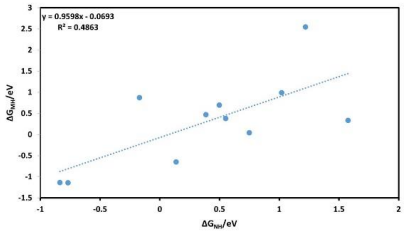
y = 0.9598x - 0.0693
R² = 0.4863
ΔG_NNH/eV
ΔG_NH/eV

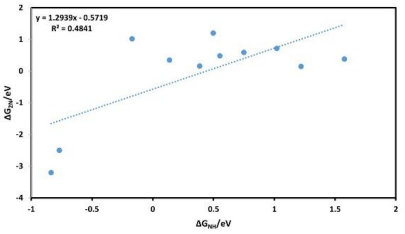
y = 1.2939x - 0.5719
R² = 0.4841
ΔG_NH2/eV
ΔG_NH/eV

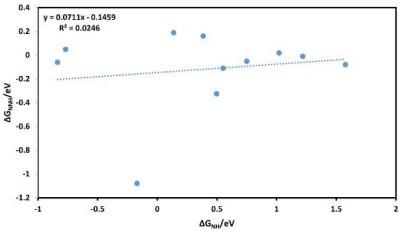
y = 0.0711x - 0.1459
R² = 0.0246
ΔG_NNH2/eV
ΔG_NH/eV

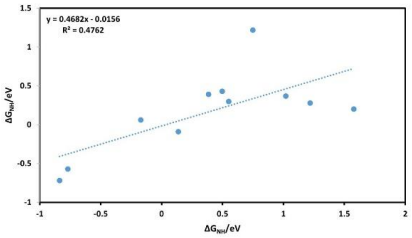
y = 0.4682x - 0.0156
R² = 0.4762
ΔG_NH/eV
ΔG_NH/eV

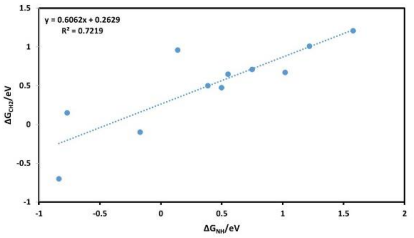
y = 0.6062x + 0.2629
R² = 0.7219
ΔG_OH/eV
ΔG_NH/eV

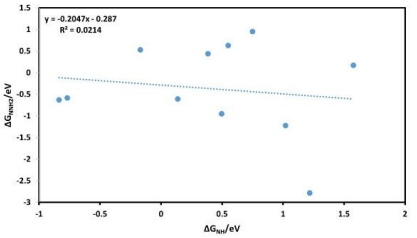
y = -0.2047x - 0.287
R² = 0.0214
ΔG_NNH2/eV
ΔG_NH/eV

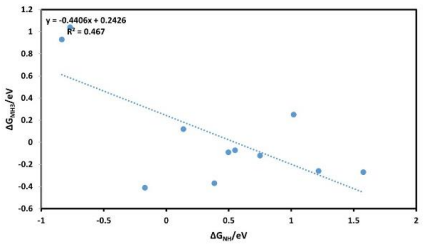
y = -0.4406x + 0.2426
R² = 0.467
ΔG_NH3/eV
ΔG_NH/eV

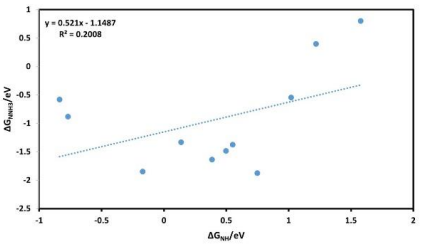
y = 0.521x - 1.1487
R² = 0.2008
ΔG_NH3/eV
ΔG_NH/eV

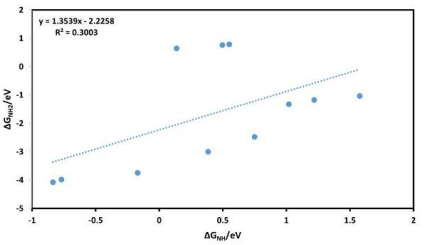
y = 1.3539x - 2.2258
R² = 0.3003
ΔG_NH3/eV
ΔG_NH/eV

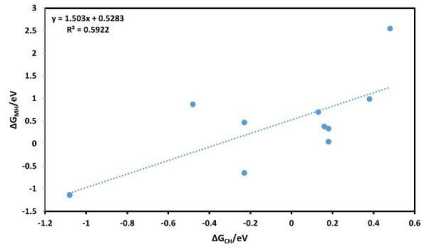
y = 1.503x + 0.5283
R² = 0.5922
ΔG_NH/eV
ΔG_OH/eV

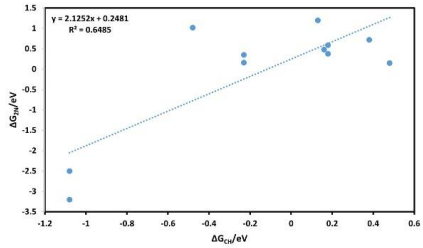
y = 2.1252x + 0.2481
R² = 0.6485
ΔG_OH/eV
ΔG_OH/eV

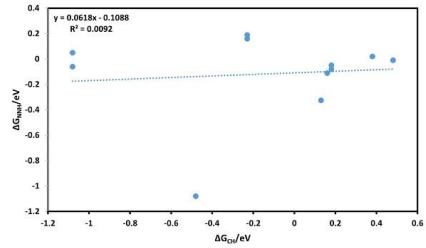
y = 0.0618x - 0.1088
R² = 0.0092
ΔG_NNH/eV
ΔG_OH/eV

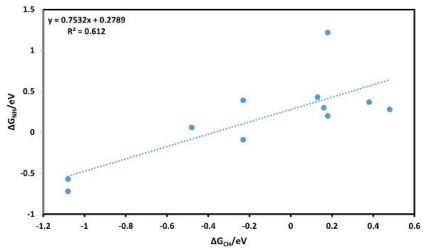
y = 0.7532x + 0.2789
R² = 0.612
ΔG_NH/eV
ΔG_OH/eV

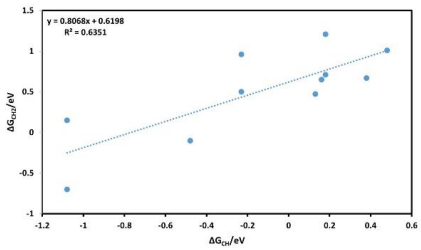
y = 0.8068x + 0.6198
R² = 0.6351
ΔG_OH/eV
ΔG_OH/eV

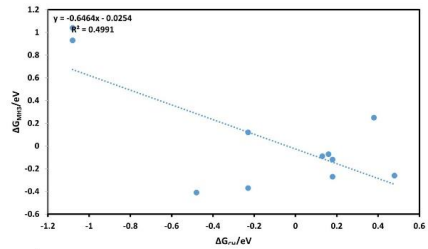
y = -0.6464x - 0.0254
R² = 0.4991
ΔG_NNH/eV
ΔG_OH/eV

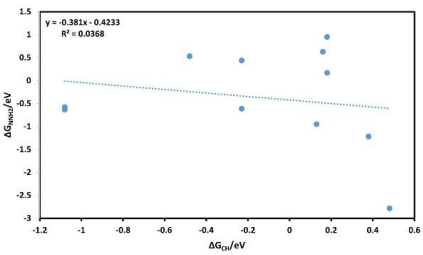
y = -0.381x - 0.4233
R² = 0.0368
ΔG_NNH2/eV
ΔG_OH/eV

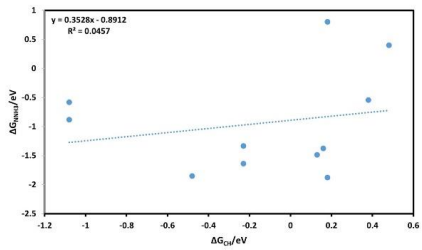
y = 0.3528x - 0.8912
R² = 0.0457
ΔG_NNH2/eV
ΔG_OH/eV

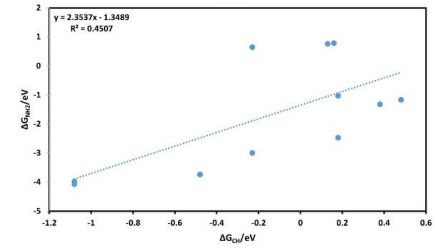
y = 2.3537x - 1.3489
R² = 0.4507
ΔG_NH2/eV
ΔG_OH/eV

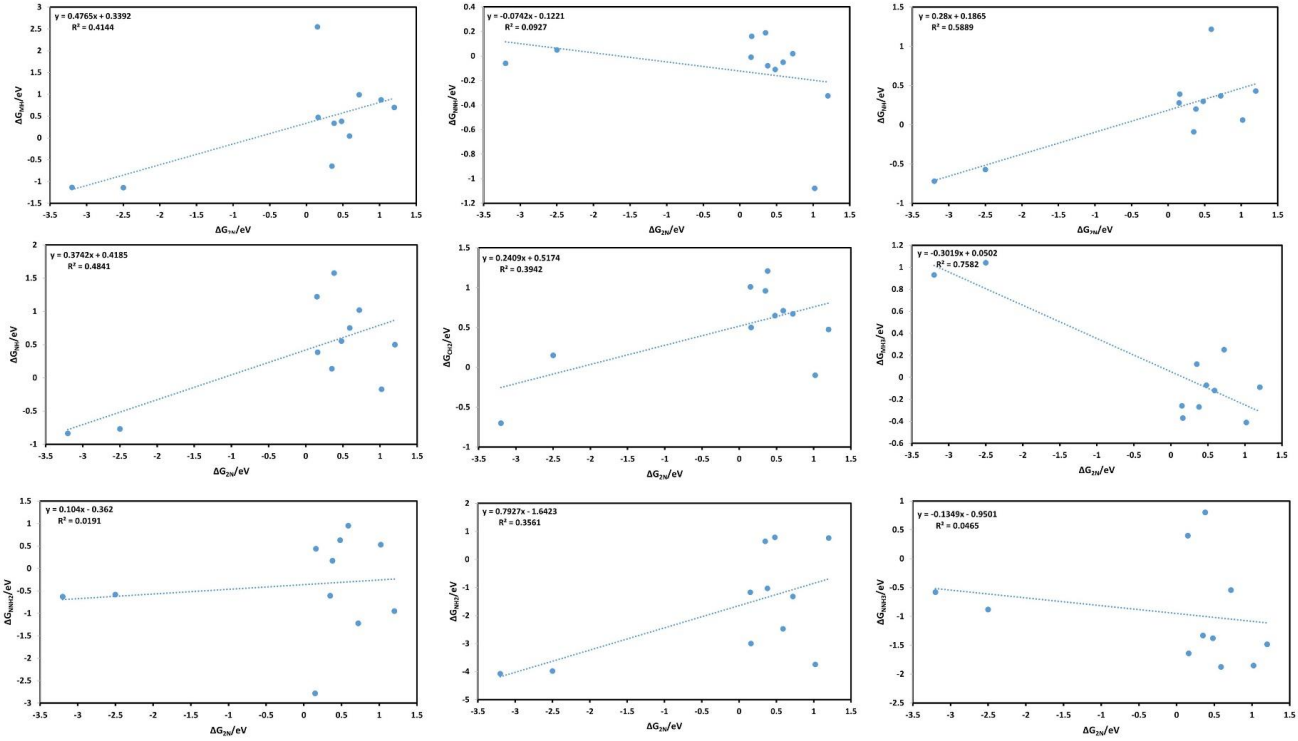

Figure S15: The figures above depict the scaling relations investigated in this study, utilizing descriptors such as *CH, *NH, and *2N. Although some of these relations are not a good fit, they are used to construct the volcano lines to guide the eye.

Electronic properties of TMCNs

Figure S16 and S17 illustrate the band structures and partial density of states (PDOS) of TMCNs. Carbonitrides of transition metals have a limited PDOS at the Fermi level, hence all of these compounds exhibit metallic characteristics. At energies between 5 and 0 eV, it consists mostly of p–d hybridization of N-p and C-p with Metal-d. Thus, covalent bonds are established between metal atoms and N or C atoms, which contribute to the material's incompressibility, hardness, and shear strength. C-p, N-p, and orbital Metal-d produced ionic bonds above the Fermi level. C, N, and metal atoms have two potential electron transport routes [27]. One refers to p–d hybridized covalent bonding between carbon or nitrogen atoms and metal atoms, in which electrons are transferred from metal to carbon or nitrogen atoms. The conductivity of these carbonitrides depends on a significant number of electrons in metal atoms due to the metallic or covalent bonding induced by metal atoms. The positive overlap populations of C–M and N–M links indicate the existence of covalent connections between nitrogen or carbon atoms and metal atoms.

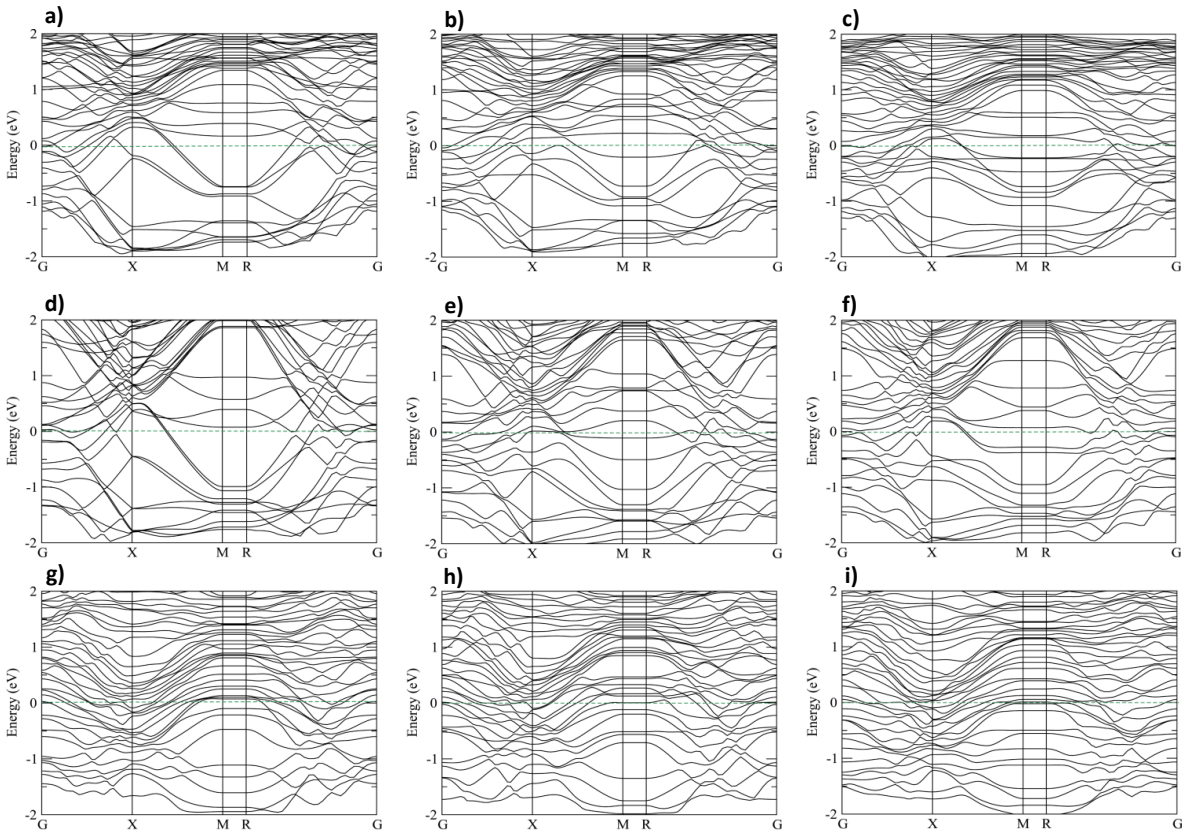

Figure S16: shows the band structure of clean, nitrogen vacancy, N_2 adsorption in nitrogen-vacancy of VCN (a) (b) (c), NbCN (d) (e) (f), WCN (g) (h) (i). The horizontal dashed line indicates the Fermi energy.

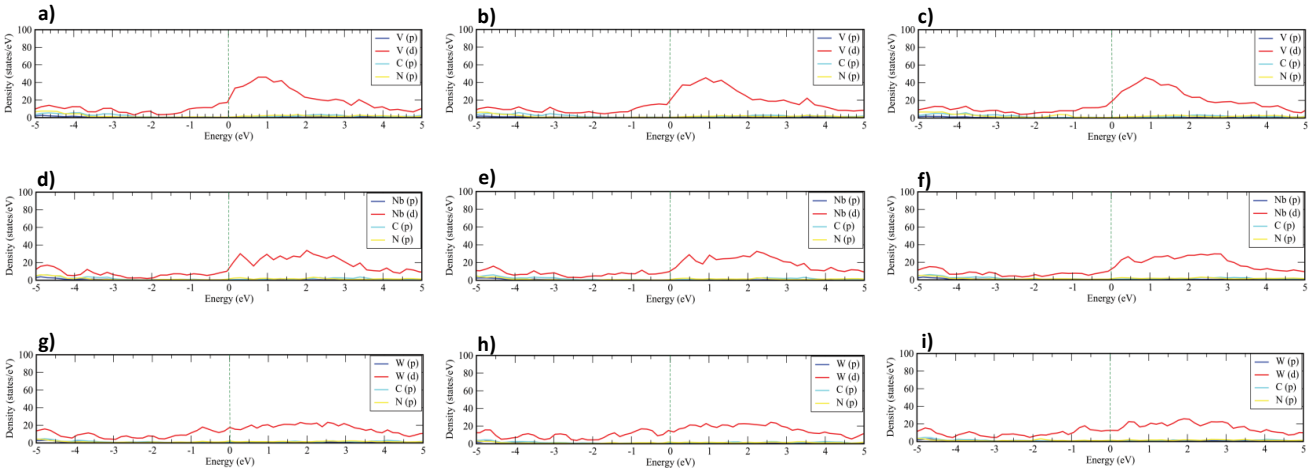

Figure S17: shows the partial density of state (PDOS) of clean, nitrogen vacancy, N_2 adsorption in nitrogen-vacancy of VCN (a) (b) (c), NbCN (d) (e) (f), WCN (g) (h) (i). The vertical dashed line indicates the Fermi energy.

The optimized coordinates for the most promising material VCN reported in this work are now provided below:

V N C
1.00000000000000
5.8293374101345865 0.0065571992961559 0.0011262042234723
0.0065495026666190 5.8286149340491118 0.0020226429541500
0.0041023398254764 0.0073882086794221 21.5779981704560733
V N C
20 10 10
Selective dynamics
Direct
0.0218654509633538 0.9668763998910860 0.1239199443669039 F F F
0.0216822288330379 0.9677804349450756 0.4987269825482828 T T T
0.5567899648606058 0.5016056063032797 0.1239924107167099 F F F
0.5543611834998371 0.5004446824953164 0.4988045445989259 T T T
0.5255554410705114 0.4709597524576060 0.3111752710670819 T T T
0.0520139714153678 -0.0021837774245068 0.3114566234042226 T T T
0.7952190682018964 0.2388534769358657 0.2158185710997035 F F F
0.2839949183396585 0.7285783121042130 0.2158345594550471 F F F
0.2908056963123454 0.7367415095096662 0.4068725928032824 T T T
0.7852398943253143 0.2322239204457455 0.4068519025507968 T T T

0.2831911511809935 0.2396596313120298 0.2149478404431165 F F F
0.7944156816423558 0.7291271874736651 0.2106795270443627 F F F
0.7856812610143717 0.7361543876935056 0.4115350938867108 T T T
0.2907888896776144 0.2319096449364655 0.4082149633927615 T T T
0.0528682668344658 0.4708465560061725 0.1224071951900928 F F F
0.0517645879511728 0.4702784545761368 0.4996369753289359 T T T
0.5252426863402002 0.9983308170338816 0.1237246889494658 F F F
0.5246480102097899 0.9975966112988419 0.5001899298675180 T T T
0.5483113418273270 0.9745883951243387 0.3098330996793784 T T T
0.0290210803858008 0.4941416065552286 0.3130077466178915 T T T
0.2890731077755503 0.2347822378144289 0.1166303231553272 F F F
0.2882162670944374 0.2339059724747761 0.5064054194477129 T T T
0.7889692019101417 0.7346514955932907 0.1127809288512084 F F F
0.7878481401256616 0.7342405545647860 0.5095755722425785 T T T
0.7888575391760708 0.7345365096437346 0.3113156814059166 T T T
0.2889417213242161 0.2344473282696644 0.3115110351731758 T T T
0.0378692312611051 0.9827214623075605 0.2142909955854577 F F F
0.5404173674496002 0.4852803426644172 0.2142329707910235 F F F
0.5390898152890631 0.4855978470181555 0.4085384839546952 T T T
0.0364903043277461 0.9831516535270117 0.4085423002717983 T T T
0.0390458448143107 0.4842762401247434 0.2142504900932209 F F F
0.5387512475515465 0.9845671897730103 0.2134589317751221 F F F
0.5379913713667701 0.9845092351629054 0.4089422354392104 T T T
0.0386579398604508 0.4838391951079152 0.4093820160172701 T T T
0.7892899101817790 0.2342090993777649 0.1108624964086504 F F F
0.7880177104696375 0.2341114613484917 0.5122157188803430 T T T
0.2894139005060339 0.7344227858291745 0.1108931834197195 F F F
0.2879789265155085 0.7340766739281529 0.5121958351732022 T T T
0.2888143003909897 0.7343913184180687 0.3114012538927560 T T T
0.7886763774176736 0.2342448206953180 0.3113921775609909 T T T

V N C H
1.00000000000000
5.8293374101345865 0.0065571992961559 0.0011262042234723
0.0065495026666190 5.8286149340491118 0.0020226429541500
0.0041023398254764 0.0073882086794221 21.5779981704560733
V N C H
20 10 10 1
Selective dynamics
Direct
0.0218654509633538 0.9668763998910874 0.1239199443669046 F F F
0.0237697153080301 0.9747117744715170 0.4989370035094572 T T T
0.5567899648606058 0.5016056063032797 0.1239924107167099 F F F
0.5526879216390618 0.4933952711825683 0.4989608612407719 T T T
0.5266381565293591 0.4704186251513964 0.3109760389401015 T T T
0.0512238857560980 0.9981069963831889 0.3112271887068630 T T T
0.7952190682018985 0.2388534769358657 0.2158185710997046 F F F
0.2839949183396585 0.7285783121042181 0.2158345594550472 F F F

0.2904792201606983 0.7361067976896110 0.4033997920752176 T T T
0.7858334016889288 0.2322856797632531 0.4067882531811348 T T T
0.2831911511809935 0.2396596313120298 0.2149478404431165 F F F
0.7944156816423558 0.7291271874736651 0.2106795270443627 F F F
0.7862780078380264 0.7359103926373443 0.4121395747282211 T T T
0.2905424743027929 0.2320404328848591 0.4096217463345125 T T T
0.0528682668344658 0.4708465560061725 0.1224071951900935 F F F
0.0458943054240020 0.4715559626897453 0.5001420563795931 T T T
0.5252426863402002 0.9983308170338816 0.1237246889494661 F F F
0.5311282289470382 0.9966704891486403 0.5005632369805579 T T T
0.5494952453613912 0.9755587581256649 0.3097676110399841 T T T
0.0280263380375678 0.4929908634944171 0.3128344468533334 T T T
0.2890731077755503 0.2347822378144300 0.1166303231553272 F F F
0.2879932168167569 0.2340329871734272 0.5080773101843618 T T T
0.7889692019101417 0.7346514955932907 0.1127809288512090 F F F
0.7878707076642820 0.7344352201725343 0.5102760658102616 T T T
0.7889009548535529 0.7344548650764570 0.3114172002915781 T T T
0.2890696885544078 0.2341465653077862 0.3120881354303026 T T T
0.0378692312611053 0.9827214623075651 0.2142909955854577 F F F
0.5404173674496033 0.4852803426644172 0.2142329707910235 F F F
0.5383634209248980 0.4857912839256745 0.4086245870200889 T T T
0.0376740766523640 0.9828875741699443 0.4086719881861676 T T T
0.0390458448143107 0.4842762401247455 0.2142504900932209 F F F
0.5387512475515507 0.9845671897730103 0.2134589317751221 F F F
0.5379138051091472 0.9835749641778762 0.4092729735768029 T T T
0.0389040057675178 0.4846884252079784 0.4097881860141862 T T T
0.7892899101817790 0.2342090993777657 0.1108624964086509 F F F
0.7881377139357220 0.2340299764927158 0.5116209033190092 T T T
0.2894139005060339 0.7344227858291745 0.1108931834197195 F F F
0.2881101571479892 0.7339108100124878 0.5303985764783180 T T T
0.2889840416340645 0.7343214081082754 0.3114376518295716 T T T
0.7887844395609203 0.2340738679155108 0.3116593031868885 T T T
0.2898353892235309 0.7343082234535055 0.5822659580505282 T T T

V N C H
1.00000000000000
5.8293374101345865 0.0065571992961559 0.0011262042234723
0.0065495026666190 5.8286149340491118 0.0020226429541500
0.0041023398254764 0.0073882086794221 21.5779981704560733
V N C H
20 10 10 2
Selective dynamics
Direct
0.0218654509633538 0.9668763998910874 0.1239199443669046 F F F
0.0318033373437947 0.9758814121852762 0.4988620225910083 T T T
0.5567899648606058 0.5016056063032797 0.1239924107167099 F F F
0.5447962651028457 0.4922461222147601 0.4989630807656121 T T T
0.5274052079038233 0.4725977928743706 0.3113898542043417 T T T

0.0500272838283265 0.9957756643668353 0.3118804646974874 T T T
0.7952190682018985 0.2388534769358657 0.2158185710997046 F F F
0.2839949183396585 0.7285783121042252 0.2158345594550472 F F F
0.2912905155436304 0.7371036445228213 0.4039193220218136 T T T
0.7846880486782514 0.2321562348176835 0.4038318219432869 T T T
0.2831911511809935 0.2396596313120298 0.2149478404431165 F F F
0.7944156816423558 0.7291271874736651 0.2106795270443627 F F F
0.7849977066404672 0.7368942928367820 0.4116704630065065 T T T
0.2917794841027219 0.2315787413451309 0.4102031139261444 T T T
0.0528682668344658 0.4708465560061725 0.1224071951900935 F F F
0.0450752667665621 0.4781999236583538 0.5002141037011617 T T T
0.5252426863402002 0.9983308170338816 0.1237246889494661 F F F
0.5310226448183387 0.9900172988947707 0.5008511495164544 T T T
0.5474245487283393 0.9755040557776183 0.3096730605737086 T T T
0.0300773736321880 0.4929706616739977 0.3134125574574179 T T T
0.2890731077755503 0.2347822378144300 0.1166303231553272 F F F
0.2876396900831756 0.2344538686827002 0.5092961850185982 T T T
0.7889692019101417 0.7346514955932907 0.1127809288512090 F F F
0.7880161838243075 0.7345717729248136 0.5103410275055854 T T T
0.7888450081436245 0.7344903069626403 0.3113992631699451 T T T
0.2887444855518108 0.2342186281044648 0.3124219846617337 T T T
0.0378692312611053 0.9827214623075723 0.2142909955854577 F F F
0.5404173674496104 0.4852803426644172 0.2142329707910235 F F F
0.5382673224767869 0.4852145542975005 0.4086760141520879 T T T
0.0373544931332724 0.9843435632606174 0.4088313787408074 T T T
0.0390458448143107 0.4842762401247455 0.2142504900932209 F F F
0.5387512475515581 0.9845671897730103 0.2134589317751221 F F F
0.5385946430514021 0.9840541427141117 0.4092087972238694 T T T
0.0378175280225222 0.4847833280832405 0.4100313274643827 T T T
0.7892899101817790 0.2342090993777657 0.1108624964086509 F F F
0.7877925331324928 0.2338874791007368 0.5283170258667249 T T T
0.2894139005060339 0.7344227858291745 0.1108931834197195 F F F
0.2883124588204288 0.7342079746395421 0.5297587500327784 T T T
0.2889055408819841 0.7344586951318434 0.3118517824403333 T T T
0.7885275943526237 0.2341508701026027 0.3118536967957285 T T T
0.2874609776787003 0.7314851457172463 0.5818325018641229 T T T
0.7903055249583142 0.2335925144382651 0.5803835242227765 T T T

V N C H
1.00000000000000
5.8293374101345865 0.0065571992961559 0.0011262042234723
0.0065495026666190 5.8286149340491118 0.0020226429541500
0.0041023398254764 0.0073882086794221 21.5779981704560733
V N C H
20 10 10 3
Selective dynamics
Direct
0.0218654509633538 0.9668763998910874 0.1239199443669048 F F F

0.0399266546925958 0.9849791365827202 0.4987129880080235 T T T
0.5567899648606058 0.5016056063032797 0.1239924107167099 F F F
0.5375984821873444 0.4831351788848672 0.4988022207969802 T T T
0.5328754450530875 0.4781976887463050 0.3129350001459590 T T T
0.0447979561268896 0.9898786259390074 0.3135086001633425 T T T
0.7952190682018985 0.2388534769358657 0.2158185710997052 F F F
0.2839949183396585 0.7285783121042346 0.2158345594550472 F F F
0.2911908744019912 0.7362185714959688 0.4041490748954661 T T T
0.7856382310082967 0.2323159087926454 0.4041594252824944 T T T
0.2831911511809935 0.2396596313120298 0.2149478404431165 F F F
0.7944156816423558 0.7291271874736651 0.2106795270443627 F F F
0.7863252209702650 0.7356395790672762 0.4039260181197665 T T T
0.2918171294089352 0.2315033735800500 0.4090119007965837 T T T
0.0528682668344658 0.4708465560061725 0.1224071951900939 F F F
0.0423349516869141 0.4805438864270046 0.5003113735127431 T T T
0.5252426863402002 0.9983308170338816 0.1237246889494661 F F F
0.5347943470697765 0.9876317320358493 0.5009200712245612 T T T
0.5408500813739295 0.9822996323891384 0.3104754640286462 T T T
0.0365453359681436 0.4863492705225920 0.3134218309804121 T T T
0.2890731077755503 0.2347822378144300 0.1166303231553272 F F F
0.2886842728106263 0.2342334116787570 0.5073525727553537 T T T
0.7889692019101417 0.7346514955932907 0.1127809288512093 F F F
0.7888062159619998 0.7340767764751704 0.5299139983530889 T T T
0.7888712098441707 0.7344343575598672 0.3110278484446797 T T T
0.2888849948611755 0.2341564296412468 0.3120863403689612 T T T
0.0378692312611053 0.9827214623075814 0.2142909955854583 F F F
0.5404173674496190 0.4852803426644172 0.2142329707910235 F F F
0.5388418787404591 0.4851074332188873 0.4092704454653654 T T T
0.0373646390476049 0.9834823575422987 0.4093821753489063 T T T
0.0390458448143108 0.4842762401247465 0.2142504900932209 F F F
0.5387512475515669 0.9845671897730103 0.2134589317751221 F F F
0.5402343839082645 0.9824466959608830 0.4099522596007108 T T T
0.0373326703195843 0.4853096884275764 0.4104282290933309 T T T
0.7892899101817790 0.2342090993777657 0.1108624964086512 F F F
0.7885717081762355 0.2338520020895159 0.5287815323469430 T T T
0.2894139005060339 0.7344227858291745 0.1108931834197195 F F F
0.2887476205608719 0.7340502458293423 0.5290011522091812 T T T
0.2890481224927192 0.7343859611321423 0.3120443594801114 T T T
0.7886279294768733 0.2339844581292566 0.3120507990306932 T T T
0.2879101078854829 0.7325552788256664 0.5811698670670949 T T T
0.7899159888933796 0.2339110817827224 0.5809370788156029 T T T
0.7890156658337032 0.7336091446425643 0.5779005949111411 T T T

V N C H
1.00000000000000
5.8293374101345865 0.0065571992961559 0.0011262042234723
0.0065495026666190 5.8286149340491118 0.0020226429541500
0.0041023398254764 0.0073882086794221 21.5779981704560733

V N C H
20 10 10 4
Selective dynamics
Direct
0.0218654509633538 0.9668763998910874 0.1239199443669064 F F F
0.0378884116612850 0.9889081295274470 0.5034534437429498 T T T
0.5567899648606058 0.5016056063032797 0.1239924107167099 F F F
0.5192882547486288 0.4715886571898071 0.4947852075067063 T T T
0.5378150159347955 0.4822692410520293 0.3162719229429836 T T T
0.0406564172706702 0.9854029805646702 0.3115627687302837 T T T
0.7952190682018984 0.2388534769358657 0.2158185710997079 F F F
0.2839949183396604 0.7285783121042534 0.2158345594550472 F F F
0.2883058715682661 0.7445748435520854 0.4049922471865312 T T T
0.7902870748976487 0.2239442345554456 0.4056346704886648 T T T
0.2831911511809935 0.2396596313120298 0.2149478404431165 F F F
0.7944156816423558 0.7291271874736651 0.2106795270443627 F F F
0.7914610709177210 0.7415360436988148 0.4056583634763378 T T T
0.2887934523509560 0.2253065542069367 0.4067687478173929 T T T
0.0528682668344658 0.4708465560061725 0.1224071951900958 F F F
0.0569786128819930 0.4723132715190917 0.4977800945131753 T T T
0.5252426863402002 0.9983308170338816 0.1237246889494661 F F F
0.5377789848771150 0.9895668752510020 0.5047878651175981 T T T
0.5426726945113439 0.9810278873457896 0.3104185711425324 T T T
0.0362646180481776 0.4862174544663116 0.3139075808886591 T T T
0.2890731077755503 0.2347822378144300 0.1166303231553272 F F F
0.2873113546090229 0.2233155669660298 0.5081748587108874 T T T
0.7889692019101417 0.7346514955932907 0.1127809288512106 F F F
0.7914925510877339 0.8617968920029531 0.5691674645153071 T T T
0.7887036500323268 0.7334400102549038 0.3108822459050941 T T T
0.2897532287234879 0.2336094451131791 0.3121248693026205 T T T
0.0378692312611053 0.9827214623075992 0.2142909955854634 F F F
0.5404173674496333 0.4852803426644172 0.2142329707910235 F F F
0.5397292738609135 0.4842944057206360 0.4086046443726410 T T T
0.0381084016043139 0.9822386635935525 0.4113247121868368 T T T
0.0390458448143112 0.4842762401247585 0.2142504900932209 F F F
0.5387512475515847 0.9845671897730176 0.2134589317751221 F F F
0.5412604622271163 0.9811689653100247 0.4118983703871913 T T T
0.0388290895359800 0.4842133381764987 0.4095887218905730 T T T
0.7892899101817790 0.2342090993777662 0.1108624964086525 F F F
0.7866841822914509 0.2718326801051276 0.5258621039879547 T T T
0.2894139005060339 0.7344227858291745 0.1108931834197195 F F F
0.2900480222204753 0.7255286462316366 0.5283227885326204 T T T
0.2894835182466226 0.7345769956928987 0.3123600901469223 T T T
0.7890820721400180 0.2327582396182912 0.3125498525058473 T T T
0.2888327178369829 0.7028038016260998 0.5801069592927763 T T T
0.7817063308934340 0.2790306106944048 0.5780041128284070 T T T
0.7955756360515639 0.9618150791888451 0.6083816447542696 T T T
0.7908841642820719 0.6958937222640527 0.5845545221059194 T T T

V N C H
1.00000000000000
5.8293374101345865 0.0065571992961559 0.0011262042234723
0.0065495026666190 5.8286149340491118 0.0020226429541500
0.0041023398254764 0.0073882086794221 21.5779981704560733
V N C H
20 10 10 5
Selective dynamics
Direct
0.0218654509633538 0.9668763998911006 0.1239199443669089 F F F
0.0493674234242796 0.9941065299549174 0.5057960267326638 T T T
0.5567899648606058 0.5016056063032797 0.1239924107167099 F F F
0.5295584494096754 0.4738411594094759 0.4945264280724150 T T T
0.5402588033541369 0.4851743340193941 0.3166861893187185 T T T
0.0401381785460526 0.9851889877501683 0.3118769081377813 T T T
0.7952190682018953 0.2388534769358691 0.2158185710997192 F F F
0.2839949183396631 0.7285783121042934 0.2158345594550472 F F F
0.2831796173392335 0.7413969507220570 0.4051284515378006 T T T
0.7949488257065537 0.2263239505553447 0.4051569038746131 T T T
0.2831911511809935 0.2396596313120298 0.2149478404431165 F F F
0.7944156816423558 0.7291271874736651 0.2106795270443627 F F F
0.7954065992627085 0.7418180383286446 0.4055516557470366 T T T
0.2802428478058552 0.2239076341202692 0.4075708287041704 T T T
0.0528682668344658 0.4708465560061725 0.1224071951900986 F F F
0.0523419202716689 0.4711590887227384 0.4994607812920742 T T T
0.5252426863402002 0.9983308170338816 0.1237246889494661 F F F
0.5268333760520048 0.9971916731170276 0.4995822582908891 T T T
0.5411009382385255 0.9819775846016339 0.3113591897053665 T T T
0.0360985795840997 0.4863874303864815 0.3132497507500720 T T T
0.2890731077755503 0.2347822378144300 0.1166303231553272 F F F
0.2881193063669954 0.2325078675001414 0.5074863496614060 T T T
0.7889692019101417 0.7346514955932907 0.1127809288512127 F F F
0.9866266553265655 0.9289385499452828 0.6123534348129158 T T T
0.7886861203403269 0.7342730266526375 0.3109590084729300 T T T
0.2896515409400811 0.2349902560654729 0.3120849246828436 T T T
0.0378692312611053 0.9827214623076366 0.2142909955854759 F F F
0.5404173674496590 0.4852803426644172 0.2142329707910235 F F F
0.5387007744997281 0.4841088305004807 0.4084262027071923 T T T
0.0367451000331800 0.9816688639946419 0.4116444953873434 T T T
0.0390458448143115 0.4842762401247734 0.2142504900932209 F F F
0.5387512475516006 0.9845671897730698 0.2134589317751294 F F F
0.5396262113330915 0.9828377548937842 0.4101948738600138 T T T
0.0376244551014168 0.4847173277169091 0.4104983723416048 T T T
0.7892899101817790 0.2342090993777702 0.1108624964086547 F F F
0.7837879183862115 0.2462499404604142 0.5269272838386748 T T T
0.2894139005060339 0.7344227858291745 0.1108931834197195 F F F
0.3018667758931733 0.7282654728590643 0.5266574299917405 T T T

0.2888448312192737 0.7345645187340124 0.3124109582241380 T T T
0.7890588590596695 0.2335967776447935 0.3124122770517948 T T T
0.3284192693160123 0.6974526316794165 0.5780104993359103 T T T
0.7535706182895218 0.2725981422949607 0.5783463344791194 T T T
0.9193367872643304 1.0663652255792277 0.6356394748824957 T T T
0.8666807879316430 0.8011839586878097 0.6134690417434908 T T T
1.1273904635531007 0.8711081939298746 0.6360574459663596 T T T

V N C H
1.00000000000000
5.8293374101345865 0.0065571992961559 0.0011262042234723
0.0065495026666190 5.8286149340491118 0.0020226429541500
0.0041023398254764 0.0073882086794221 21.5779981704560733
V N C H
20 9 10 2
Selective dynamics
Direct
0.0218654509633538 0.9668763998911102 0.1239199443669117 F F F
0.0502148816189686 0.9952439184962140 0.4978850847681887 T T T
0.5567899648606058 0.5016056063032797 0.1239924107167099 F F F
0.5277397701990798 0.4720862288165903 0.4979839710540316 T T T
0.5379145864827601 0.4830158869100590 0.3139442540660460 T T T
0.0403644770770353 0.9853224739825281 0.3140760600050302 T T T
0.7952190682018953 0.2388534769358677 0.2158185710997189 F F F
0.2839949183396664 0.7285783121043035 0.2158345594550472 F F F
0.2906302631534894 0.7356360427241546 0.4045094225951565 T T T
0.7868284545994267 0.2324454100084640 0.4044908828192029 T T T
0.2831911511809935 0.2396596313120298 0.2149478404431165 F F F
0.7944156816423558 0.7291271874736651 0.2106795270443627 F F F
0.7872299810408074 0.7354657367664087 0.4054373859141763 T T T
0.2909398548976380 0.2325041074984912 0.4075476265523744 T T T
0.0528682668344658 0.4708465560061725 0.1224071951901007 F F F
0.0499838745546714 0.4727882731847691 0.5001525012759617 T T T
0.5252426863402002 0.9983308170338816 0.1237246889494661 F F F
0.5281147224961383 0.9950058558373156 0.5005651073566088 T T T
0.5413534950101642 0.9820257509379555 0.3110031078081150 T T T
0.0364472948584335 0.4867101993244128 0.3133851402949087 T T T
0.2890731077755503 0.2347822378144300 0.1166303231553272 F F F
0.2890623750887167 0.2335501281154645 0.5065734710580609 T T T
0.7889692019101417 0.7346514955932907 0.1127809288512161 F F F
0.7889534355176965 0.7344758570130373 0.3108096597691156 T T T
0.2890832068944170 0.2342768945006114 0.3119986342769610 T T T
0.0378692312611052 0.9827214623076431 0.2142909955854810 F F F
0.5404173674496603 0.4852803426644176 0.2142329707910235 F F F
0.5393794183617734 0.4850488091697124 0.4098276619704502 T T T
0.0378489508525983 0.9836264670797867 0.4098197360346751 T T T
0.0390458448143109 0.4842762401247739 0.2142504900932209 F F F
0.5387512475516019 0.9845671897730759 0.2134589317751307 F F F

0.5401884933871444 0.9828220510302301 0.4105006313340256 T T T
0.0376489191597822 0.4852943108428332 0.4108189477464687 T T T
0.7892899101817790 0.2342090993777731 0.1108624964086581 F F F
0.7890941032293632 0.2338250242662049 0.5283053795290680 T T T
0.2894139005060339 0.7344227858291745 0.1108931834197195 F F F
0.2892593822955334 0.7336602181104712 0.5281169171807099 T T T
0.2892391054443999 0.7344497669389363 0.3122774045634754 T T T
0.7888498512509925 0.2339446262598805 0.3122655812123373 T T T
0.2916765622269811 0.7334327050352760 0.5804706304111836 T T T
0.7910249899072338 0.2353206791892579 0.5806679919890313 T T T

V N C H
1.00000000000000
5.8293374101345865 0.0065571992961559 0.0011262042234723
0.0065495026666190 5.8286149340491118 0.0020226429541500
0.0041023398254764 0.0073882086794221 21.5779981704560733
V N C H
20 11 10 3
Selective dynamics
Direct
0.0218654509633537 0.9668763998911722 0.1239199443669108 F F F
0.0251586316944213 0.9704217990414679 0.4966491757557795 T T T
0.5567899648606058 0.5016056063032797 0.1239924107167099 F F F
0.5488833558293447 0.4936665436146911 0.5386295333829786 T T T
0.5307808592140365 0.4760235368407484 0.3115946623440943 T T T
0.0395789646588676 0.9849085967728026 0.3188481678421641 T T T
0.7952190682018953 0.2388534769358791 0.2158185710997225 F F F
0.2839949183396655 0.7285783121043405 0.2158345594550472 F F F
0.2979540276642479 0.7233630034888393 0.4038807578254723 T T T
0.7762878831832396 0.2414893844697215 0.4038658041666201 T T T
0.2831911511809935 0.2396596313120298 0.2149478404431165 F F F
0.7944156816423558 0.7291271874736651 0.2106795270443627 F F F
0.7795253575471917 0.7255049942854468 0.4116588137813498 T T T
0.3009047938706987 0.2454994665893078 0.4090642383880406 T T T
0.0528682668344658 0.4708465560061725 0.1224071951901031 F F F
0.0486191612848979 0.4736939099449702 0.5014016315017951 T T T
0.5252426863402002 0.9983308170338816 0.1237246889494661 F F F
0.5289315061359418 0.9939220308409330 0.5015607325115830 T T T
0.5434634710697338 0.9772664578049144 0.3107218575490042 T T T
0.0317869896332429 0.4888199417407035 0.3131894201308018 T T T
0.2890731077755503 0.2347822378144300 0.1166303231553272 F F F
0.2969002600508532 0.2418432597282331 0.5079938076794071 T T T
0.7889692019101417 0.7346514955932907 0.1127809288512179 F F F
0.7873234110481533 0.7330068966923534 0.3106842058074930 T T T
0.2858318137808329 0.2310882192821398 0.3118139257802581 T T T
0.0378692312611055 0.9827214623076788 0.2142909955854862 F F F
0.5404173674496842 0.4852803426644176 0.2142329707910235 F F F

0.5384679593833873 0.4842537231066825 0.4087682842714097 T T T
0.0370645097337800 0.9831604831929315 0.4098895666031488 T T T
0.7809423726838650 0.7255213476403062 0.5084509530123086 T T T
0.5514584398394057 0.4958290062181052 0.6155484479717375 T T T
0.0390458448143110 0.4842762401247876 0.2142504900932209 F F F
0.5387512475516019 0.9845671897731181 0.2134589317751343 F F F
0.5368849848731836 0.9826429186960144 0.4104446665074043 T T T
0.0372227646629300 0.4822265486937729 0.4106954065531952 T T T
0.7892899101817790 0.2342090993777764 0.1108624964086598 F F F
0.8035009923010449 0.2186160825170756 0.5305524021795913 T T T
0.2894139005060339 0.7344227858291745 0.1108931834197195 F F F
0.2741048760468779 0.7482943272864803 0.5302538061791755 T T T
0.2873228624612704 0.7336161867231979 0.3123566823666183 T T T
0.7879111750572334 0.2322296499151299 0.3123259340848275 T T T
0.2412158554585573 0.7844237477971353 0.5804221361279365 T T T
0.8401015318918731 0.1862140512511463 0.5807192119250253 T T T
0.5547826389979197 0.4983123286445693 0.6628559773564234 T T T

V N C H
1.00000000000000
5.8293374101345865 0.0065571992961559 0.0011262042234723
0.0065495026666190 5.8286149340491118 0.0020226429541500
0.0041023398254764 0.0073882086794221 21.5779981704560733
V N C H
20 11 10 4
Selective dynamics
Direct
0.0218654509633537 0.9668763998912132 0.1239199443669108 F F F
0.0307522649883433 0.9764803014720698 0.4970845797898052 T T T
0.5567899648606058 0.5016056063032797 0.1239924107167099 F F F
0.5456265550405626 0.4907446697846753 0.5261561185364262 T T T
0.5325029494875868 0.4783432099372200 0.3118209174270367 T T T
0.0388760552063742 0.9847621510508033 0.3188889388592034 T T T
0.7952190682018953 0.2388534769358799 0.2158185710997284 F F F
0.2839949183396664 0.7285783121043636 0.2158345594550472 F F F
0.2990823605151253 0.7239902252384450 0.4041023376672326 T T T
0.7762013711676041 0.2434639338615826 0.4041254974113384 T T T
0.2831911511809935 0.2396596313120298 0.2149478404431165 F F F
0.7944156816423558 0.7291271874736651 0.2106795270443627 F F F
0.7815116484042931 0.7285520582240319 0.4101523291378406 T T T
0.2988695097825865 0.2438414380273712 0.4085932764339366 T T T
0.0528682668344658 0.4708465560061725 0.1224071951901093 F F F
0.0458983925139960 0.4777516565401504 0.5015199111259745 T T T
0.5252426863402002 0.9983308170338816 0.1237246889494661 F F F
0.5320052002821518 0.9913801146735157 0.5016860140653731 T T T
0.5428299289510841 0.9790379730557190 0.3111282176925574 T T T
0.0329383926150309 0.4886274536705874 0.3134014395488510 T T T
0.2890731077755503 0.2347822378144300 0.1166303231553272 F F F

0.2936407841503468 0.2391469306239996 0.5067879494228913 T T T
0.7889692019101417 0.7346514955932907 0.1127809288512173 F F F
0.7876290796751483 0.7338730260545184 0.3104331760717860 T T T
0.2861532600915213 0.2320169409910288 0.3115016831401424 T T T
0.0378692312611054 0.9827214623077024 0.2142909955854862 F F F
0.5404173674497023 0.4852803426644172 0.2142329707910235 F F F
0.5388372788946847 0.4854173117055688 0.4100254767419559 T T T
0.0380472976413864 0.9848254266138891 0.4100059257209360 T T T
0.7843046232295600 0.7297781457323710 0.5067480985804149 T T T
0.5465535030172928 0.4914079222947403 0.6140414733149395 T T T
0.0390458448143109 0.4842762401247996 0.2142504900932209 F F F
0.5387512475516024 0.9845671897731538 0.2134589317751402 F F F
0.5376780016839018 0.9838313878394120 0.4104942784499085 T T T
0.0378139427115811 0.4837337326739484 0.4107599779280348 T T T
0.7892899101817790 0.2342090993777824 0.1108624964086593 F F F
0.8029351765320457 0.2202640575032448 0.5324731221664067 T T T
0.2894139005060339 0.7344227858291745 0.1108931834197195 F F F
0.2750290199868037 0.7484073210571937 0.5323739337115544 T T T
0.2877120882955574 0.7342029535257245 0.3124351907245487 T T T
0.7879887260820594 0.2331890041844558 0.3124382463188084 T T T
0.2386455135807034 0.7848137859519464 0.5825815941592731 T T T
0.8395442404990090 0.1837228801243110 0.5826908063134777 T T T
0.4471753981884762 0.5949192758658551 0.6411996903762913 T T T
0.6523550927636061 0.3943491197338408 0.6411827313050986 T T T

V N C H
1.00000000000000
5.8293374101345865 0.0065571992961559 0.0011262042234723
0.0065495026666190 5.8286149340491118 0.0020226429541500
0.0041023398254764 0.0073882086794221 21.5779981704560733
V N C H
20 11 10 5
Selective dynamics
Direct
0.0218654509633538 0.9668763998912363 0.1239199443669108 F F F
0.0310272971141399 0.9766762483565716 0.4960373807512902 T T T
0.5567899648606058 0.5016056063032797 0.1239924107167099 F F F
0.5480100721470301 0.4935587649239760 0.5071418648158776 T T T
0.5248098186308157 0.4701795174254417 0.3089694260374285 T T T
0.0487705245748590 0.9944304133755998 0.3156951779866033 T T T
0.7952190682018953 0.2388534769358799 0.2158185710997348 F F F
0.2839949183396655 0.7285783121043750 0.2158345594550472 F F F
0.2963286808097413 0.7271201166140824 0.4043689842087587 T T T
0.7785199339072838 0.2398505690578666 0.4043911932900744 T T T
0.2831911511809935 0.2396596313120298 0.2149478404431165 F F F
0.7944156816423558 0.7291271874736651 0.2106795270443627 F F F
0.7792911976144958 0.7269408017128198 0.4130039372094169 T T T
0.2966007289286503 0.2403475695918538 0.4106850664798236 T T T

0.0528682668344658	0.4708465560061725	0.1224071951901088	F	F	F
0.0467356875530143	0.4775856079448564	0.5001711199399692	T	T	T
0.5252426863402002	0.9983308170338816	0.1237246889494661	F	F	F
0.5316128575538337	0.9925587229460598	0.5004083491849510	T	T	T
0.5474481179119848	0.9741292716983505	0.3104308974153660	T	T	T
0.0287657552921709	0.4929779395776793	0.3130717741744489	T	T	T
0.2890731077755503	0.2347822378144300	0.1166303231553272	F	F	F
0.2871052534047095	0.2332050786853737	0.5092877935753274	T	T	T
0.7889692019101417	0.7346514955932907	0.1127809288512170	F	F	F
0.7879976347743292	0.7335082531357294	0.3117298231048951	T	T	T
0.2874086147237056	0.2324419523442253	0.3124897683764234	T	T	T
0.0378692312611053	0.9827214623077137	0.2142909955854862	F	F	F
0.5404173674497146	0.4852803426644172	0.2142329707910235	F	F	F
0.5383883552443987	0.4848587846889631	0.4088012922398836	T	T	T
0.0371282979507285	0.9838005860414413	0.4082853406259949	T	T	T
0.7907962522588883	0.7367034462419790	0.5107464781304887	T	T	T
0.5473641768191740	0.4929797223720641	0.6152819987705974	T	T	T
0.0390458448143111	0.4842762401248055	0.2142504900932209	F	F	F
0.5387512475516019	0.9845671897731710	0.2134589317751466	F	F	F
0.5380968203972817	0.9831214688062988	0.4095866995797552	T	T	T
0.0372693358082684	0.4840862223631967	0.4099952719184136	T	T	T
0.7892899101817790	0.2342090993777889	0.1108624964086589	F	F	F
0.7952795629298987	0.2285055611198442	0.5285275904386924	T	T	T
0.2894139005060339	0.7344227858291745	0.1108931834197195	F	F	F
0.2830189743046010	0.7411997703062740	0.5286487619600917	T	T	T
0.2885401724947789	0.7334132929491712	0.3120738763083463	T	T	T
0.7876069760564900	0.2337615251077638	0.3120703869257738	T	T	T
0.2537436086988656	0.7737171756129814	0.5794881023720672	T	T	T
0.8294085281105521	0.1988046042783820	0.5793342007558245	T	T	T
0.3911493583485021	0.5339055276786986	0.6338233335178423	T	T	T
0.6003673303195299	0.3404972465188190	0.6338983387012992	T	T	T
0.6613569932843780	0.6164131979618835	0.6286627743024542	T	T	T

References:

[1] Che, M. and J.C. Védrine, *Characterization of solid materials and heterogeneous catalysts: From structure to surface reactivity*. 2012: John Wiley & Sons.

[2] Skulason, E., Bligaard, T., Gudmundsdóttir, S., Studt, F., Rossmeisl, J., Abild-Pedersen, F., Vegge, Jonsson. H., & Nørskov, J. K. (2012). A theoretical evaluation of possible transition metal electro-catalysts for N_2 reduction. Physical Chemistry Chemical Physics, 14(3), 1235-1245.

Paper III

Electrochemical Nitrogen Reduction to Ammonia at Ambient Condition on the (111) Facets of Transition Metal Carbonitrides

Iqbal, A., E. Skulason, and Y. Abghoui,

ChemPhysChem, DOI: 10.1002/cphc. 202300991

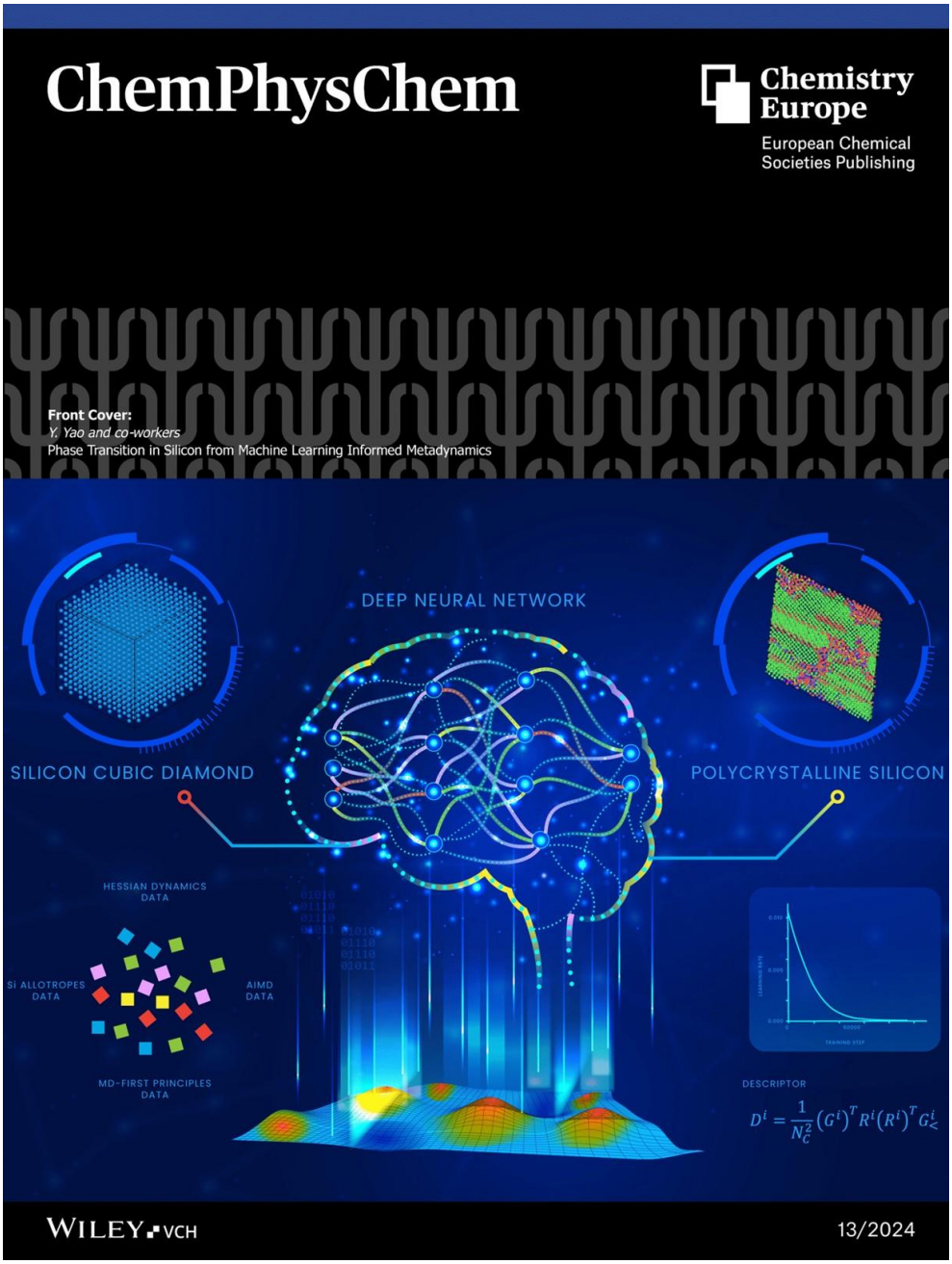
ChemPhysChem
Chemistry Europe
European Chemical Societies Publishing
Front Cover:
Y. Yao and co-workers
Phase Transition in Silicon from Machine Learning Informed Metadynamics
DEEP NEURAL NETWORK
SILICON CUBIC DIAMOND
POLYCRYSTALLINE SILICON
HESSIAN DYNAMICS DATA
Si ALLOTROPES DATA
AIMD DATA
MD-FIRST PRINCIPLES DATA
DESCRIPTOR
$D^i = \frac{1}{N_c^2}(G^i)^T R^i (R^i)^T G^i_<$
WILEY VCH
13/2024

ChemPhysChem

Research Article
doi.org/10.1002/cphc.202300991

Chemistry Europe
European Chemical Societies Publishing

www.chemphyschem.org

Electrochemical Nitrogen Reduction to Ammonia at Ambient Condition on the (111) Facets of Transition Metal Carbonitrides

Atef Iqbal,[a] Egill Skulason,*[b] and Younes Abghoui*[a]

We conducted Density Functional Theory calculations to investigate a class of materials with the goal of enabling nitrogen activation and electrochemical ammonia production under ambient conditions. The source of protons at the anode could originate from either water splitting or H_2, but our specific focus was on the cathode reaction, where nitrogen is reduced into ammonia. We examined the conventional associative mechanism, dissociative mechanism, and Mars-van Krevelen mechanism on the (111) facets of the NaCl-type structure found in early transition metal carbonitrides, including Ti, V, Cr, Zr, Nb, Mo, Hf, Ta, Sc, Y, and W. We explored the catalytic activity by calculating the free energy of all intermediates along the reaction pathway and constructing free energy diagrams to identify the steps that determine the reaction's feasibility. Additionally, we closely examined the potential for catalyst poisoning within the electrochemical environment, considering the bias required to drive the reaction. Furthermore, we assessed the likelihood of catalyst decomposition and the potential for catalyst regeneration among the most intriguing carbonitrides. Our findings revealed that the only carbonitride catalyst considered here exhibiting both activity and stability, capable of self-regeneration and nitrogen-to-ammonia activation, is NbCN with a low potential-determining step energy of 0.58 eV. This material can facilitate ammonia formation via a mixed associative-MvK mechanism. In contrast, other carbonitrides of this crystallographic orientation are likely to undergo decomposition, reverting to their parent metals under operational conditions.

1. Introduction

The conventional method of producing chemicals and fuels on an industrial scale has primarily relied on fossil feedstocks. However, these feedstocks have limited reserves and are causing environmental issues. As a result, there is a growing demand for renewable energy technologies that can generate chemicals and fuels using solar and wind energy. An illustrative example is the manufacture of ammonia (NH_3), a crucial component in agricultural N-fertilizers, through the energy-intensive Haber-Bosch process, which operates at high temperatures and pressures and consumes 3–5% of the world's natural gas output.[1] Consequently, extensive efforts have been directed towards creating technologies and processes for the sustainable production of NH_3.[2] In particular, there has been significant interest in the electrochemical reduction of N_2 to NH_3 under normal environmental conditions. This method has gained attention because it can be integrated with intermittent renewable energy sources like solar, wind, hydro, and geothermal power and has the potential for eco-friendly, decentralized NH_3 production.[3,4]

In 1909, Fritz Haber introduced a method to transform nitrogen (N_2) and hydrogen (H_2) into ammonia (NH_3), a process swiftly adapted for commercial use by Carl Bosch in 1913.[1] This innovation has played a pivotal role in the growth of the global population from two billion to over eight billion over the past century, primarily through its vital contribution to the production of nitrogen fertilizers for agriculture. Even in the present day, more than 80% of the world's population indirectly benefits from this conversion process.[5] Furthermore, ammonia holds significant promise in terms of its potential to reduce carbon emissions for several compelling reasons. Enhancing the sustainability of the massive industrial catalytic production of ammonia, which currently exceeds a few million metric tons annually and accounts for 1–2% of global energy consumption, has the potential to lower the production costs of ammonia. Moreover, ammonia is gaining increasing attention as a possible fuel for transportation.[6] As an energy carrier, ammonia offers several advantages, including its suitability for highly efficient fuel cells like solid oxide fuel cells (SOFCs) or direct ammonia fuel cells (DAFCs).[7] Additionally, it possesses an intriguing feature: it does not emit CO_2 while maintaining a high energy density comparable to traditional fossil fuels in both volume and weight.[6,8] Hence, there is a strong need for a significantly more energy-efficient approach to produce NH_3 from molecular N_2. Presently, ammonia synthesis primarily relies on the Haber-Bosch process, which involves the initial dissociation of N_2 followed by the protonation of each nitrogen atom - known as the dissociative mechanism.[9] This method is characterized by its high energy consumption, reliance on elevated temperature

[a] A. Iqbal, Y. Abghoui
Science Institute of the University of Iceland
E-mail: younes@hi.is

[b] E. Skulason
Faculty of Industrial Engineering, Mechanical Engineering and Computer Science, University of Iceland
E-mail: egillsk@hi.is

Supporting information for this article is available on the WWW under https://doi.org/10.1002/cphc.202300991

and pressure, and significant capital expenditures for the construction of production facilities.

The simplest catalyst for the electrochemical generation of ammonia would involve using a catalyst composed solely of a transition metal. Nevertheless, many of these metals necessitate a rather substantial OP, sometimes as high as −1.5 V compared to the standard hydrogen electrode (SHE), to trigger nitrogen activation and ammonia production.[10] This is far from the equilibrium potential for ammonia formation, which is approximately +0.06 V under these conditions.[11] Furthermore, in addition to the vulnerability of certain pure metals to oxidize readily, the rapid generation of $H_{2(g)}$ on most of these surfaces poses a significant obstacle to efficient ammonia production. Theoretical investigations unveiled the potential use of undercoordinated molybdenum nanoclusters, both with[12] and without[13] a nitrogen skin, for the activation of nitrogen and the electrochemical synthesis of ammonia. These studies have shown that ammonia can be produced at −0.6 V compared to SHE, but it has been observed that the N-vacant sites generated in this process become contaminated with oxygen from the electrolyte.[14]

In recent years, two-dimensional (2D) materials have opened up exciting prospects for crafting electrocatalysts for nitrogen reduction reactions (NRR) with enhanced efficiency, owing to their remarkable mechanical and electrical characteristics.[15–18] Nitrides are promising materials because they enable the possibility of NRR via (Mars-van Krevelen) MvK,[19–22] but the problem with the nitrides is some of them suffer from instability.[23] To address the instability challenge of the nitrides, oxides[24] and carbides[25] were investigated which show promise for NRR. Similarly, to the case of oxynitrides[26] where the presence of oxygen stabilizes the nitrides, the presence of carbon in the nitride structures in the form of carbonitrides may offer stability as well and this is the reason, we want to investigate carbonitrides in this work.[27] In the case of transition metal carbides, their electronic structures bear a resemblance to noble metals near the Fermi edge,[28] thanks to the bonding interactions between the 2s and 2p orbitals of carbon atoms and the d orbitals of transition metals. This reinforces the inherent electronic properties of these catalysts and facilitates the transfer of electrons from the catalyst surface to the reactants during the NRR. This, in turn, may enhance the rate of charge transfer and NRR kinetics. In contrast, transition metal nitrides contain intrinsic nitrogen atoms that initiate the NRR process on these catalysts.[29] Essentially, the competition between the NRR and the hydrogen evolution reaction (HER) arises due to the competition for adsorption selectivity between protons and nitrogen molecules on the catalyst surface.[30,31] However, in this scenario, the unique MvK mechanism may tilt the balance in favor of NRR over HER.[32]

In this research, we employ theoretical calculations to assess the stability and catalytic activity of various rock-salt (RS) transition metal carbonitride (TMCN) surfaces for electrochemical nitrogen activation and ammonia formation, using the (111) facet as a model system in this study. Our approach utilizes Density Functional Theory (DFT) calculations to examine the thermodynamics of the cathode reaction. We construct free energy diagrams (FED) to elucidate the electrochemical protonation of surface nitrogen, carbon, or metal atoms, thus determining the onset potentials (OP) necessary for ammonia synthesis on these carbonitride structures. We account for the influence of an external bias by using the computational hydrogen electrode (CHE) model,[33] and we estimate the lowest OP required for ammonia production for each carbonitride. We also take into consideration the stability of active sites in an electrochemical environment, and the possibility of catalyst poisoning under an applied bias and explore the likelihood of catalyst regeneration versus decomposition for the most promising RS (111) materials. Furthermore, we explicitly examine the competing HER on all these carbonitride surfaces within the framework of our mechanistic model.

2. Methodology

2.1. Modeling Parameters

In all computational simulations, we employ the DFT with the Revised Perdew-Burke-Ernzerhof (RPBE)[34] exchange-correlation functional. The Vienna ab initio simulation package (VASP)[35] is utilized, employing a Monkhorst-Pack K-point grid of 4×4×1 and a 500-eV energy cutoff for each surface calculation. We used the projector augmented wave (PAW)[36] method in VASP code, which allows for the use of computationally efficient pseudopotentials, resulting in significant reductions in computational time.[37,38] To account for electron distribution, we applied a Fermi-Dirac distribution with a smearing value of $k_BT = 0.1$ eV to smooth the Kohn-Sham orbital occupancy. All surfaces were subjected to analysis within the RS crystallographic structure, maintaining a (111) surface orientation. This choice is based on the enhanced stability of this structure and its facets, facilitating comparison with previous studies conducted on TMN surfaces by the same research group.[39,20–22,40] The TMCN surfaces are represented using a 5-layer 2×2 unit cell comprising 20 metal atoms, 10 carbon atoms, and 10 nitrogen atoms as shown in Figure 1.

The lowest two layers are kept fixed in their equilibrium bulk structure, while the three top layers and any adsorbates were permitted to undergo relaxation. Periodic boundary conditions were upheld along the x and y dimensions, and a minimum gap of 15 Å in the z direction was maintained between each surface slab. The structural optimization is considered satisfactory when the combined forces acting on all mobile atoms fell below 0.01 eV. To calculate activation energies, we apply the climbing image nudged elastic band technique (CI-NEB) to pinpoint the highest point along the minimum energy path (MEP).[41] The Bader analysis and the charge density difference are also used in this work as detailed previously.[42,43]

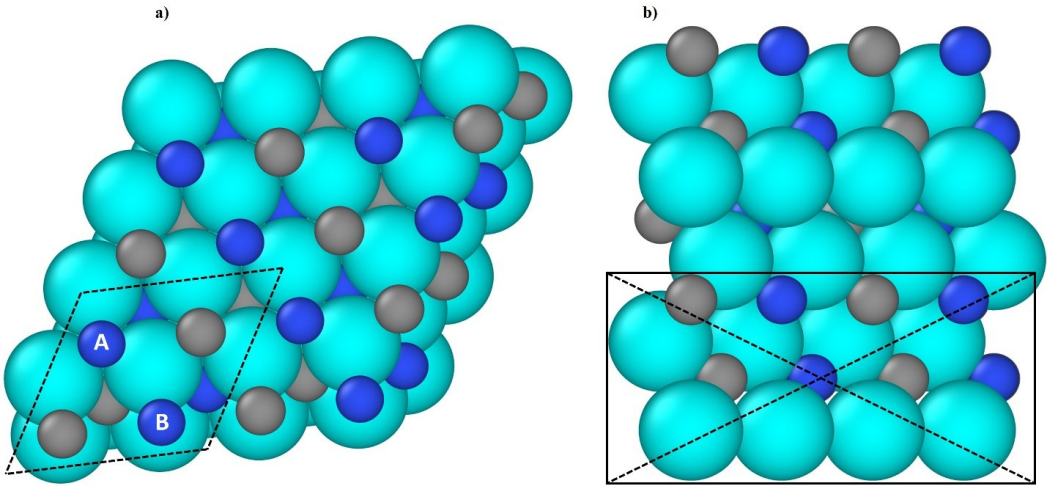

Figure 1. Model diagram of a 5-layer TMCN (a) Top view and (b) Side view in the (111) facets of the RS surface used in the computational simulations. The cyan, gray, and blue spheres represent metal, carbon, and nitrogen atoms respectively.

2.2. Electrochemical Modeling and Reaction Pathways

To model the complete chemical pathway responsible for ammonia production, we employed the following equations:

$$N_2 + 6(H^+ + e^-) \rightleftharpoons 2NH_3 \quad (1)$$

$$H_2 \rightleftharpoons 2(H^+ + e^-) \quad (2)$$

Inside the electrochemical cell, the fundamental elements required for ammonia synthesis at the cathode (Equation 1) include nitrogen molecules, protons produced at the anode (Equation 2), and electrons stemming from the applied voltage. Since the essential protons are exclusively generated at the anode, and we conduct the modelling at zero pH, we can directly correlate the applied voltage with either the standard hydrogen electrode (SHE) or the reversible hydrogen electrode (RHE). For a thorough comprehension of a catalyst's catalytic efficiency and the resulting products, the preferred approach involves employing an unrestricted mechanism. The following equation is applied to compute the change in free energy for each reaction step:

$$\Delta G_i(U_{RHE}) = \Delta G_i\ (U_{RHE} = 0) + neU_{RHE} \quad (3)$$

$$eU_{RHE} = eU_{SHE} + 2.3\ k_B TpH \quad (4)$$

Here, U_{SHE} represents the applied potential relative to the standard hydrogen electrode, n denotes the number of electrons, e is the elementary charge, k_B is the Boltzmann constant, and T signifies the temperature. By inserting Eq. (4) into Eq. (3), we obtain:

$$\Delta G_i(U_{RHE},\ pH) = \Delta G_i\ (U_{RHE} = 0) + n(eU_{SHE} + 2.3\ k_B TpH) \quad (5)$$

In this study, we adopt a pH value of 0. Importantly, overpotentials are typically unaffected by the electrolyte pH, and as such, our predicted overpotentials remain valid across different pH values. The calculation of $\Delta G_i(U=0)$ for each elementary step is carried out as follows:

$$\Delta G_i(U = 0) = \Delta E_{DFT} + \Delta E_{ZPE} + \Delta H_{0K\rightarrow T} - T\Delta S \quad (6)$$

where ΔE_{DFT} is calculated with DFT and ΔE_{ZPE} and ΔS are zero-point energy corrections and entropy differences which are calculated within harmonic approximation of the adsorbed intermediates but taken from table values for gas phase molecules.[44]

Within any given reaction pathway, the potential determinant step (PDS) refers to the electrochemical reaction with the most significant positive change in free energy. Starting from the PDS, the OP can be defined as the potential required to counteract the change in the free energy of the PDS. Subsequently, as described by Equation 6, all subsequent reaction steps experience a reduction in free energy, leading to a downhill trajectory. Therefore, the OP becomes:

$$OP = -\Delta G/e \quad (7)$$

The OP (in volts) is essentially the electron-volt magnitude of the negative change in free energy of the PDS.

3. Results and Discussion

At first, a computational screening is applied to a range of transition metal carbonitride catalysts from group III to XII in

the RS structure with the (111) facets, including both surfaces with carbon-nitrogen termination and surfaces with metal-termination. For most of these surfaces, the carbon-nitrogen termination was found to be more stable than the metal termination by comparing the total energy of the systems after optimization. Therefore, we focused on the former structures only. In total, 11 TMCN surfaces are explored initially in this study, two of which (ScCN and YCN) were found not to be stable during structural optimization. VCN, NbCN, ZrCN, TiCN, TaCN, CrCN, MoCN, HfCN, and WCN were stable and thus explored further as potential catalysts for NRR. We examined eight factors to assess the potential of all these candidates for electrochemically producing ammonia under ambient conditions. We will address each of the following aspects sequentially: (i) The mechanism for the NRR, (ii) surface toxicity, (iii) catalytic performance, (iv) catalyst surface vacancy poisoning, (v) the stability of a surface N/C-vacancy as an indicator of decomposition, (vi) the calculated kinetic barrier required for N_2 to dissociate and occupy the vacancy, (vii) volcano-plot analysis to display OP for each TMCN as a function of descriptor of reactivity, and (viii) Bader charge analysis and charge distribution analysis through charge iso-surfaces.

3.1. Mechanism of Nitrogen Reduction Reaction

We explored three mechanisms for the NRR: 1) An associative mechanism (AM), 2) a dissociative mechanism (DM), and 3) an MvK mechanism. Figure 2 shows schematically these three main mechanisms as well as a mixture of those mechanisms, e.g.

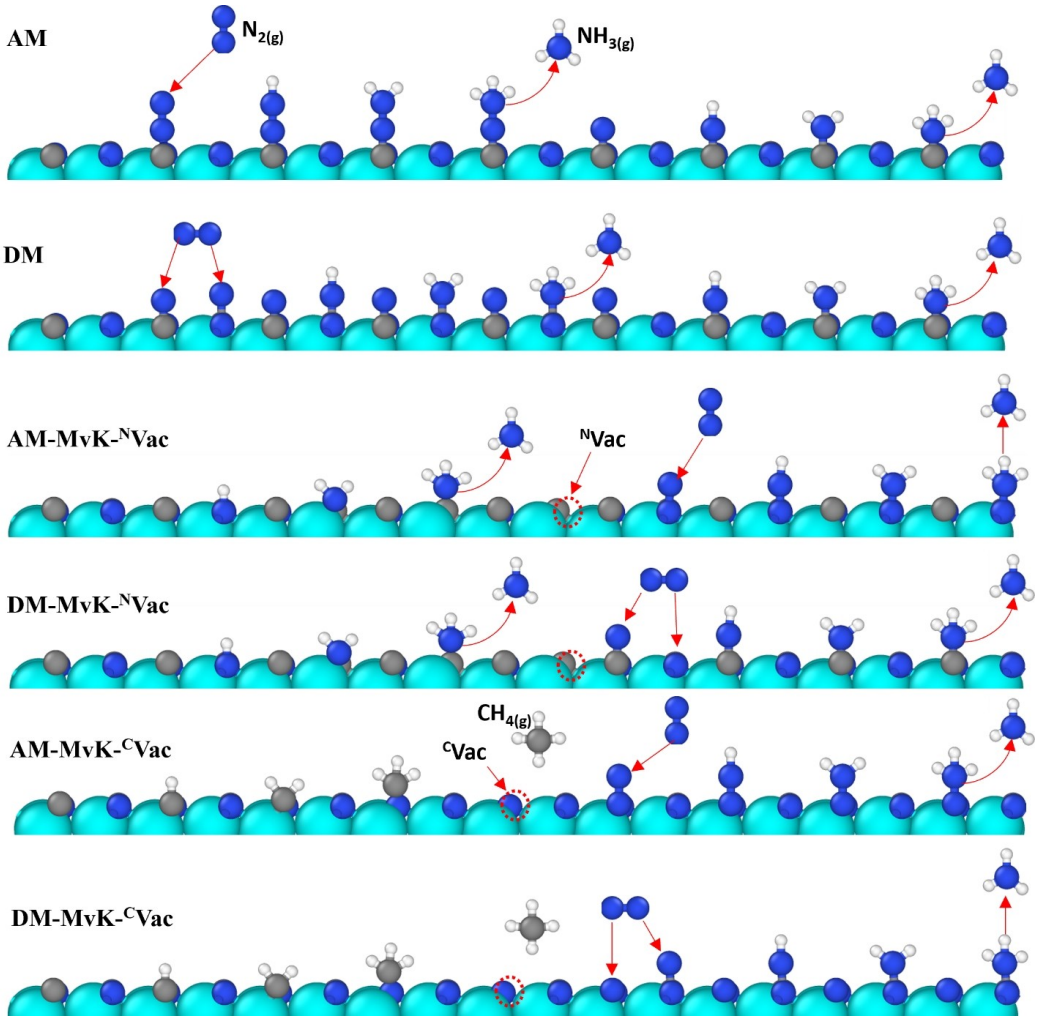

Figure 2. shows the schematic diagram for the nitrogen reduction reaction. White color shows hydrogen, blue color shows nitrogen, gray color shows carbon and cyan shows metal in this case.

when MvK is used creating either a C-vacancy or an N-vacancy where the second half of the mechanism can either be AM or DM. For all mechanisms, In the DM, the strong N_2 triple bond is cleaved during the adsorption, leading to the separate adsorption of N atoms at carbon sites, spaced apart from each other. Notice that at this point we only calculate the thermodynamics of N_2 dissociative adsorption, not the kinetic barriers. Later in the study we see that this mechanism results in significantly high OP of some of the reaction steps which prevents this mechanism to be predicted feasible and therefore the kinetic barriers are not computed in the end. In the subsequent stages, the hydrogenation of each N atom leads to the production of ammonia, which is subsequently released. In the case of the AM, the N_2 bond remains intact after N_2 adsorption and only undergoes breaking at a specific stage in the hydrogenation process. Within the AM, we also examined the possibility of *NNH formation and included it in the free energy diagrams. In the MvK mechanism, the lattice N/C atoms on the surface of TMCNs can be converted into ammonia or methane, generating vacancies in the process. These vacancies can be chemically refilled by nitrogen molecules either through an associative process (via associative MvK) or through a dissociative process (via dissociative MvK) to regenerate the catalyst. It was observed that different species adsorb only on carbon sites rather than nitrogen, metal, or three-folded sites.

3.2. Surface Poisoning

To initiate any reactivity, it is essential to examine the adsorption of nitrogen species onto the surface, while also considering the presence of competing species such as H, O, and OH. In the context of nitrogen adsorption, the associative adsorption of nitrogen gas ($*N_2$), the dissociative adsorption of nitrogen gas (*2N), and the associative adsorption of NNH (*NNH) are compared with the adsorption of H, O, and OH. The results related to the adsorption of nitrogen and the potential for active site poisoning by other species are depicted in Figure 3. As can be seen, the NbCN and WCN bind O more exergonically at zero potential, and this will be of no concern as upon applying a negative potential (NRR potential) the O-based species will be reduced to water and the surface becomes free

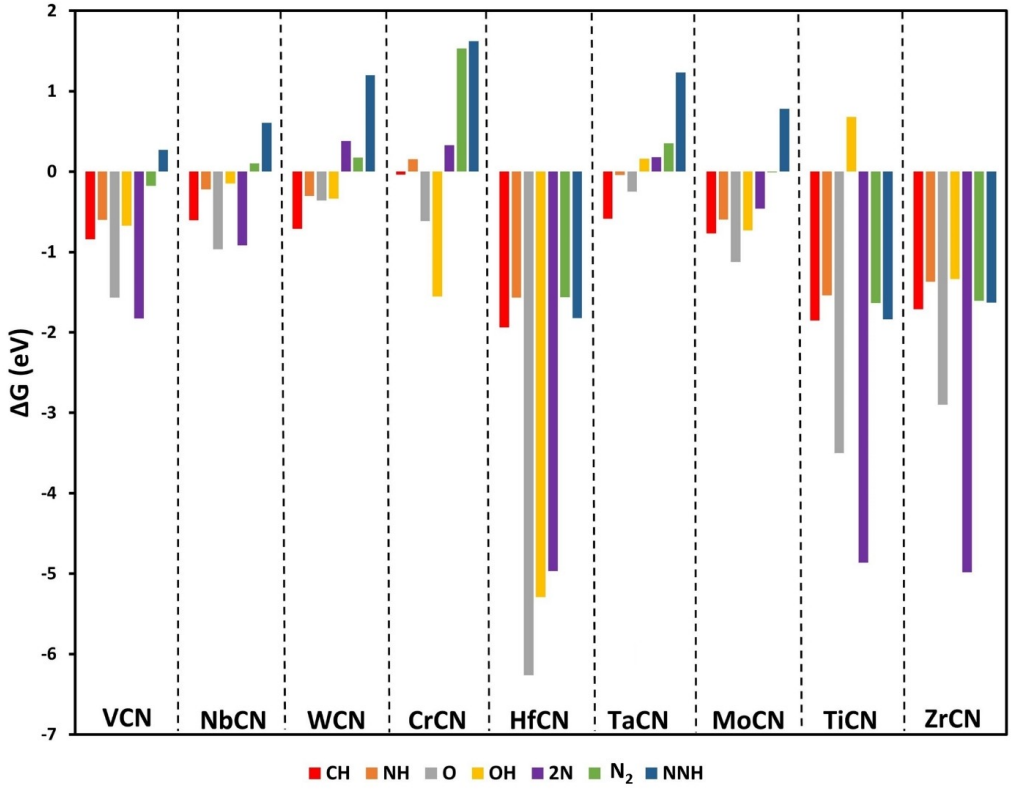

Figure 3. illustrates a comparison of adsorption-free energies for different nitrogen and oxygen species on pristine TMCN surfaces. It also depicts the protonation of metal, nitrogen, and carbon sites at zero potential. The most favorable adsorption site for all the computed species was found to be the carbon site. In this context, $*N_2$ represents the associative binding of $N_{2(g)}$, 2N represents the dissociative binding of $N_{2(g)}$, and *NNH stands for the associative binding of NNH which could be achieved via a concerted mechanism.

for nitrogen adsorption. Additionally, we assessed the adsorption of protons on the metal sites (which is an indication of HER), and surprisingly, the protons always migrated to the carbon or nitrogen sites, indicating that proton adsorption on metal sites contributing to the HER is unlikely for all TMCNs. In summary, understanding surface nitrogen adsorption and considering competing species like H, O, and OH is crucial for initiating reactivity. Results indicate favorable nitrogen adsorption and minimal active site poisoning. Proton adsorption analysis suggests metal sites are unlikely contributors to the hydrogen evolution reaction for all TMCNs.

3.3. Catalytic Activity

We conducted a comprehensive analysis of the reaction on the RS (111) facets of TMCNs through various mechanisms explained above for all nine TMCNs. However, we have chosen to display the free energy diagrams only for the most promising candidates, while the data for the remaining TMCNs is provided in the electronic supplementary information (ESI.) As depicted in Figure 4, the most favorable route for ammonia production on NbCN involves a mixed associative-MvK mechanism where N_2 is adsorbed on the surface (with the free energy change being slightly endergonic here, but only 0.09 eV) and block half of the carbon sites but protons then prefer binding to the surface N-atoms rather than the adsorbed N_2 or the remaining surface C-atoms. In this mechanism, the PDS corresponds to the fifth protonation step, which is linked to the formation of the first $*NH_3$ formation. This step exhibits ΔG_{PDS} values of 0.58 eV for NbCN. In this mechanism we explore the possibility of forming a dimer vacancy (while N_2 is adsorbed on the surface, as shown in Figure 4) to generate a second ammonia molecule, resulting in the release of two ammonia molecules after a transfer of $6(H^+ + e)$. The two N-vacancies are found to be exergonically refilled by diffusion of the already adsorbed N_2 from the surface C atom to the N-vacancies. This process is found to have a small energy barrier (0.29 eV) when we did the NEB-CI calculations as shown in Figure S10(c).

Additionally, we have included the MvK mechanism for NbCN (without the presence of N_2 on the clean surface, see the black pathway in Figure S1(a)), in which the reaction goes through dimer C-vacancy and PDS is comparatively higher (1.4 eV). After the dimer vacancies, we should fill the vacancy

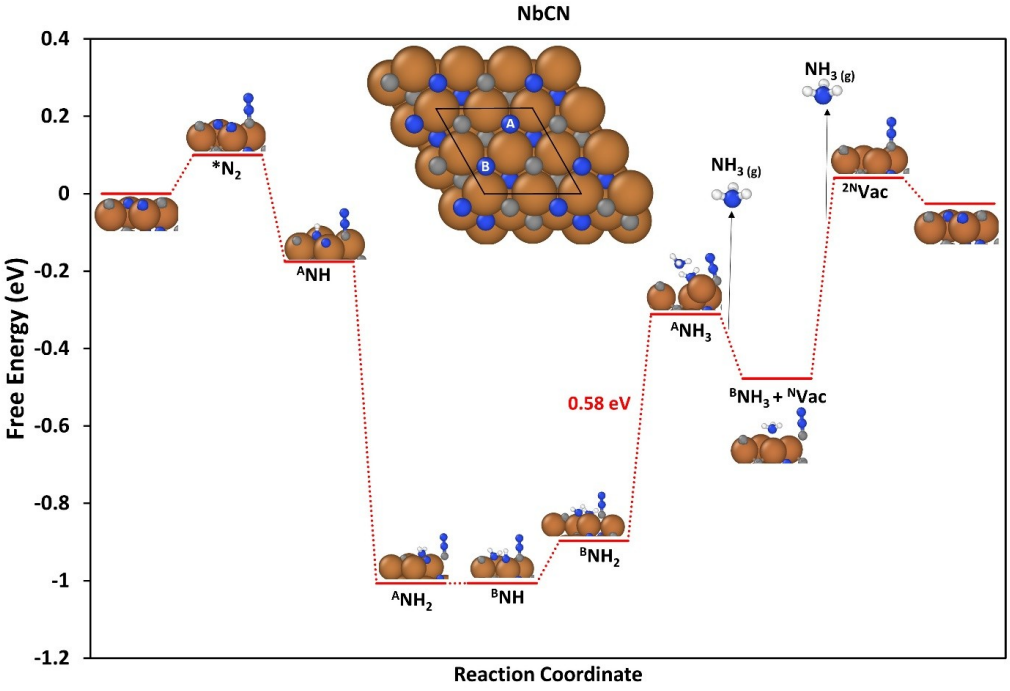

Figure 4. presents a Free Energy Diagram (FED) depicting the nitrogen activation process leading to ammonia through the formation of a dimer-vacancy via a mixed associative-MvK mechanism on NbCN. The PDS is highlighted as the fifth protonation step with a ΔG_{PDS} of 0.58 eV. The inset showcases a top view of the RS (111) TMCN unit cell, which has been repeated once in the lateral directions. In this unit cell, golden spheres represent metal atoms, gray spheres represent carbon atoms, dark blue spheres represent nitrogen atoms and white represent hydrogen atom. The nitrogen atoms of the TMCNs are labeled A and B, and the adsorption site at each step in the FEDs indicates which N atoms are reduced during each stage. The labeling A, B of N in the final step indicates that a dimer-vacancy has been filled by the dissociation of N_2, which was adsorbed on the carbon site.

either with N_2 dissociatively or go for the third and fourth vacancies. It has been seen that none of these possibilities work at reasonable OP under ambient conditions (see Figure S1 in the ESI).

In the case of WCN, the ΔG_{PDS} amounts to 0.73 eV via the mixed-MvK mechanism (the red pathway in Figure S2), specifically associated with the fifth protonation step and the generation of $*NH_3$. An examination of the free energy diagram reveals that all other mechanisms considered here as shown in Figure S2 get to even more endergonic steps and thus even less favorable for NRR. Therefore, we tested an associative N_2 adsorption before initiating protonation. Upon initiating the protonation process, it became evident that two ammonia molecules were eventually released after the transfer of $6(H^+ + e)$. When examining the kinetics of N_2 dissociation into dimer N-vacancies on WCN, we found a relatively high activation energy of 1.7 eV for N_2 dissociation from our NEB calculations as shown in Figure S10(a). This value suggests that the process will be slow under ambient conditions.

In the case of all other materials, there is no viable route to ammonia formation following several protonation steps, as elaborated in Figures S1–S9, primarily due to either a high PDS or the generation of undesired byproducts (CH_4). For instance, ZrCN, MoCN, and TiCN are not regarded as promising candidates due to the elevated PDS identified in the MvK mechanism or the unfavorable pathway via alternative mechanisms because the PDS for all is above 1.0 eV. The FEDs for NbCN and MoCN as presented in Figures S1(b) and S3(b) show a possible pathway for the first NH_3 molecule formation through the DM. However, this mechanism only works if all the surface C sites can be occupied by dissociated nitrogen. Otherwise, it results in the formation of CH_4 and creates a carbon vacancy as long as a carbon site remains available for protonation. The diagrams also illustrate various other mechanisms, and it is evident that none of these mechanisms are conducive to ammonia formation under ambient conditions. In conclusion, our analysis of the reaction on the RS (111) facets of TMCNs highlights the most promising routes for ammonia production, particularly focusing on NbCN and WCN. These mechanisms involve mixed associative-MvK processes and reveal insights into protonation steps and ammonia generation. For NbCN, a mixed associative-MvK mechanism demonstrates favorable energetics, while for WCN, associative N_2 adsorption precedes protonation. However, other TMCNs exhibit less favorable pathways due to high activation energies or undesired byproducts, making them less suitable for NRR under ambient conditions. Further details for each material are provided in the supplementary information.

3.4. Poisoning of the Defects/Vacancies

To sustain the catalytic cycle, it is essential for N_2 to refill the surface vacancies generated. However, there exists a possibility that the nitrogen vacancy remains unoccupied by nitrogen due to obstruction by a proton, an oxygen atom, or a hydroxyl species from the aqueous electrolyte solution. Consequently, we examine the competition between N and O, H, or OH for filling the surface vacancy by comparing the free energy of filling the vacancy with any of these species relative to nitrogen ($\Delta G(*2N\text{-}*X)$), where X is O^{2-}, H^+, or OH^-. At operational conditions, these ions are generated from the water present in the electrolyte, leading to the formation of O^{2-}, OH^-, and H^+. A negative value of $\Delta G(*2N\text{-}*X)$ indicates that nitrogen adsorption is the thermodynamically favored phenomenon compared to the adsorption of other three species for occupying the vacancy. These values are depicted in Figure 5 for NbCN and WCN, both of which are somewhat catalytically active carbonitrides for NRR. The data illustrates that in the case of NbCN, nitrogen exhibits stronger adsorption to surface vacancies compared to H, O and OH. Consequently, it is anticipated that the surface vacancies in NbCN will not be subject to poisoning by these species, and the vacancies are more likely to be occupied by nitrogen. Therefore, the catalytic cycle may continue on NbCN, facilitating ammonia production. However, in the case of WCN, it appears that H, O, and OH exhibit a higher affinity for binding to surface vacancies compared to N species. Overall, NbCN emerges as the most promising choice, excelling in both catalytic activity (Figure 4) and resilience against poisoning (Figure 5), demonstrating its ability to convert nitrogen into ammonia at a potential of −0.58 V. However, at the OP (refer to Figure 5), it will be reduced to water and adsorb from the electrode surface. In summary, sustaining the catalytic cycle for nitrogen reduction requires refilling surface vacancies with nitrogen. However, competition from protons, oxygen, and hydroxyl species in the electrolyte solution may hinder nitrogen occupancy. Analysis of the thermodynamic favorability of nitrogen adsorption relative to these species indicates that NbCN exhibits stronger nitrogen affinity, suggesting resilience against poisoning. Consequently, NbCN emerges as the most promising candidate for ammonia production due to its catalytic activity and resistance to poisoning, outperforming WCN.

3.5. Stability Against Decomposition

Reducing a nitrogen/carbon atom on the surface of MvK results in the generation of NH_3/CH_4. Subsequently, a gaseous N_2 molecule may occupy the vacant site. The stability of the surface nitrogen/carbon vacancy is a crucial factor for this replenishment process to take place. If the surface nitrogen/carbon vacancy is not stable, it might migrate into the catalyst's bulk, where it would be refilled with additional nitrogen/carbon from the catalyst's bulk, rather than gaseous N_2. In theory, this cycle continues until all nitrogen and carbon atoms in carbonitrides are reduced to produce NH_3/CH_4. This scenario could ultimately lead to the decomposition of TMCN into the parent metal. The kinetic barriers for vacancy migration (E_{arvac}) are calculated, and Figure 6 provides the kinetics associated with this process. In the case of NbCN, it has been observed that due to the substantial kinetic barrier (around 2.0–2.5 eV) for vacancy migration, NbCN is likely to maintain stable surface vacancies, as it is improbable for this barrier to be overcome at room temperature. Conversely, in the case of WCN, the kinetic

Research Article
doi.org/10.1002/cphc.202300991
Chemistry Europe
European Chemical Societies Publishing

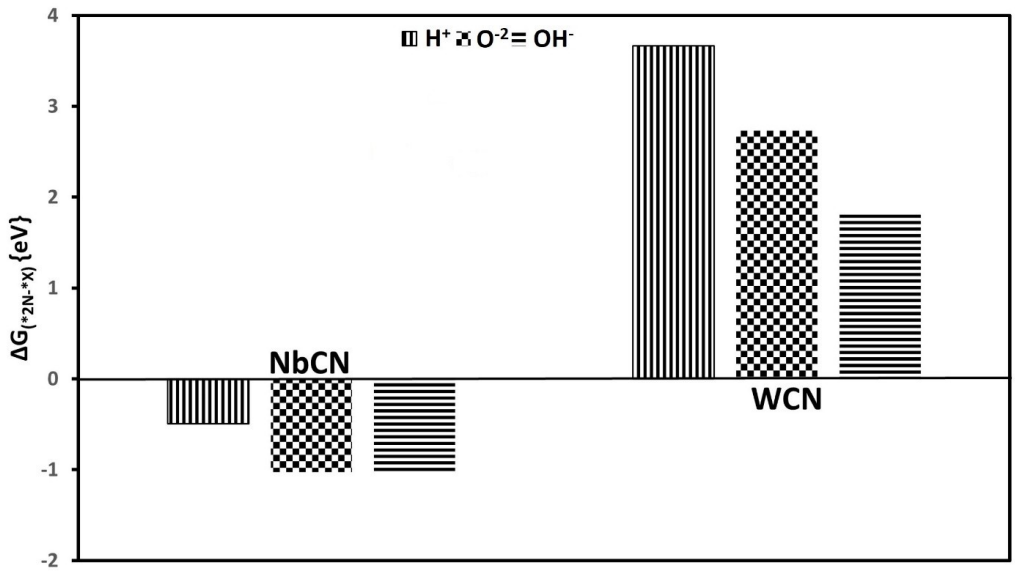

Figure 5. shows the free energy of O, H, or OH adsorption relative to dissociated nitrogen on the surface vacancy of catalytically active carbonitrides. These free energies are computed with reference to $N_{2(g)}$, $H_{2(g)}$, and $H_2O_{(g)}$. All free energies are assessed based on the calculated OP for each carbonitride, with NbCN at −0.58 V and WCN at −0.73 V.

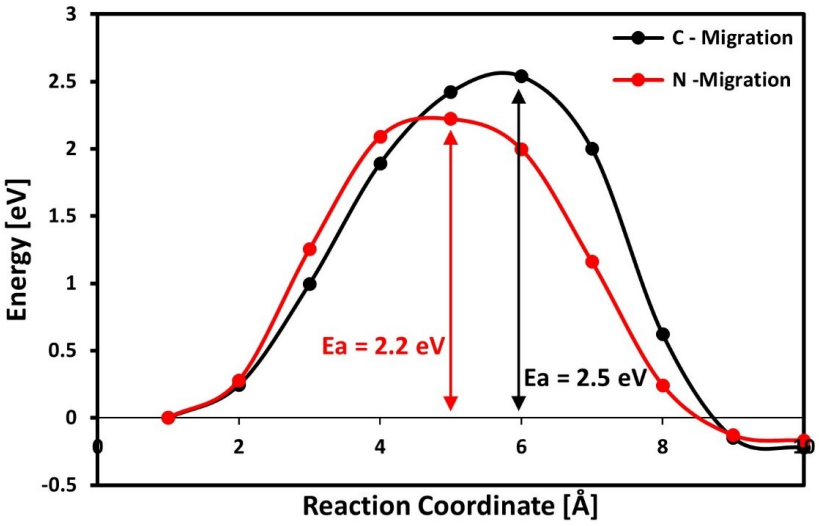

Figure 6. Minimum energy path (MEP) of the migration of a carbon/nitrogen atom from a sub-layer to fill a vacancy on the surface for NbCN. The corresponding energy barrier values are denoted by their respective colors for nitrogen and carbon migration to the surface.

considerations indicate that the vacancies might not be stable enough at ambient conditions with regards to nitrogen migration from sub-surface to the surface as the kinetic barrier of nitrogen migration (0.7 eV) is smaller than the kinetic barrier

for carbon migration (2.7 eV), see Figure S10(b). Kinetic barriers for vacancy migration play a significant role in determining stability. For NbCN, the substantial kinetic barrier suggests stable surface vacancies, while for WCN, lower barriers imply potential instability, impacting nitrogen migration. These insights are vital for understanding the long-term stability and performance of TMCNs in catalytic ammonia production.

3.6. Exploring the Scaling Relations and Volcano Plot for Ammonia Formation

By employing linear correlations that relate different reaction steps to the ΔG of *NH (utilized as a descriptor) we can construct a volcano diagram. We have looked at several possible descriptors such as N, NH, and so on but only ΔG of *NH gave a proper correlation. This diagram helps us to identify the specific ΔG of *NH that leads to the lowest OP for electrochemical ammonia synthesis. A similar approach was described in reference[45] for the electrolysis of water on oxide surfaces. In this analysis, the binding free energy of *NH serves as a direct indicator of electrocatalytic activity. The free energy associated with each reaction step can be represented as a function of the applied bias (U) and the ΔG of *NH. Utilizing the linear scaling relationships presented in Figure S11, we can create a volcano plot, as depicted in Figure 7, via the MvK mechanism. The scaling relations are only used to guide the eye whereas the explicit OP values are used for each candidate. Notably, NbCN and WCN are positioned at the peak of the MvK volcano, indicating that they are the most promising materials for ammonia formation under ambient conditions. In conclusion, linear correlations with ΔG of *NH allow for constructing a volcano diagram, aiding in identifying optimal conditions for electrochemical ammonia synthesis. NbCN stands out as the most promising material, positioned at the peak of the MvK volcano plot, indicating its potential for efficient ammonia formation under ambient conditions.

4. Conclusions

Using DFT calculations, we conducted an investigation into various potential reaction mechanisms for ammonia formation, specifically considering the MvK, AM, and DM pathways, focusing on the (111) facets of nine carbonitride materials, namely TiCN, VCN, CrCN, ZrCN, NbCN, MoCN, HfCN, TaCN, and WCN in a rock salt structure. We computed the free energies associated with stable intermediates along these reaction pathways. By constructing free energy diagrams for each carbonitride, we were able to assess the free energy changes at each step that determine the OP. Additionally, we determined the activation energy for N_2 dissociation and evaluated the free energy of N_2 admolecules on the pristine surfaces of all the studied TMCNs and within nitrogen vacancies only for the NRR-promising TMCNs, i.e NbCN and WCN. Our findings suggest that, for these carbonitrides, achieving the reduction of nitrogen to ammonia under ambient conditions through either DM or AM mechanisms may not be favorable. Under ambient conditions, the DM mechanism is generally ineffective for ammonia formation in most of these materials due to the

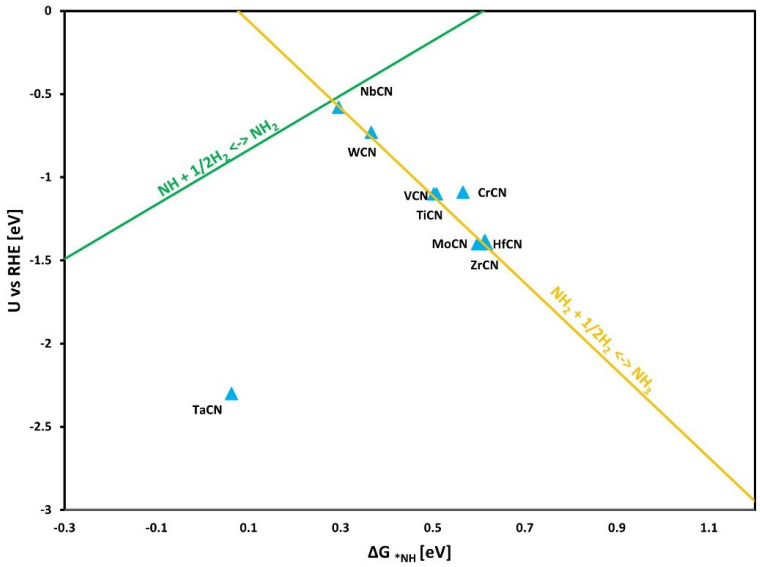

Figure 7. Shows a theoretical volcano graph to assess ammonia formation using *NH as a descriptor. It becomes apparent that NbCN occupies the highest position at the peak of the curve. The scaling relations have been used to plot the lines of the volcano and they are to guide the eye. The explicit OP values are used for given TMCN which is the most endergonic and PDS in the FEDs computed in this study.

presence of high PDS. In this study, we employed a thermochemical model and the computational hydrogen electrode model to predict the OP for these various processes. All of the carbonitrides on (111) facets were found to have the ability to inhibit the HER because they do not tend to bind protons on the metal sites. However, the majority of them do not favor NRR either at ambient conditions. The WCN was found to be susceptible to poisoning in electrochemical environments and only NbCN was found favoring NRR via a mixed associative-MvK mechanism. NbCN was found to require a low OP (−0.58 V vs. RHE) for ammonia synthesis under ambient conditions, however, the N_2 adsorption step is slightly uphill in free energy (0.09 eV) using the xc-functional of choice here which could slow down the reaction.

Funding

This work was supported by the Icelandic Research Fund [grant number 207056-053].

Conflict of Interests

The authors declare no conflict of interest.

Data Availability Statement

The data that support the findings of this study are available from the corresponding author upon reasonable request.

Keywords: DFT calculations · (111) facets · rock salt structure · transition metal carbonitrides · nitrogen reduction reaction · ammonia · ambient conditions

[1] J. W. Erisman, et al., *Nat. Geosci.* **2008**, *1*(10), 636–639.
[2] J. G. Chen, et al., *Science* **2018**, *360*(6391), eaar6611.
[3] M. A. Shipman, M. D. Symes, *Catalysis Today* **2017**, *286*, 57–68.
[4] G. Qing, et al., *Chem. Rev.* **2020**, *120*(12), 5437–5516.
[5] V. Smil, *Nature* **1999**, *400*(6743), 415–415.
[6] A. Klerke, et al., *J. Mater. Chem.* **2008**, *18*(20), 2304–2310.
[7] T. Vegge, et al., *Indirect hydrogen storage in metal ammines, in Solid-State Hydrogen Storage.* **2008**, Elsevier. p. 533–564.
[8] D. R. Lide, *CRC handbook of chemistry and physics.* Vol. 85. **2004**, CRC press.
[9] A. S. Travis, A. S. Travis, *The Direct Synthesis of Ammonia. Nitrogen Capture, The Growth of an International Industry* (1900–1940), **2018**, 93–127.
[10] E. Skulason, et al., *Phys. Chem. Chem. Phys.* **2012**, *14*(3), 1235–1245.
[11] X. Ji, D. S. Silvester, L. Aldous, C. Hardacre, R. G. Compton, *J. Phys. Chem. C* **2007**, *111*(26), 9562–9572.
[12] J. G. Howalt, T. Vegge, *Phys. Chem. Chem. Phys.* **2013**, *15*(48), 20957–20965.
[13] J. G. Howalt, et al., *Phys. Chem. Chem. Phys.* **2013**, *15*(20), 7785–7795.
[14] J. G. Howalt, T. Vegge, *Beilstein J. Nanotechnol.* **2014**, *5*(1), 111–120.
[15] X. Wen, J. Guan, *Nanoscale* **2020**, *12*(15), 8065–8094.
[16] X. Guo, et al., *J. Mater. Chem. A* **2019**, *7*(8), 3531–3543.
[17] H. Jin, et al., *Chem. Rev.* **2018**, *118*(13), 6337–6408.
[18] L. Hui, et al., *J. Am. Chem. Soc.* **2019**, *141*(27), 10677–10683.
[19] Y. Abghoui, A. Iqbal, E. Skúlason, *Frontiers in Catalysis* **2023**, *2*, 1096824.
[20] Y. Abghoui, A. L. Garden, J. G. Howalt, T. Vegge, E. Skúlason, *ACS Catal.* **2016**, *6*(2), 635–646.
[21] M. Gudmundsson, V. Ellingsson, E. Skúlason, Y. Abghoui, *Top. Catal.* **2022**, *65*(1–4), 252–261.
[22] Y. Abghoui, A. L. Garden, V. F. Hlynsson, S. Björgvinsdóttir, H. Ólafsdóttir, E. Skúlason, *Phys. Chem. Chem. Phys.* **2015**, *17*(7), 4909–4918.
[23] F. Hanifpour, et al., *J. Catal.* **2022**, *413*, 956–967.
[24] Á. B. Höskuldsson, et al., *Cell Rep. Phys. Sci.* **2023**, *4*(10).
[25] Á. B. Ellingsson, et al., *ChemSusChem* **2023**, *16*(22), e202300947.
[26] F. Hanifpour, C. P. Canales, E. G. Fridriksson, A. Sveinbjörnsson, T. K. Tryggvason, E. Lewin, F. Lewin, Á. Magnus, E. Ingason, H. Skúlason, D. Flosadóttir, *Electrochim. Acta* **2022**, *403*, 139551.
[27] A. Iqbal, E. Skúlason, Y. Abghoui, *Are (100) Facets of Transition Metal Carbonitrides Suitable as Electrocatalysts for Nitrogen Reduction to Ammonia at Ambient Conditions? Under-review*.
[28] Z. Li, Y. Wu, *Small* **2019**, *15*(29), 1804736.
[29] H. Wang, et al., *Chem. Soc. Rev.* **2021**, *50*(2), 1354–1390.
[30] Y. Abghoui, E. Skúlason, *J. Phys. Chem. C* **2017**, *121*(43), 24036–24045.
[31] Y. Abghoui, *Top. Catal.* **2022**, *65*(1–4), 262–269.
[32] Z. Qiao, D. Johnson, A. Djire, *Cell Reports Physical Science* **2021**, *2*(5).
[33] J. K. Nørskov, et al., *J. Phys. Chem. B* **2004**, *108*(46), 17886–17892.
[34] B. Hammer, L. B. Hansen, J. K. Nørskov, *Phys. Rev. B* **1999**, *59*(11), 7413.
[35] G. Kresse, *Phys. Rev. B* **1996**, *54*(11), 169.
[36] G. Kresse, D. Joubert, *Phys. Rev. B* **1999**, *59*(3), 1758.
[37] G. Kresse, J. Furthmüller, *Phys. Rev. B* **1996**, *54*(16), 11169.
[38] P. E. Blöchl, *Phys. Rev. B* **1994**, *50*(24), 17953.
[39] E. Dražević, E. Skulason, *iScience* **2020**, *23*(12).
[40] Y. Abghoui, E. Skúlason, *J. Phys. Chem. C* **2017**, *121*(11), 6141–6151.
[41] G. Henkelman, B. P. Uberuaga, H. Jónsson, *J. Chem. Phys.* **2000**, *113*(22), 9901–9904.
[42] G. Henkelman, A. Arnaldsson, H. Jónsson, *Comput. Mater. Sci.* **2006**, *36*(3), 354–360.
[43] S. Gudmundsdóttir, W. Tang, G. Henkelman, H. Jónsson, E. Skúlason, *J. Chem. Phys.* **2012**, *137*(16).
[44] A. Bagger, R. M. Arán-Ais, J. Halldin Stenlid, E. Campos dos Santos, L. Arnarson, K. Degn Jensen, J. Rossmeisl, *ChemPhysChem* **2019**, *20*(22), 3096–3105.
[45] J. Rossmeisl, et al., *J. Electroanal. Chem.* **2007**, *607*(1–2), 83–89.

Manuscript received: December 27, 2023
Revised manuscript received: March 21, 2024
Accepted manuscript online: April 3, 2024
Version of record online: ■■, ■■

RESEARCH ARTICLE

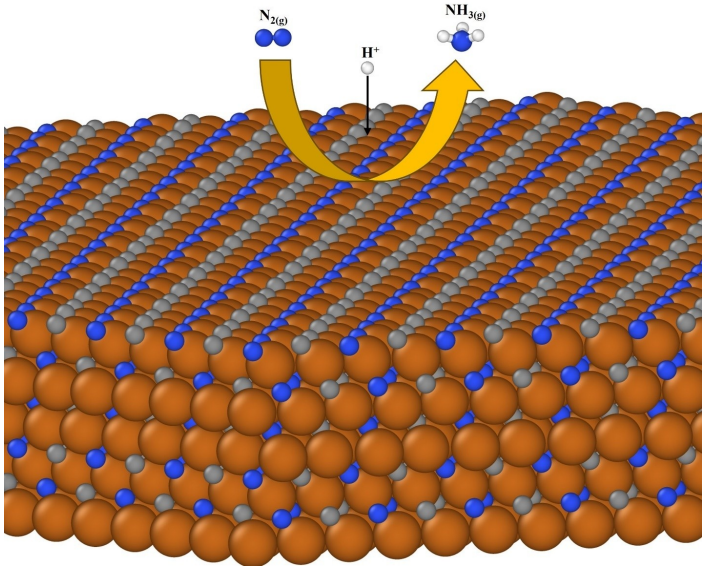

A. Iqbal, E. Skulason, Y. Abghoui**

Through the application of Density Functional Theory, we investigate the electrocatalytic potential of the (111) facets of the cubic structure of the transition metal carbonitrides for generating ammonia under ambient conditions.

ChemPhysChem

Supporting Information

Electrochemical Nitrogen Reduction to Ammonia at Ambient Condition on the (111) Facets of Transition Metal Carbonitrides

Atef Iqbal, Egill Skulason,* and Younes Abghoui*

Electrochemical Nitrogen Reduction to Ammonia at Ambient Condition on the (111) Facets of Transition Metal Carbonitrides

-Electronic supplementary information

Authors: Atef Iqbal, Egill Skúlason*, Younes Abghoui*

Zero-point energy and entropy corrections

Table S1: The ZPE and entropy correction values for all of the used adsorbed and gas phase species. The values for the adsorbed species were calculated on the [111] NbCN surface, and gas phase values were taken from ref [1]. For the adsorbed species, denoted by *, adsorption onto the surface is differentiated from adsorption into a vacancy by the ^{vac} notation.

[111] TMCN surfaces	ZPE (eV)	TΔS (eV)
NH_3 (g)	0.89	0.74
H_2 (g)	0.27	0.41
CH_4 (g)	0.82	0.57
N_2 (g)	0.15	0.6
*NH	0.29	0.008
*NH_2	0.7	0.06
*NH_3	1.03	0.119
*N_2^{vac}	0.2	0.112
*NNH vac	0.47	0.109
*NNH_2 vac	0.79	0.102
*$2N^{vac}$	0.19	0.117
*$N.NH^{vac}$	0.49	0.129
*$N.NH_2^{vac}$	0.78	0.115
*NHNH	0.72	0.128
*$NH.NH_2$	1.1	0.101
*$NH_2.NH_2$	1.44	0.16
*H^{vac}	0.17	0.006
*CH	0.25	0.013
*CH_2	0.61	0.069
*CH_3	0.89	0.086
*OH^-	0.38	0.068
*O^{2-}	0.1	0.062
*$OH^{- vac}$	0.38	0.052
*$O^{2- vac}$	0.09	0.029

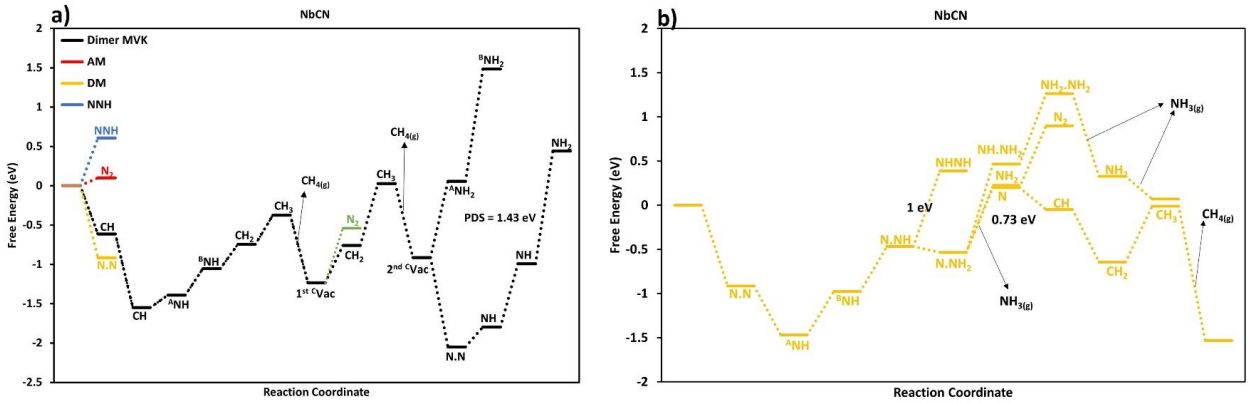

Figure S1 shows (a) MvK mechanism together with the first initial steps of AM and DM (b) complete DM for carbon-nitrogen terminated surface of NbCN at zero potential.

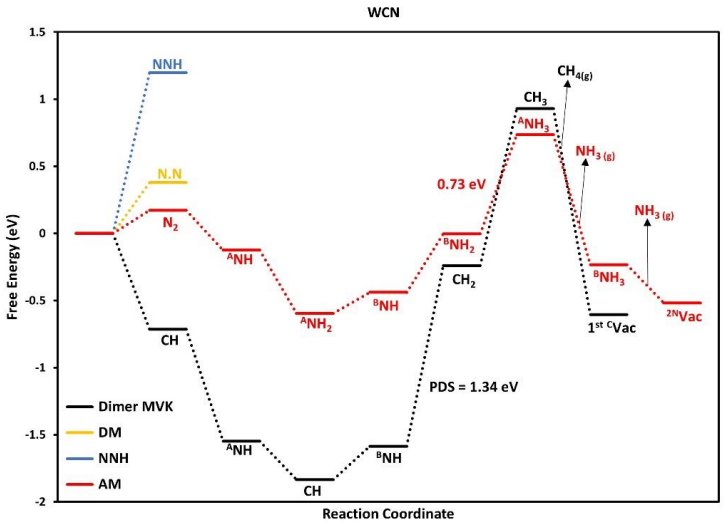

Figure S2 shows MvK, AM, and DM for carbon-nitrogen terminated WCN surface at zero potential.

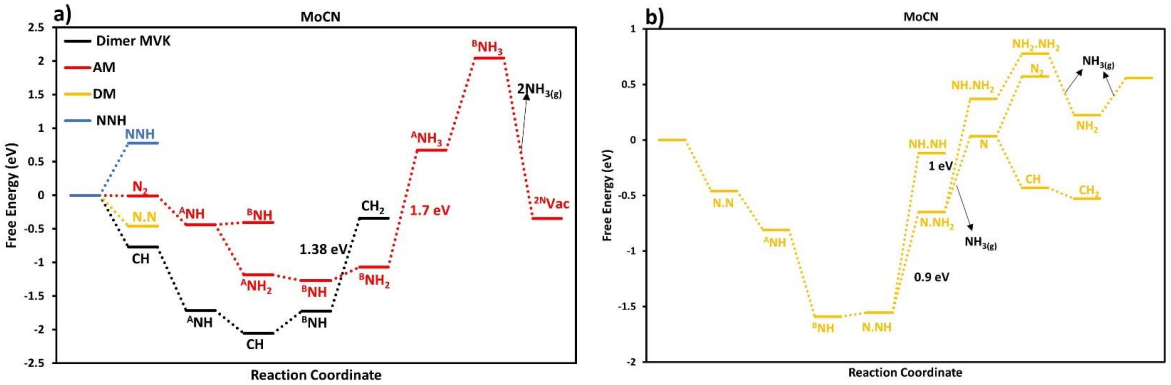

Figure S3 shows (a) MvK and AM, (b) DM for carbon-nitrogen terminated surface of MoCN at zero potential.

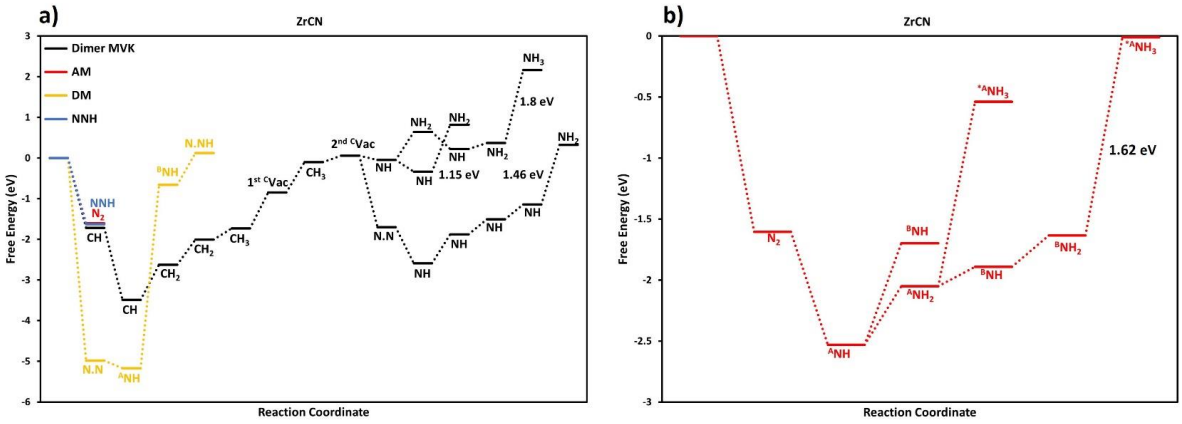

Figure S4 shows (a) MvK and DM (b) AM for carbon-nitrogen terminated surface of ZrCN at zero potential.

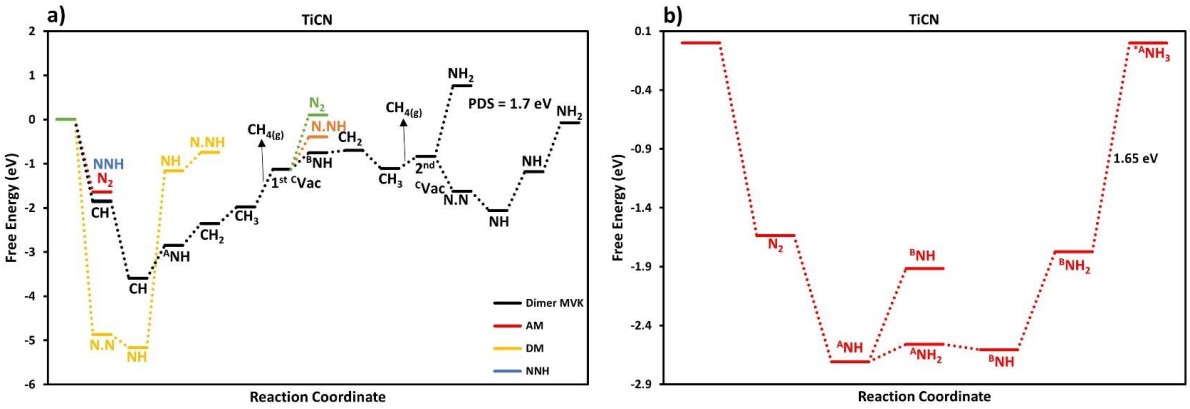

Figure S5 shows (a) MvK and DM (b) AM for carbon-nitrogen terminated surface of TiCN at zero potential.

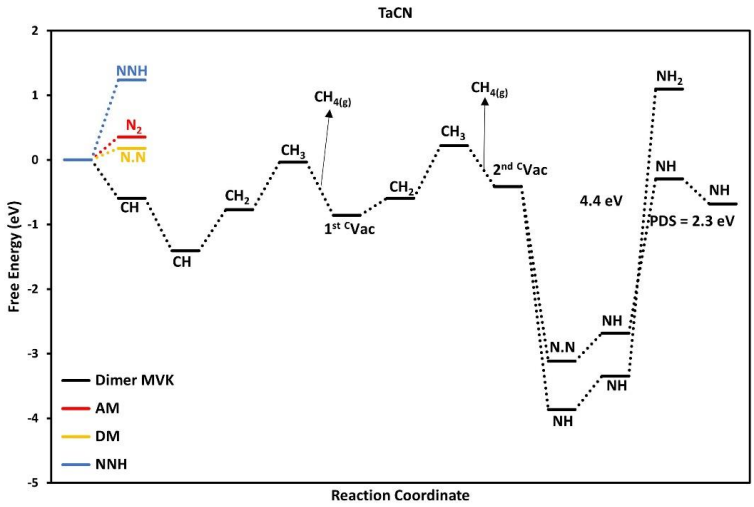

Figure S6 shows MvK, AM, and DM for carbon-nitrogen terminated surface of TaCN at zero potential.

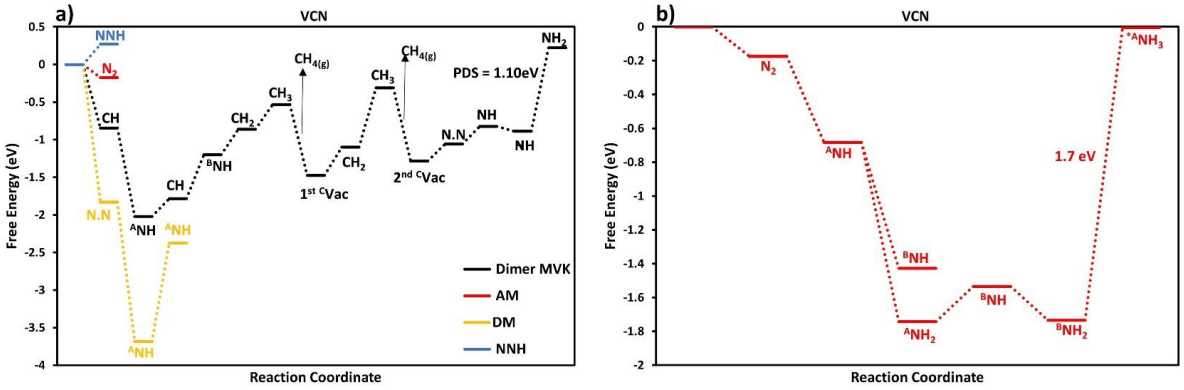

Figure S7 shows (a) MvK and DM (b) AM for carbon-nitrogen terminated surface of VCN at zero potential.

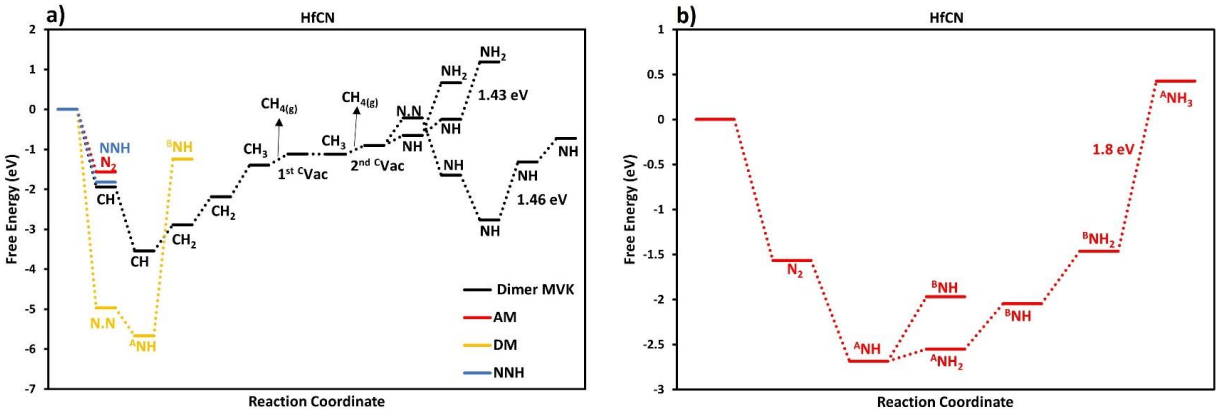

Figure S8 shows (a) MvK and DM (b) AM for carbon-nitrogen terminated surface of HfCN at zero potential.

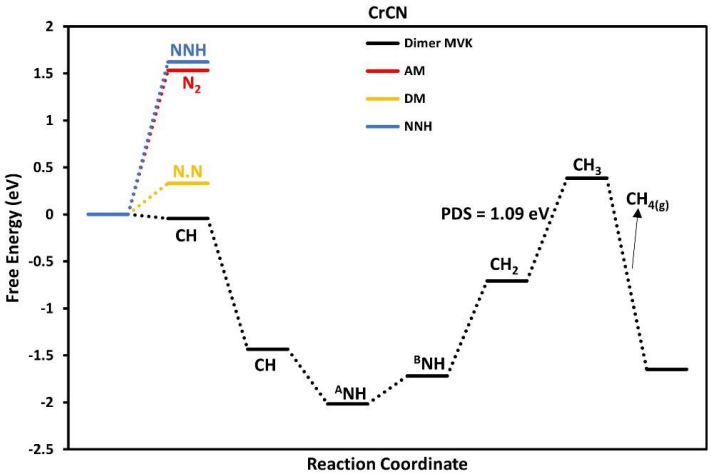

Figure S9 shows MvK, AM, and DM for carbon-nitrogen terminated surface of CrCN at zero potential.

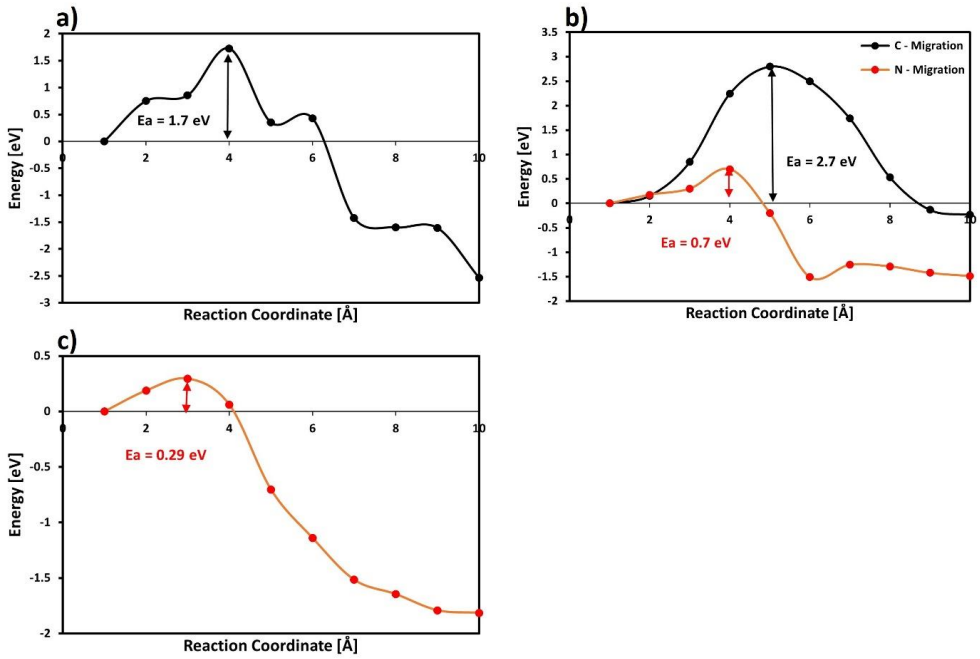

Figure S10: (a) The minimum energy path (MEP) for dissociating N_2 on WCN in the presence of dimer vacancy (b) migration of a carbon/nitrogen atom for WCN from a sub-layer to fill a vacancy on the surface, along with MEP computed for WCN and (c) Dissociation of N_2 to dimer N-vacancies on NbCN. The corresponding kinetic barrier values are denoted by their respective colors.

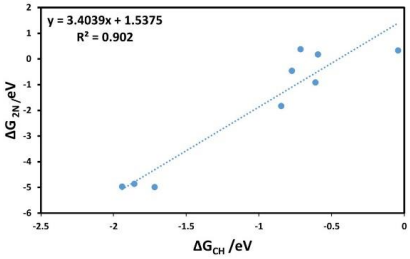
y = 3.4039x + 1.5375
R² = 0.902
ΔG2N /eV
ΔGCH /eV

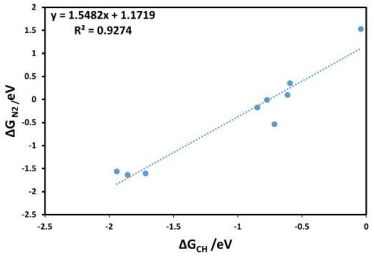
y = 1.5482x + 1.1719
R² = 0.9274
ΔGN2 /eV
ΔGCH /eV

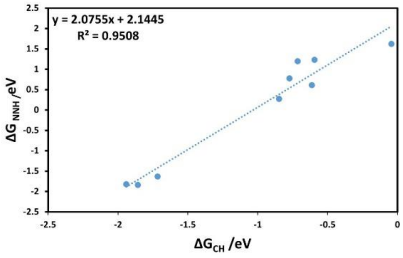
y = 2.0755x + 2.1445
R² = 0.9508
ΔGNNH /eV
ΔGCH /eV

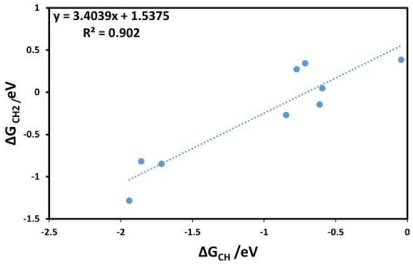
y = 3.4039x + 1.5375
R² = 0.902
ΔGCH2 /eV
ΔGCH /eV

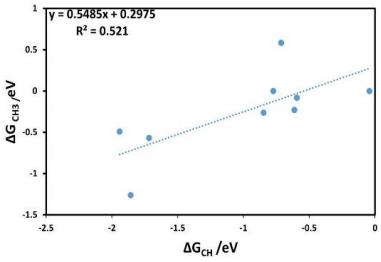
y = 0.5485x + 0.2975
R² = 0.521
ΔGCH3 /eV
ΔGCH /eV

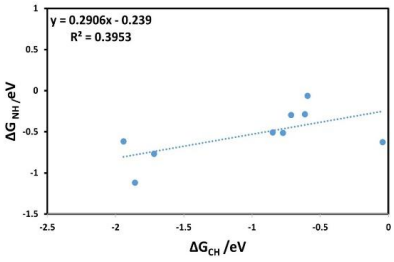
y = 0.2906x - 0.239
R² = 0.3953
ΔGNH /eV
ΔGCH /eV

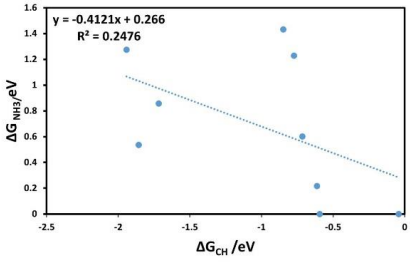
y = -0.4121x + 0.266
R² = 0.2476
ΔGNH3 /eV
ΔGCH /eV

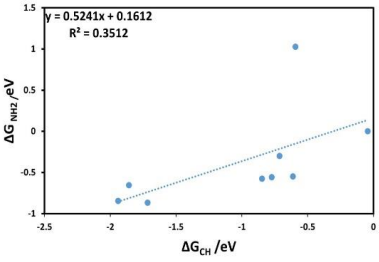
y = 0.5241x + 0.1612
R² = 0.3512
ΔGNH2 /eV
ΔGCH /eV

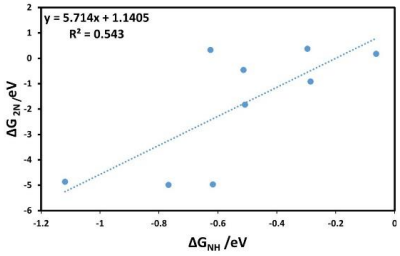
y = 5.714x + 1.1405
R² = 0.543
ΔG 2N /eV
ΔG NH /eV

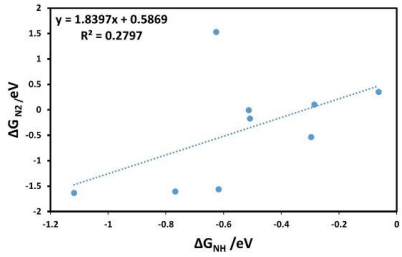
y = 1.8397x + 0.5869
R² = 0.2797
ΔG N2 /eV
ΔG NH /eV

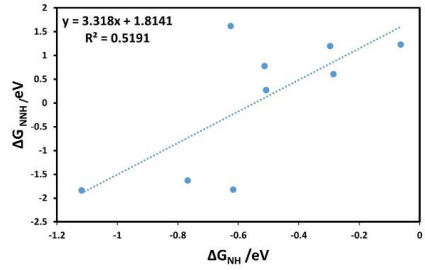
y = 3.318x + 1.8141
R² = 0.5191
ΔG NNH /eV
ΔG NH /eV

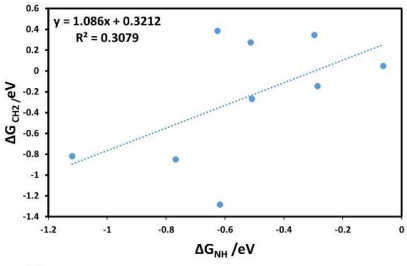
y = 1.086x + 0.3212
R² = 0.3079
ΔG CH2 /eV
ΔG NH /eV

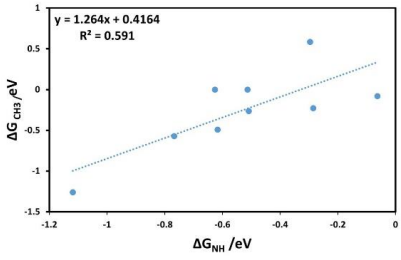
y = 1.264x + 0.4164
R² = 0.591
ΔG CH3 /eV
ΔG NH /eV

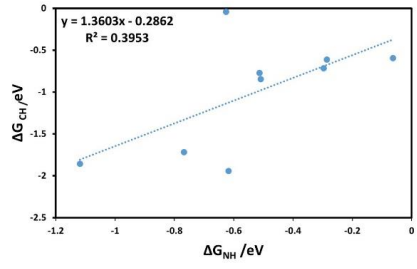
y = 1.3603x - 0.2862
R² = 0.3953
ΔG CH /eV
ΔG NH /eV

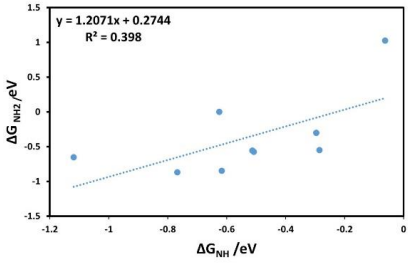
y = 1.2071x + 0.2744
R² = 0.398
ΔG NH2 /eV
ΔG NH /eV

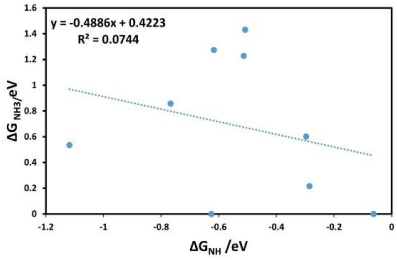
y = -0.4886x + 0.4223
R² = 0.0744
ΔG NH3 /eV
ΔG NH /eV

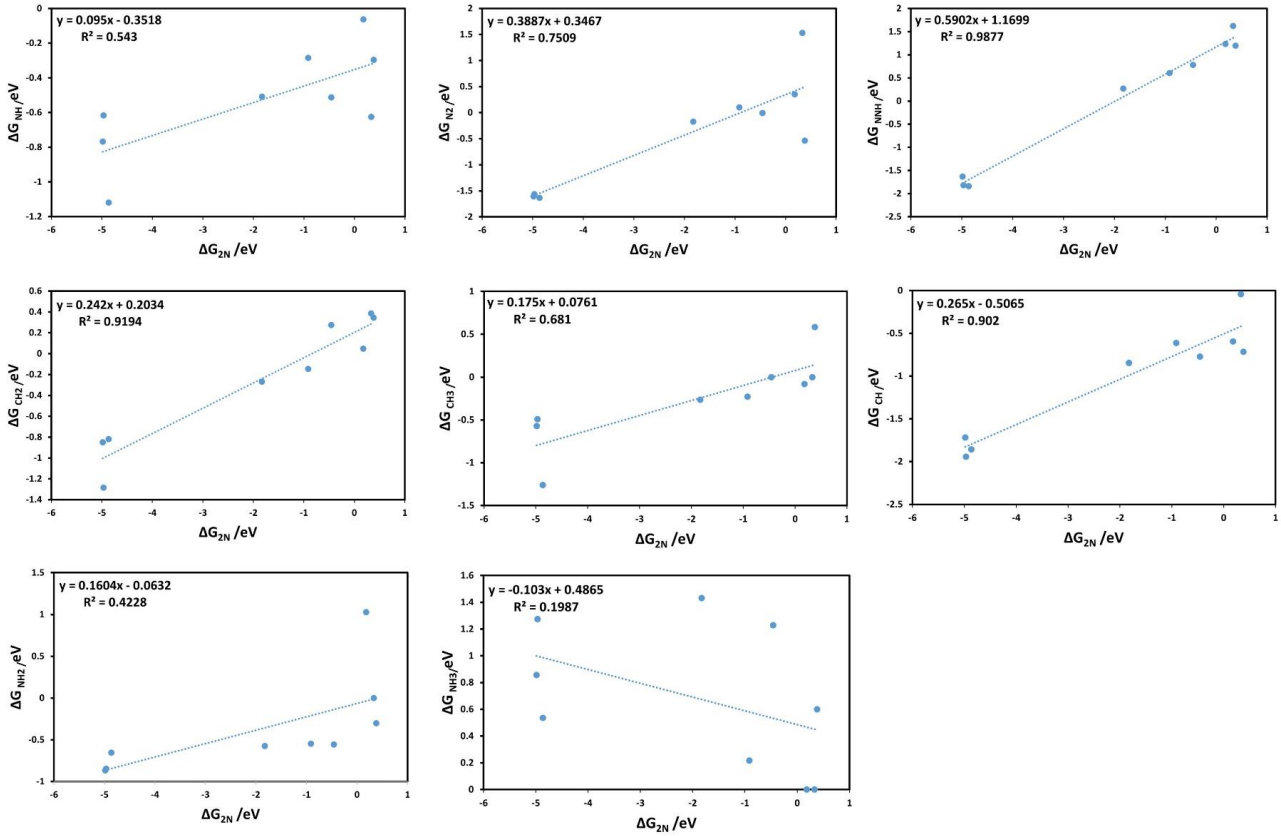

Figure S11: Scaling relations studied in this work are illustrated in the above figures where *CH, *NH and *2N is used as a descriptor. Although some of these relations are not a good fit, they are used to construct the volcano lines to guide the eye.

Bader charge analysis and charge iso-surfaces

We calculated the charge iso-surfaces by taking the charge density differences using the relation:

$\Delta P = P_{tot} - P_{pristine} - P_{gas}$

Here, P_{tot}, $P_{pristine}$, and P_{gas} represent the charge density for the species adsorbed on NbCN, the pristine NbCN system, and the isolated gas molecules, respectively. The colors yellow and cyan are used to represent charge accumulation and depletion, respectively. Figure S12(a)–(c) illustrates the charge density difference in N_2 adsorption on NbCN systems. To quantify the extent of charge transfer, we conducted a Bader charge analysis, and the outcomes are detailed in Table S2.

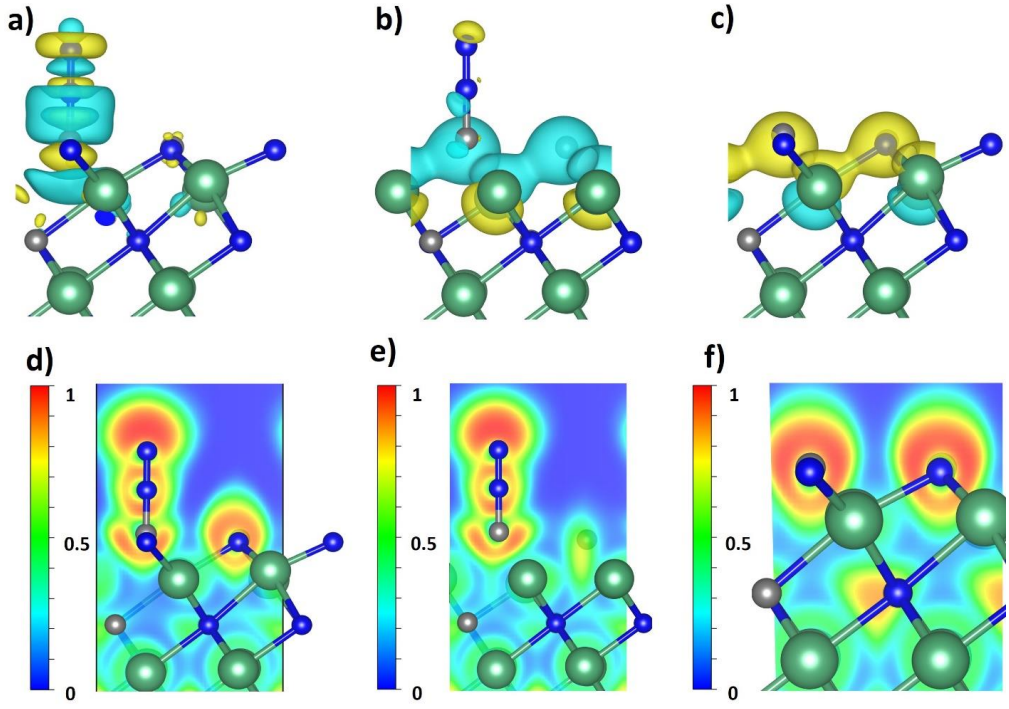

Figure S12. Charge density difference of (a) N_2 adsorbed on the pristine NbCN surface (b) N_2 adsorbed on the surface with a dimer N-vacancy while (c) vacancy filled by N_2. The yellow color shows charge accumulation and cyan represents charge depletion. Electron localization function of (d) N_2 adsorbed on the surface, (e) dimer N vacancies, and (f) vacancy filled by

N_2. The red (1) is associated with high values of electron localization function (ELF), indicating regions where electrons are more localized or confined, such as around lone pairs or in localized bonds. On the other hand, blue (0) is associated with low ELF values, representing regions where electrons are more delocalized or spread out.

Table S2. Adsorption Energy (ΔE), vertical distance (d_0), and charge transfer (ΔQ). All the distances, energies, and charge transfer are measured in Å, eV, and e, respectively. The reaction energies of all species are referenced to H_2, H_2O, and N_2.

System	H	O	OH	N_2	2N	NNH
ΔE (eV)	-0.91	-0.97	-0.17	-0.43	-1.43	0.60
d_o (Å)	1.10	1.16	1.32	1.29	1.19	1.21
ΔQ (e)	0.10	-1.05	-0.47	-0.48	-2.02	-0.60

It is important to note that a positive ΔQ value in Table S2 indicates a charge transfer from the NbCN layer to the gas molecule, while a negative ΔQ value suggests the opposite, where the charge transfers from the gas molecule to the NbCN layer. Examining Table S2, we can clearly see that in the H-adsorbed system, there was an overall charge transfer of 0.10 electrons from the adatom to the substrate. Conversely, in the N_2 adsorbed system, there was a charge transfer of 0.48 electrons from the substrate to the admolecule. The charge density difference and iso-surface for H, O, OH, 2N, and NNH are provided in Figure S13. For comparative purposes, we have also included the charge density differences and iso-surfaces for various species in vacancies, which can be found in the Figure S14. The ELF assesses electron density behavior, aiding in the distinction between localized regions with paired or lone pairs of electrons and more distributed areas shared across multiple atoms [2]. In our study, we explored ELF based on the most favorable adsorption sites for various species on the NbCN system. ELF values, ranging from 0 to 1, signify complete delocalization (as in metallic systems) to strong localization (such as lone pairs or covalent bonds). The anticipated ELF results for species on NbCN (111) facets are depicted in Figure S12(d–f), Figure S13 (f-j) and Figure S14 (g-l). Overall, the ELF outcomes highlight the covalent bonding characteristics of all species on NbCN, indicating shared-electron interactions. In summary, our analysis of charge transfer in the NbCN system reveals distinct behaviors between

different gas molecules, with H-adsorbed systems showing a transfer from adatom to substrate and N_2-adsorbed systems exhibiting the opposite trend. Additionally, examination of charge density differences and iso-surfaces, along with electron localization function (ELF) assessments, underscores the covalent bonding nature across various species on the NbCN substrate.

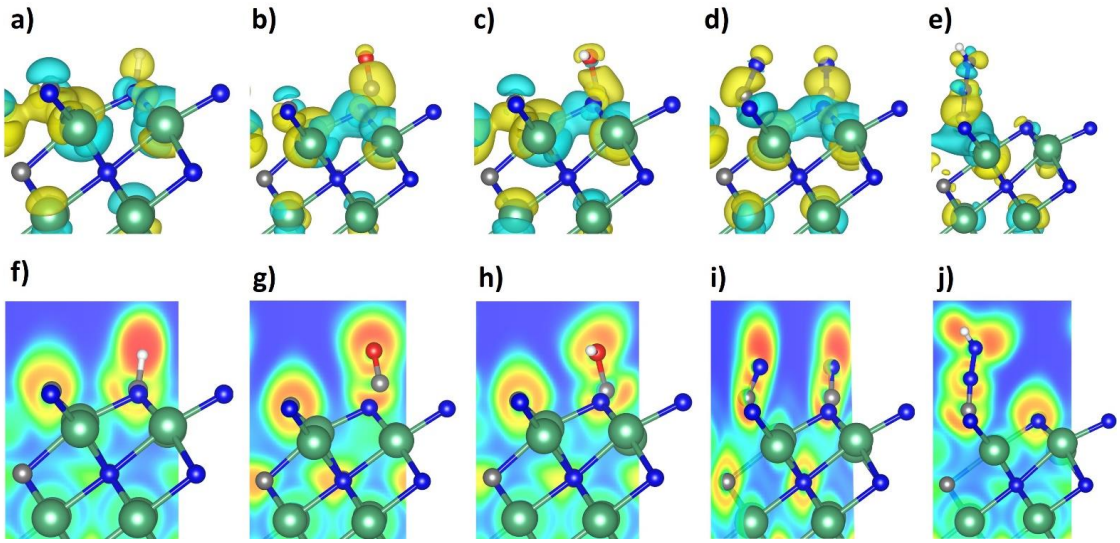

Figure S13 show Charge density difference of (a) H adsorbed on the surface (b) O adsorbed on the surface (c) OH adsorbed on the surface (d) N_2 dissociative adsorbed on the surface (e) NNH adsorbed on the surface and (f), (g), (h), (i), (j), are the isosurface for the mention species. The yellow colors show charge accumulation and the cyan shows charge depletion.

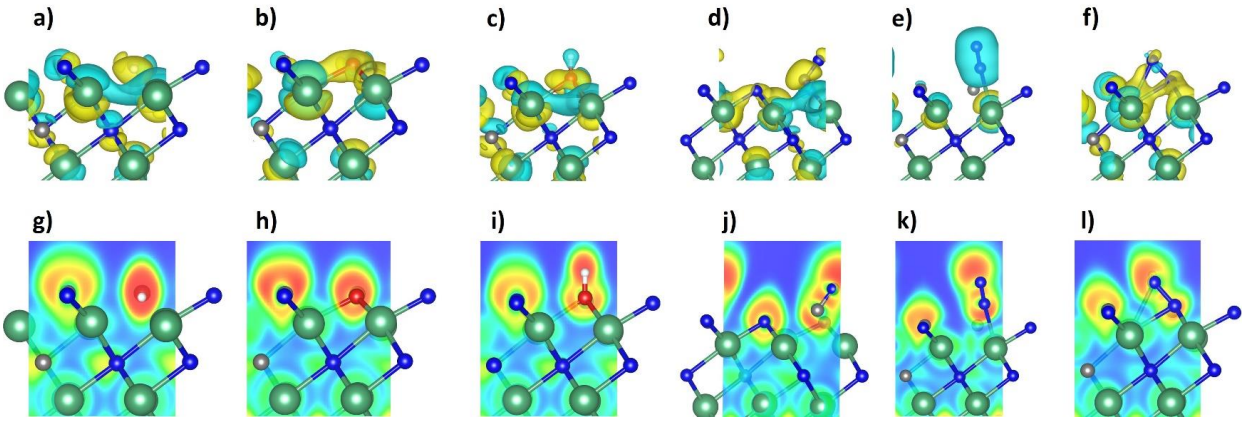

Figure S14 show Charge density difference of (a) H adsorbed in nitrogen vacancy (b) O adsorbed in nitrogen vacancy (c) OH adsorbed in nitrogen vacancy (d) N_2 dissociative adsorbed in nitrogen vacancy, (e) N_2 associatively adsorbed in nitrogen vacancy (f) NNH adsorbed in nitrogen vacancy and (g), (h), (i), (j), (k), (l) are the isosurface for the mention species. The yellow colors show charge accumulation and the cyan shows charge depletion.

References:

[1] Che, M. and J.C. Védrine, *Characterization of solid materials and heterogeneous catalysts: From structure to surface reactivity*. 2012: John Wiley & Sons.

[2] Fan, K., Ying, Y., Li, X., Luo, X., & Huang, H. (2019). Theoretical investigation of V3C2 MXene as prospective high-capacity anode material for metal-ion (Li, Na, K, and Ca) batteries. The Journal of Physical Chemistry C, 123(30), 18207-18214.

Paper IV

Catalytic Nitrogen Reduction on the Transition Metal Carbonitride (110) Facet: DFT Predictions and Mechanistic Insights

Iqbal, A., E. Skulason, and Y. Abghoui,

The Journal of Physical Chemistry C. DOI: 10.1021/acs.jpcc.4c02148

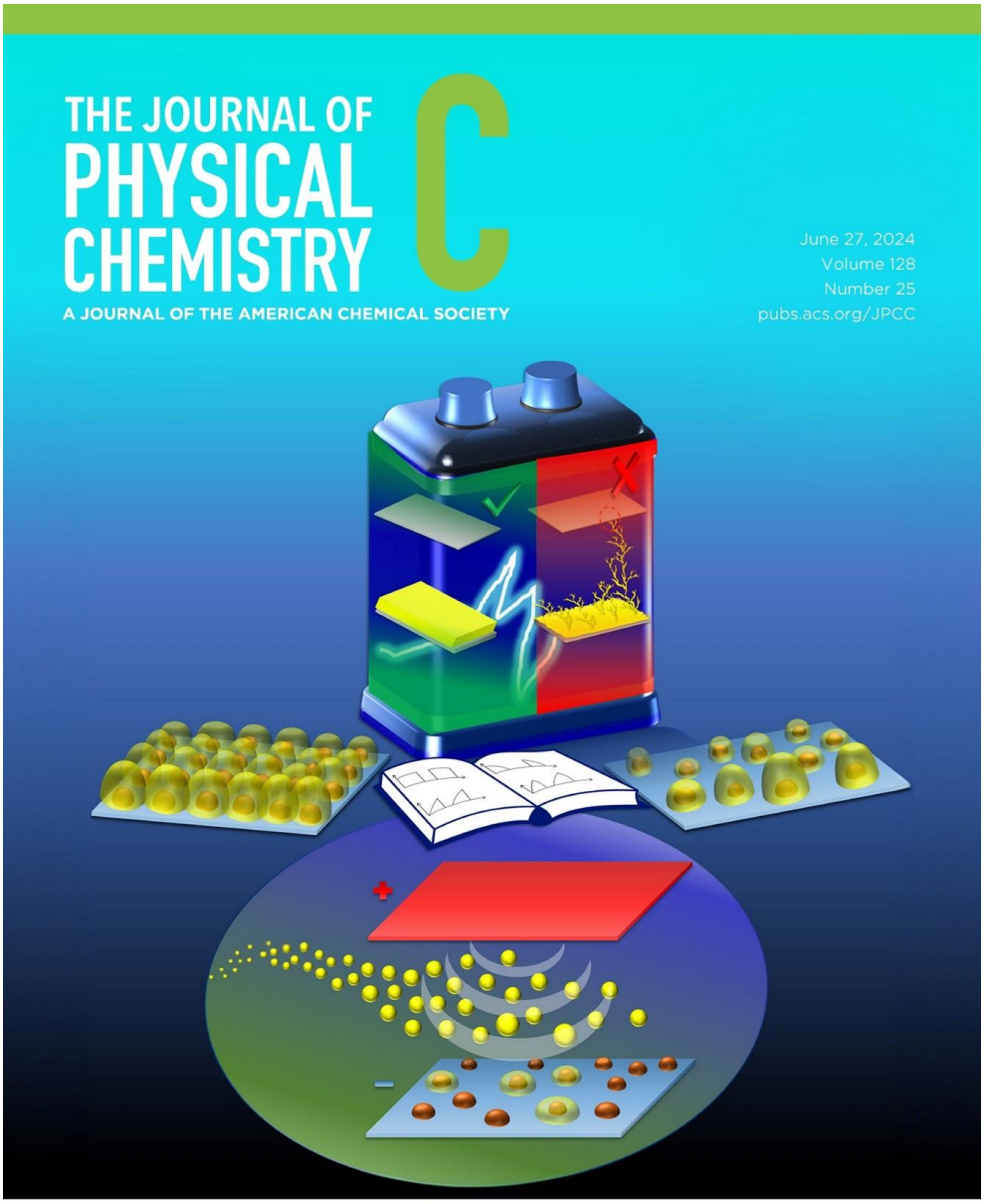
THE JOURNAL OF
PHYSICAL
CHEMISTRY
C
A JOURNAL OF THE AMERICAN CHEMICAL SOCIETY
June 27, 2024
Volume 128
Number 25
pubs.acs.org/JPCC
ACS Publications
Most Trusted. Most Cited. Most Read.
www.acs.org

THE JOURNAL OF PHYSICAL CHEMISTRY C
A JOURNAL OF THE AMERICAN CHEMICAL SOCIETY

pubs.acs.org/JPCC

Article

Catalytic Nitrogen Reduction on the Transition Metal Carbonitride (110) Facet: DFT Predictions and Mechanistic Insights

Published as part of The Journal of Physical Chemistry C virtual special issue "Jens K. Nørskov Festschrift".

Atef Iqbal, Egill Skúlason, and Younes Abghoui*

Cite This: https://doi.org/10.1021/acs.jpcc.4c02148

Read Online

ACCESS | Metrics & More | Article Recommendations | Supporting Information

ABSTRACT: We present a comprehensive exploration of potential catalysts for the electroreduction of nitrogen at ambient conditions through theoretical analyses using density functional theory (DFT) calculations. Our focus is on the (110) texture orientations of rock salt (RS) structures of 11 transition metal carbonitrides (TMCN). The catalytic activity is assessed by constructing free energy diagrams for three different reaction mechanisms: associative, dissociative, and Mars−van Krevelen mechanisms. Additionally, we scrutinize the stability of these materials against poisoning in electrochemical media and decomposition to parental metals under operational conditions. Among the carbonitrides studied, VCN and NbCN emerge as stable and active catalysts for nitrogen reduction reactions (NRRs), exhibiting low onset potentials (−0.42 and −0.78 V vs RHE) at ambient conditions, while MoCN is active at nonambient conditions because of a relatively high kinetic barrier (1.18 eV) for N_2 splitting. However, TaCN and ScCN show activity for ammonia under ambient conditions but are found to be unstable during vacancy migration. An important discovery in our present research is that hydrogen evolution is predicted to have a higher overpotential than nitrogen reduction to ammonia on the carbonitride candidates studied herein.

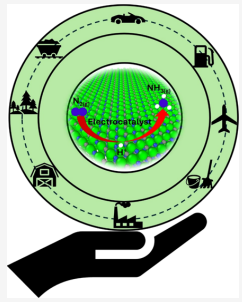

1. INTRODUCTION

Nitrogen stands as a fundamental component of biological entities and holds intimate ties with human existence.[1] Despite comprising approximately 78% of the atmosphere in the form of nitrogen gas, it predominantly exists as diatomic molecules (N_2), inaccessible to most plants and animals.[2] The conversion of nitrogen into ammonia holds paramount importance due to the versatility of ammonia's applications. Apart from its role as a crucial raw material in agricultural processes, ammonia finds utility in pharmaceuticals, dyes, textiles, and various industrial productions.[3−5] Furthermore, ammonia serves a pivotal function in energy conversion endeavors, being recognized as a portable, carbon-free energy carrier with high energy density, poised to contribute significantly to the prospective hydrogen economy.[6,7] Consequently, the conversion of nitrogen gas (N_2) to ammonia emerges as a vital biochemical process essential for sustaining life on Earth. In nature, the biological fixation of N_2 takes place through nitrogenase enzymes in specific bacteria, operating under mild conditions.[8,9] However, this natural mechanism falls short of meeting industrial demands. The advent of the Haber−Bosch process in the early 20th century brought about a significant shift in the global nitrogen cycle. Typically, ammonia is artificially produced via the Haber−Bosch process ($N_2 + 3H_2 \rightarrow 2NH_3$), which necessitates high temperatures (300−500 °C), exceedingly high pressures (150−300 atm), and the use of high-purity nitrogen and hydrogen gases.[10] Consequently, this process is estimated to constitute approximately 1−3% of the world's annual energy consumption and generate substantial greenhouse gas emissions.[11,12] Clearly, this approach lacks long-term economic viability and environmental sustainability. Hence, it is imperative to devise a carbon-neutral and sustainable method for ammonia synthesis to address the fossil energy crisis and mitigate global warming.

In recent years, a range of alternative methods have been explored to achieve cost-effective artificial nitrogen fixation, encompassing biochemical catalysis, photocatalysis, thermal catalysis, and electrocatalysis.[13−17] Among these strategies, electrochemical reduction of N_2 emerges as particularly promising, leveraging the advantages of utilizing electric energy sourced from renewable solar and wind energy, along with direct proton utilization from water as the hydrogen source.[18,19] Hence, the advancement of the electrocatalytic nitrogen reduction reaction (NRR) holds profound significance in reshaping the energy landscape, mitigating the energy crisis, and addressing environmental concerns. The primary challenge in NH_3 synthesis lies in the intrinsic inertness of diatomic N_2, characterized by a robust N≡N bond and

Received: April 2, 2024
Revised: May 27, 2024
Accepted: May 28, 2024

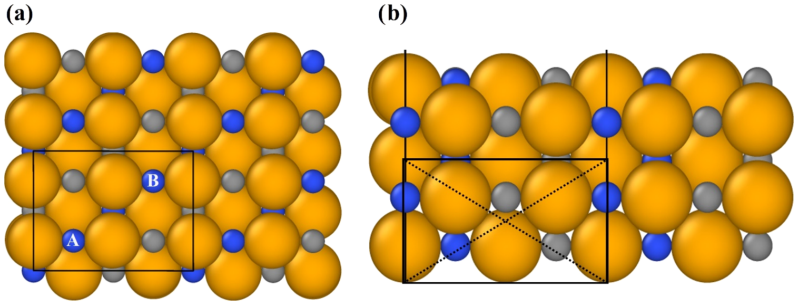

Figure 1. (a) Top view and (b) side view of a 5-layer TMCN model system on the (110) facets of the RS surface, as employed in computational simulations. Metal, carbon, and nitrogen atoms are depicted by dark yellow, gray, and blue spheres, respectively.

consequent lack of a permanent dipole, alongside low solubility in aqueous solutions.[20−22] Additionally, progress in the electrochemical NRR faces obstacles posed by the prevalent competition from the hydrogen evolution reaction (HER), attributable to the preferential adsorption of H atoms over N atoms on conventional NRR catalysts, including Fe and Ru.[23,24] Consequently, the majority of NRR endeavors report a limited ammonia yield and faradaic efficiency.

So far, a variety of electrocatalysts for the NRR have been developed, including noble metals,[25,26] transition metal sulfides,[27] transition metal nitrides (TMN),[28−31] transition metal oxides (TMO),[32,33] transition metal oxynitrides (TMON),[34,35] transition metal carbides (TMC),[36] transition metal carbonitrides (TMCN),[37,38] and metal-free materials.[39−44] Enhancing NRR performance requires comprehensive optimization of the entire electrochemical system, encompassing the cell configuration, electrolyte, and electrocatalysts.[45] Notably, electrocatalysts play a crucial role in accelerating reaction rates and improving the selectivity and efficiency in electrochemical NRR systems. Achieving a high-selectivity and high-performance NRR under ambient conditions necessitates the rational design of efficient electrocatalysts capable of activating inert N≡N bonds, expediting their dissociation, and mitigating the competing HER. Typically, there are two avenues for enhancing activity in electrocatalyst design: augmenting apparent activity or promoting intrinsic activity.[46] In terms of the former, the apparent activity of electrocatalysts hinges on the abundance of exposed electrochemically active sites. In contrast, intrinsic activity relates to the effectiveness of the active site, which is influenced by the electronic structure of the electrocatalysts. Rational catalyst design, which involves methods like introducing various vacancies and heteroatoms, crafting specific structures, exposing active crystal facets, inducing amorphization, and fabricating novel heterointerfaces, serves as an effective means to boost apparent activity and/or enhance intrinsic activity.[47−54] Moreover, other strategies such as altering electrolytes, improving mass transfer rates, and devising specific electrolytic systems can also contribute to achieving high NRR performance.[55−57] Over the past few decades, these strategies have been successfully applied in the design of heterogeneous electrocatalysts for various applications including the HER,[58,59] oxygen evolution reaction (OER),[60,61] oxygen reduction reaction (ORR),[62,63] and carbon dioxide reduction reaction (CO_2RR).[64−67]

In this investigation, we utilize theoretical calculations to sift through a spectrum of rock salt (RS) (110) TMCN surfaces, aiming to identify a stable and efficacious catalyst for electrochemical nitrogen activation and subsequent ammonia production. Employing density functional theory (DFT) calculations, we delve into the thermodynamics of the cathode reaction. To delineate the electrochemical protonation of surface nitrogen or metal atoms, we construct free energy diagrams, thereby discerning the onset potentials necessary for the ammonia synthesis on these TMCN structures. The impact of an external bias is factored in by referencing the computational standard hydrogen electrode,[68] enabling estimation of the lowest onset potential required for ammonia production on each carbonitride. We have seen that using this simple model of including the effect of bias implicitly compares well with more detailed calculations on both Ru and W electrodes where the bias is included explicitly and energy barriers are low for the NRR, concluding that the thermodynamics of adsorbed intermediates is sufficient in order to predict overpotentials.[69,70] Furthermore, we evaluated the stability of active sites in an electrochemical environment and the susceptibility of the catalyst to poisoning under applied bias. Additionally, we explore the probability of catalyst regeneration versus decomposition for the most promising candidates among these RS (110) materials.

2. METHODOLOGY

In all computational simulations, we utilize the revised Perdew−Burke−Ernzerhof (RPBE)[71] exchange-correlation functional within the framework of DFT. The Vienna Ab initio Simulation Package (VASP)[72] is employed, using a Monkhorst−Pack *K*-point grid of 4 × 4 × 1 and 500 eV energy cutoff for each surface calculation. The VASP code incorporates the projector augmented wave (PAW)[73] method, enabling the use of computationally efficient pseudopotentials and leading to significant reductions in computational time.[74,75] To address electron distribution, a Fermi−Dirac distribution with a smearing value of k_BT = 0.1 eV is applied to smooth the Kohn−Sham orbital occupancy. All surfaces are analyzed within the RS crystallographic structure, maintaining a (110) surface orientation. This choice is motivated by the enhanced stability of this structure and its facets, allowing for a comparison with previous studies on TMN, TMC, and TMCN surfaces of other orientations conducted by the same research group.[33−35,76−78] The TMCN surfaces are depicted using a 5-layer 2 × 2 unit cell, comprising 20 metal atoms, 10 carbon atoms, and 10 nitrogen atoms, as illustrated in Figure 1 on the (110) facets.

The lower two layers are held in their equilibrium bulk structure, while the three upper layers and any adsorbates are

https://doi.org/10.1021/acs.jpcc.4c02148
J. Phys. Chem. C XXXX, XXX, XXX−XXX

allowed to undergo relaxation. Periodic boundary conditions are applied along the x and y dimensions, and lattice constants are shown in Table S2; a minimum separation of 15 Å is maintained in the z direction between each surface slab. The structural optimization is considered satisfactory when the collective forces on all movable atoms fall below 0.01 eV/Å. To compute activation energies, the climbing image nudged elastic band technique (CI-NEB) is employed to identify the highest point along the minimum energy path (MEP).[79] Additionally, Bader analysis and charge density difference, as previously detailed, are utilized in this study.[80,81] The electrochemical methodology has been explained in detail in our previous work.[37,38]

3. RESULTS AND DISCUSSION

Initially, computational screening is employed on a variety of transition metal carbonitride catalysts spanning from group III to group XII in the RS structure with (110) facets. This study explores a total of 11 TMCN surfaces, namely, ScCN, YCN, TiCN, ZrCN, HfCN, VCN, NbCN, TaCN, CrCN, MoCN, and WCN, which prove to be stable and are consequently further investigated as potential catalysts for the NRR. The assessment of these candidates for electrochemically producing ammonia under ambient conditions involves an examination of eight factors. These factors include (i) the mechanism for the NRR, (ii) surface poisoning, (iii) catalytic performance, (iv) catalyst surface vacancy poisoning, (v) the stability of a surface N/C vacancy as an indicator of decomposition, (vi) the calculated kinetic barrier required for N_2 to dissociate and occupy the vacancy, (vii) volcano plot analysis to display OP for each TMCN as a function of the descriptor of reactivity, and (viii) Bader charge analysis and charge distribution analysis through charge isosurfaces.

3.1. Mechanism of the Nitrogen Reduction Reaction. We investigated three mechanisms for the NRR: (1) associative mechanism (AM), (2) dissociative mechanism (DM), and (3) Mars–van Krevelen (MvK) mechanism. Figure 2 illustrates these three primary mechanisms schematically, along with possible combinations, such as when MvK is employed to create either a C vacancy or an N vacancy with the second half of the mechanism being either AM or DM.

In the DM, the N_2 triple bond undergoes cleavage during adsorption, resulting in the separate adsorption of N atoms at carbon sites. It is important to note that, at this stage, we exclusively calculated the thermodynamics of N_2 dissociative adsorption, without the consideration of kinetic barriers because later in the analysis, it was observed that the DM yields significantly high OP along the reaction path, making it unfeasible, and as a result, kinetic barriers are not computed in the end for N_2 dissociation.

In the case of AM, N_2 is adsorbed on the surface and undergoes breaking later at a specific stage in the hydrogenation process. Within the AM, we also explored the possibility of *NNH adsorption as the initial step in the reaction and incorporated it into the free energy diagrams.

In the MvK mechanism, the lattice N/C atoms on the surface of TMCNs can be converted into ammonia or methane, depending on favorable proton adsorption on N or C, generating vacancies in the process. These vacancies can be chemically refilled by nitrogen molecules either through an associative process (via associative MvK) or through a dissociative process (via dissociative MvK) to regenerate the catalyst. It was observed that different species adsorb exclusively on bridge sites between two metal atoms rather than on carbon, nitrogen, or metal sites.

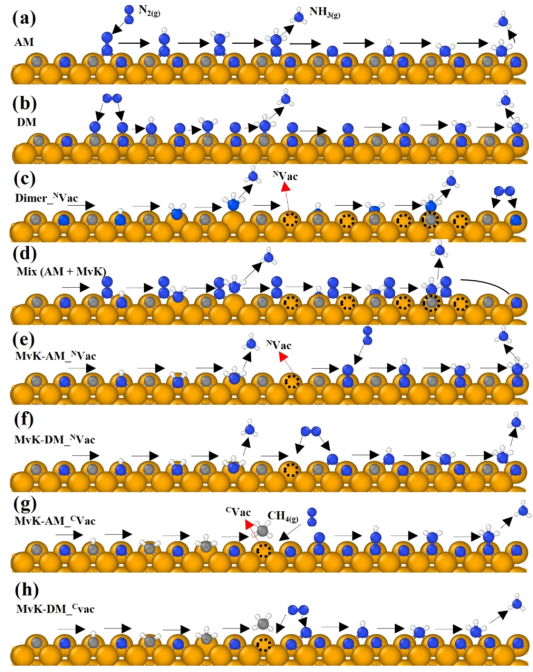

Figure 2. General schematic diagram of the possible reaction mechanisms investigated in this work.

3.2. Surface Poisoning. To initiate any reactivity, it is crucial to scrutinize the adsorption of nitrogen species onto the surface, taking into account the presence of competing species such as H, O, and OH. In the realm of nitrogen adsorption, we compared the associative adsorption of nitrogen gas ($*N_2$), the dissociative adsorption of nitrogen gas (*2N), and the associative adsorption of NNH (*NNH) with the adsorption of H, O, and OH. The findings regarding nitrogen adsorption and the potential for active site poisoning by other species are illustrated in Figure 3. As observed, most of the TMCNs absorb 2N more strongly compared to other species except NbCN, MoCN, HfCN, and ZrCN. Additionally, we examined the adsorption of protons on the metal sites (indicative of the HER), and surprisingly, protons were consistently found to migrate to the carbon or nitrogen sites in all cases except NbCN, MoCN, and CrCN where the respective free energy values were 0.21, 0.12, and 2.37 eV. This implies that proton adsorption on metal sites contributing to the HER is unlikely for all TMCNs.

3.3. Catalytic Activity. We conducted an extensive analysis of the reaction on the RS (110) facets of TMCNs, considering various mechanisms as outlined earlier for all 11 TMCNs. However, we have chosen to present the free energy diagrams exclusively for the most promising candidates, while the data for the remaining TMCNs can be found in the Supporting Information (ESI). As illustrated in Figure 4, the optimal path for ammonia production on VCN is the MvK mechanism. In this mechanism, we started protonation from the clean surface, and after the sixth protonation step, we formed the first ammonia and a nitrogen vacancy. We

https://doi.org/10.1021/acs.jpcc.4c02148
J. Phys. Chem. C XXXX, XXX, XXX−XXX

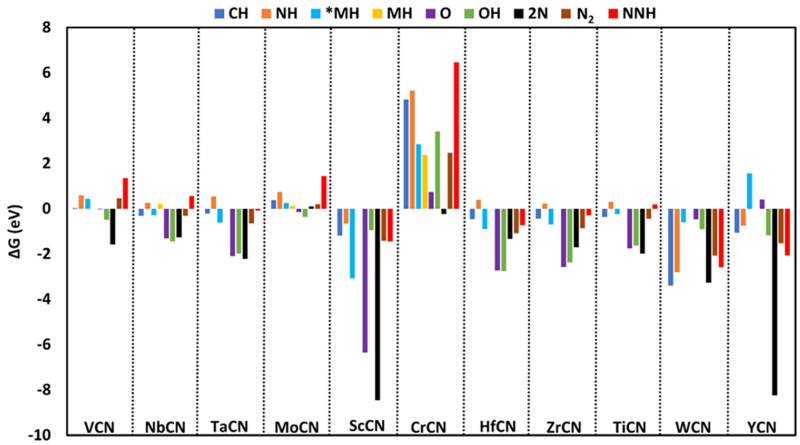

Figure 3. Comparison of the adsorption energies of various species on clean TMCN surfaces.

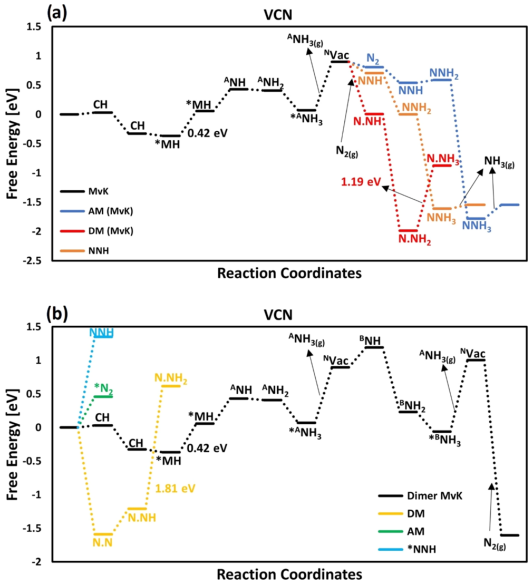

Figure 4. (a) Free energy diagrams for NH_3 formation via the most favorable pathway of RS structures in (110) facets: (a) VCN with a single vacancy and replenished with N_2 and (b) VCN for the dimer vacancy and replenished with N_2.

replenish that vacancy with nitrogen gas associatively (N_2) and dissociatively (2N) and NNH associatively. It can be seen from Figure 4a that MvK-DM does not work at ambient conditions because of the high potential-determining step (PDS) (1.19 eV), while MvK-AM and NNH work with the PDS corresponding to the sixth protonation step, linked to the proton sitting on the bridge side between two metal atoms, exhibiting ΔG_{PDS} values of 0.42 eV. The NH_3 desorption is not an electrochemical step, and in the experiment, it may be reduced further to NH_4^+ in acidic electrolytes and then released from the surface.[82,83] However, in neutral or alkaline media, this may become a bottleneck.

We have explored the possibility of forming a dimer to generate a second ammonia molecule, resulting in the release of two ammonia molecules after a transfer of $10(H^+ + e)$ as shown in Figure 4b. The two N vacancies are found to be exergonically refilled by N_2 from air to the N vacancies. This process is determined to have a small energy barrier (0.42 eV) based on the NEB-CI calculations, as shown in Figure S11(a). For NbCN with MvK as shown in Figure S1(a), the PDS corresponds to the sixth protonation step, resulting in the formation of NH_2. Following the creation of the first N vacancy, we replenish this vacancy with N_2 through a different mechanism as shown in Figure S1(a). Additionally, we investigated the dimer vacancy with N_2 on the surface, which can tune the PDS to 0.81 eV (the green path) as shown in Figure S1(b). Upon examination of the kinetics of N_2 dissociation into dimer N vacancies on NbCN, our NEB calculations revealed an activation energy of 0.78 eV, as depicted in Figure S11(b). In the case of MoCN, we first carried out protonation with DM, which is only a bit endergonic (0.1 eV) resulting in the release of two ammonia molecules after a transfer of $6(H^+ + e)$ with the ΔG_{PDS} of 0.69 eV. Furthermore, we calculated the kinetic energy for N_2 splitting and found a high energy barrier (1.18 eV) on MoCN as shown in Figure S11(d) and is active for the NRR at nonambient conditions. With the MvK, it can be seen in Figure S2 that it is difficult to release ammonia (1.31 eV). Although TaCN and ScCN release two ammonia molecules with the PDS of 1.0 and 1.06 eV, respectively, they are unstable upon vacancy migration, which will be discussed later in Section 3.5. A clear path to making ammonia from other materials is not obvious even after trying many steps involving protonation, as explained in Figures S3–S10. This difficulty is mostly due to either a high PDS or the creation of unwanted byproducts like CH_4. Hence, it is apparent from our analysis that VCN stands out as the only one capable of releasing two ammonia molecules with a minimal PDS of 0.42 eV.

3.4. Poisoning of the Defects/Vacancies. For the catalytic cycle to proceed, it is imperative the created surface vacancies be filled by N_2. However, there exists a likelihood that the nitrogen vacancy remains unoccupied by nitrogen due to obstruction by a proton, an oxygen atom, or a hydroxyl atom from the aqueous electrolyte. Consequently, the free

https://doi.org/10.1021/acs.jpcc.4c02148
J. Phys. Chem. C XXXX, XXX, XXX−XXX

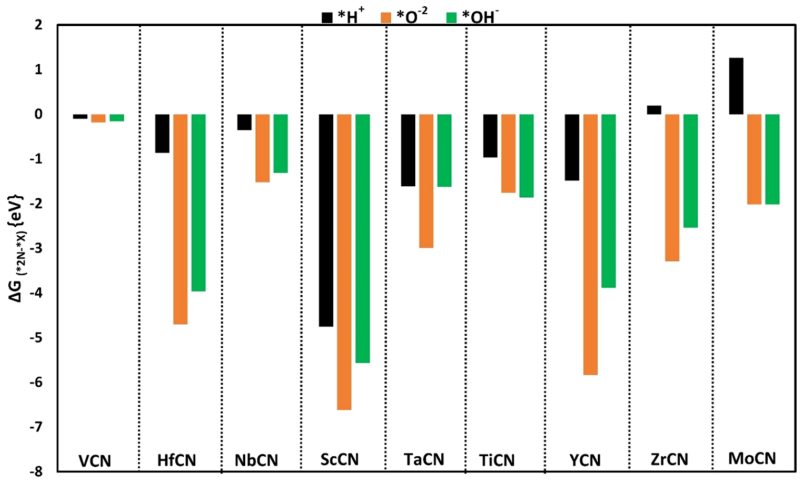

Figure 5. Vacancy poisoning with different species at the onset potential predicted for the NRR.

energy of filling the vacancy with any of these species in comparison to nitrogen ($\Delta G(*2N-*X)$), where X = O, H, or OH, is employed to analyze the competition between N with O, H, and OH for filling the surface vacancy. In practical scenarios, these ions are derived from water in the electrolyte, leading to the formation of O^{2-}, OH^-, and H^+. A negative value of $\Delta G(*2N-*X)$ indicates that nitrogen adsorption is thermodynamically more favorable than the other three species for filling the vacancy. The corresponding values are depicted in Figure 5 for the entire group of catalytically active carbonitrides at the predicted onset potential.

Nitrogen atoms exhibit stronger absorption to surface vacancies compared to H, O, and OH in all carbonitrides, with the exception of ZrCN and MoCN. Notably, placing N on the H atom in the case of ZrCN and MoCN, which is adsorbed in the surface vacancy, forms NH without encountering any barrier. This prediction suggests that the surface vacancies of all of these carbonitrides will not be susceptible to poisoning by these species. In summary, VCN and NbCN emerged as the most promising choice, showcasing both high activity (as shown in Figures 4 and S1(b)) and stability against poisoning (as depicted in Figure 5). These carbonitrides possess the capability to convert nitrogen to ammonia at potentials of −0.42 and −0.78 V, respectively.

3.5. Stability against Decomposition. The reduction of a surface nitrogen−carbon atom within the MvK mechanism results in NH_3/CH_4 formation, followed by the occupation of the ensuing vacancy by a gaseous N_2 molecule. The stability of the surface N/C vacancy is crucial for this replenishment process. If the N/C vacancy is not stable, there is a risk that the sublayer's C or N atoms might migrate to the surface of the catalyst and get further reduced. This cycle could continue until all carbon and nitrogen atoms in carbonitrides had reduced to form NH_3/CH_4, potentially leading to the decomposition of TMCN to the original metal. The energy difference between a carbonitride slab with a single N/C vacancy in the surface layer ($E_{vac,1}$) and the first subsurface layer ($E_{vac,2}$) serves as a determinant of the stability of the N/C vacancy at the catalytic surface. The energy difference ($\Delta E_{vac} = E_{vac,2} - E_{vac,1}$) is utilized to assess the thermodynamic stability of the vacancy at the carbonitride's surface. The kinetics of this process was also investigated and is shown in Figure 6 together with the thermodynamics.

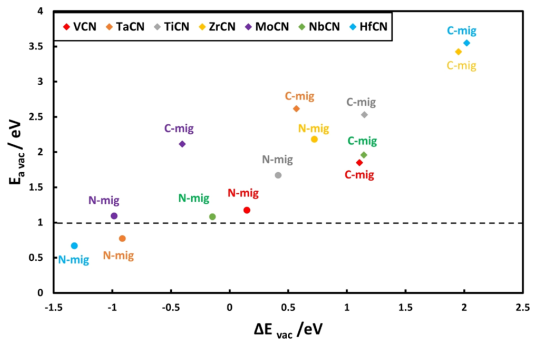

Figure 6. Thermodynamics and kinetics of vacancy migration between the sublayer and the surface layer.

It is revealed that for the majority of carbonitrides, it is thermodynamically favorable for the vacancy to migrate to the bulk. However, a large kinetic energy was found for most of the TMCNs for the vacancy migration that could slow down this process at ambient conditions and thus enable stability until the vacancy replenished with N_2. Thus, most of these carbonitrides are expected to have stable surface vacancies except TaCN, HfCN, and ScCN where N from the sublayer migrates to the surface layer.

3.6. Exploring the Scaling Relations and Formation of Volcano Plots. By employing linear relationships for various reaction steps as a function of the ΔG of *NH (used as a descriptor), we can construct a volcano diagram. This methodology, as described in the ref 84, was previously applied to the electrolysis of water on oxide surfaces. In this approach, the potential associated with the potential-limiting step serves as a direct indicator of the electrocatalytic activity. The free energy of each fundamental step in the reaction can be expressed as a function of the applied bias (U) and the ΔG of

https://doi.org/10.1021/acs.jpcc.4c02148
J. Phys. Chem. C XXXX, XXX, XXX−XXX

NH denoted by *NH. Utilizing the linear scaling relationships from Figures S12 and S13, we can construct the volcano plot, as illustrated in Figure 7, considering the MvK. Significantly, VCN is situated at the peak of the MvK volcano, with MoCN and NbCN nearby, indicating low overpotentials.

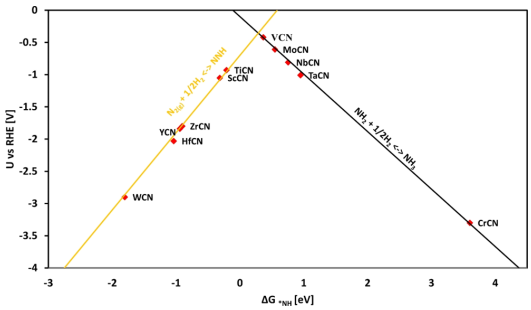

Figure 7. Theoretical volcano plot.

4. CONCLUSIONS

We presented a theoretical analysis exploring the potential of nitrogen electroreduction to ammonia under ambient conditions, focusing on the (110) facets of rock salt structures of ScCN, YCN, TiCN, ZrCN, HfCN, VCN, NbCN, TaCN, CrCN, MoCN, and WCN. Among these, WCN, TiCN, YCN, HfCN, CrCN, and ZrCN were found to be inactive for ammonia formation, while TaCN and ScCN were found to be unstable. Considering the kinetics, we evaluated whether the nitrogen vacancy created during the catalytic cycle would be regenerated with N_2 molecules or become unstable and migrate into the bulk of the nitride. The calculation of activation free energy for both processes revealed that only VCN and NbCN are anticipated to be promising candidates capable of regeneration and sustaining the catalytic cycle of nitrogen activation and ammonia formation under ambient conditions with overpotentials of −0.42 and −0.78 V vs RHE, respectively.

■ ASSOCIATED CONTENT

Supporting Information

The Supporting Information is available free of charge at https://pubs.acs.org/doi/10.1021/acs.jpcc.4c02148.

Gibbs free energy, lattice constants, Bader charge analysis, and free energy diagrams for all other transition metal carbonitrides (PDF)

■ AUTHOR INFORMATION

Corresponding Author

Younes Abghoui − *Science Institute of the University of Iceland, Reykjavík 102, Iceland;* orcid.org/0000-0001-5116-6666; Email: younes@hi.is

Authors

Atef Iqbal − *Science Institute of the University of Iceland, Reykjavík 102, Iceland*

Egill Skúlason − *Faculty of Industrial Engineering, Mechanical Engineering and Computer Science, University of Iceland, Reykjavík 102, Iceland;* orcid.org/0000-0002-0724-680X

Complete contact information is available at: https://pubs.acs.org/10.1021/acs.jpcc.4c02148

Notes

The authors declare no competing financial interest.

■ ACKNOWLEDGMENTS

This work was supported by the Icelandic Research Fund [grant number 207056]. Computational resources were provided by the Icelandic research high-performance computing cluster.

■ REFERENCES

(1) Rosca, V.; Duca, M.; de Groot, M. T.; Koper, M. T. Nitrogen cycle electrocatalysis. *Chem. Rev.* **2009**, *109* (6), 2209−2244.

(2) Brown, K. A.; Harris, D. F.; Wilker, M. B.; Rasmussen, A.; Khadka, N.; Hamby, H.; Keable, S.; et al. Light-driven dinitrogen reduction catalyzed by a CdS: nitrogenase MoFe protein biohybrid. *Science* **2016**, *352* (6284), 448−450.

(3) Tang, C.; Qiao, S.-Z. How to explore ambient electrocatalytic nitrogen reduction reliably and insightfully. *Chem. Soc. Rev.* **2019**, *48* (12), 3166−3180.

(4) Suryanto, B. H. R.; Du, H. L.; Wang, D.; Chen, J.; Simonov, A. N.; MacFarlane, D. R. Challenges and prospects in the catalysis of electroreduction of nitrogen to ammonia. *Nat. Catal.* **2019**, *2* (4), 290−296.

(5) Deng, J.; Iñiguez, J. A.; Liu, C. Electrocatalytic nitrogen reduction at low temperature. *Joule* **2018**, *2* (5), 846−856.

(6) Galloway, J. N.; Townsend, A. R.; Erisman, J. W.; Bekunda, M.; Cai, Z.; Freney, J. R.; Martinelli, L. A.; et al. Transformation of the nitrogen cycle: recent trends, questions, and potential solutions. *Science* **2008**, *320* (5878), 889−892.

(7) Chen, G. F.; Ren, S.; Zhang, L.; Cheng, H.; Luo, Y.; Zhu, K.; Ding, L.; Wang, H. Advances in electrocatalytic N2 reduction—strategies to tackle the selectivity challenge. *Small Methods* **2019**, *3* (6), No. 1800337.

(8) Eady, R. R. Structure− function relationships of alternative nitrogenases. *Chem. Rev.* **1996**, *96* (7), 3013−3030.

(9) Rod, T. H.; Nørskov, J. K. Modeling the nitrogenase FeMo cofactor. *J. Am. Chem. Soc.* **2000**, *122* (51), 12751−12763.

(10) Qing, G.; Ghazfar, R.; Jackowski, S. T.; Habibzadeh, F.; Ashtiani, M. M.; Chen, C. P.; Smith, M. R.; Hamann, T. W. Recent advances and challenges of electrocatalytic N2 reduction to ammonia. *Chem. Rev.* **2020**, *120* (12), 5437−5516.

(11) Guo, C.; Ran, J.; Vasileff, A.; Qiao, S. Z. Rational design of electrocatalysts and photo (electro) catalysts for nitrogen reduction to ammonia (NH 3) under ambient conditions. *Energy Environ. Sci.* **2018**, *11* (1), 45−56.

(12) Song, P.; Wang, H.; Kang, L.; Ran, B.; Song, H.; Wang, R. Electrochemical nitrogen reduction to ammonia at ambient conditions on nitrogen and phosphorus co-doped porous carbon. *Chem. Commun.* **2019**, *55* (5), 687−690.

(13) Guo, W.; Zhang, K.; Liang, Z.; Zou, R.; Xu, Q. Electrochemical nitrogen fixation and utilization: theories, advanced catalyst materials and system design. *Chem. Soc. Rev.* **2019**, *48* (24), 5658−5716.

(14) Cao, S.; Chen, H.; Jiang, F.; Wang, X. Nitrogen photofixation by ultrathin amine-functionalized graphitic carbon nitride nanosheets as a gaseous product from thermal polymerization of urea. *Appl. Catal., B* **2018**, *224*, 222−229.

(15) Wang, S.; Guo, D.; Zong, M.; Fan, C.; Jun, X.; Wang, D. H. Unravelling the strong metal-support interaction between Ru quantum dots and g-C3N4 for visible-light photocatalytic nitrogen fixation. *Appl. Catal., A* **2021**, *617*, No. 118112.

(16) Sveinbjornsson, A.; Gunnarsdottir, A. B.; Creel, E. B.; Canales, C. P.; Zulevi, B.; Lyu, X.; Jafta, C. J.; Skulason, E.; Serov, A.; Flosadottir, H. D. Demonstration of no catalytical activity of Fe-N-C and Nb-N-C electrocatalysts toward nitrogen reduction using in-line quantification. *SusMat* **2022**, *2* (4), 476−486.

(17) Garden, A. L.; Skúlason, E. The mechanism of industrial ammonia synthesis revisited: calculations of the role of the associative mechanism. *J. Phys. Chem. C* **2015**, *119* (47), 26554−26559.
(18) Li, Y.; Wang, H.; Priest, C.; Li, S.; Xu, P.; Wu, G. Advanced electrocatalysis for energy and environmental sustainability via water and nitrogen reactions. *Adv. Mater.* **2021**, *33* (6), No. 2000381.
(19) Chen, S.; Perathoner, S.; Ampelli, C.; Wei, H.; Abate, S.; Zhang, B.; Centi, G. Enhanced performance in the direct electrocatalytic synthesis of ammonia from N2 and H2O by an in-situ electrochemical activation of CNT-supported iron oxide nanoparticles. *J. Energy Chem.* **2020**, *49*, 22−32.
(20) Yang, Y.; Zhang, L.; Hu, Z.; Zheng, Y.; Tang, C.; Chen, P.; Wang, R.; et al. The crucial role of charge accumulation and spin polarization in activating carbon-based catalysts for electrocatalytic nitrogen reduction. *Angew. Chem., Int. Ed.* **2020**, *59* (11), 4525−4531.
(21) Deng, G.; Wang, T.; Alshehri, A. A.; Alzahrani, K. A.; Wang, Y.; Ye, H.; Luo, Y.; Sun, X. Improving the electrocatalytic N 2 reduction activity of Pd nanoparticles through surface modification. *J. Mater. Chem. A* **2019**, *7* (38), 21674−21677.
(22) Shilov, A. E. Catalytic reduction of molecular nitrogen in solutions. *Russ. Chem. Bull.* **2003**, *52*, 2555−2562.
(23) Zhu, H.; Ren, X.; Yang, X.; Liang, X.; Liu, A.; Wu, G. Fe-based catalysts for nitrogen reduction toward ammonia electrosynthesis under ambient conditions. *SusMat* **2022**, *2* (3), 214−242.
(24) Yao, Y.; Wang, H.; Yuan, X. Z.; Li, H.; Shao, M. Electrochemical nitrogen reduction reaction on ruthenium. *ACS Energy Lett.* **2019**, *4* (6), 1336−1341.
(25) Skúlason, E.; Bligaard, T.; Gudmundsdóttir, S.; Studt, F.; Rossmeisl, J.; Abild-Pedersen, F.; Vegge, T.; et al. A theoretical evaluation of possible transition metal electro-catalysts for N 2 reduction. *Phys. Chem. Chem. Phys.* **2012**, *14* (3), 1235−1245.
(26) Andersen, S. Z.; Čolić, V.; Yang, S.; Schwalbe, J. A.; Nielander, A. C.; McEnaney, J. M.; Enemark-Rasmussen, K.; et al. A rigorous electrochemical ammonia synthesis protocol with quantitative isotope measurements. *Nature* **2019**, *570* (7762), 504−508.
(27) Abghoui, Y.; Sigtryggsson, S. B.; Skúlason, E. Biomimetic nitrogen fixation catalyzed by transition metal sulfide surfaces in an electrolytic cell. *ChemSusChem* **2019**, *12* (18), 4265−4273.
(28) Abghoui, Y.; Garden, A. L.; Howalt, J. G.; Vegge, T.; Skúlason, E. Electroreduction of N2 to ammonia at ambient conditions on mononitrides of Zr, Nb, Cr, and V: A DFT guide for experiments. *ACS Catal.* **2016**, *6* (2), 635−646.
(29) Abghoui, Y.; Garden, A. L.; Hlynsson, V. F.; Björgvinsdóttir, S.; Ólafsdóttir, H.; Skúlason, E. Enabling electrochemical reduction of nitrogen to ammonia at ambient conditions through rational catalyst design. *Phys. Chem. Chem. Phys.* **2015**, *17* (7), 4909−4918.
(30) Hanifpour, F.; Canales, C. P.; Fridriksson, E. G.; Sveinbjörnsson, A.; Tryggvason, T. K.; Yang, J.; Arthur, C.; et al. Operando quantification of ammonia produced from computationally-derived transition metal nitride electro-catalysts. *J. Catal.* **2022**, *413*, 956−967.
(31) Abghoui, Y.; Skúlason, E. Electrochemical synthesis of ammonia via Mars-van Krevelen mechanism on the (111) facets of group III−VII transition metal mononitrides. *Catal. Today* **2017**, *286*, 78−84.
(32) Höskuldsson, Á. B.; Dang, T.; Sakai, Y.; Ishikawa, A.; Skúlason, E. High-throughput computational screening of doped transition metal oxides as catalysts for nitrogen reduction. *Cell Rep. Phys. Sci.* **2023**, *4* (10), No. 101595.
(33) Höskuldsson, Á. B.; Abghoui, Y.; Gunnarsdottir, A. B.; Skulason, E. Computational screening of rutile oxides for electrochemical ammonia formation. *ACS Sustainable Chem. Eng.* **2017**, *5* (11), 10327−10333.
(34) Hanifpour, F.; Canales, C. P.; Fridriksson, E. G.; Sveinbjörnsson, A.; Tryggvason, T. K.; Lewin, E.; Magnus, F.; et al. Investigation into the mechanism of electrochemical nitrogen reduction reaction to ammonia using niobium oxynitride thin-film catalysts. *Electrochim. Acta* **2022**, *403*, No. 139551.
(35) Pan, J.; Hansen, H. A.; Vegge, T. Vanadium oxynitrides as stable catalysts for electrochemical reduction of nitrogen to ammonia: the role of oxygen. *J. Mater. Chem. A* **2020**, *8* (45), 24098−24107.
(36) Ellingsson, V.; Iqbal, A.; Skúlason, E.; Abghoui, Y. Nitrogen Reduction Reaction to Ammonia on Transition Metal Carbide Catalysts. *ChemSusChem* **2023**, *16* (22), No. e202300947.
(37) Iqbal, A.; Skúlason, E.; Abghoui, Y. Are (100) facets of transition metal carbonitrides suitable as electrocatalysts for nitrogen reduction to ammonia at ambient conditions? *Int. J. Hydrogen Energy* **2024**, *64*, 744−753.
(38) Iqbal, A.; Skúlason, E.; Abghoui, Y. Electrochemical Nitrogen Reduction to Ammonia at Ambient Condition on the (111) Facets of Transition Metal Carbonitrides. *ChemPhysChem* **2024**, No. e202300991.
(39) Liu, Y.; Li, Q.; Guo, X.; Kong, X.; Ke, J.; Chi, M.; Li, Q.; et al. A highly efficient metal-free electrocatalyst of F-doped porous carbon toward N2 electroreduction. *Adv. Mater.* **2020**, *32* (24), No. 1907690.
(40) Peng, G.; Wu, J.; Wang, M.; Niklas, J.; Zhou, H.; Liu, C. Nitrogen-defective polymeric carbon nitride nanolayer enabled efficient electrocatalytic nitrogen reduction with high faradaic efficiency. *Nano Lett.* **2020**, *20* (4), 2879−2885.
(41) Liu, C.; Li, Q.; Wu, C.; Zhang, J.; Jin, Y.; MacFarlane, D. R.; Sun, C. Single-boron catalysts for nitrogen reduction reaction. *J. Am. Chem. Soc.* **2019**, *141* (7), 2884−2888.
(42) Zou, H.; Rong, W.; Long, B.; Ji, Y.; Duan, L. Corrosion-induced Cl-doped ultrathin graphdiyne toward electrocatalytic nitrogen reduction at ambient conditions. *ACS Catal.* **2019**, *9* (12), 10649−10655.
(43) Zhang, X.; Wu, T.; Wang, H.; Zhao, R.; Chen, H.; Wang, T.; Wei, P.; et al. Boron nanosheet: An elemental two-dimensional (2D) material for ambient electrocatalytic N2-to-NH3 fixation in neutral media. *ACS Catal.* **2019**, *9* (5), 4609−4615.
(44) Zhang, L.; Ding, L. X.; Chen, G. F.; Yang, X.; Wang, H. Ammonia synthesis under ambient conditions: selective electroreduction of dinitrogen to ammonia on black phosphorus nanosheets. *Angew. Chem.* **2019**, *131* (9), 2638−2642.
(45) Zhang, G.; Li, Y.; He, C.; Ren, X.; Zhang, P.; Mi, H. Recent progress in 2D catalysts for photocatalytic and electrocatalytic artificial nitrogen reduction to ammonia. *Adv. Energy Mater.* **2021**, *11* (11), No. 2003294.
(46) Seh, Z. W.; Kibsgaard, J.; Dickens, C. F.; Chorkendorff, I. B.; Nørskov, J. K.; Jaramillo, T. F. Combining theory and experiment in electrocatalysis: Insights into materials design. *Science* **2017**, *355* (6321), No. eaad4998.
(47) Wan, Y.; Xu, J.; Lv, R. Heterogeneous electrocatalysts design for nitrogen reduction reaction under ambient conditions. *Mater. Today* **2019**, *27*, 69−90.
(48) Liang, X.; Ren, X.; Yang, Q.; Gao, L.; Gao, M.; Yang, Y.; Zhu, H.; et al. A two-dimensional MXene-supported metal−organic framework for highly selective ambient electrocatalytic nitrogen reduction. *Nanoscale* **2021**, *13* (5), 2843−2848.
(49) Huang, J.; Yuan, M.; Li, X.; Wang, Y.; Li, M.; Li, J.; You, Z. Cs-Promoted ruthenium catalyst supported on Ba5Ta4O15 with abundant oxygen vacancies for ammonia synthesis. *Appl. Catal., A* **2021**, *615*, No. 118058.
(50) Yu, S.; Wang, Q.; Wang, J.; Xiang, Y.; Niu, X.; Li, T. Zinc doped Fe2O3 for boosting Electrocatalytic Nitrogen Fixation to ammonia under mild conditions. *Int. J. Hydrogen Energy* **2021**, *46* (27), 14331−14337.
(51) Chu, K.; Liu, Y. P.; Li, Y. B.; Zhang, H.; Tian, Y. Efficient electrocatalytic N 2 reduction on CoO quantum dots. *J. Mater. Chem. A* **2019**, *7* (9), 4389−4394.
(52) Niu, L.; An, L.; Wang, X.; Sun, Z. Effect on electrochemical reduction of nitrogen to ammonia under ambient conditions: Challenges and opportunities for chemical fuels. *J. Energy Chem.* **2021**, *61*, 304−318.
(53) Li, L.; Tang, C.; Xia, B.; Jin, H.; Zheng, Y.; Qiao, S. Z. Two-dimensional mosaic bismuth nanosheets for highly selective ambient

https://doi.org/10.1021/acs.jpcc.4c02148
J. Phys. Chem. C XXXX, XXX, XXX−XXX

electrocatalytic nitrogen reduction. *ACS Catal.* **2019**, *9* (4), 2902−2908.
(54) Yao, D.; Tang, C.; Li, L.; Xia, B.; Vasileff, A.; Jin, H.; Zhang, Y.; Qiao, S. Z. In situ fragmented bismuth nanoparticles for electrocatalytic nitrogen reduction. *Adv. Energy Mater.* **2020**, *10* (33), No. 2001289.
(55) Hawtof, R.; Ghosh, S.; Guarr, E.; Xu, C.; Sankaran, R. M.; Renner, J. N. Catalyst-free, highly selective synthesis of ammonia from nitrogen and water by a plasma electrolytic system. *Sci. Adv.* **2019**, *5* (1), No. eaat5778.
(56) Wang, Y. H.; Dong, J. H.; Tan, Z.; Wang, X. F.; Song, X. Z. The journey of iron-based electrocatalytic materials for nitrogen reduction reaction: from current status to future prospects. *J. Mater. Chem. A* **2023**, *11* (21), 11048−11077.
(57) Wu, T.; Fan, W.; Zhang, Y.; Zhang, F. Electrochemical synthesis of ammonia: Progress and challenges. *Mater. Today Phys.* **2021**, *16*, No. 100310.
(58) Abghoui, Y. Superiority of the (100) over the (111) facets of the nitrides for hydrogen evolution reaction. *Top. Catal.* **2022**, *65* (1), 262−269.
(59) Abghoui, Y.; Skúlason, E. Hydrogen evolution reaction catalyzed by transition-metal nitrides. *J. Phys. Chem. C* **2017**, *121* (43), 24036−24045.
(60) Song, J.; Wei, C.; Huang, Z. F.; Liu, C.; Zeng, L.; Wang, X.; Xu, Z. J. A review on fundamentals for designing oxygen evolution electrocatalysts. *Chem. Soc. Rev.* **2020**, *49* (7), 2196−2214.
(61) Schmidt, T. O.; Wark, A.; Haid, R. W.; Kluge, R. M.; Suzuki, S.; Kamiya, K.; Bandarenka, A. S.; et al. Elucidating the Active Sites and Synergies in Water Splitting on Manganese Oxide Nanosheets on Graphite Support. *Adv. Energy Mater.* **2023**, *13* (43), No. 2302039.
(62) Chung, D. Y.; Yoo, J. M.; Sung, Y. E. Highly durable and active Pt-based nanoscale design for fuel-cell oxygen-reduction electrocatalysts. *Adv. Mater.* **2018**, *30* (42), No. 1704123.
(63) Gíslason, P. M.; Skúlason, E. Catalytic trends of nitrogen doped carbon nanotubes for oxygen reduction reaction. *Nanoscale* **2019**, *11* (40), 18683−18690.
(64) Atrak, N.; Tayyebi, E.; Skúlason, E. Electrochemical CO2 reduction towards formic acid and methanol on transition metal oxide surfaces as a function of CO coverage. *Catal. Sci. Technol.* **2023**, *13* (11), 3321−3336.
(65) Hussain, J.; Jónsson, H.; Skúlason, E. Calculations of product selectivity in electrochemical CO2 reduction. *ACS Catal.* **2018**, *8* (6), 5240−5249.
(66) Tayyebi, E.; Hussain, J.; Abghoui, Y.; Skúlason, E. Trends of electrochemical CO2 reduction reaction on transition metal oxide catalysts. *J. Phys. Chem. C* **2018**, *122* (18), 10078−10087.
(67) Weal, G. R.; Gudmundsson, K. I.; Mackenzie, F. D.; Whiting, J. R.; Smith, N. B.; Skúlason, E.; Garden, A. L. Calculations of the effect of catalyst size and structure on the electrocatalytic reduction of CO2 on Cu nanoclusters. *Nanoscale* **2024**, *16*, 5242−5256.
(68) Nørskov, J. K.; Rossmeisl, J.; Logadottir, A.; Lindqvist, L. R.; Kitchin, J. R.; Bligaard, T.; Jonsson, H. Origin of the overpotential for oxygen reduction at a fuel-cell cathode. *J. Phys. Chem. B* **2004**, *108* (46), 17886−17892.
(69) Tayyebi, E.; Abghoui, Y.; Skulason, E. Elucidating the mechanism of electrochemical N2 reduction at the Ru (0001) electrode. *ACS Catal.* **2019**, *9* (12), 11137−11145.
(70) Höskuldsson, Á. B.; Tayyebi, E.; Skúlason, E. Computational examination of the kinetics of electrochemical nitrogen reduction and hydrogen evolution on a tungsten electrode. *J. Catal.* **2021**, *404*, 362−370.
(71) Hammer, B.; Hansen, L. B.; Nørskov, J. K. Improved adsorption energetics within density-functional theory using revised Perdew-Burke-Ernzerhof functionals. *Phys. Rev. B* **1999**, *59* (11), No. 7413.
(72) Kresse, G.; Furthmüller, J. Software vasp, vienna, 1999. *Phys. Rev. B* **1996**, *54* (11), No. 169.
(73) Kresse, G.; Joubert, D. From ultrasoft pseudopotentials to the projector augmented-wave method. *Phys. Rev. B* **1999**, *59* (3), No. 1758.
(74) Kresse, G.; Furthmüller, J. Efficient iterative schemes for ab initio total-energy calculations using a plane-wave basis set. *Phys. Rev. B* **1996**, *54* (16), No. 11169.
(75) Blöchl, P. E. Projector augmented-wave method. *Phys. Rev. B* **1994**, *50* (24), No. 17953.
(76) Abghoui, Y.; Skúlason, E. Computational predictions of catalytic activity of zincblende (110) surfaces of metal nitrides for electrochemical ammonia synthesis. *J. Phys. Chem. C* **2017**, *121* (11), 6141−6151.
(77) Abghoui, Y.; Iqbal, A.; Skúlason, E. The role of overlayered nitride electro-materials for N2 reduction to ammonia. *Front. Catal.* **2023**, *2*, No. 1096824.
(78) Abghoui, Y.; Skúlason, E. Onset potentials for different reaction mechanisms of nitrogen activation to ammonia on transition metal nitride electro-catalysts. *Catal. Today* **2017**, *286*, 69−77.
(79) Henkelman, G.; Uberuaga, B. P.; Jónsson, H. A climbing image nudged elastic band method for finding saddle points and minimum energy paths. *J. Chem. Phys.* **2000**, *113* (22), 9901−9904.
(80) Henkelman, G.; Arnaldsson, A.; Jónsson, H. A fast and robust algorithm for Bader decomposition of charge density. *Comput. Mater. Sci.* **2006**, *36* (3), 354−360.
(81) Gudmundsdóttir, S.; Tang, W.; Henkelman, G.; Jónsson, H.; Skúlason, E. Local density of states analysis using Bader decomposition for N2 and CO2 adsorbed on Pt (110)-(1× 2) electrodes. *J. Chem. Phys.* **2012**, *137* (16), No. 164705.
(82) Han, L.; Liu, X.; Chen, J.; Lin, R.; Liu, H.; Lü, F.; Bak, S.; et al. Atomically dispersed molybdenum catalysts for efficient ambient nitrogen fixation. *Angew. Chem.* **2019**, *131* (8), 2343−2347.
(83) Chalkley, M. J.; Del Castillo, T. J.; Matson, B. D.; Peters, J. C. Fe-mediated nitrogen fixation with a metallocene mediator: Exploring p K a effects and demonstrating electrocatalysis. *J. Am. Chem. Soc.* **2018**, *140* (19), 6122−6129.
(84) Rossmeisl, J.; Qu, Z. W.; Zhu, H.; Kroes, G. J.; Nørskov, J. K. Electrolysis of water on oxide surfaces. *J. Electroanal. Chem.* **2007**, *607* (1−2), 83−89.

https://doi.org/10.1021/acs.jpcc.4c02148
J. Phys. Chem. C XXXX, XXX, XXX−XXX

Title: Catalytic Nitrogen Reduction on Transition Metal Carbonitride (110) Facet: DFT Predictions and Mechanistic Insights

-Electronic supplementary information

Authors: Atef Iqbal[1], Egill Skúlason[2], Younes Abghoui*[1]

Affiliation: [1]Science Institute of the University of Iceland, Reykjavík, 102, Iceland [2]Faculty of Industrial Engineering, Mechanical Engineering and Computer Science, University of Iceland, Reykjavík, 102, Iceland

Corresponding Author: Younes Abghoui (younes@hi.is, ORCID: 0000-0001-5116-6666)

Zero-point energy and entropy corrections

Table S1: The zero-point energy (ZPE) and entropy correction parameters have been determined for all the employed adsorbed and gas phase substances. ZPE values for adsorbed substances were computed on the [110] VCN surface, while gas phase values were sourced from reference [1]. In the case of adsorbed species, indicated by *, the distinction between surface adsorption and vacancy adsorption is denoted by the vac notation.

[110] TMCN surfaces	ZPE (eV)	TΔS (eV)
NH_3 (g)	0.89	0.74
H_2 (g)	0.27	0.41
CH_4 (g)	0.82	0.57
N_2 (g)	0.15	0.6
*NH	0.29	0.008
*NH_2	0.7	0.06
*NH_3	1.03	0.119
*N_2^{vac}	0.2	0.112
*NNH vac	0.47	0.109
*NNH_2 vac	0.79	0.102
*$2N^{vac}$	0.19	0.117
*$N.NH^{vac}$	0.49	0.129
*$N.NH_2^{vac}$	0.78	0.115
*NHNH	0.72	0.128
*$NH.NH_2$	1.1	0.101
*$NH_2.NH_2$	1.44	0.16
*H^{vac}	0.17	0.006
*CH	0.25	0.013
*CH_2	0.61	0.069
*CH_3	0.89	0.086
*OH^-	0.38	0.068
*O^{2-}	0.1	0.062
*$OH^{- vac}$	0.38	0.052
*$O^{2- vac}$	0.09	0.029

Table S2 shows the optimized lattice constant of all the TMCNs

TMCN	VCN	NbCN	WCN	ZrCN	HfCN	TaCN	TiCN	MoCN	CrCN	ScCN	YCN
a (Å)	8.07	8.77	8.34	9.14	9.00	8.70	8.38	8.31	7.84	9.05	9.80
b (Å)	6.04	6.48	6.48	6.77	6.66	6.43	6.30	6.66	6.26	6.75	7.37

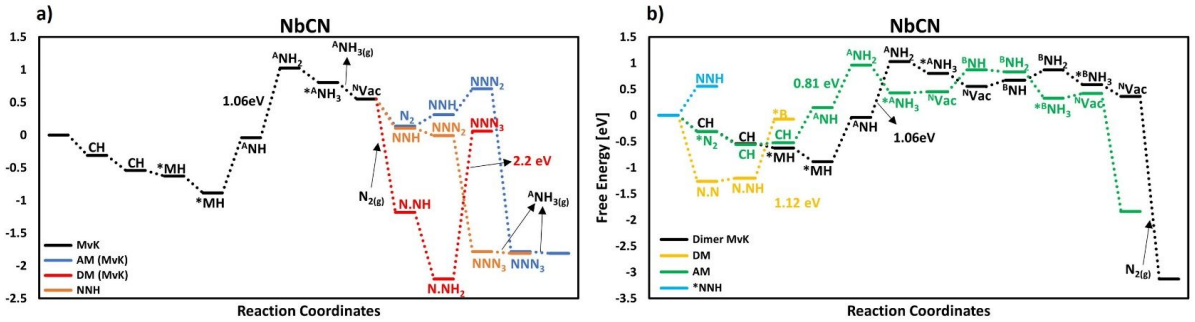

Figure S1 shows (a) the free energy diagram for a single vacancy with different mechanisms and (b) dimer vacancies along with other mechanisms with different color codes for NbCN.

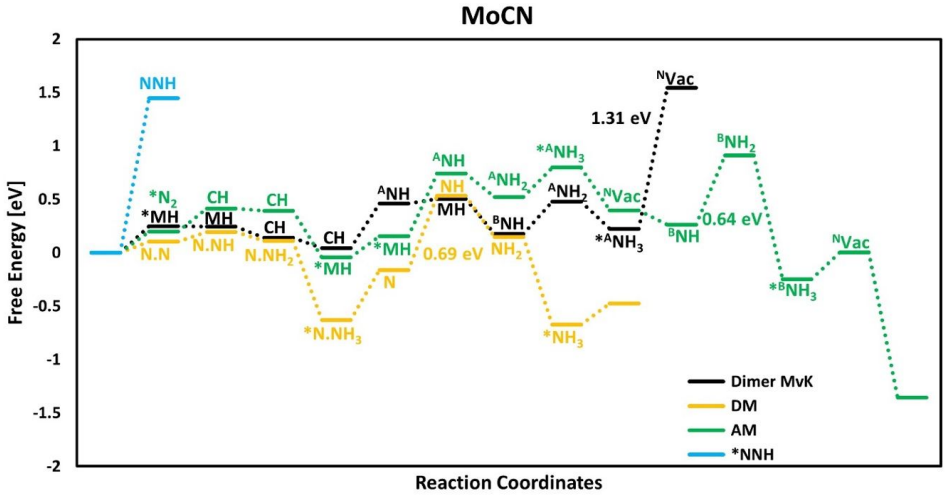

Figure S2 shows the free energy diagram for a single vacancy and dimer vacancies along with other mechanisms with different color codes for MoCN.

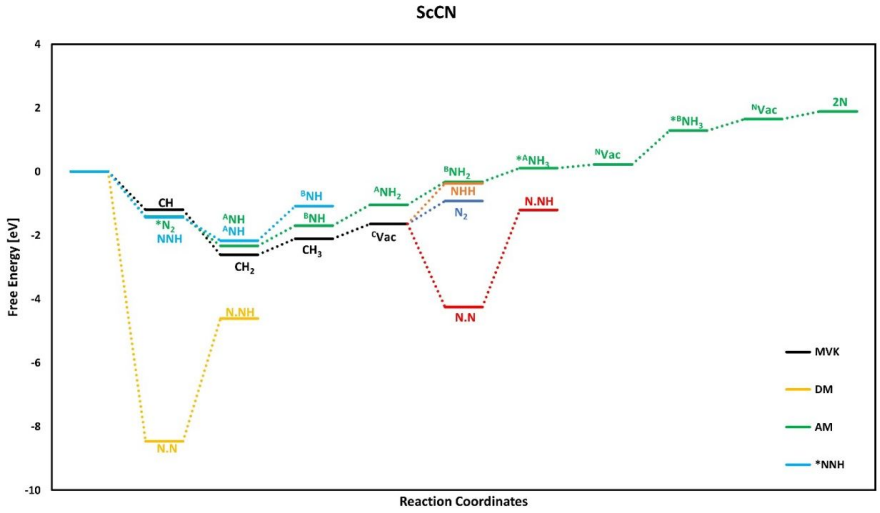

Figure S3 shows (a) the free energy diagram for a single vacancy with different mechanisms and (b) dimer vacancies along with other mechanisms with different color codes for TaCN

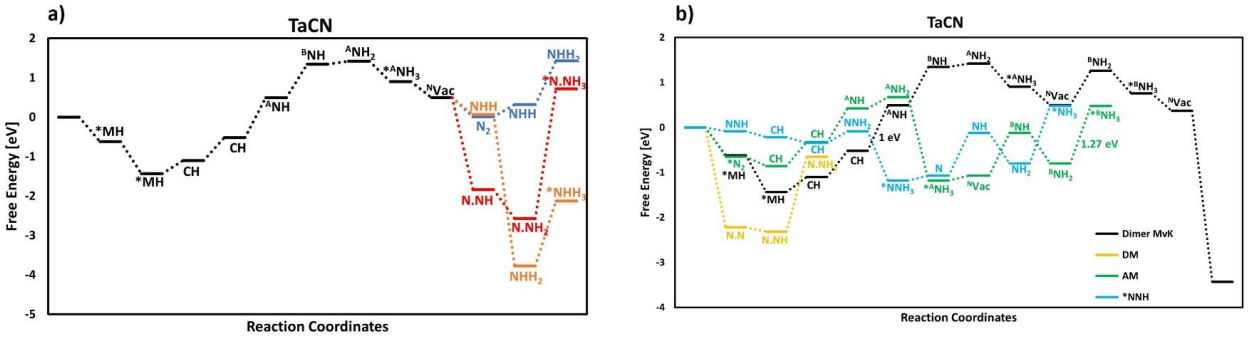

Figure S4 shows the free energy diagram for a single vacancy and dimer vacancies along with other mechanisms with different color codes for ScCN.

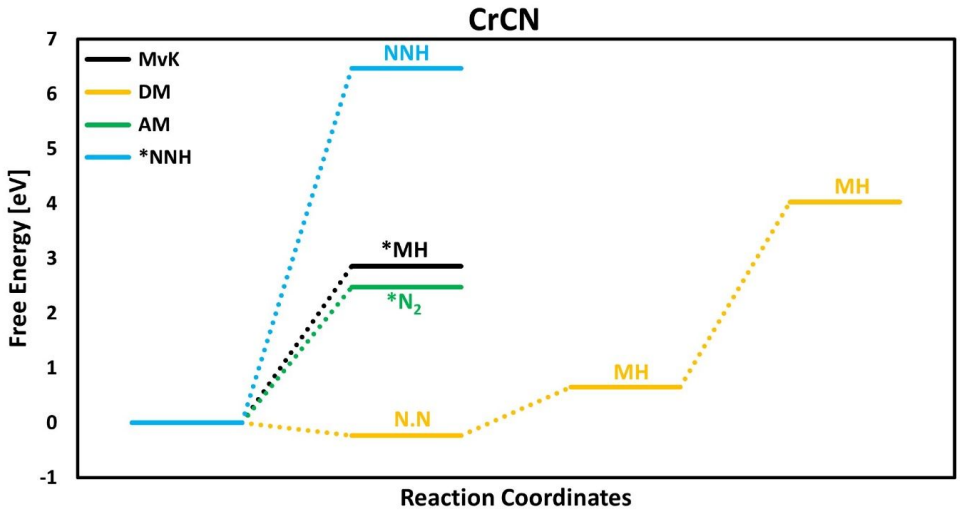

Figure S5 shows the free energy diagram for different mechanisms with different color codes for CrCN.

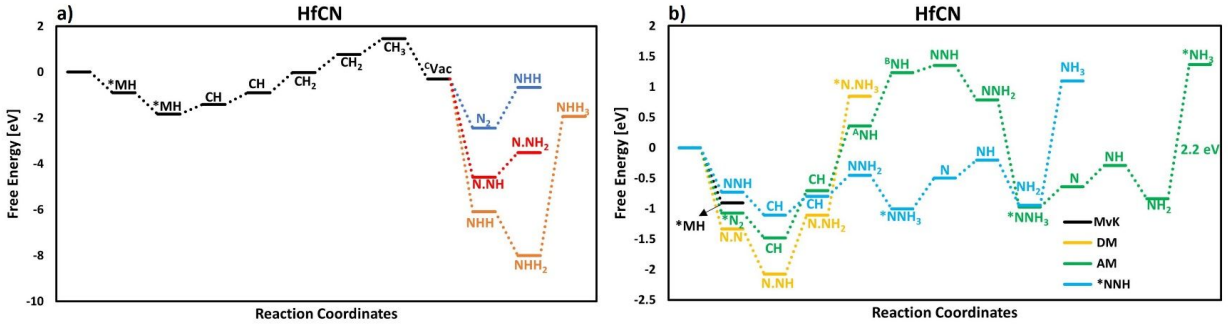

Figure S6 shows (a) the free energy diagram for a single vacancy with different mechanisms and (b) dimer vacancies along with other mechanisms with different color codes for HfCN

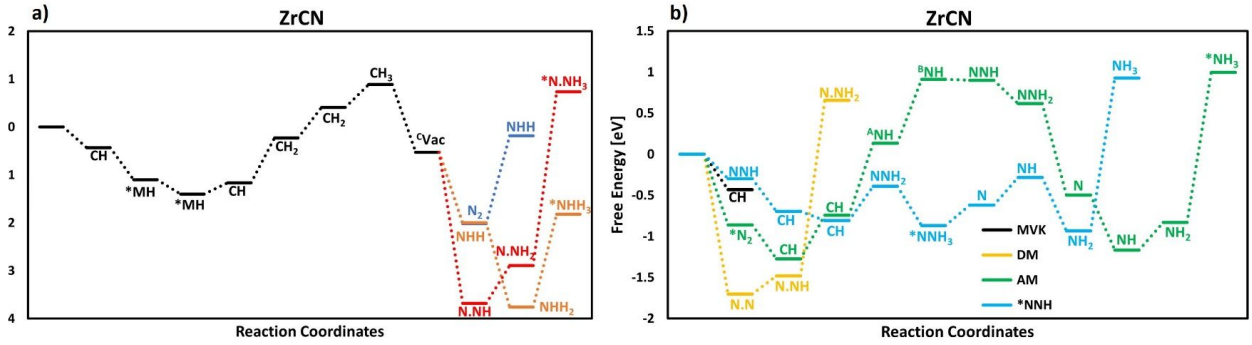

Figure S7 shows (a) the free energy diagram for a single vacancy with different mechanisms and (b) dimer vacancies along with other mechanisms with different color codes for ZrCN

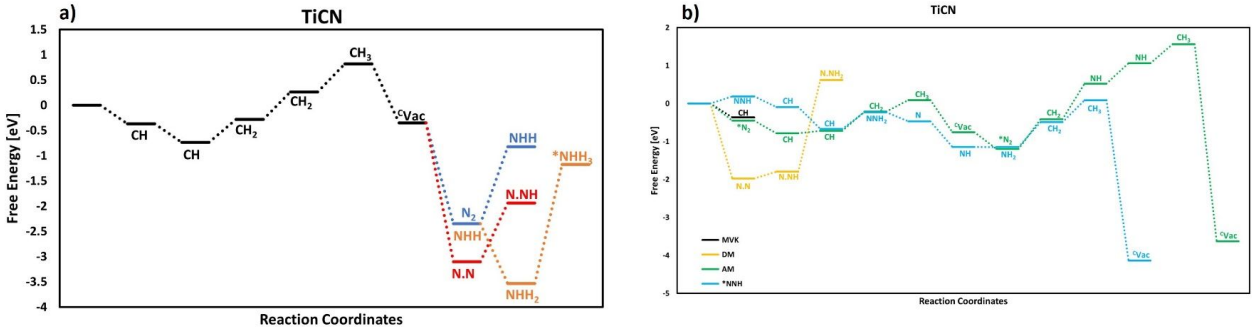

Figure S8 shows (a) the free energy diagram for a single vacancy with different mechanisms and (b) dimer vacancies along with other mechanisms with different color codes for TiCN

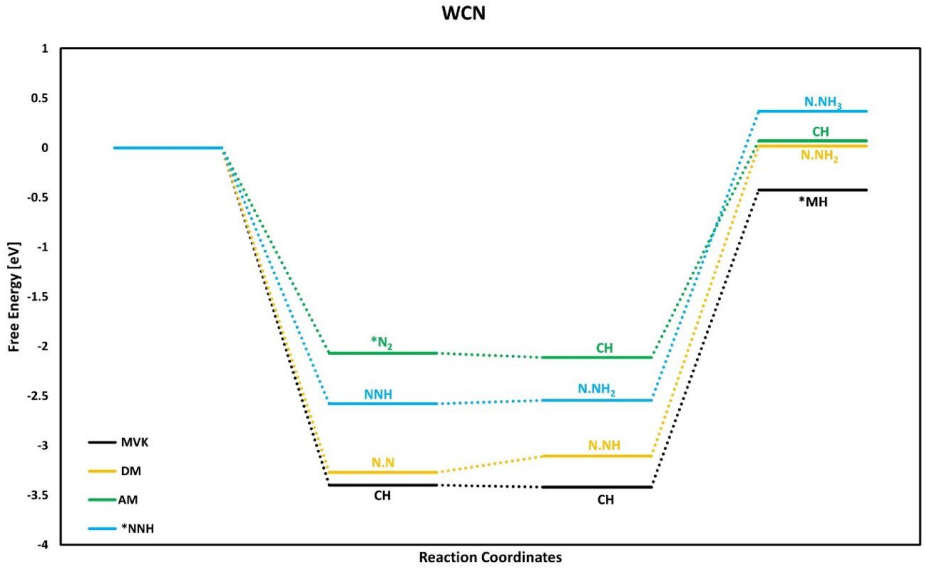

Figure S9 shows the free energy diagram for different mechanisms with different color codes for WCN.

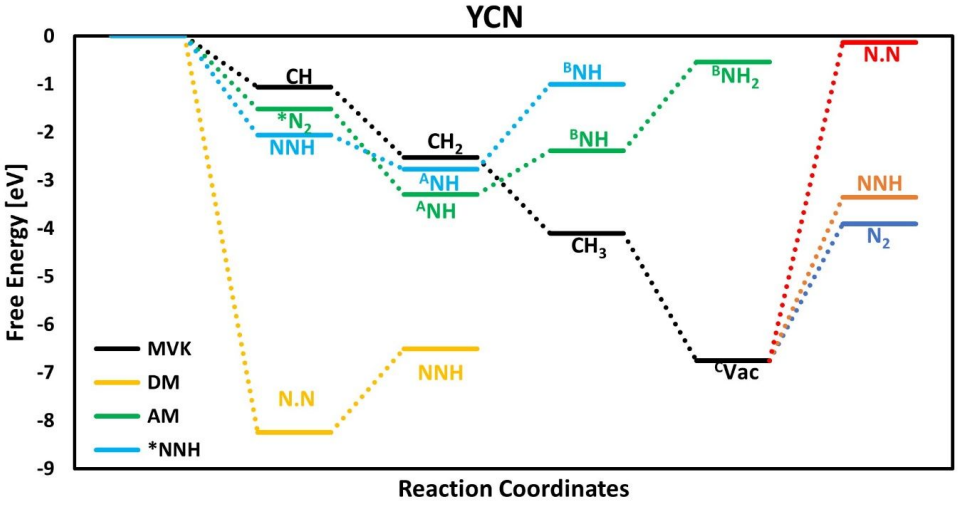

Figure S10 shows the free energy diagram for different mechanisms with different color codes for YCN.

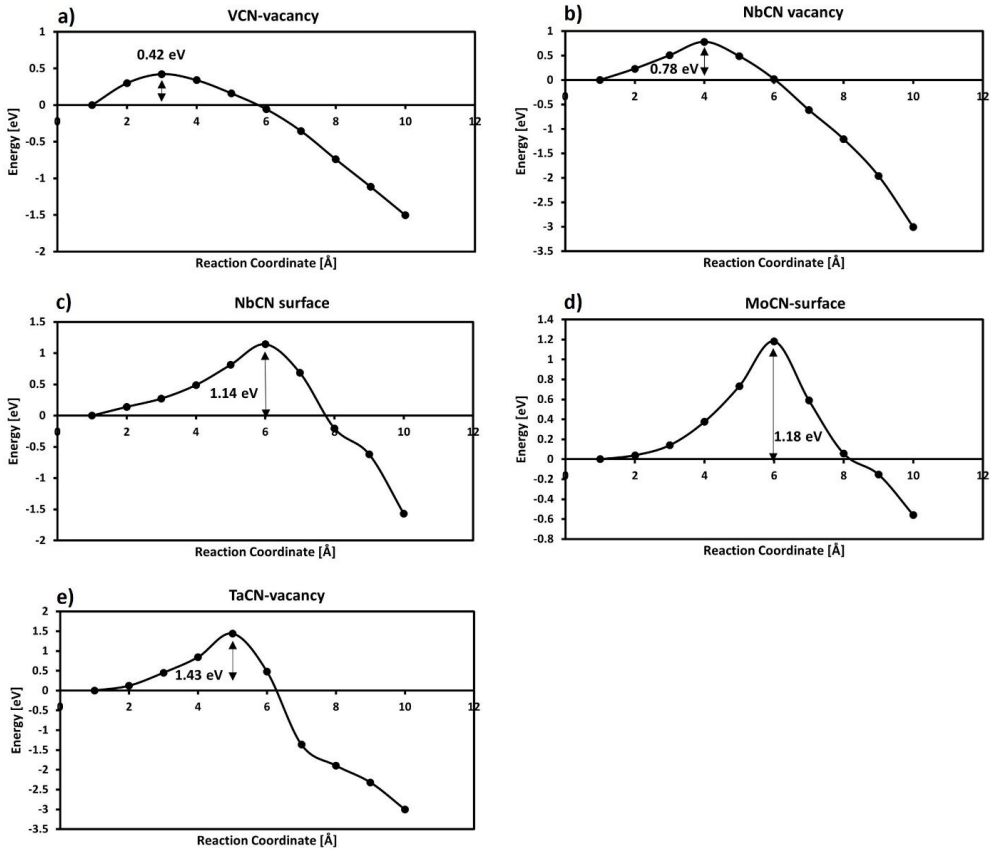

Figure S11 shows the kinetic barrier for (a) N_2 splitting in dimer vacancies of VCN (b) N_2 splitting in dimer vacancies of NbCN in mix MvK+AM mechanism (c) N_2 splitting on the surface of NbCN in DM (d) N_2 splitting on the surface of MoCN in DM (e) N_2 splitting in dimer vacancies of TaCN in MvK mechanism.

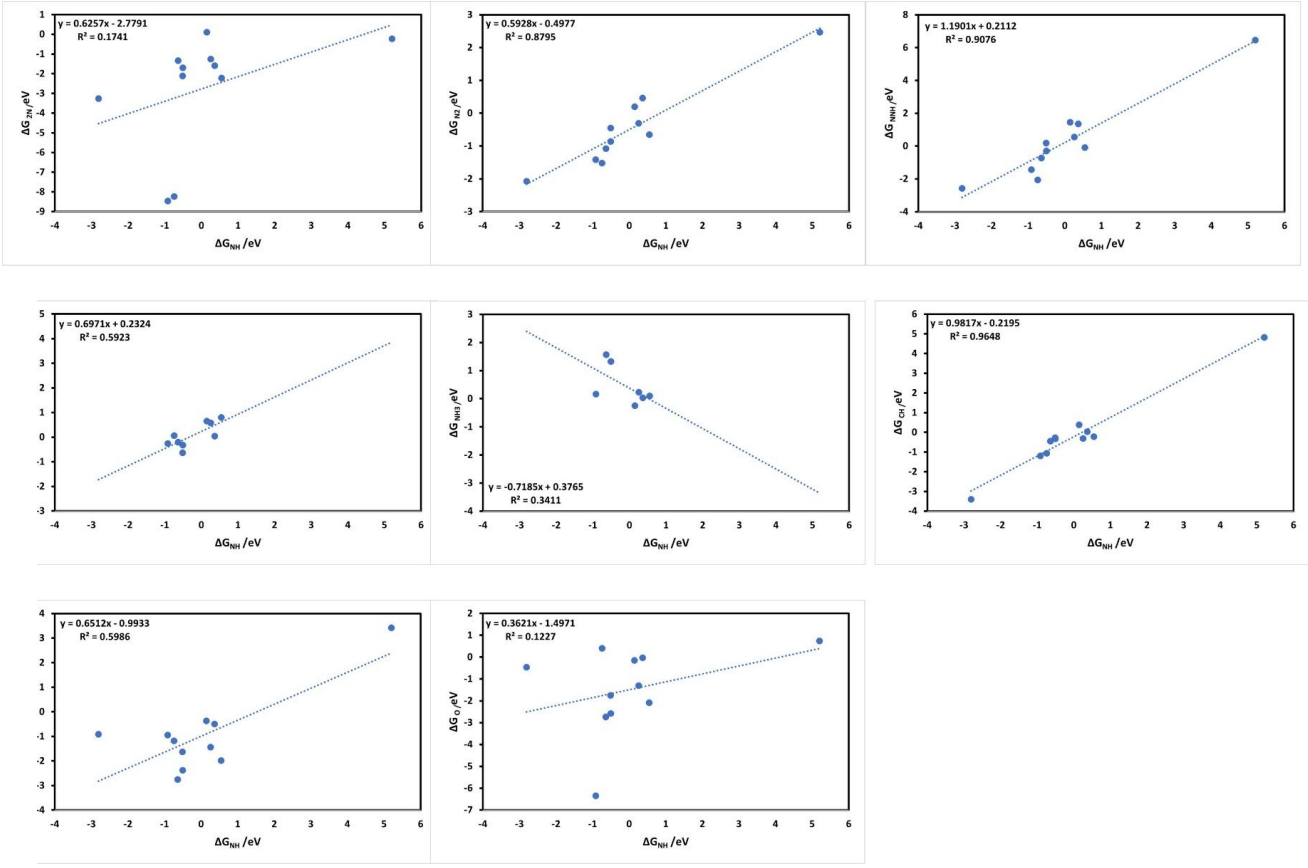

Figure S12 shows the scaling relation with *NH as a descriptor on the x-axis and different species on the y-axis.

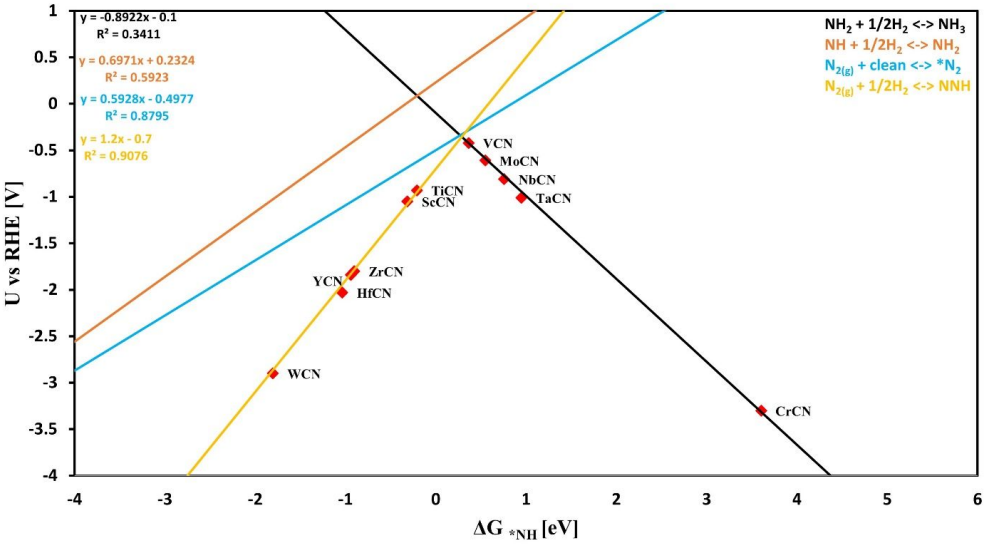

Figure S13 shows the theoretical volcano diagram constructed using all the scaling relations.

Bader charge analysis and charge iso-surfaces

We determined charge iso-surfaces by calculating charge density differences using the equation:

$\Delta P = P_{tot} - P_{pristine} - P_{gas}$

Here, P_{tot}, $P_{pristine}$, and P_{gas} represent the charge density for the species adsorbed on VCN, the pristine VCN system, and the isolated gas molecules, respectively. Yellow and cyan colors are utilized to denote charge accumulation and depletion, respectively. Figures S14(a)–(f) depict the charge density difference of various species on the surface of VCN systems. To quantify the extent of charge transfer, a Bader charge analysis was conducted, and the results are presented in Table S3.

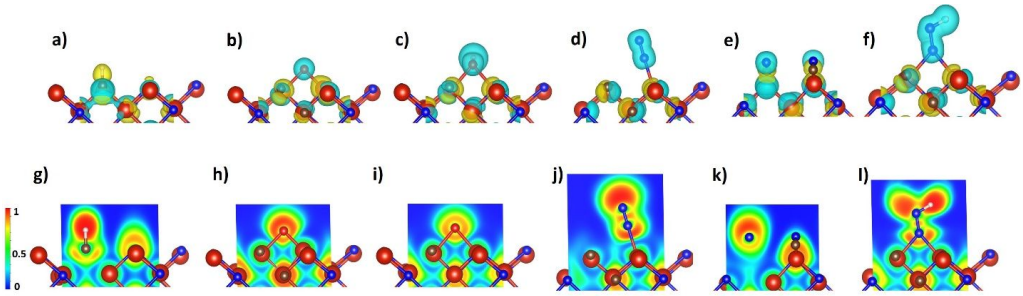

Figure S14 shows charge density difference of (a) H adsorbed on the surface (b) O adsorbed on the surface (c) OH adsorbed on the surface (d) N_2 associatively adsorbed on the surface I N_2 dissociatively adsorbed on the surface (f) NNH associatively adsorbed on the surface and (g), (h), (i), (j), (k), (l) are the isosurface for the mention species on VCN. The yellow (cyan) colors shows charge accumulation (depletion). The red (1) is associated with high values of electron localization function (ELF), indicating regions where electrons are more localized or confined, such as around lone pairs or in localized bonds. On the other hand, blue (0) is associated with low ELF values, representing regions where electrons are more delocalized or spread out.

Table S3 shows Bader charges (ΔQ) in the unit of *e* for electron charge for VCN.

ΔQ(e)	H	O	OH	N_2	2N	NNH
VCN	0.01	-0.88	-0.57	-0.25	-2.73	-0.51

It's crucial to emphasize that a positive ΔQ value in Table S3 denotes a charge transfer from the VCN layer to the gas molecule, while a negative ΔQ value implies the opposite—charge transfer from the gas molecule to the following layer. Analyzing Table S3 reveals that in the H-adsorbed system, there was an overall charge transfer of 0.01 electrons from the adatom to the substrate in VCN. Conversely, in the N_2 adsorbed system, there was a charge transfer of 0.25 electrons from the substrate to the admolecule.

The Electron Localization Function (ELF) assesses electron density behavior, aiding in distinguishing between localized regions with paired or lone pairs of electrons and more distributed areas shared across multiple atoms [47]. In our study, we explored ELF based on the most favorable adsorption sites for various species on the VCN system. ELF values, ranging from 0 to 1, signify complete delocalization (as in metallic systems) to strong localization (such as lone pairs or covalent bonds). The anticipated ELF results for species on VCN (110) facets are depicted in Figure S14(g–l). Overall, the ELF outcomes highlight the covalent bonding characteristics of all species on VCN, indicating shared-electron interactions.

References:

[1] Che, M. and J.C. Védrine, Characterization of solid materials and heterogeneous catalysts: From structure to surface reactivity. 2012: John Wiley & Sons.

[2] Fan, K., Ying, Y., Li, X., Luo, X., & Huang, H. (2019). Theoretical investigation of V_3C_2 MXene as prospective high-capacity anode material for metal-ion (Li, Na, K, and Ca) batteries. The Journal of Physical Chemistry C, 123(30), 18207-18214.

Paper V

Understanding the Mechanistic Pathways of N_2 Reduction to Ammonia on (110) Facets of Transition Metal Carbides,

Iqbal, A., E. Skulason, and Y. Abghoui,

Crystals, DOI: 10.3390/cryst14090770.

crystals

Impact Factor 2.4
CiteScore 4.2

ISSN 2073-4352

Mechanistic Pathways of N2 Reduction to Ammonia on (110) Facets of TMCs

Volume 14 · Issue 9 September 2024

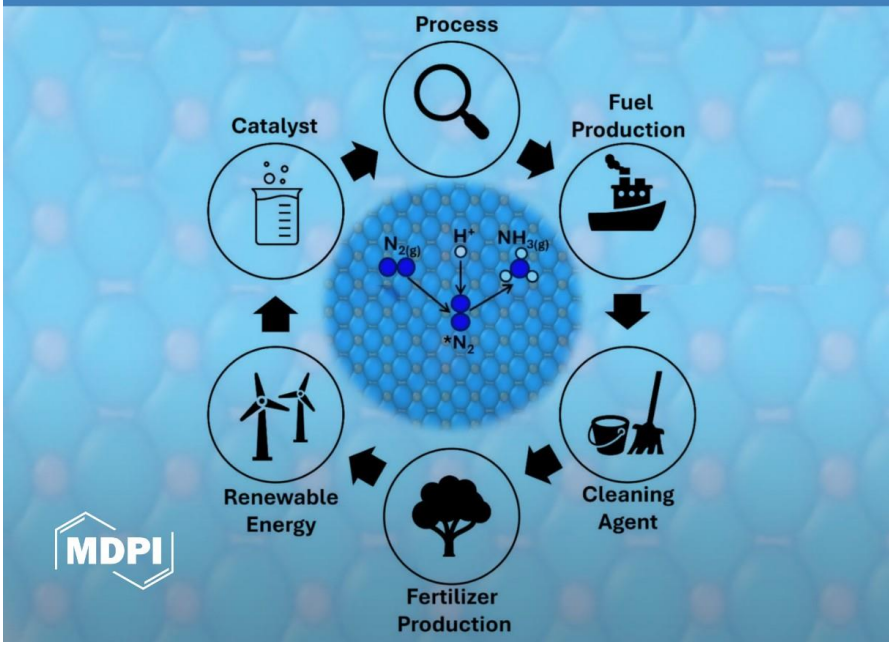

crystals

MDPI

Article

Understanding the Mechanistic Pathways of N_2 Reduction to Ammonia on (110) Facets of Transition Metal Carbides

Atef Iqbal [1], Egill Skúlason [2] and Younes Abghoui [1,*]

[1] Science Institute, Faculty of Physical Sciences, University of Iceland, Sæmundargata 2, 102 Reykjavík, Iceland; ati4@hi.is
[2] Faculty of Industrial Engineering, Mechanical Engineering and Computer Science, University of Iceland, Sæmundargata 2, 102 Reykjavík, Iceland; egillsk@hi.is
* Correspondence: younes@hi.is

Abstract: The conversion of molecular dinitrogen into ammonia under mild conditions is a significant pursuit in chemistry due to its potential for sustainable and clean ammonia production. The electrochemical reduction of N_2 offers a promising route for achieving this goal with reduced energy consumption, utilizing renewable energy sources. However, the exploration of effective electrocatalysts for this process, particularly at room temperature and atmospheric pressure, remains under exploration. This study addresses this gap by conducting a comprehensive investigation of potential catalysts for nitrogen electro-reduction to ammonia under ambient conditions. Using density functional theory calculations, we explore the (110) facets of rock salt structures across 11 transition metal carbides. Catalytic activity is evaluated through the construction of free energy diagrams for associative, dissociative, and Mars–van Krevelen reaction mechanisms. Additionally, we assess material stability against electrochemical poisoning and decomposition of parent metals during operation. Our findings suggest that a few of the candidates are promising for nitrogen reduction reactions, such as TaC and WC, with moderate onset potentials (−0.66 V and −0.82 V vs. RHE) under ambient conditions.

Keywords: DFT; transition metal carbides; ammonia synthesis; associative mechanism

Citation: Iqbal, A.; Skúlason, E.; Abghoui, Y. Understanding the Mechanistic Pathways of N_2 Reduction to Ammonia on (110) Facets of Transition Metal Carbides. *Crystals* **2024**, *14*, 770. https://doi.org/10.3390/cryst14090770

Academic Editor: Zongyou Yin

Received: 7 August 2024
Revised: 25 August 2024
Accepted: 27 August 2024
Published: 29 August 2024

1. Introduction

Ammonia (NH_3) is an important part of human life because it is used in a variety of vital compounds. It is necessary for the production of fertilizers, dyes, explosives, and nitric acid, and it is also acknowledged as a clean energy carrier [1–11]. Nitrogen gas (N_2), which makes up around 78% of the Earth's atmosphere by volume, is regarded as an inexhaustible and almost infinite source of ammonia production. Still, very few prokaryotic species in the natural environment are able to fix atmospheric nitrogen [6,12]. Ammonia is most often produced in industries using the Haber–Bosch process ($N_2 + 3H_2 \rightarrow 2NH_3$). Its effectiveness makes this method commonly utilized, although it requires a lot of energy. At roughly 940.95 kJ/mol, the nitrogen triple bond (N≡N) is one of the bonds that contributes to the high energy expenditure [1]. Moreover, significant levels of CO_2 are released by the Haber–Bosch process, which harms the environment. A crucial manufacturing step, the production of hydrogen (H_2), uses a lot of energy and releases additional CO_2 [13–15]. The Haber–Bosch process is still very inefficient despite its high energy requirements and environmental effect; ammonia outputs range in conversion rate from 10% to 15%. Extensive research into alternative ammonia production methods has been encouraged by this inefficiency. The objective is to create procedures that run under less harmful conditions, reducing energy use and preventing environmental harm [3].

In recent years, numerous experimental [16–28] and theoretical [29–38] investigations have addressed ammonia synthesis, providing useful insights into the challenges of producing new catalytic materials for this process. Previous studies have revealed that ammonia

production on metal surfaces is very structure-sensitive, with the majority happening on the surface steps of Fe and Ru [39–41].

Fuel cells and electrolyzers frequently require large amounts of precious metals like platinum (Pt), palladium (Pd), and iridium (Ir), thus greatly raising the cost of these devices. According to research, early transition metal carbides (TMCs) from groups 4 to 6 have electrical and catalytic properties similar to Pt-group metals [42,43]. These TMCs can be utilized as supports, reducing the overall amount of precious metal required [44]. TMCs' parent early transition metals are substantially more common in the Earth's crust and much less expensive than Pt-group metals. As a result, replacing Pt with TMCs can significantly reduce catalyst costs [45,46]. The good qualities of TMCs make them good support for metals of the Pt group. According to earlier work, an ultralow loading of just one monolayer (ML) of Pt can be maintained on different TMC substrates and yet have catalytic activity for the hydrogen evolution process (HER) that is on par with bulk Pt. It has already been explored that Pt-group metals can be effectively supported by TMCs, leading to a good catalytic performance with a much lower precious metal percentage [46,47].

We already showed the catalytic activity of the (100) facets of the TMCs in our previous work [32], and due to the polycrystallinity of these surfaces, we consider the (110) facets of these TMCs in this work for NRR. The thermodynamics of the cathode reaction is studied by means of Density Functional Theory (DFT) calculations. Free energy diagrams are built to clarify the electrochemical protonation of surface carbon or metal atoms, and we obtain the onset potentials needed for ammonia production on these TMC structures. Incorporating the influence of an external bias, we determine the lowest onset potential required for ammonia generation on each carbide by referring to the computational hydrogen electrode [48]. This supports the conclusion that the thermodynamics of adsorbed intermediates is sufficient to predict onset potential [35,49].

2. Materials and Methods

2.1. Modeling Parameters

Within the framework of DFT, we employ the Revised Perdew–Burke–Ernzerhof (RPBE) [50] exchange–correlation functional in our computer simulations. The Vienna ab initio simulation package (VASP) [51] is utilized in these simulations, with a 400 eV energy cutoff for each surface calculation and a Monkhorst-Pack K-point grid of $4 \times 4 \times 1$. VASP integrates the projector augmented wave (PAW) technique [52], which minimizes calculation time by using computationally efficient pseudopotentials [53]. With a smearing value of $k_BT = 0.1$ eV, we apply a Fermi–Dirac distribution to control the electron distribution and guarantee a smooth Kohn–Sham orbital occupancy. With an emphasis on the (110) surface orientation, every surface is examined within the framework of the rock salt (RS) crystallographic structure. As seen in Figure 1, the TMC surfaces are modeled using a 5-layer 2×2-unit cell with 20 metal atoms and 20 carbon atoms on the (110) facets.

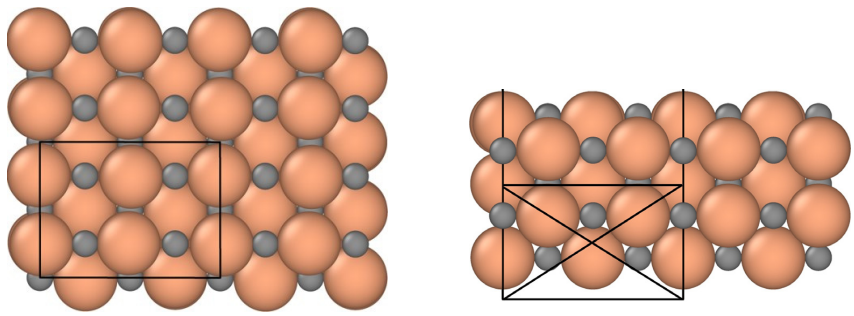

(**a**) (**b**)

Figure 1. The (**a**) top view and the (**b**) side view of a model diagram of the TMC used in this simulation. The orange and gray circles show the metal and carbon atoms, respectively.

In our model, the top three layers and any adsorbates are permitted to relax, while the bottom two layers hold onto their equilibrium bulk structure. In the x and y dimensions, we impose periodic boundary conditions, while keeping a minimum distance of 15 Å in the z direction between each surface slab. When the collective forces on all mobile atoms are less than 0.01 eV/Å, structural optimization is said to be optimized. We utilize the climbing image nudged elastic band (CI-NEB) technique to determine the highest point along the minimum energy path (MEP) [54] in order to compute activation energies. In this work, we also use the previously described Bader analysis and charge density difference [55,56]. Supplementary Table S2 lists the optimized lattice constants.

2.2. Electrochemical Modeling and Reaction Pathways

We used the subsequent equations to model the whole chemical pathway responsible for ammonia synthesis:

$$N_2 + 6(H^+ + e^-) \rightleftharpoons 2NH_3 \quad (1)$$

$$H_2 \rightleftharpoons 2(H^+ + e^-) \quad (2)$$

Nitrogen molecules, protons produced at the anode (Equation (2)), and electrons coming from the applied voltage, are the essential components of the electrochemical cell for ammonia synthesis at the cathode (Equation (1)). We can directly link the applied voltage with either the standard hydrogen electrode (SHE) or the reversible hydrogen electrode (RHE) because the required protons are exclusively created at the anode and our modeling is carried out under zero pH circumstances. Our modeling stays unaffected by the experimental arrangement, whether it is a flow cell, batch cell, or gas diffusion electrode (GDE) cell. The chemical process is simulated utilizing an unconstrained mechanism in which the most thermodynamically favorable adsorption site is investigated for each protonation step and serves as the foundation for succeeding protonation stages that lead to product formation. The preferred way for thoroughly understanding a catalyst's catalytic efficiency and the resultant products is to use an unrestricted mechanism. The following equation is used to compute the change in free energy for each reaction step.

$$\Delta G_i(U_{RHE}) = \Delta G_i\ (U_{RHE} = 0) + neU_{RHE} \quad (3)$$

$$eU_{RHE} = eU_{SHE} + 2.3k_BTpH \quad (4)$$

In this case, U_{SHE} symbolizes the applied potential in reference to the standard hydrogen electrode, n the number of electrons, e the elementary charge, k_B the Boltzmann constant, and T the temperature. By adding Equation (4) into Equation (3), we obtain the following:

$$\Delta G_i(U_{RHE}, pH) = \Delta G_i\ (U_{RHE} = 0) + n(eU_{SHE} + 2.3k_BTpH) \quad (5)$$

Here, the onset potential is pH-independent, as it is reported vs. RHE. Every elementary step has its $\Delta G_i(U = 0)$, computed as follows:

$$\Delta G_i(U = 0) = \Delta E_{DFT} + \Delta E_{ZPE} + \Delta H_{0K\rightarrow T} - T\Delta S \quad (6)$$

Whereas ΔE_{ZPE} and ΔS stand for zero-point energy corrections and entropy differences, DFT is used to calculate ΔE_{DFT}. These adjustments are determined for the adsorbed intermediates using the harmonic approximation; however, for gas-phase molecules, they are taken from Reference [57].

$\Delta H_{0K\rightarrow T}$ is the temperature-related change in internal energy and is calculated as follows:

$$\Delta H_{0K\rightarrow T} = \int_0^T C_P\ (T')\ dT' \quad (7)$$

The specific heat capacity at constant pressure is represented by $Cp(T')$ in Equation (7). The internal energy at ambient temperature is negligibly affected by the integral term in the equation, with a potential contribution of less than 0.1 eV [58].

The electrochemical reaction that results in the most substantial positive change in free energy within a specific reaction pathway is known as the potential determinant step (PDS). The onset potential (OP) is the potential required to neutralize the change in the free energy of the PDS. As a result, the free energy of all subsequent reaction steps decreases, resulting in a downward trajectory, as described in Equation (6). The OP is subsequently expressed as follows:

$$OP = -\Delta G/e \quad (8)$$

The negative shift in free energy connected with the PDS is measured in volts and is known as the OP.

3. Results

Initially, a computational screening technique is applied to assess a variety of TMC catalysts. These catalysts include elements from groups III to VI and have an RS structure with (110) facets. This extensive investigation analyzes a total of 12 TMC surfaces, including ScC, YC, TiC, VC, CrC, YC, ZrC, NbC, MoC, HfC, TaC, and WC. These catalysts exhibit stability and are thus chosen for further comprehensive study as candidate catalysts for the NRR.

The evaluation method for these TMC candidates, aiming to generate ammonia electrochemically at ambient conditions, consists of a comprehensive analysis of five important variables: (i) The mechanism of the NRR is determined by examining the distinct paths and reactions facilitated by each TMC. (ii) The evaluation of surface poisoning is conducted to determine the vulnerability of each TMC surface to chemicals that may hinder their catalytic activity. (iii) An evaluation is conducted to assess the overall catalytic performance of each TMC to determine its level of efficiency and efficacy in promoting the NRR. (iv) A volcano-plot analysis is performed to show the optimal performance of each TMC based on a reactivity descriptor. (v) A Bader charge analysis and charge distribution analysis are performed, utilizing charge iso-surfaces to visually comprehend the electronic charge transfer on the TMC surfaces.

This study attempts to discover the most promising catalysts among 12 TMC(110) surfaces for sustainable ammonia synthesis using the NRR under ambient conditions by incorporating these five comprehensive variables.

3.1. Mechanism of Nitrogen Reduction Reaction

As discussed in our previous work [29–31], we looked into three different mechanisms for the NRR. These mechanisms include the dissociative mechanism (DM), the associative mechanism (AM), and the Mars–van Krevelen mechanism (MvK). The strong triple bond that exists between nitrogen atoms in the DM is broken when N_2 binds the surface of the catalyst, which could be an atom of carbon or metal. The ultimate result of this mechanism is that each nitrogen atom independently binds to the catalyst.

In the AM, N_2 adsorbs onto the surface of the catalyst and goes through bond cleavage at a certain step of the hydrogenation reaction. This is the opposite to the direct cleavage that occurs in the DM. Within the confines of this framework, we investigated the possibility that adsorbed NNH (*NNH) (In the case of adsorbed species, indicated by *) should play the role of an intermediate in the reaction pathway. Incorporating the adsorption of NNH into our free energy diagrams was necessary in order to acquire a complete comprehension of the mechanism itself. We were able to provide greater insights into the overall reaction paths and the efficiency of the AM in boosting ammonia synthesis as a result of this addition, which enabled us to more precisely define the energy environment and identify steps that were thermodynamically beneficial.

In the MvK mechanism, lattice carbon atoms on the surfaces of TMCs are converted into methane. This conversion is dependent on whether proton adsorption takes place

on carbon sites or the metal site, respectively. During this process, surface vacancies are created, which are essential for the continuation of catalytic activity. It is possible for nitrogen molecules to fill these vacancies through either an associative MvK or dissociative MvK process, which will result in the catalyst being efficiently regenerated.

3.2. Surface Poisoning

Before initiating any reaction, it is critical to thoroughly investigate how nitrogen species adhere to the catalyst surface. This is especially relevant when competing species such as H, oxygen (O), and hydroxyl (OH) are present in the aqueous environment. We looked at three types of nitrogen adsorption: associative adsorption of N_2 molecules, dissociative adsorption of nitrogen molecules (*2N), and associative adsorption of NNH molecules. These scenarios were compared to the adsorption of H, O, OH, and H_2O to determine how they would compete with one another and how likely it is that these species will block the active site. Figure 2 shows more information about the results, helping us to understand how the adsorption works and how the competing forces affect it.

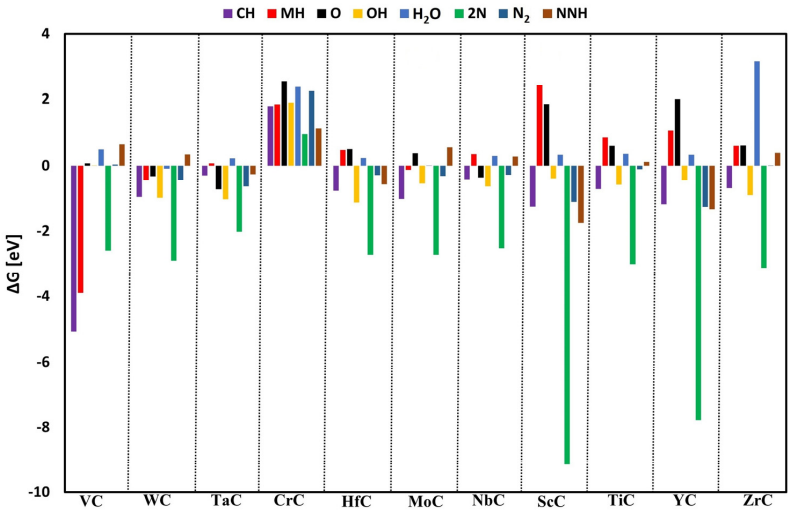

Figure 2. Adsorption of different intermediates on the pristine structures of TMCs at zero potential.

The results showed that most TMCs are better at attracting dissociated nitrogen (*2N) than other species. The only one that did not do this well was VC, which had a different binding pattern. Because of this, it seems that TMCs generally prefer the dissociative adsorption route for nitrogen, which could be good for the NRR. In addition, we looked at how protons attached to the metal surfaces to see how likely it was that the hydrogen evolution reaction (HER) would take place. It is interesting to see that protons always move to the carbon sites instead of staying on the metal sites. This pattern of activity suggests that proton adsorption on metal sites, which would lead to HER, is not likely for all the TMCs that were tested.

3.3. Catalytic Activity

We conducted a thorough examination of the reactions that occur on the RS (110) facets of TMCs, assessing several processes previously described for all TMCs under consideration. However, for the sake of simplicity and clarity, we included free energy diagrams only for the most promising candidates, with comprehensive data for the remaining TMCs accessible in the Supplementary Materials/electronic supplementary information (ESI).

Figure 3 shows that the AM is the best pathway for creating ammonia on TaC and WC. N_2 is adsorbed exergonically onto the catalyst surface, and the initial proton preferentially

binds to the surface carbon rather than the adsorbed nitrogen. When the surface has reached a half-monolayer coverage of protons, the fifth proton binds with N_2 to create NNH, as shown in Supplementary Figure S1. After ten protonation steps, we have two ammonia molecules, with a PDS of 0.69 eV. Furthermore, adsorbing NNH rather N_2 on the surface tuned the PDS from 0.69 to 0.66 eV, favoring NH_3 generation.

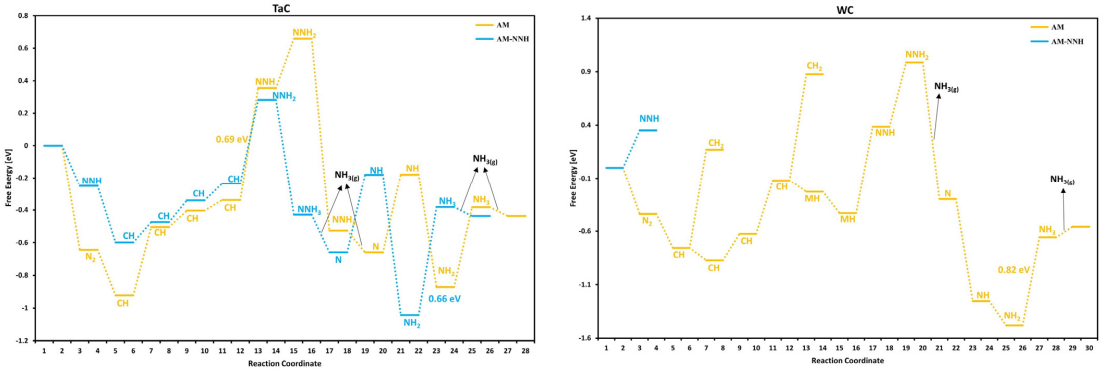

(**a**) (**b**)

Figure 3. Free energy diagrams for (**a**) TaC and (**b**) WC at zero potential.

We also investigated the MvK mechanism, which considers carbon vacancies as either CH_4 or surface defects and fills them with nitrogen gas in several types of forms: associatively as N_2, dissociatively as 2N, and associatively as NNH. Supplementary Figure S2a indicates that the MvK mechanism is ineffective at ambient temperatures due to the high PDS.

In the instance of WC, the adsorption of NNH is endergonic; thus, we begin with the AM pathway. After a half-monolayer of protons, the fifth proton attaches to metal rather than N_2. Following the ninth protonation step, the first ammonia molecule is released automatically, resulting in the synthesis of two ammonia molecules after twelve steps with a PDS of 0.82 eV. The MvK mechanism was also tested for WC; however, it was ineffectual due to the high PDS, which prevents ammonia production, as shown in Supplementary Figure S2b. We did not account for solvation in this study because Hoskuldsson et al. [49] recently found that, for a Wolfram catalyst with and without a water bilayer, the solvation effect is minimal in most cases (less than 0.05 eV), except for the NNH species (0.14 eV) and NH_3 species (0.13 eV). This minor correction has not been included here, as it falls within the typical uncertainty range of DFT calculations, especially as we are conducting a screening study for several surfaces, and this minor addition will be ruled out.

None of the other materials examined, as shown in Supplementary Figures S3–S11, were active for NRR in ambient circumstances.

3.4. Exploring the Scaling Relations and Formation of Volcano Plots

A key graphic tool in electrocatalysis, the volcano plot, shows how different catalysts' binding energy to reaction intermediates relates to their catalytic activity. This plot, so named because of its characteristic "volcano" appearance, shows that catalytic activity peaks at an ideal binding energy and decreases on either side of this peak. The peak of the volcano represents the perfect equilibrium between the energies of adsorption and desorption: the catalyst binds intermediate strongly enough to promote reaction without binding so strongly that it prevents desorption. Reaction rates are lowered by too-strong binding, which is seen in catalysts on the left slope of the volcano plot. On the other hand, too weakly bound intermediates by catalysts on the right slope cause insufficient adsorption to efficiently drive the process.

As it gives researchers a precise target at the top of the volcano, where binding energy is optimized for maximal catalytic activity, the volcano plot is an important tool in catalyst

design. We can build a volcano diagram by using linear relations for different reaction steps as a function of the Gibbs free energy change (ΔG) of $*N_2$ (used as a descriptor). This technique, which is described in Reference [59], has already been used to electrolyze water on oxide surfaces. With this method, electrocatalytic activity is directly indicated by the potential connected with the PDS. Every elementary step in the overall reaction has its free energy stated as a function of the applied bias (U) and the ΔG of N_2, represented by $*N_2$. Figure 4, however, shows only the two PDSs.

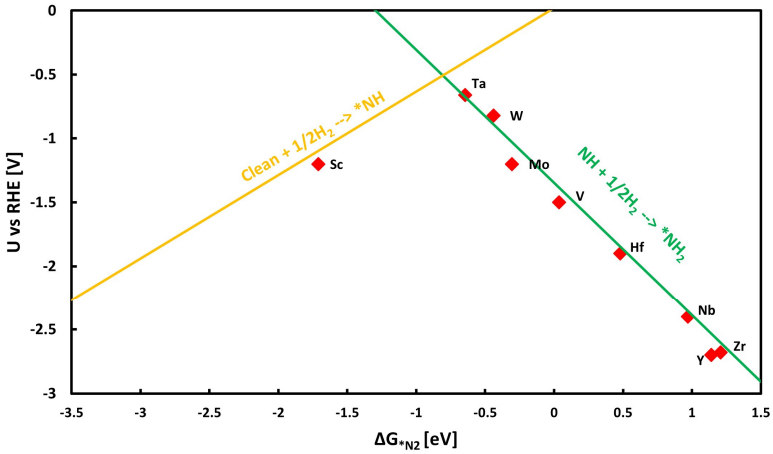

Figure 4. Volcano plot illustrates the relationship between the free energy change of nitrogen adsorption (ΔG*N_2) and the applied voltage (U vs. RHE) for various TMCs.

Assuming the AM, we may build the volcano figure, as seen in Figure 4, using the linear scaling relationships from Supplementary Figures S12 and S13. Notably, TaC and WC are shown to have better catalytic performance with low onset potential by being at the top of the volcano plot. A logical design and selection of very effective electrocatalysts is made possible by this thorough knowledge of the relation between binding energy and catalytic activity.

3.5. Bader Charge Analysis and Charge Iso-Surfaces

We determined charge iso-surfaces by calculating charge density differences using the following equation:

$$\Delta P = Ptot - Ppristine - Pgas \quad (9)$$

In this equation, Ptot, Ppristine, and Pgas represent the charge density for the species adsorbed on the TaC and WC system, and the isolated gas molecules, respectively. The color scheme employed uses yellow to denote regions of charge accumulation and cyan to indicate areas of charge depletion. Figure 5a–g illustrate the charge density difference for various species adsorbed on the TaC surfaces, while the data for WC can be seen in Supplementary Figure S14.

To quantify the extent of charge transfer, we conducted a Bader charge analysis, with the results detailed in Table 1. It is crucial to note that a positive ΔQ value in Table 1 indicates a charge transfer from the TaC and WC layer to the gas molecule, whereas a negative ΔQ value suggests a charge transfer from the gas molecule to the TaC and WC layer. An examination of Table 1 reveals that, in the hydrogen-adsorbed system, there was a net charge transfer of 0.02 and 0.09 electrons from the hydrogen adatom to the TaC and WC substrate. Conversely, in the nitrogen (N_2)-adsorbed system, a charge transfer of 0.74 and 0.19 electrons occurred from the TaC and WC substrate to the nitrogen molecule.

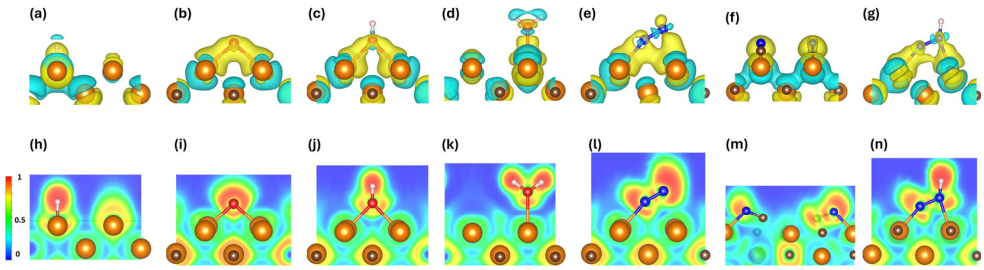

Figure 5. The charge density difference of (**a**) H adsorbed on the surface, (**b**) O on the surface, (**c**) OH on the surface, (**d**) H_2O on the surface, (**e**) N_2 associatively on the surface, (**f**) N_2 dissociatively on the surface, (**g**) NNH on the surface, and (**h–n**) represent the Electron Localization Function (ELF) of these species on TaC system. The yellow color shows charge accumulation and cyan represents charge depletion. The red (1) is associated with high values of electron localization function (ELF), indicating regions where electrons are more localized or confined, such as around lone pairs or in localized bonds. On the other hand, blue (0) is associated with low ELF values, representing regions where electrons are more delocalized or spread out.

Table 1. Bader charges (ΔQ) in the unit of e for electron charge for TaC and WC.

ΔQ(e)	H	O	OH	H_2O	N_2	2N	NNH
TaC	0.02	−1.0	−0.38	0.02	−0.74	−2.77	−0.87
WC	0.09	−0.84	−0.49	0.06	−0.19	−2.62	−0.44

Additionally, we employed the ELF to assess electron density behavior, which aids in distinguishing between localized regions (indicative of paired or lone pairs of electrons) and more distributed areas (shared among multiple atoms) [60]. In our study, we examined ELF values for the most favorable adsorption sites of various species on the TaC and WC systems. ELF values range from 0 to 1, representing complete delocalization, as seen in metallic systems, to strong localization, such as in lone pairs or covalent bonds. The expected ELF results for species absorbed on TaC (110) facets are shown in Figure 5h–n, while for WC, such results are shown in Supplementary Figure S14.

Overall, the ELF outcomes underscore the covalent bonding characteristics of all species on TaC and WC, indicating shared-electron interactions. This analysis provides insight into the nature of the chemical bonds formed between the adsorbed species and the TaC and WC substrate, revealing the extent and nature of electron sharing in these systems.

4. Conclusions

Achieving environmentally friendly and sustainable ammonia production can be accomplished by converting N_2 to NH_3 efficiently. One promising approach to achieve this, using less energy and renewable power, is the electrochemical reduction of N_2. This paper addresses this gap by investigating possible catalysts for nitrogen electro-reduction to ammonia at ambient temperature. Using density functional theory calculations, we study the (110) facets of rock salt structures for 12 different transition metal carbides. We evaluate the catalytic activity of these materials using free energy diagrams of the Mars–van Krevelen, associative, and dissociative reaction mechanisms. Additionally, we assess the materials' resistance to electrochemical poisoning and degradation into their constituent metals during operation. Under ambient conditions, tantalum carbide (TaC) and tungsten carbide (WC) exhibit low onset potentials (−0.66 V and −0.82 V vs. RHE, respectively) following the associative mechanism, indicating that only a few candidates show potential for nitrogen reduction processes. This study enhances our understanding of nitrogen electro-reduction and paves the way for more efficient and environmentally friendly ammonia production methods.

Supplementary Materials: The following supporting information can be downloaded at https://www.mdpi.com/article/10.3390/cryst14090770/s1, Table S1: The zero-point energy (ZPE) and entropy correction parameters have been determined for all the employed adsorbed and gas phase substances. ZPE values for adsorbed substances were computed on the [110] TaC surface, while gas phase values were sourced from reference [1]. In the case of adsorbed species, indicated by *. Table S2: shows the lattice constants of TMC in (110) facets. Figure S1: shows the associative pathway for TaC; Figure S2: The MvK path for (a) TaC and (b) WC at zero potential; Figure S3: The free energy diagram for CrC at zero potential; Figure S4: The free energy diagram for HfC at zero potential; Figure S5: The free energy diagram for MoC at zero potential; Figure S6: The free energy diagram for NbC at zero potential; Figure S7: The free energy diagram for ScC at zero potential; Figure S8: The free energy diagram for TiC at zero potential; Figure S9: The free energy diagram for VC at zero potential; Figure S10: The free energy diagram for YC at zero potential; Figure S11: The free energy diagram for ZrC at zero potential; Figure S12: The scaling relation from which the volcano plot has been made; Figure S13: The theoretical volcano plot; Figure S14: The charge density difference of (a) H adsorbed on the surface (b) O on the surface (c) OH on the surface (d) H_2O on the surface (e) N_2 associatively on the surface (f) N_2 dissociatively on the surface (g) NNH on the surface and (h–n) represent the ELF of these species on WC system; Reference [61] is cited in supplementary materials.

Author Contributions: A.I. conducted the modeling and calculations, extracted the data, constructed the figures, and wrote the first draft of the manuscript; E.S. read the manuscript and commented on it; Y.A. conceptualized the idea, read the manuscript, commented on it, and provided funding for performing the research. All authors have read and agreed to the published version of the manuscript.

Funding: This work was supported by the Icelandic Research Fund [grant number 207056].

Data Availability Statement: The data are provided in the Supplementary Materials.

Acknowledgments: Computational resources were provided by the Icelandic research high-performance computing cluster.

Conflicts of Interest: The authors declare no conflict of interest.

References

1. Bao, D.; Zhang, Q.; Meng, F.L.; Zhong, H.X.; Shi, M.M.; Zhang, Y.; Yan, J.M.; Jiang, Q.; Zhang, X.B. Electrochemical reduction of N_2 under ambient conditions for artificial N_2 fixation and renewable energy storage using N_2/NH_3 cycle. *Adv. Mater.* **2017**, *29*, 1604799. [CrossRef]
2. Howalt, J.G.; Vegge, T. Electrochemical ammonia production on molybdenum nitride nanoclusters. *Phys. Chem. Chem. Phys.* **2013**, *15*, 20957–20965. [CrossRef]
3. Zhang, L.; Ji, X.; Ren, X.; Ma, Y.; Shi, X.; Tian, Z.; Asiri, A.M.; Chen, L.; Tang, B.; Sun, X. Electrochemical ammonia synthesis via nitrogen reduction reaction on a MoS_2 catalyst: Theoretical and experimental studies. *Adv. Mater.* **2018**, *30*, 1800191. [CrossRef]
4. Liu, C.; Li, Q.; Zhang, J.; Jin, Y.; MacFarlane, D.R.; Sun, C. Theoretical evaluation of possible 2D boron monolayer in N_2 electrochemical conversion into ammonia. *J. Phys. Chem. C* **2018**, *122*, 25268–25273. [CrossRef]
5. Zhang, X.; Wu, T.; Wang, H.; Zhao, R.; Chen, H.; Wang, T.; Wei, P.; Luo, Y.; Zhang, Y.; Sun, X. Boron nanosheet: An elemental two-dimensional (2D) material for ambient electrocatalytic N_2-to-NH_3 fixation in neutral media. *ACS Catal.* **2019**, *9*, 4609–4615. [CrossRef]
6. Zhao, J.; Zhang, L.; Xie, X.Y.; Li, X.; Ma, Y.; Liu, Q.; Fang, W.-H.; Shi, X.; Cui, G.; Sun, X. Ti_3C_2Tx (T = F, OH) MXene nanosheets: Conductive 2D catalysts for ambient electrohydrogenation of N_2 to NH_3. *J. Mater. Chem. A* **2018**, *6*, 24031–24035. [CrossRef]
7. Azofra, L.M.; Li, N.; MacFarlane, D.R.; Sun, C. Promising prospects for 2D d^2–d^4 M_3C_2 transition metal carbides (MXenes) in N_2 capture and conversion into ammonia. *Energy Environ. Sci.* **2016**, *9*, 2545–2549. [CrossRef]
8. Azofra, L.M.; Sun, C.; Cavallo, L.; MacFarlane, D.R. Feasibility of N_2 binding and reduction to ammonia on Fe-deposited MoS_2 2D sheets: A DFT study. *Chem.–A Eur. J.* **2017**, *23*, 8275–8279. [CrossRef]
9. Luo, Y.; Chen, G.F.; Ding, L.; Chen, X.; Ding, L.X.; Wang, H. Efficient electrocatalytic N_2 fixation with MXene under ambient conditions. *Joule* **2019**, *3*, 279–289. [CrossRef]
10. Schlögl, R. Catalytic synthesis of ammonia—A "never-ending story"? *Angew. Chem. Int. Ed.* **2003**, *42*, 2004–2008. [CrossRef]
11. Koebel, M.; Madia, G.; Elsener, M. Selective catalytic reduction of NO and NO_2 at low temperatures. *Catal. Today* **2002**, *73*, 239–247. [CrossRef]
12. Le, Y.-Q.; Gu, J.; Tian, W.Q. Nitrogen-fixation catalyst based on graphene: Every part counts. *Chem. Commun.* **2014**, *50*, 13319–13322. [CrossRef]
13. Chirik, P.J. One electron at a time. *Nat. Chem.* **2009**, *1*, 520–522. [CrossRef]
14. Van der Ham, C.J.; Koper, M.T.; Hetterscheid, D.G. Challenges in reduction of dinitrogen by proton and electron transfer. *Chem. Soc. Rev.* **2014**, *43*, 5183–5191. [CrossRef] [PubMed]

15. Kadac-Czapska, K.; Knez, E.; Gierszewska, M.; Olewnik-Kruszkowska, E.; Grembecka, M. Microplastics derived from food packaging waste—Their origin and health risks. *Materials* **2023**, *16*, 674. [CrossRef]
16. Paal, Z.; Ertl, G.; Lee, S. Interactions of potassium, oxygen and nitrogen with polycrystalline iron surfaces. *Appl. Surf. Sci.* **1981**, *8*, 231–249. [CrossRef]
17. Ertl, G.; Weiss, M.; Lee, S. The role of potassium in the catalytic synthesis of ammonia. *Chem. Phys. Lett.* **1979**, *60*, 391–394. [CrossRef]
18. Spencer, N.; Schoonnaker, R.; Somorjai, G. *Structure Sensitivity in the Iron Single Crystal Catalysed Synthesis of Ammonia*; Lawrence Berkeley National Laboratory: Berkeley, CA, USA, 1981.
19. Ertl, G.; Lee, S.; Weiss, M. Kinetics of nitrogen adsorption on Fe (111). *Surf. Sci.* **1982**, *114*, 515–526. [CrossRef]
20. Ertl, G.; Lee, S.; Weiss, M. Adsorption of nitrogen on potassium promoted Fe (111) and (100) surfaces. *Surf. Sci.* **1982**, *114*, 527–545. [CrossRef]
21. Bragulla, S.C.H.; von Seggern, A.R.; Lorenz, J.; Harms, C.; Wark, M.; Friedrich, K.A. Improving the Ca-assisted Urea-Glass Method for the Synthesis of Zirconium Nitride as Potential Electrocatalyst for the Nitrogen Reduction Reaction. *ChemCatChem* **2024**, e202400613. [CrossRef]
22. Ješić, D.; Pomeroy, B.; Kamal, K.M.; Kovačič, Ž.; Huš, M.; Likozar, B. Photo-and Photoelectrocatalysis in Nitrogen Reduction Reactions to Ammonia: Interfaces, Mechanisms, and Modeling Simulations. *Adv. Energy Sustain. Res.* **2024**, 2400083. [CrossRef]
23. Guo, P.; Yin, F.; Ni, Z.; Li, G.; Chen, B. MIL-101 (Fe) supported Au-Cu nanoalloy for enhanced electrochemical nitrogen fixation in gas–liquid-solid three-phase reactor. *Chem. Eng. J.* **2024**, *494*, 153134. [CrossRef]
24. Macfarlane, D.R.; Skúlason, E.; Hosono, H.; Shao, M. Preface to Special Issue on Sustainable Ammonia Synthesis. *ChemSusChem* **2024**, *17*, e20230139. [CrossRef] [PubMed]
25. Hanifpour, F.; Canales, C.P.; Fridriksson, E.G.; Sveinbjörnsson, A.; Tryggvason, T.K.; Yang, J.; Arthur, C.; Jónsdóttir, S.; Garden, A.L.; Ólafsson, S.; et al. Operando quantification of ammonia produced from computationally-derived transition metal nitride electro-catalysts. *J. Catal.* **2022**, *413*, 956–967. [CrossRef]
26. Hanifpour, F.; Sveinbjörnsson, A.; Canales, C.P.; Skúlason, E.; Flosadóttir, H.D. Preparation of nafion membranes for reproducible ammonia quantification in nitrogen reduction reaction experiments. *Angew. Chem.* **2020**, *132*, 23138–23142. [CrossRef]
27. He, T.; Chen, M.; Sun, H.; Mei, J.; Noufal, M.; Liu, Q.; Santiago, A.R.P. Chemical insights into the interfacial phenomena of low-dimensional heterointerfaces. *Chem* **2024**, *10*, 1974–1993. [CrossRef]
28. He, T.; Santiago AR, P.; Kong, Y.; Ahsan, M.A.; Luque, R.; Du, A.; Pan, H. Atomically dispersed heteronuclear dual-atom catalysts: A new rising star in atomic catalysis. *Small* **2022**, *18*, 2106091. [CrossRef]
29. Iqbal, A.; Sku, E.; Abghoui, Y. Catalytic Nitrogen Reduction on the Transition Metal Carbonitride (110) Facet: DFT Predictions and Mechanistic Insights. *J. Phys. Chem. C* **2024**, *128*, 10300–10307. [CrossRef]
30. Iqbal, A.; Skúlason, E.; Abghoui, Y. Are (100) facets of transition metal carbonitrides suitable as electrocatalysts for nitrogen reduction to ammonia at ambient conditions? *Int. J. Hydrogen Energy* **2024**, *64*, 744–753. [CrossRef]
31. Iqbal, A.; Skulason, E.; Abghoui, Y. Electrochemical Nitrogen Reduction to Ammonia at Ambient Condition on the (111) Facets of Transition Metal Carbonitrides. *ChemPhysChem* **2024**, *25*, e202300991. [CrossRef]
32. Ellingsson, V.; Iqbal, A.; Skúlason, E.; Abghoui, Y. Nitrogen reduction reaction to ammonia on transition metal carbide catalysts. *ChemSusChem* **2023**, *16*, e202300947. [CrossRef] [PubMed]
33. Abghoui, Y.; Iqbal, A.; Skúlason, E. The role of overlayered nitride electro-materials for N_2 reduction to ammonia. *Front. Catal.* **2023**, *2*, 1096824. [CrossRef]
34. Höskuldsson, Á.B.; Dang, T.; Sakai, Y.; Ishikawa, A.; Skúlason, E. High-throughput computational screening of doped transition metal oxides as catalysts for nitrogen reduction. *Cell Rep. Phys. Sci.* **2023**, *4*, 101595. [CrossRef]
35. Tayyebi, E.; Abghoui, Y.; Skulason, E. Elucidating the mechanism of electrochemical N_2 reduction at the Ru (0001) electrode. *ACS Catal.* **2019**, *9*, 11137–11145. [CrossRef]
36. Abghoui, Y.; Sigtryggsson, S.B.; Skúlason, E. Biomimetic nitrogen fixation catalyzed by transition metal sulfide surfaces in an electrolytic cell. *ChemSusChem* **2019**, *12*, 4265–4273. [CrossRef]
37. Abghoui, Y.; Garden, A.L.; Howalt, J.G.; Vegge, T.; Skúlason, E. Electroreduction of N_2 to ammonia at ambient conditions on mononitrides of Zr, Nb, Cr, and V: A DFT guide for experiments. *ACS Catal.* **2016**, *6*, 635–646. [CrossRef]
38. Abghoui, Y.; Skúlason, E. Electrochemical synthesis of ammonia via Mars-van Krevelen mechanism on the (111) facets of group III–VII transition metal mononitrides. *Catal. Today* **2017**, *286*, 78–84. [CrossRef]
39. Dahl, S.; Logadottir, A.; Egeberg, R.C.; Larsen, J.H.; Chorkendorff, I.; Törnqvist, E.; Nørskov, J.K. Role of steps in N_2 activation on Ru (0001). *Phys. Rev. Lett.* **1999**, *83*, 1814. [CrossRef]
40. Skulason, E.; Bligaard, T.; Gudmundsdóttir, S.; Studt, F.; Rossmeisl, J.; Abild-Pedersen, F.; Vegge, T.; Jónsson, H.; Nørskov, J.K. A theoretical evaluation of possible transition metal electro-catalysts for N_2 reduction. *Phys. Chem. Chem. Phys.* **2012**, *14*, 1235–1245. [CrossRef]
41. Jacobsen, C.J.; Dahl, S.; Hansen, P.L.; Törnqvist, E.; Jensen, L.; Topsøe, H.; Prip, D.V.; Møenshaug, P.B.; Chorkendorff, I. Structure sensitivity of supported ruthenium catalysts for ammonia synthesis. *J. Mol. Catal. A Chem.* **2000**, *163*, 19–26. [CrossRef]
42. Ham, D.J.; Lee, J.S. Transition metal carbides and nitrides as electrode materials for low temperature fuel cells. *Energies* **2009**, *2*, 873–899. [CrossRef]
43. Hwu, H.H.; Chen, J.G. Surface chemistry of transition metal carbides. *Chem. Rev.* **2005**, *105*, 185–212. [CrossRef]

44. Kelly, T.G.; Chen, J.G. Metal overlayer on metal carbide substrate: Unique bimetallic properties for catalysis and electrocatalysis. *Chem. Soc. Rev.* **2012**, *41*, 8021–8034. [CrossRef] [PubMed]
45. Esposito, D.V.; Chen, J.G. Monolayer platinum supported on tungsten carbides as low-cost electrocatalysts: Opportunities and limitations. *Energy Environ. Sci.* **2011**, *4*, 3900–3912. [CrossRef]
46. Esposito, D.V.; Hunt, S.T.; Stottlemyer, A.L.; Dobson, K.D.; McCandless, B.E.; Birkmire, R.W.; Chen, J.G. Low-cost hydrogen-evolution catalysts based on monolayer platinum on tungsten monocarbide substrates. *Angew. Chem. Int. Ed.* **2010**, *51*, 9859–9862. [CrossRef]
47. Kimmel, Y.C.; Yang, L.; Kelly, T.G.; Rykov, S.A.; Chen, J.G. Theoretical prediction and experimental verification of low loading of platinum on titanium carbide as low-cost and stable electrocatalysts. *J. Catal.* **2014**, *312*, 216–220. [CrossRef]
48. Nørskov, J.K.; Rossmeisl, J.; Logadottir, A.; Lindqvist, L.; Kitchin, J.R.; Bligaard, T.; Jónsson, H. Origin of the overpotential for oxygen reduction at a fuel-cell cathode. *J. Phys. Chem. B* **2004**, *108*, 17886–17892. [CrossRef]
49. Höskuldsson, Á.B.; Tayyebi, E.; Skúlason, E. Computational examination of the kinetics of electrochemical nitrogen reduction and hydrogen evolution on a tungsten electrode. *J. Catal.* **2021**, *404*, 362–370. [CrossRef]
50. Hammer, B.; Hansen, L.B.; Nørskov, J.K. Improved adsorption energetics within density-functional theory using revised Perdew-Burke-Ernzerhof functionals. *Phys. Rev. B* **1999**, *59*, 7413. [CrossRef]
51. Kresse, G.; Furthmüller, J. Efficient iterative schemes for ab initio total-energy calculations using a plane-wave basis set. *Phys. Rev. B* **1996**, *54*, 11169. [CrossRef]
52. Kresse, G.; Joubert, D. From ultrasoft pseudopotentials to the projector augmented-wave method. *Phys. Rev. B* **1999**, *59*, 1758. [CrossRef]
53. Blöchl, P.E. Projector augmented-wave method. *Phys. Rev. B* **1994**, *50*, 17953. [CrossRef] [PubMed]
54. Henkelman, G.; Uberuaga, B.P.; Jónsson, H. A climbing image nudged elastic band method for finding saddle points and minimum energy paths. *J. Chem. Phys.* **2000**, *113*, 9901–9904. [CrossRef]
55. Henkelman, G.; Arnaldsson, A.; Jónsson, H. A fast and robust algorithm for Bader decomposition of charge density. *Comput. Mater. Sci.* **2006**, *36*, 354–360. [CrossRef]
56. Gudmundsdóttir, S.; Tang, W.; Henkelman, G.; Jónsson, H.; Skúlason, E. Local density of states analysis using Bader decomposition for N_2 and CO_2 adsorbed on Pt (110)-(1 × 2) electrodes. *J. Chem. Phys.* **2012**, *137*, 164705. [CrossRef]
57. Bagger, A.; Arán-Ais, R.M.; Halldin Stenlid, J.; Campos dos Santos, E.; Arnarson, L.; Degn Jensen, K.; Escudero-Escribano, M.; Cuenya, B.R.; Rossmeisl, J. Ab initio cyclic voltammetry on Cu (111), Cu (100) and Cu (110) in acidic, neutral and alkaline solutions. *ChemPhysChem* **2019**, *20*, 3096–3105. [CrossRef]
58. Nørskov, J.K.; Studt, F.; Abild-Pedersen, F.; Bligaard, T. *Fundamental Concepts in Heterogeneous Catalysis*; John Wiley & Sons: Hoboken, NJ, USA, 2014.
59. Rossmeisl, J.; Qu, Z.-W.; Zhu, H.; Kroes, G.-J.; Nørskov, J. Electrolysis of water on oxide surfaces. *J. Electroanal. Chem.* **2007**, *607*, 83–89. [CrossRef]
60. Fan, K.; Ying, Y.; Li, X.; Luo, X.; Huang, H. Theoretical investigation of V_3C_2 MXene as prospective high-capacity anode material for metal-ion (Li, Na, K, and Ca) batteries. *J. Phys. Chem. C* **2019**, *123*, 18207–18214. [CrossRef]
61. Che, M.; Védrine, J.C. *Characterization of Solid Materials and Heterogeneous Catalysts: From Structure to Surface Reactivity*; John Wiley & Sons: Hoboken, NJ, USA, 2012.

Understanding the Mechanistic Pathways of N_2 Reduction to Ammonia on (110) Facets of Transition Metal Carbides

-Electronic supplementary information

Authors: Atef Iqbal, Egill Skulason, Younes Abghoui*

Zero-point energy and entropy corrections

Table S1: The zero-point energy (ZPE) and entropy correction parameters have been determined for all the employed adsorbed and gas phase substances. ZPE values for adsorbed substances were computed on the [110] TaC surface, while gas phase values were sourced from reference [1]. In the case of adsorbed species, indicated by *.

[110] TMC Surface	ZPE (eV)	TΔS (eV)
NH_3 (g)	0.89	0.74
H_2 (g)	0.27	0.41
CH_4 (g)	0.82	0.57
N_2 (g)	0.15	0.6
H_2O	0.58	0.65
*N	0.1	0.029
*NH	0.35	0.063
*NH_2	0.71	0.068
*NH_3	1.02	0.1429
*N_2^{vac}	0.23	0.137
*NNH	0.49	0.107
*NNH_2	0.86	0.088
*2N	0.23	0.075
*N.NH	0.47	0.175
*N.NH_2	0.86	0.112
*NHNH	0.76	0.1108
*NH.NH_2	1.09	0.1364
*NH_2.NH_2	1.41	0.16
*N.NH_3	1.41	0.2339
*NH_2.NH_3	1.68	0.106
*NH_3.NH_3	2.02	0.3227
*H^{vac}	0.17	0.0097
*CH	0.24	0.0184
*CH_2	0.61	0.069
*CH_3	0.94	0.071
*O^{2-}	0.07	0.07
*OH^-	0.38	0.07
*H_2O	0.67	0.14

Table S2 shows the lattice constants of TMC in (110) facets.

TMC	VC	NbC	WC	ZrC	HfC	TaC	TiC	MoC	CrC	ScC	YC
a (Å)	8.12	8.82	8.34	9.16	9.04	8.78	8.45	8.34	8.34	9.18	9.18
b (Å)	6.03	6.52	5.89	6.78	6.70	6.46	6.29	5.89	5.89	6.82	6.82

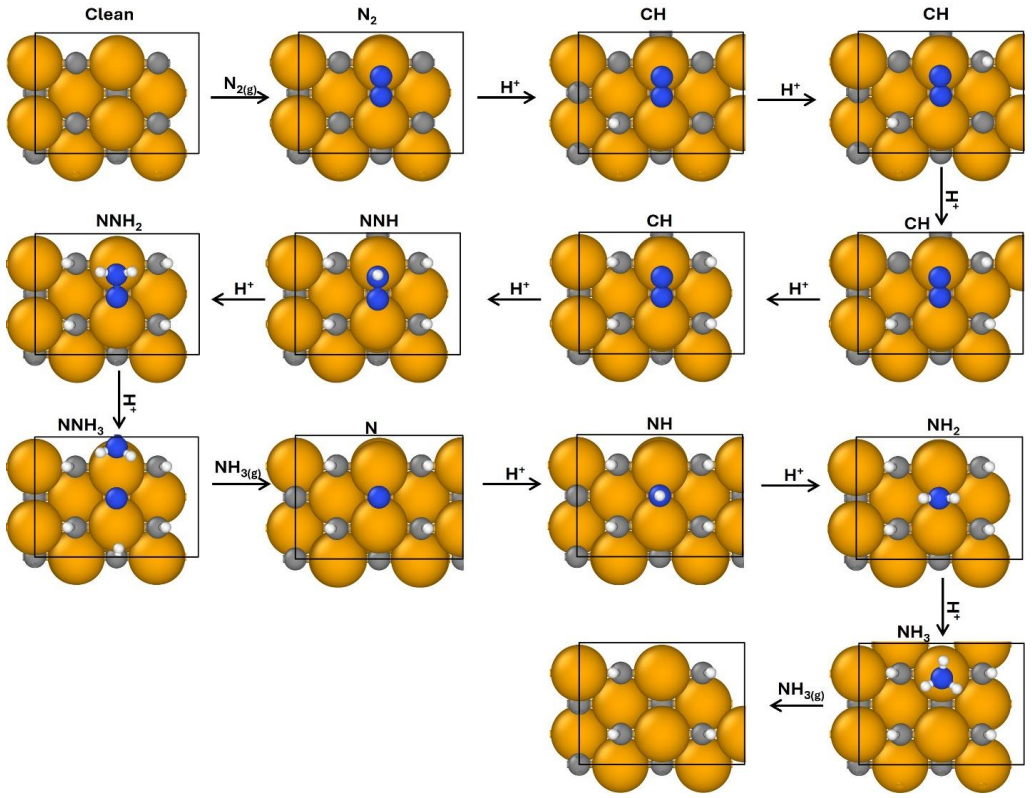

Figure S1 shows the associative pathway for TaC.

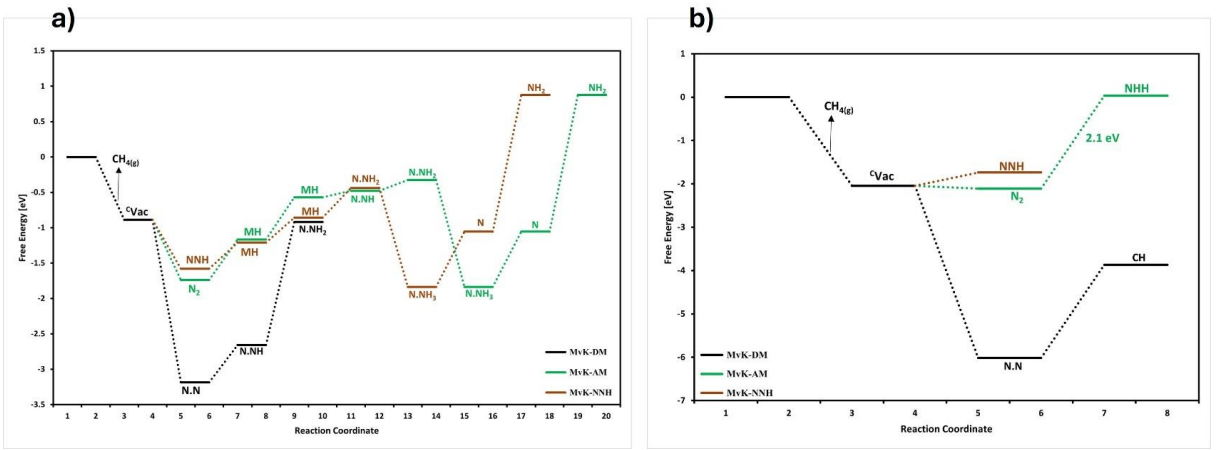

Figure S2 The MvK path for (a) TaC and (b) WC at zero potential.

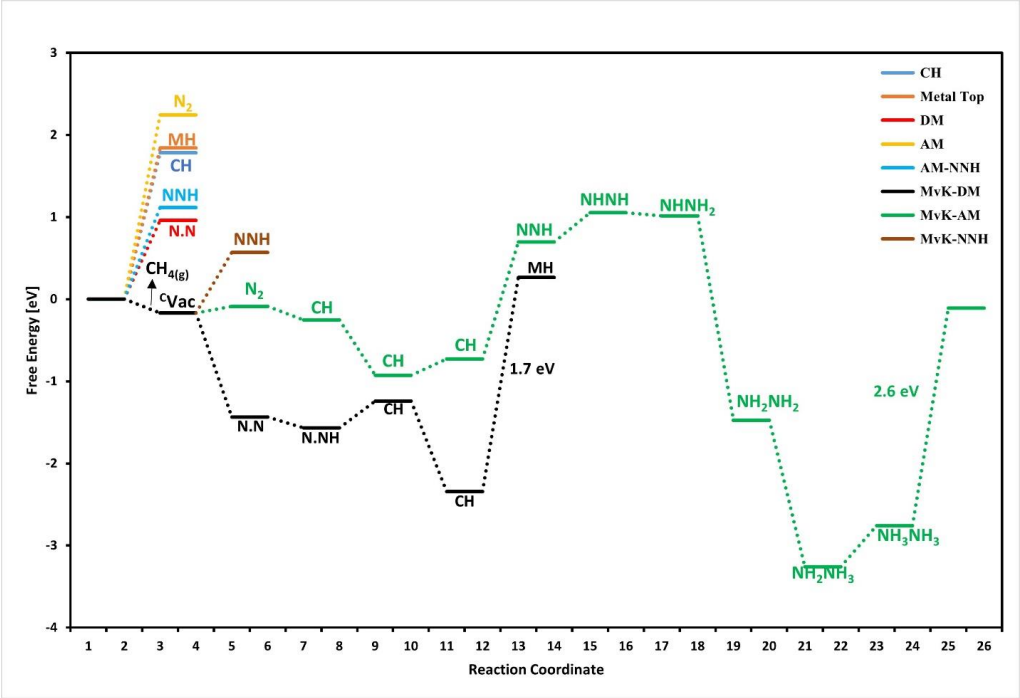

Figure S3: The free energy diagram for CrC at zero potential.

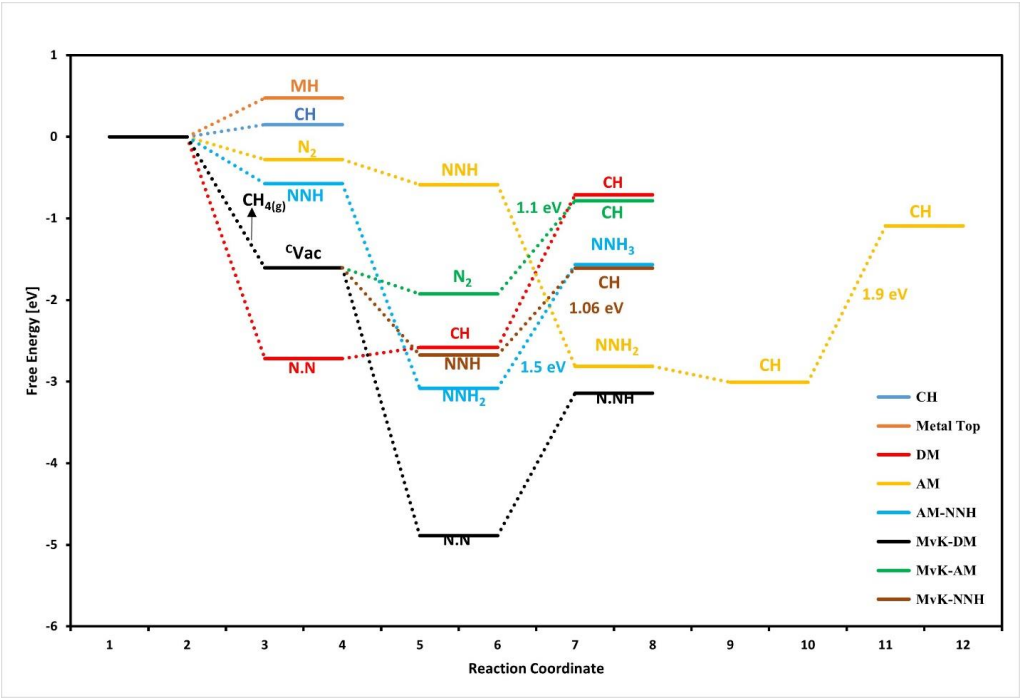

Figure S4: The free energy diagram for HfC at zero potential

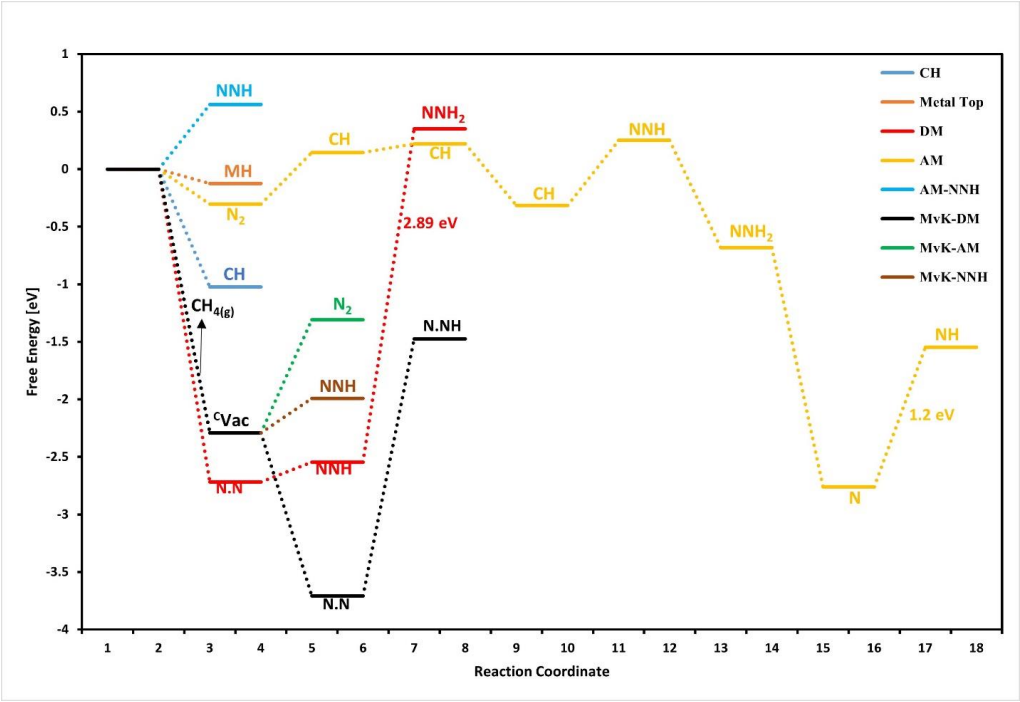

Figure S5: The free energy diagram for MoC at zero potential

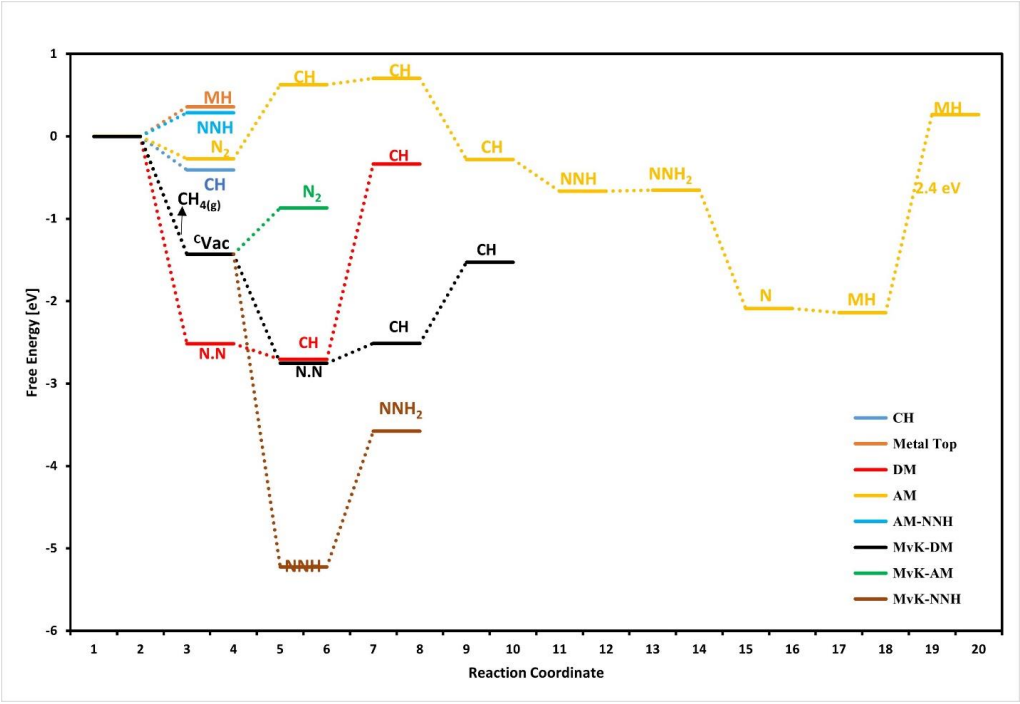

Figure S6: The free energy diagram for NbC at zero potential

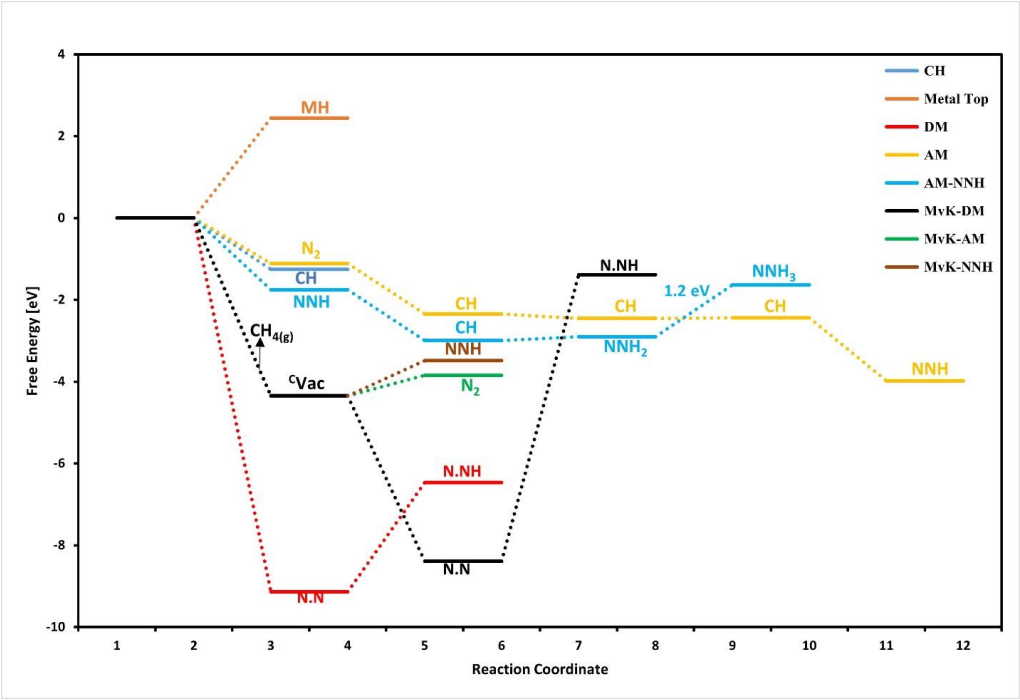

Figure S7: The free energy diagram for ScC at zero potential

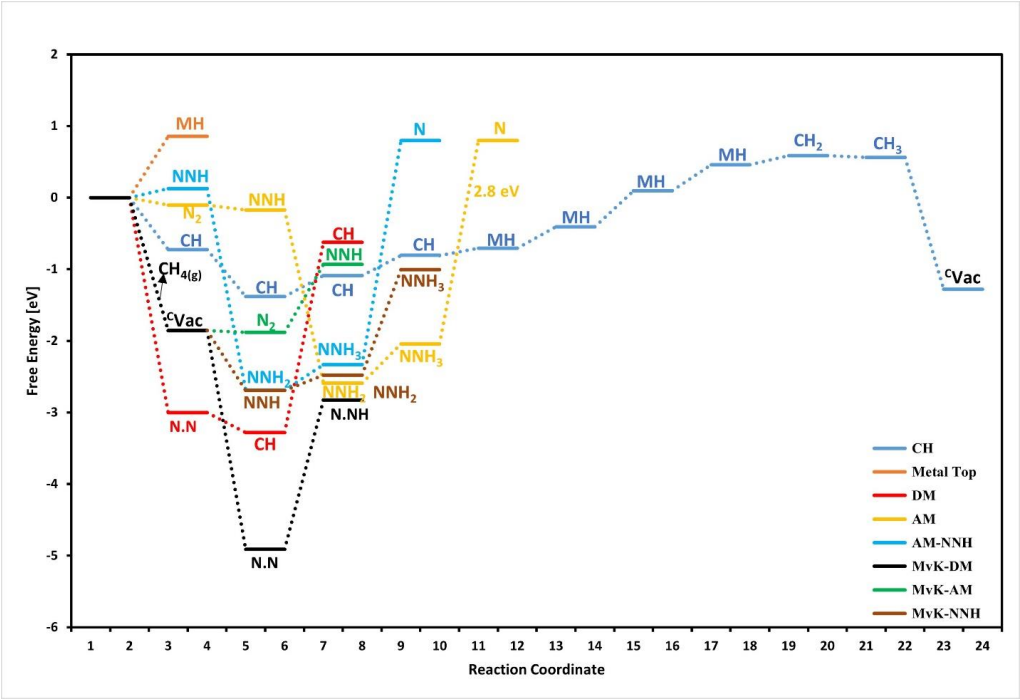

Figure S8: The free energy diagram for TiC at zero potential

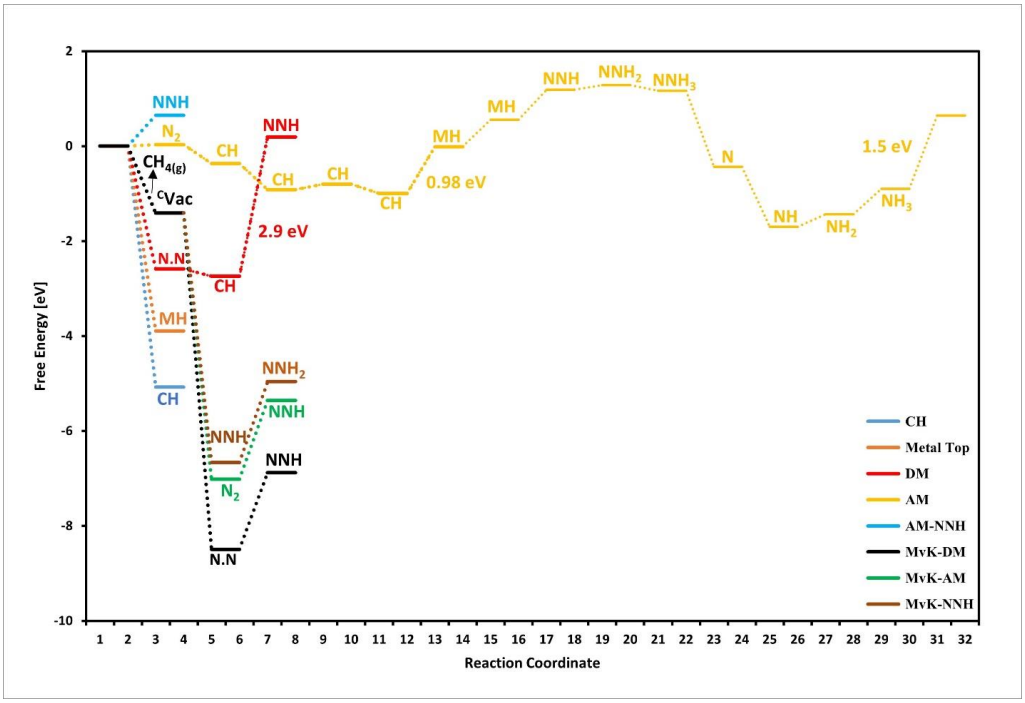

Figure S9: The free energy diagram for VC at zero potential

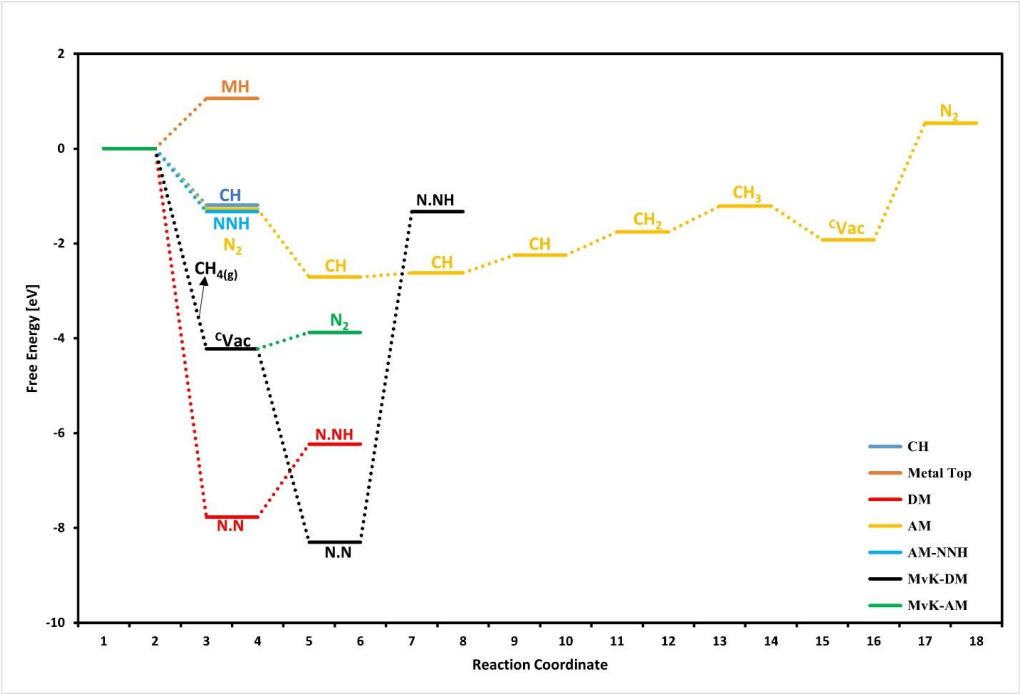

Figure S10: The free energy diagram for YC at zero potential

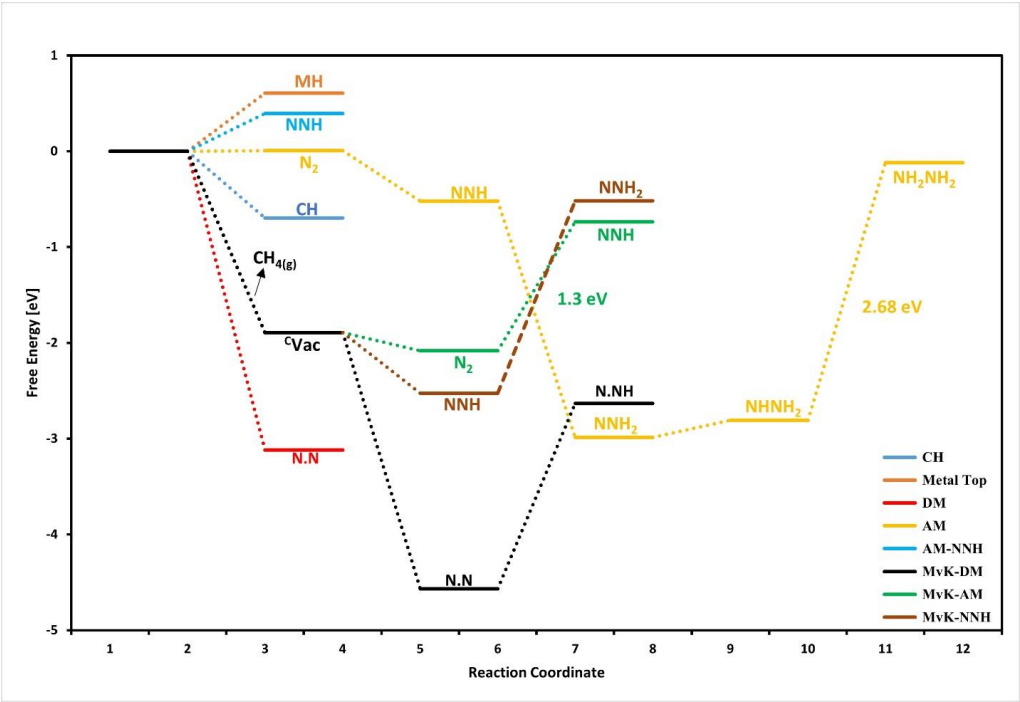

Figure S11: The free energy diagram for ZrC at zero potential

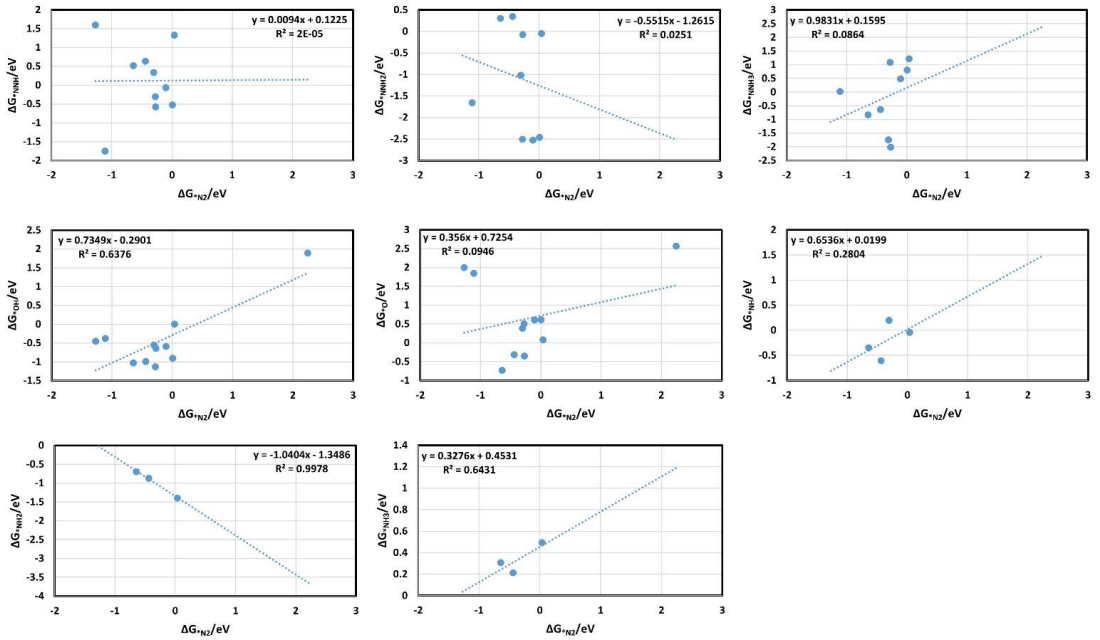

Figure S12: The scaling relation from which the volcano plot has been made.

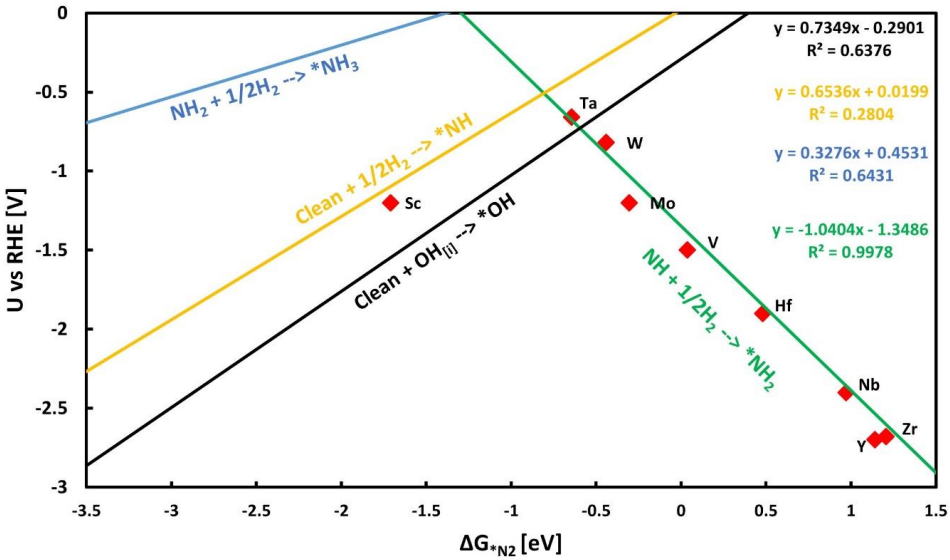

Figure S13: The theoretical volcano plot.

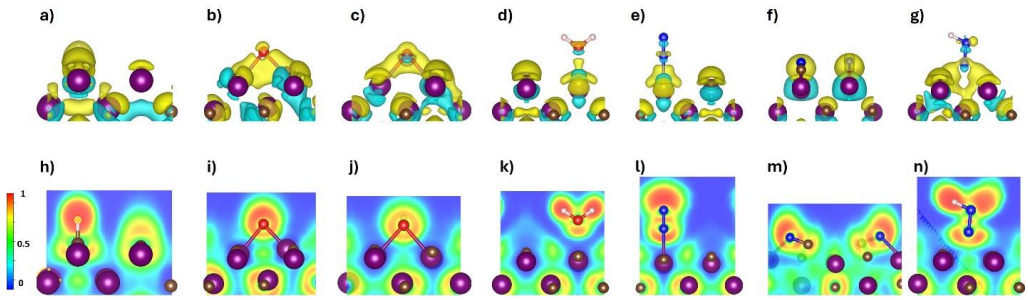

Figure S14: The charge density difference of (a) H adsorbed on the surface (b) O on the surface (c) OH on the surface (d) H_2O on the surface (e) N_2 associatively on the surface (f) N_2 dissociatively on the surface (g) NNH on the surface and (h-n) represent the ELF of these species on WC system.

References:

[1] Che, M. and J.C. Védrine, Characterization of solid materials and heterogeneous catalysts: From structure to surface reactivity. 2012: John Wiley & Sons.